High-Purity Oxygen Production by VPSA

Daniel António Santos Silva Ferreira

Dissertation presented to obtain the degree of

Doctor in Chemical and Biological Engineering

by the

University of Porto

Supervisor:

Adélio Miguel Magalhães Mendes, Full Professor

Coordinator at Sysadvance:

Patrick da Silva Bárcia, R&D Manager

LEPABE – Faculty of Engineering

University of Porto

Sysadvance – Sistemas de Engenharia, S.A.

2016

Acknowledgments

I would like to acknowledge Portuguese Foundation for Science and Technology (FCT) and Sysadvance, Sistemas de Engenharia, S.A. for my Ph.D grant (ref SFRH/BDE/51186/2010) and for all the support. Also, I would like to acknowledge Agência de Inovação (AdI), in the context of research project HPOVPSA (ref 13488), for funding.

My gratitude goes to my supervisors Professor Adélio Mendes, Dr. Patrick Bárcia and Eng. Pedro Taveira. I would like to thank Prof. Adélio Mendes for his supervision and support, to Dr. Patrick Bárcia for all the help and friendship, and Eng. Pedro Taveira for his advice.

I would like to express my gratitude to Dr. José Vale Machado for the opportunity to work and develop my PhD in business environment. Also, I would like to thank everyone at Sysadvance for always making me feel welcome there.

My thankful words are also directed to LEPABE, DEQ and FEUP for providing the necessary conditions to carry out my work, and my special recognition to D. Fátima Faustino, through her help and kindness in solving all kinds of administrative problems. Thanks to all my colleagues, particularly my PSA lab mate, Roberto Magalhães, for the companionship over these years.

I would like to special thank Air Products and Chemicals, Inc., namely Dr. Roger D. Whitley, for his valuable comments and for supplying the AgLiLSX zeolite.

Many thanks to all my friends and Redemptorist family, especially my fellow theologians and Andreia, for all the encouragement, life shared and common faith.

I want to special thank all my family, my parents, Maria Júlia and António, and brothers, Sérgio and Bernardo, for your trust and presence in my life.

My last and deepest gratitude goes to my wife, my joyful companion *pela vinha e pela vida*, Margarida. Thank you for your love and for making me truly happy.

Preface

The present work was developed in cooperation between FEUP (Faculty of Engineering of University of Porto) and Sysadvance, Sistemas de Engenharia, S.A. and was carried out at the Laboratory for Process Engineering, Environmental, Biotechnology and Energy (LEPABE) and Sysadvance facilities. All work was accomplished under FCT PhD scholarship SFRH/BDE/51186/2010.

Sysadvance, a spin-off of FEUP, is a Portuguese company specialized in producing and commercializing pressure swing adsorption (PSA) units. This company is leader in the Iberian Peninsula market, exporting for more than 35 countries all over the world. Throughout the years, Sysadvance developed a broad portfolio of solutions which accounts with PSA for nitrogen and oxygen production from air (respectively up to 99.999 % and 95 %), helium purification, methane separation from biogas and purification of fluorinated gases. This work was driven by the increase demand for PSA units to produce high-purity oxygen (99+%) and benefited from a contract with NASA (Wyle Integrated Science and Engineering Laboratories) who ordered a PSA prototype for producing 1 $L_{STP} \cdot min^{-1}$ of oxygen 99.0 % from air. NASA imposed as well limits for the weight (≤ 120 kg), volume (≤ 0.3 m^3) and energy consumption (≤ 1.1 kW), which were all of them met with the developed technology. Also, Sysadvance benefited from this project incorporating in their portfolio the vacuum pressure swing adsorption (VPSA) technology and high-purity oxygen PSA units.

This thesis comprises four scientific articles submitted for publication during the PhD period.

Abstract

High-purity oxygen (≥ 99 %) is required for several industrial, military, medical or aerospace applications. Oxygen generation from air by conventional pressure swing adsorption (PSA) or vacuum pressure swing adsorption (VPSA) has noticeably increased in the past decade. However, until now, single-stage PSA units have been limited to the production of oxygen with a maximum concentration of 95 % (balanced with argon) since commercial adsorbents do not exhibit argon/oxygen selectivity above 1. Presently, purer oxygen streams are only possible using two-stage PSA/VPSA technologies, which are far more complex.

Motivated by the significant demand for 99+% oxygen, this thesis targets the development of a single-stage VPSA for the production of high-purity oxygen from air. Additionally, two-stage VPSA processes were considered and studied to produce higher oxygen purities (≥ 99.5 %).

Argon/oxygen selective lithium low silica-X silver-based zeolite, AgLiLSX, was characterized to assess its potential for high-purity oxygen production in a single-stage VPSA unit. Nitrogen, oxygen and argon adsorption isotherms, uptake curves and breakthroughs were obtained at different temperature conditions. Moderate argon/oxygen selectivity, α_{Ar/O_2} = 1.14 at 1 bar and 25 °C, and high working capacity, 0.45 mol·kg^{-1} for nitrogen between 1.4 bar and 0.2 bar at 25 °C, were observed.

Water vapor and carbon dioxide isotherms were obtained on AgLiLSX and a deactivation study was conducted to evaluate the extent of adsorbent contamination and consequent loss of capacity and selectivity when exposed to untreated atmospheric air. Since carbon dioxide and water vapor present in atmosphere were found to act as contaminants deactivating AgLiLSX, a protective layer must be applied. Two 13X-type zeolites, one activated alumina and one silica were characterized and

their ability for carbon dioxide and water vapor removal assessed. Cyclic adsorption isotherms and breakthrough curves were obtained and effective adsorption isotherms and transport properties were computed.

A compact, lightweight and low energy consuming stand-alone single-stage VPSA unit for producing 1 L_{STP}·min^{-1} of high-purity oxygen from air was designed, assembled, studied and optimized. The VPSA main columns were loaded with AgLiLSX. Layered adsorption pre-columns containing silica, KC-Trockenperlen WS 2050, and 13X-type zeolite, ZEOX OII, were used for protecting AgLiLSX absorbent from deactivating. An innovative and very efficient cycle was developed to synchronize the pre-columns four-step cycle for carbon dioxide and water vapor removal (< 5 ppm of CO_2 and $-40\,^{\circ}C$ of dew point) with the main columns seven-step cycle. RSM methodology applied to the experimental set-up and developed ASPEN-based simulator were used to study the role of several operating variables on the product purity and recovery and to optimize the performance of the unit. For a product concentration of 99.13 % oxygen, the recovery obtained was 6.2 % and the productivity was 9.0 m^3·hr^{-1}·ton^{-1}.

Targeting higher oxygen purities, several two-stage VPSA processes, combining equilibrium based PSA (EPSA) or kinetic based PSA (KPSA) with VPSA using AgLiLSX, were studied and optimized. ASPEN simulator was used to study the role of several operating variables on product purity and recovery. A KPSA/RP/VPSA – a configuration with an intermediate blower to repressurize (RP) the product stream from the KPSA to feed the VPSA unit – was proposed and experimentally validated to produce 99.5 % oxygen from air with a recovery of 14.2 % and (AgLiLSX stage) productivity of 25.4 m^3·hr^{-1}·ton^{-1}.

Sumário

O oxigénio de elevada pureza (≥ 99 %) é utilizado em diversas aplicações, tais como aplicações industriais, militares, médicas ou aeroespaciais. A produção de oxigénio a partir do ar, a partir de processos convencionais de adsorpção com modulação de pressão (PSA) ou adsorção com modulação de pressão e vácuo (VPSA), aumentou significativamente na última década. Porém, até hoje, as unidades PSA de estágio único estavam limitadas a uma produção de oxigénio com uma concentração máxima de 95 % (sendo o restante argon) uma vez que os adsorventes comerciais não apresentam selectividade argon/oxigénio. O obtenção de correntes de oxigénio mais puras apenas era possível recorrendo à tecnologia de PSA/VPSA de dois estágios, consideravelmente mais complexa.

Motivada pela crescente procura por oxigénio com concentração superior a 99 %, esta tese tem como objectivo o desenvolvimento de uma unidade VPSA de estágio simples para produção de oxigénio de elevada pureza a partir do ar. Além disso, duas unidades VPSA de estágio duplo foram consideradas e estudadas para produzir oxigénio com purezas mais elevadas (≥ 99.5 %).

O adsorvente zeólito AgLiLSX foi caracterizado para avaliar o seu potencial para produção de oxigénio de elevada pureza numa unidade VPSA de estágio simples. Isotérmicas de adsorção, curvas de carga e curvas de cedência para o azoto, oxigénio e árgon foram obtidas a diferentes temperaturas. Observou-se que este possui uma selectividade argon/oxigénio moderada, α_{Ar/O_2} = 1.14 a 1 bar e 25 °C, e elevada capacidade em operação, 0.45 mol·kg^{-1} para o azoto entre 1.4 bar e 0.2 bar a 25 °C.

Determinaram-se isotérmicas de adsorção do dióxido de carbono e do vapor de água no AgLiLSX e foi feito um estudo de desactivação para avaliar a extensão da contaminação do adsorvente e consequente perda de capacidade de adsorção e de

selecitividade quando exposto ao ar atmosférico não tratado. Uma vez que o dióxido de carbono e o vapor de água presentes na atmosfera actuam como contaminantes, desactivando o adsorvente AgLiLSX, dois zeólitos do tipo 13X, uma alumina activada e uma sílica foram caracterizados e a sua capacidade para remoção do dióxido de carbono e de vapor de água atmosféricos avaliada. Procedeu-se também à determinação de isotérmicas de adsorção e curvas de cedência cíclicas até obtenção das isotérmicas de adsorção e coeficientes de difusão efectivos.

Uma unidade VPSA de estágio simples, autónoma, compacta, leve e de baixo consumo energético foi concebida, assemblada, estudada e optimizada para a produção de 1 $L_{PTN}\cdot min^{-1}$ de oxigénio de elevada pureza a partir do ar. As colunas principais da unidade VPSA foram empacotadas com AgLiLSX. As pré-colunas, contendo duas camadas, uma de sílica, KC-Trockenperlen WS 2050, e outra de zeólito do tipo 13X, ZEOX OII, foram usadas para proteger o adsorvente AgLiLSX de desactivação. Um ciclo inovador e muito eficiente foi desenvolvido para sincronizar o ciclo de quatro etapas das pré-colunas para remoção do dióxido de carbono e vapor de água (abaixo dos 5 ppm de CO_2 e – 40 $^{\circ}C$ de ponto de orvalho) com o ciclo de sete etapas das colunas principais. A metodologia de superfície de resposta (RSM) aplicada à unidade experimental e o simulador desenvolvido com base no software ASPEN foram usados para estudar o papel de diversas variáveis de operação na pureza e recuperação da corrente de producto, assim como para optimizar o desempenho da unidade. Para uma concentração de producto de 99.13 % de oxigénio, a recuperação obtida foi de 6.2 % e a productividade foi de 9.0 $m^3\cdot hr^{-1}\cdot ton^{-1}$.

Tendo ainda em vista a obtenção de purezas de oxigénio superiores, estudaram-se e optimizaram-se diferentes processos VPSA de dois estágios, combinando separação de equilíbrio (EPSA) ou separação cinética (KPSA) com um VPSA usando AgLiLSX. O simulador ASPEN foi usado para estudar a influência de diversas variáveis de operação na pureza e recuperação do producto. Uma unidade

KPSA/RP/VPSA – uma configuração que inclui um compressor intermédio para repressurizar (RP) o produto da unidade KPSA e alimentá-lo à unidade VPSA – foi proposta e experimentalmente validada para produzir 99.5 % de oxigénio a partir do ar, com uma recuperação de 14.2 % e uma productividade (do adsorvente AgLiLSX) de 25.4 $m^3 \cdot hr^{-1} \cdot ton^{-1}$.

Contents

Figure Captions

CHAPTER I

CHAPTER II

CHAPTER III

CHAPTER IV

CHAPTER V

APPENDIX A

Table Captions

CHAPTER IV

CHAPTER V

Nomenclature

A	area, m^2
a_p	specific particle surface per unit volume of the bed, m^{-1}
b	Langmuir affinity constant, bar^{-1}
b_∞	Langmuir affinity constant at infinite temperature, bar^{-1}
c	fluid-phase molar concentration, $mol \cdot m^{-3}$
C_{BET}	BET fitting parameter
C_{pg}	gas-phase heat capacity at constant pressure, $J \cdot kg^{-1} \cdot K^{-1}$
C_{vg}	gas-phase heat capacity at constant volume, $J \cdot kg^{-1} \cdot K^{-1}$
C_V	valve parameter
C_p	heat capacity, $J \cdot kg^{-1} \cdot K^{-1}$
d	empirical parameter from Aranovich and Donohue equation
D	difusivity, $m^2 \cdot s^{-1}$
D_μ	apparent time constant, s^{-1}
$D_{\mu 0}$	apparent time constant at zero pressure, s^{-1}
D_B	bed diameter, m
D_{ax}	axial dispersion coefficient, $m^2 \cdot s^{-1}$
D_K	Knudsen diffusion coefficient, $m^2 \cdot s^{-1}$
D_m	molecular diffusion coefficient, $m^2 \cdot s^{-1}$
D_p	macropore diffusion coefficient, $m^2 \cdot s^{-1}$

E	characteristic energy of the adsorbent, J·mol^{-1}
E_a	activation energy, J·mol^{-1}
F	fractional uptake or flow rate, L_{STP}·min^{-1}
h_p	gas-solid heat transfer coefficient, W·m^{-2}·K^{-1}
h_w	gas-wall heat transfer coefficient, W·m^{-2}·K^{-1}
h_∞	wall-environmental heat transfer coefficient, W·m^{-2}·K^{-1}
ΔH	adsorption heat, J·mol^{-1}
k	iteration or LDF coefficient, s^{-1}
k_f	film mass-transfer coefficient, s^{-1}
k_{gx}	axial gas-phase thermal conductivity, W·m^{-1}·K^{-1}
k_{sx}	axial solid-phase thermal conductivity, W·m^{-1}·K^{-1}
$\bar{K}_K$	dimensionless Henry's constant
L_B	bed length, m
m	Dubinin-Astakhov exponent or Bae-Lee equation parameter
M	molecular weight, kg·mol^{-1}
N	molar flow rate, mol·m^{-3}·s^{-1}
Nu_w	Nusselt number for gas-wall heat transfer, $\mathrm{Nu}_\mathrm{w} = 2r_p h_w / k_{gx}$
p	partial pressure, Pa
P	total pressure, bar or Pa
P_0	water saturation pressure, bar
P/F	purge to feed
Pe_M	Peclet number for mass transfer, $\mathrm{Pe}_\mathrm{M} = L_B u_{ref} / D_{ax}$

$\mathrm{Pe_H}$ heat-transfer Peclet number, $\mathrm{Pe_H} = 2r_p M \rho_g C_{pg} u / k_{gx}$

Pr Prandl number, $\mathrm{Pr} = \mu C_{pg} / k_{gx} M$

Pur product purity, %

q molar concentration in the adsorbed phase, mol·kg^{-1}

q_m isotherm parameter, maximum adsorption capacity, mol·kg^{-1}

r radius, m

R_g^s energy balance dimensionless parameter

R_g^w energy balance dimensionless parameter

R_g^h energy balance dimensionless parameter

R_p^b ratio between bed time constant and particle diffusion time constant

$\Re$ ideal gas constant, J·mol^{-1}·K^{-1}

Re particle Reynolds number, $\mathrm{Re} = 2r_p M \rho_g u / \mu$

Rec product recovery, %

t empirical parameter from Toth equation or time variable, s

T temperature, K

u interstitial molar average velocity, m·s^{-1}

U overall heat transfer coefficient

x spatial coordinate, m

y gas-phase mol fraction

Greek symbols

α adsorption selectivity

α_w ratio of the internal surface area to the volume of the column wall, m^{-1}

α^D	ratio between the diffusivity coefficients
ε_b	interparticle voidage
ε_p	intraparticle voidage
ε_t	total bed void fraction
ε_w	ratio between the cross-sectional wall area and column area
θ	dimensionless time variable
λ	axial heat dispersion coefficient
π	spreading pressure, $J \cdot m^{-3}$
ρ	density, $kg \cdot m^{-3}$
ς_a	adsorbed phase capacity factor
ς_p	fluid phase capacity factor
μ	dynamic viscosity, $N \cdot s \cdot m^{-2}$
τ_p	tortuosity
τ_b	bed time constant

Subscripts

b	adsorbent bulk
d	downstream
F	feed
g	gas
H	high
i	component
in	initial

k	mumber of observations
L	low
nc	number of mixture components
p	particle
PROD	product
RAFF	Raffinate
ref	reference
s	adsorbent
u	upstream
w	column wall
∞	environmental
AD	adsorption (or production) step
B	backfill step
BD	blowdown step
E	equalization step
PG	purge step or purge
PR	pressurization step
VA	evacuation step
VP	purge under vacuum step

Superscripts

exp	experimentally obtained
cal	obtained by fitting equations
stp	standard temperature and pressure
*	dimensionless
0	pure component

e	external
i	internal
ml	mean logarithm

CHAPTER I

1 Introduction

The industry of gas separation and purification has been searching for more efficient processes in terms of energy-consumption, environmental impact and costs. Cryogenic distillation is widely recognized as the most used gas separation process [1]. The widespread use of the cryogenic distillation is due to its simplicity and ability to produce high-purity products. Despite these advantages, it is fundamentally an energy-intensive and very expensive process [2]. Pressure swing adsorption (PSA) is a cyclic adsorption process that has been emerged as an energy and cost efficient alternative for many gas separation and purification applications [3, 4]. The onset commercialization of PSA units has started in the 1970s [4]. PSA has become the state-of-the-art separation technology in several areas, mainly for small and medium-scale applications [3].

PSA processes have been developed for a variety of applications, such as air drying, air separation, hydrogen separation from reformate streams, mostly methane steam reforming, and from petroleum refinery off-gases, separation of methane from landfill gas, carbon dioxide-hydrogen separation, normal and iso-paraffins separation, noble gases purification and alcohol dehydration, among others (Table 1.1). There are several hundred thousand PSA units operating all over the world [3]. Sysadvance, a spin-off of FEUP, is the only Portuguese company producing and commercializing PSA units. Throughout the years, Sysadvance installed PSA units into different industrial processes, which resulted in a broad portfolio of solutions for nitrogen and oxygen generation (respectively up to 99.999 % and 95 %), helium purification, methane separation from landfill gas and purification of fluorinated gases. Sysadvance is, in fact, the PSA manufacturer leader in the Iberian Peninsula region, exporting for more than 35 countries all over the world.

Table 1.1 – Major applications of pressure swing adsorption technology.

Gas drying	
Air drying	[5-8]
Alcohol dehydration	[9-14]
Air separation	
Production of oxygen (≤ 95 %) from air	[15-23]
Production of high-purity oxygen (> 95 %) from air	[24-31]
Production of nitrogen from air	[2, 4, 32-41]
Landfill gas upgrading	[42-49]
Carbon monoxide recovery	[50, 51]
Carbon dioxide recovery and removal	[4, 36, 52-55]
Hydrogen recovery and purification	[56-63]
Separation of normal and iso-paraffins	[64-67]
Hydrocarbons purification	[68-72]
Noble gases purification	
Helium purification	[73-78]
Xenon purification	[79, 80]
Argon purification	[81-83]
Fluorinated gases purification	[84]
Purification of ammonia syngas	[85-87]

1.1 Pressure swing adsorption and its evolution

The basic principles of PSA technology are described in a patent disclosed by Finlayson and Sharp, in 1932 [4]. Despite, Skarstrom [15], Montgareuil and Dominé [88] often receive the credits for inventing the PSA technology, apparently because of the thoroughness of their patents, simultaneously filled in 1958. Skarstrom's patent

discloses a unit (Figure 1.1) made of two beds packed with an adsorbent, zeolite 4A, running a four-step cycle comprising:

1. pressurization;
2. adsorption (also known as production);
3. counter-current blowdown;
4. counter-current purge.

The original Skarstrom cycle was used for oxygen enrichment from air (up to 85 % with very low recovery) [4].

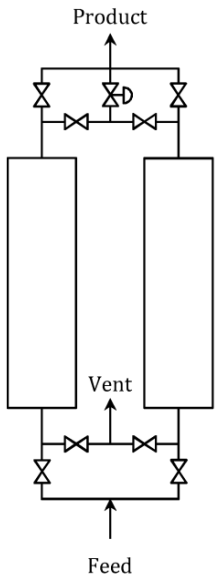

Figure 1.1 – Sketch of Skarstrom two-bed pressure swing adsorption (adapted from [4]).

The individual half-cycle steps are illustrated in Figure 1.2. In step 1, bed 1 is pressurized with feed to the higher operating pressure while bed 2 is counter-currently blowdown to the atmospheric pressure. In step 2, high-pressure feed flows through bed 1. The more adsorbed component, in this case nitrogen, is retained in the bed and a gas stream enriched in the less adsorbed component, in this case oxygen, leaves as product at a pressure only slightly below that of the feed – raffinate.

During this step, a fraction of the product stream is used to counter-currently purge bed 2 at low operating pressure. Steps 3 and 4 follow a symmetric sequence.

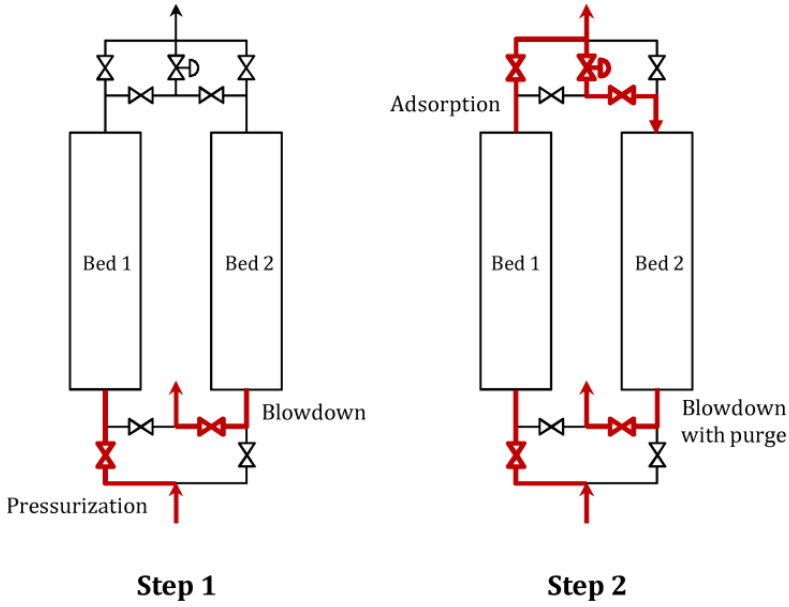

Figure 1.2 – Sequence steps of the original Skarstrom half-cycle (adapted from [4]). The other half-cycle is symmetric to the above-illustrated one.

Montgareuil and Dominé also disclosed a unit for oxygen enrichment, 98 %, from air (without argon), made of two beds packed with 5A, 10X or 13X-type zeolite (Figure 1.3) [88]. Despite the similarities with Skarstrom's patent, Montgareuil and Dominé proposed the use of vacuum during the regeneration (with the discharge end located at the middle of the bed), thus introducing the concept of vacuum swing adsorption (VSA). In fact, the simplest way to understand a VSA cycle is to consider it as PSA cycle in which the blowdown step is replaced by a vacuum desorption: the product end of the adsorption column is kept closed while vacuum is applied on the column through the feed end [4].

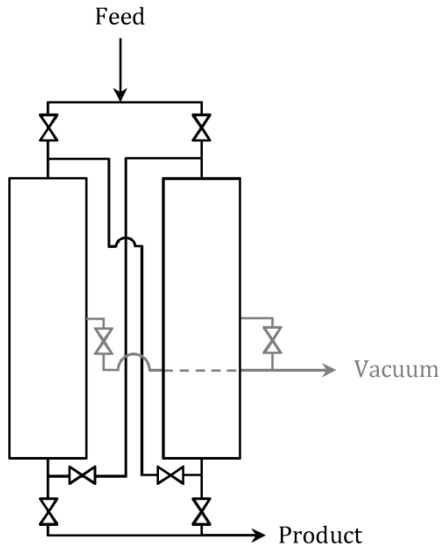

Figure 1.3 – Sketch of the two-bed VSA patented by Montgareuil and Dominé.

The recovery obtained by Montgareuil and Dominé, 51 % for 85 % purity oxygen [88], is undoubtedly superior to the performance obtained by Skarstrom [15]. However, the VSA unit had the great disadvantage of the product being delivered at sub-atmospheric pressure. Here, the gain in raffinate recovery was reached at the expense of additional mechanical energy required for the evacuation step, since the loss of the less favorably adsorbed species during the evacuation step (VSA operation) is normally less than the corresponding loss in the blowdown step [4]. Thus, the VSA cycle by Montgareuil and Dominé over-performed the PSA cycle by Skarstrom assuming that a near-ambient product is acceptable. In fact, concerning PSA/VSA operation, is the pressure ratio (the swing) and not the individual high and low pressure levels that determines the achievable purity and recovery [4]. Although promising, the VSA technology had no further chapters until the 1980s, because of the lack of adsorbents able to perform an efficient separation in such a low pressure swing operation. Contrarily, the PSA technology became fully commercial in the 1970s.

In 1966, Berlin and Matawan filed a patent, also concerning oxygen enrichment from air, disclosing an improvement to the original Skarstrom cycle [89]: the introduction of a pressure equalization step. After one of the beds has completed the high-pressure adsorption step and the other has been purged, the two beds are connected through their product ends to equalize the pressure. This means that part of the gas that normally would be loss in the blowdown step is used to pressurize the other column. This step, besides saving mechanical energy, increases the process recovery since the equalization stream is richer in oxygen than the feed. This new cycle is depicted in Figure 1.4.

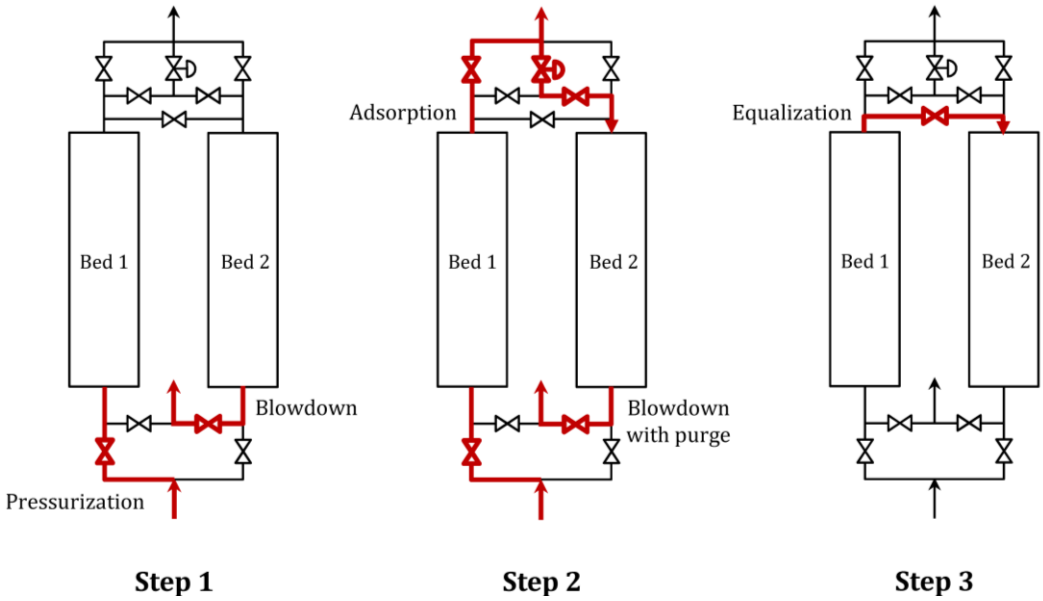

Figure 1.4 – Sequence steps of Skarstrom half-cycle with top equalization step. The other half-cycle is symmetric of the above-illustrated one.

Nowadays, equalization step is a well-establish step in the PSA cycles for several applications and different equalizations can be performed depending on the process [22, 44, 55, 63, 90-96]. Besides the aforementioned equalization through the top of both columns (top equalization) [31, 90, 97], bottom equalization [98], cross equalization [29] and total equalization (or dual-ended equalization) [4] were already reported.

In mid-1960s, a new PSA process emerged that introduced some improvements to the PSA technology. The increasing demand of high-purity hydrogen (99.9999 %) provided a strong economic motivation to develop PSA cycles to recover and purify hydrogen from petroleum refinery off-gases, reformate streams, etc. [4, 99-102]. Since hydrogen barely adsorbs compared to most of gases, this level of purity was easy to attain, whereas the challenge was to maximize the product recovery. Accordingly, multiple-bed cycles were developed, such as the one disclosed by Wagner and Lackawanna concerning a four-bed PSA for upgrading a reformate stream (77 % hydrogen, 22.5 % carbon dioxide and traces of other components) to an ultimate purity of 99.9999+% of hydrogen with 76+% recovery. In the late 1970s, new processes were developed employing up to twelve beds and comprising several equalization steps to attain recoveries between 85 – 90 % [103]. In fact, when more than two columns are employed, several pressure equalization steps can be done and, as a consequence, the overall recovery is increased [96].

Another novelty introduced by the hydrogen PSA separation technology was the use of layered beds, usually beds with a layer of activated carbon followed by zeolite 5A, as disclosed by Wagner and Lackawanna's patent, to accomplish the desired separation [102]. Also, in such cases, the use of a high-capacity adsorbent preceded by a high-selectivity adsorbent could result in better performance compared to that achieved using single-layered beds of either of the two adsorbents [96, 104, 105]. This novelty was quickly assimilated by other existing PSA process, such as for oxygen production and air drying [2, 6, 106]. In oxygen PSA processes the use of a small layer of alumina or silica to act as a desiccant and protect the second layer of zeolite became common [18, 21].

In the early-1970s, the development and commercialization of carbon molecular sieves (CMS) led to a significant evolution of the PSA technology [4]. CMS are carbonaceous adsorbents with a very narrow pore size distribution that allows small molecules to enter in the pores rather than larger molecules (kinetic selectivity).

In 1977, the first kinetic-based PSA (KPSA) was proposed by Munzner et al. [32, 33] for nitrogen production from air. The authors explored the differences between diffusion rate of oxygen and nitrogen on CMS to develop a KPSA unit which is able to produce 99.9 % of nitrogen from air with nearly 40 % of recovery. Since then, other kinetic processes were developed such as methane separation from landfill gas [48] or argon purification [82]. The adsorption cycle in KPSA processes should be adapted, since the contact time between feed gas and the adsorbent is critical: short enough to prevent the system from reaching equilibrium but not so short as to preclude significant uptake [15]. Nevertheless, with properly selected step times and the necessary adjustments specific to each process, the Skarstrom cycle can be applied to a kinetic PSA separation.

During the 1980s, a new generation of zeolite adsorbents was developed with very high capacity and selectivity, at low pressure range, towards the air separation [107]. The development of these new adsorbents, such as Li-exchanged X-type (LiX) zeolites, low-silica X-type (LSX) zeolites, and Li-exchanged LSX-type (LiLSX), was a major advance to VSA technology and VSA units for oxygen production from air became widely used and commercialized [4, 18, 108]. In 1988, Sircar disclosed a patent concerning a new process, vacuum pressure swing adsorption (VPSA), for the production of 95 % oxygen from air, where the adsorption step is carried between 1.5 bar and 8.1 bar and the regeneration step between 0.1 bar and 0.4 bar [21]. Since then, several processes were disclosed using vacuum conditions [19, 25, 30, 97, 109-113]. Provided that quite often the designation of such processes was ambiguous, Sircar provided a definition, distinguishing between PSA, VSA and VPSA [3]. According to that definition, PSA process is the one in which the adsorption step is carried at super-ambient pressure and desorption step is achieved at near-ambient pressure level. VSA process is the one in which the adsorption step is carried at a near-ambient pressure level and desorption is achieved under vacuum. It is considered a VPSA process, the process that uses the benefits of both PSA and VSA concepts [3]. The

selection on which process should be used should depend on the product desired, on the intended specifications and on the adsorbents selected to accomplish the separation, assuming that each process has its own advantages [19, 114-116].

Meanwhile, still in the 1980s, a new improvement to the original Skarstrom cycle was proposed by Russell [117]. This improvement was initially proposed to faster achieving the stationary state and to attain pre-selected high-purity levels of oxygen at the PSA start-up. During operation, the product stream is collected in a backfill/product vessel and part is used to counter-currently purge and afterwards pressurize the beds at shutdown and at the start-up. Later on, this step, named backfill step, became widely used in PSA cycles for oxygen production, when high-purity products need to be obtained. During backfill step – which occurs precisely before pressurization step – part of the product stored in a storage column (often referred as backfill column), is used to counter-currently pressurize the adsorption bed, increasing the product purity as far as possible (see Figure 1.5) [118].

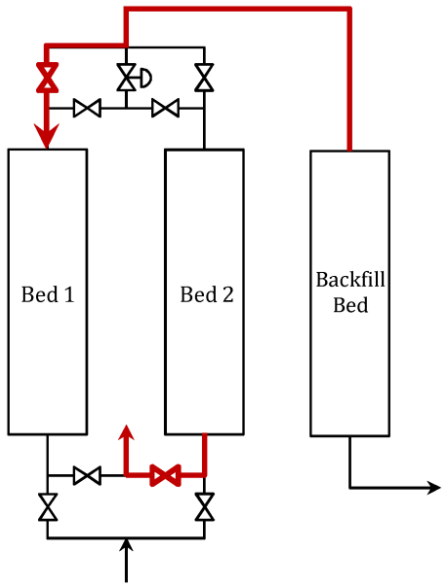

Figure 1.5 – Sketch of the backfill step in bed 1.

Also in the 1980s, a new process called rapid PSA (RPSA), was disclosed by Jones et al. [119] pushing the fast cycling of kinetic-selective PSA processes close to the limits allowed by fluid mechanics and valve dynamics. The RPSA proposed employed step times of about 0.5 to 2.0 s and a total cycle time of less than 30 s. As a result of rapid cycling, the RPSA unit showed unique advantages such as nearly isothermal operation, or, the most important, higher adsorbent productivity at equal purity and recovery [2, 120].

The RPSA technology has seen new developments in the past decade, after several patents being filled concerning a rotary multiport valve [121-123]. The use of a multiport rotary valve in RPSA replaces the complex and bulky network of piping and valves used in conventional PSA systems [23]. Despite the process simplicity provided by the introduction of a rotary multiport valve, this technology also allow fast cycling and high precision, since the change of the events taking place in all the columns occurs at the exact same time. Using a normal valve array, a failure of one second in opening or closing one of the valves can happen, resulting on a significant impact in a RPSA cycle and consequent decrease in product purity and recovery [96].

New PSA-based processes, such as VPSA, RPSA and combined processes, are being continuously disclosed and introduced in the market, making PSA a very dynamic area [14, 22, 23, 53, 55, 65, 67, 73, 74, 77, 96, 124-130]. These new processes target decreasing the energy consumption or the unit costs, but also target new gas separations such as high-purity oxygen (> 95 %), biogas upgrading and purification, helium or fluorinates recovery and purification, among others [96, 131]. The new PSA-based units result from a very dynamic interaction between the development of new adsorbents and the corresponding optimized PSA cycles and vice-versa.

1.1.1 Adsorbents

The adsorbent or adsorbents are the heart of a PSA unit. Several well-known adsorbents were commercially available prior to the development of PSA technology, but it was undoubtedly the PSA that led to the development of new and better fitted adsorbents for gas separations [2, 95, 132]. Indeed, synthetic zeolites are being produced since 1950s, initially as catalysts for petrochemical reactions [133]. The development of new adsorbents was so intense after Skarstrom patent that resulted in the discovery of many porous materials nowadays used for gas separations [132, 134].

Figure 1.6 – Zeolite (ZEOX OII, sample from Zeochem).

Zeolite adsorbents are crystalline aluminosilicates that have microporous frameworks with well-defined and uniform pore structure, between 3 and 11 Å of pore opening [132]. The framework structures of these zeolites consist of tetrahedrally assemblages of SiO_2 and AlO_2 units [4]. While SiO_2 groups are neutral, $(AlO_2)^-$ groups introduce a negative charge to the structure which is compensated by the presence of cations such as Na^+, Li^+, K^+ or Ca^{2+} [135]. The first synthetic zeolites produced were from A-type, such as zeolite 4A used in Skarstrom patent, and zeolite 5A used in Montgareuil and Dominé patent. 4A and 5A zeolites allow only modest

O_2/N_2 adsorption selectivity originating low efficient PSA units for the oxygen production. The development of PSA technology led to the synthesis of new adsorbents such as X-type zeolites and later, in 1988, a new generation of zeolites with very high capacity and selectivity towards air separation [107], the lithium-exchanged X-type (LiX) zeolites, low-silica X-type (LSX) zeolites, and lithium-exchanged low-silica X-type (LiLSX) zeolites.

Pelletized zeolites have commonly about 20 wt.% of an inert binder, which has the function of binding the zeolite crystallites with particle sizes in the range of 2.5 μm into millimeter-size particles that allow fill packed bed columns with optimized pressure drop [135]. The addition of binder, however, reduces the adsorption capacity between 15 and 20 % [107], so, in the recent years, several zeolites were developed with a reduced amount of binder, the so called binderless zeolites, which even so keep the mechanical strength of the previous composite adsorbents.

Presently, the zeolites industry continues to develop new and promising materials regarding, for example, air separation [124, 136, 137]. Silver exchanged zeolites, such as AgLiLSX-type zeolite, was one of the most recent developments, allowing the production of oxygen streams of 95+% never before possible with the existing commercial adsorbents [136].

Figure 1.7 – AgLiLSX-type zeolite (sample from AirProducts).

Zeolites used in air separation are very sensitive to water vapor, easily deactivating when exposed to atmospheric air [132, 138-140]. Because of that, in the 1960s, several oxygen PSA units were disclosed using a small first layer of desiccant, such as alumina or silica, to reduce the water content in the feed stream down to parts per million (ppm) levels and therefore protect the nitrogen/oxygen selective layer, placed above the desiccant layer. Also, between 1965 and 1970 the first air drying PSA units were commercialized, using alumina or silica as adsorbents [2, 4, 36].

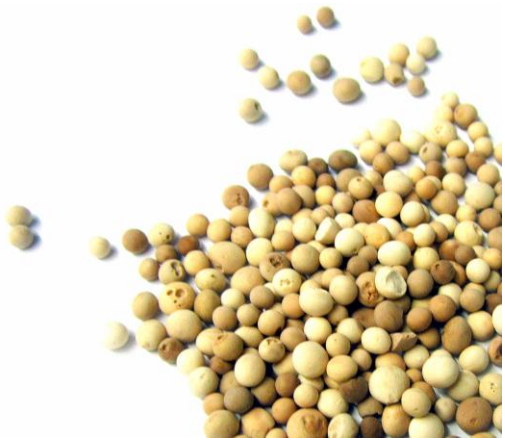

Figure 1.8 – Silica (KC-Trokenperlen WS 2050, sample from BASF).

Silica is the most used desiccant because of its large capacity for water and easy regeneration [132]. Silica adsorbents are amorphous aluminosilicates with a high content of SiO_2, and essentially mesoporous (pores > 20 Å). There are several preparation methods which result in different pore structures, however the most common type of silica, silica gel, is generally prepared by mixing a sodium silicate solution with a mineral acid such as sulfuric or hydrochloric acid [132].

Activated alumina is also widely used as desiccant, with practically the same advantages referred for silica [132]. It is also an amorphous aluminosilicate with essentially a mesoporous structure but unlike silica, alumina has a high content of

AlO_2. The surface chemistry and pore structure of alumina adsorbent can be modified by chemical or controlled thermal treatment [2].

Figure 1.9 – Activated alumina (F200 7x14 Tyler Mesh, sample from BASF).

Carbonaceous adsorbents, a large group of the available adsorbents, were used in PSA for the first time in 1965 for hydrogen purification [4, 36]. This material is one of the most versatile adsorbents because of its extremely high surface area and micropore volume but also because its tunability [4]. The structure of activated carbon is complex and it is basically composed of an amorphous and a graphite-like microcrystalline domains [141]. The activated carbon frameworks contains interconnected micro and mesopores, slit-shaped, with various shapes and sizes (between 0.3 and 10 nm) [132]. Depending on the raw material used, the desired pore size distributions are created by a carbonization followed by thermal activation steps. The precursors for activated carbon are carbonaceous materials such as wood, peat, coals, petroleum coke, bones, coconut shell and fruit nuts [4]. Manufacturing processes basically involve the following steps: raw material gridding and sieving, carbonization and thermal activation [4]. The manufacturing parameters are controlled to achieve the desired pore network morphology and surface chemistry and mechanical strength. The nature of the final product depends on both the starting material and the manufacturing procedure [4].

Figure 1.10 – Carbon molecular sieve (CMS-D, sample from Carbotech).

One of the most significant PSA developments would not be possible without the synthesis of carbon molecular sieves (CMS) in the early-1970s [4, 36]. Carbon molecular sieves, like activated carbon, are manufactured from a variety of precursors, such as coal, coconut shell, polymers and biomass materials [142]. The unique kinetic properties of these materials are due to the very narrow pore size distribution (pore width usually are in the range of 0.3 and 0.5 nm) [143, 144]. The pore size distribution of CMS are controlled by varying the precursor, the carbonization conditions and pre- and post-treatments like activation procedure, carbon vapor deposition and passivation techniques [142]. However, the key step for making CMSs – different from the steam activation step for activated carbons – is the carbon deposition step [132]. This step involves cracking a hydrocarbon under an inert atmosphere so that carbon is deposited at the pore mouths. For a given hydrocarbon, this step is accomplished by careful control of a set of operating variables, including concentration, temperature, and time [132]. The manufacturing process has great impact on shape, size and robustness of adsorbent. CMS adsorbents, unlike previous adsorbents, base their separation ability in the kinetic selectivity towards the components of the feed stream rather than in the equilibrium

selectivity [96, 145-147]. In such cases and for a binary mixture, one of the components of feed mixture experiences a very low diffusivity compared with the other and it is produced during the high-pressure step – production step [4]. CMSs were first used for producing nitrogen from air [32-34]. Nitrogen, together with argon, present a low diffusivity compared with oxygen, and leave the PSA column at high pressure during the production step. Oxygen, on the other hand, is removed during the despressurization and purge steps. CMS adsorbents opened the PSA technology to a completely new world now embracing both equilibrium and kinetic based gas separations [42-49]. Carbonaceous adsorbents show high resistance to moisture and low heat capacity. Consequently, when used in a PSA unit a desiccant layer is not needed [2].

In the past decade, a new class of synthetic porous materials emerged, the metal-organic frameworks (MOFs), an highly tunable material [148]. MOFs are inorganic-organic hybrid materials comprised of single metal ions or polynuclear metal clusters linked by organic ligands principally through coordination bonds [149-151]. Due to the strength of these coordination bonds, MOFs are geometrically and crystallographically well-defined framework structures though they may present a significant flexibility. As potential adsorbents, MOFs have attracted a great deal of interest, especially in the separation of hydrocarbons and normal and iso-paraffins [65, 149-154].

Hydrophobic dipeptides were very recently considered for adsorption based gas separations [155-157]. Also, titanium-silicates molecular sieves, such as Ag-exchanged ETS-10, were synthesized and studied for high-purity oxygen production by PSA [126, 158]. New adsorbents with high selectivity and fast kinetics are being developed for RPSA processes [159]. These new adsorbents will enable the development of high performance PSA units with significantly higher productivities. Nowadays, several companies are trying to develop new adsorbents with high resistance to contaminants and easiness of regeneration, high durability, and well

controlled microporosity, capable of better performances. Such materials have been studied and soon new adsorbents and resulting new processes will be commercialized.

1.2 High-purity oxygen

Oxygen generation technology by PSA has remarkably improved since Skarstrom pioneer work [15, 26]. In 1966, Berlin disclosed a PSA unit for the production of 93 % oxygen (balanced with argon) with unspecified recovery, using a strontium-exchanged X-type zeolite [160]. In 1970, two years after the commercialization of the first large-scale PSA unit for oxygen production [4, 135], a few processes were developed for medical use [4] and military applications [161]. In the 1980s a new generation of adsorbents, LiX-, LSX- LiLSX-type zeolites, was developed with very high capacity and selectivity towards air separation [108, 109, 132, 162-164]. These new adsorbents coupled with optimized PSA units, namely VSA and VPSA, allow to obtain higher purities, better productivity and the reduction of the operation costs [26, 41, 107, 109]. However, present PSA units are limited to a maximum oxygen concentration of 95 % (balanced mostly with argon [165]) since commercial adsorbents did not exhibit Ar/O_2 adsorption equilibrium selectivity above 1 [4, 18, 21, 166]. Still, a significant demand for high-purity oxygen (≥ 99 %) for applications such as medical surgeries – where the minimum concentration required is 99.5 % in Europe, 99.0 % in USA and 99.6 % in Japan [26]; military and aerospace applications requiring a minimum concentration of 99.5 %; or filling oxygen cylinders [167] for welding and cutting processes [168] that required a concentration of 99+ %, led to the development of PSA based processes meeting these objectives. In the present work, high-purity oxygen means concentrations not lower than 99 % [26].

In 1980, Armond et al. [27] disclosed the first two-stage process for high-purity oxygen consisting of a PSA unit packed with CMS followed by another PSA unit packed with zeolite. The CMS stage served to kinetically remove argon and the second stage produces oxygen from an argon free air stream. Since then, several processes have been disclosed related to this two-stage PSA technology for high-purity oxygen production [28-30, 97, 169-171]. Lee and co-workers conducted in the past decade a comprehensive study on the use of two-stage PSA units for producing high-purity oxygen [19, 31, 111, 145, 147, 167, 168, 172, 173]. These authors disclosed an optimized three-bed two stage VPSA unit producing 99 % oxygen with 47 % of recovery, in which the equilibrium stage comes first, followed by kinetic-stage [174]; these results were possible because of the use of a very high selective CMS adsorbent [168].

Together with the development of two-stage PSA processes for high-purity oxygen production, another two-stage technology emerged as an alternative: equilibrium PSA combined with continuous membrane column (CMC). Membrane separations have drawn great attention in the research field of gas separations [175-180] and air separation was a potential separation field in which membrane technology could be successfully applied [181]. In 1994, Mercea and Hwang found that it was possible to obtain a high-purity of oxygen from air combining a PSA with a CMC units [182]. In the same year, Tsuru and Hwang succeeded to obtain a continuous current of 99 % oxygen combining a PSA and a CMC units, this last consisting of three modules of polyimide hollow fibers [181]. Oxygen recoveries are not reported.

Despite the existing alternatives for producing high-purity oxygen from air, two-stage processes are far more complex and often unattractive. Therefore, the production of high-purity oxygen using a single-stage PSA remained a goal. In 1990, Wilkerson prepared a silver-mordenite adsorbent with two different silver-exchanged concentrations (concentrations not reported) and studied the adsorption equilibrium

of argon and oxygen [183]. The more thoroughly exchanged silver-mordenite showed equilibrium selectivity of argon towards oxygen. Following, in 1993, Knaebel and Kandybin disclosed an equilibrium-based PSA, packed with silver-mordenite adsorbent, which reached a product concentration of 99.6 % from a feed of 95 % of oxygen balanced with argon [24]. Silver-exchanged molecular sieves have since been investigated to accomplish the argon/oxygen separation in single-stage PSA units [126, 158, 184]. In 2000, in two consecutive works [185, 186], Hutson et al. studied the addition of silver to LiX-type zeolites for improving the adsorption capacity towards air separation. Although in their study adsorbents did not actually present Ar/O_2 selectivity, the argon adsorption capacity increased slightly. In 2002, Air Products and Chemicals, Inc. patented an Ar/O_2 selective zeolite, named AgLiLSX (lithium low silica-X type silver based zeolite), with a silver exchanged content of 20 – 70 % [136]. This patent refers that the new adsorbent is useful for high-purity oxygen production in a single-stage PSA or VPSA processes. In 2003, the same company disclosed a four-step VPSA unit that, accordingly to patent, could produce a stream of 99 % oxygen from air, using the newly developed AgLiLSX adsorbent [25]. In 2007, Santos et al. briefly characterized the AgLiLSX adsorbent and simulated a PSA unit for producing 98.7 % oxygen, operating between 1 and 3 bar, at 30 $^{\circ}$C and, with a recovery of ca. 6 % [26]. Following, Sebastian and Jasra [184] prepared and characterized several silver-exchanged zeolites and namely obtained the argon/oxygen adsorption selectivity. AgA, AgX, AgY, AgMordenite among others were reported to show some degree of adsorption selectivity of argon over oxygen. The authors concluded that AgA zeolite exhibited very high N_2/O_2 and Ar/O_2 adsorption selectivities compatible with the use in a single-stage PSA unit for producing higher purity oxygen (> 95 %). In 2008, Ansón et al. studied a 30 mol% silver exchanged ETS-10 and compared it with silver exchanged mordenite [158]. The authors found Ag-ETS-10 to have an equilibrium argon/oxygen selectivity of 1.28 at 1 bar and 30 $^{\circ}$C. However, despite promising, the adsorbent showed limitations such as low N_2/O_2

selectivity and smaller adsorption capacity when compared with conventional LiLSX adsorbents. More recently, Shi et al. synthesized a composite adsorbent of Ag-ETS-10 and Ludox HS-40 colloidal silica, weight ratio of 12:5, and obtained an adsorbent that has a high nitrogen/oxygen equilibrium selectivity and adsorption capacity, maintaining the high argon/oxygen equilibrium selectivity previously reported [126].

Very recently Afonso et al. [156] reported a new class of materials that can be used as adsorbents for air separation, VA-class hydrophobic dipeptides. These Ag-free materials were characterized and reported to have an Ar/O_2 maximum equilibrium selectivity of 1.30 at 5 °C, one of the highest values ever measured in equilibrium selective adsorbents [156]. However, these materials show several limitations such as low adsorption loading and N_2/O_2 equilibrium selectivity lower than 1. Nonetheless, this indicates that costless materials may be developed showing the up to now rarely observed Ar/O_2 adsorption selectivity. New low cost and highly performing materials and optimized PSA cycles should soon allow the development of a single-stage PSA unit for the production of high-purity oxygen.

1.3 Motivation and outline

The present work was developed under the framework of the cooperation protocol between FEUP (Faculty of Engineering of University of Porto) and Sysadvance S.A. The present thesis was driven by the significant demand for PSA units to produce high-purity oxygen (≥ 99 %). There are several applications that require oxygen purities of 99+% such as for medical surgeries, military and aerospace applications, filling of cylinders, and for welding and cutting processes. The existing two-stage PSA technology is complex and only very few companies worldwide offer it. In addition, there are several applications that require simple and compact units, *i.e.* field hospitals, submarines, air force aircrafts, etc. Despite that, till the present day, no

single-stage PSA/VPSA units producing 99 % of oxygen from air were found and the very few existing patents and papers refer only process simulations [25, 26, 126].

The present work benefited also from the collaboration with NASA (Wyle Integrated Science and Engineering Laboratories). This institution contracted the development of a single-stage PSA unit for producing an oxygen stream of 99.0 % from air. This request also stimulated the start up of a research project, founded by AdI, entitled “High-Purity Oxygen by Vacuum Pressure Swing Adsorption”, that allowed Sysadvance to expand its portfolio of solutions and rely on a line of high-purity oxygen PSA units, as well as VPSA technology. Several VPSA solutions were investigated to provide high-purity oxygen products with reasonable throughputs.

This thesis is divided in six chapters as follows:

Chapter I frames the work developed and reviews the relevant literature. This chapter includes an overview on high-purity oxygen production by PSA.

Chapter II characterizes several adsorbents (activated alumina F200, silica KC-Trokenperlen WS 2050, and 13X-type zeolites, Z10-02ND and ZEOX OII) targeting their use for humidity and carbon dioxide removal when inserted in a PSA column.

Chapter III fully characterizes an AgLiLSX zeolite. Adsorption equilibrium isotherms of nitrogen, oxygen, argon, carbon dioxide and water vapor are presented. In this chapter mono and multicomponent breakthrough experiments are reported and simulated to assess the adsorption kinetics and separation performance when inserted in a PSA unit. This chapter also presents a deactivation study of AgLiLSX zeolite by carbon dioxide and water vapor.

Chapter IV addresses the study and optimization of a stand-alone single-stage VPSA unit for the production of 1 $L_{STP} \cdot min^{-1}$ of high-purity oxygen, using AgLiLSX zeolite. The stand-alone VPSA unit was designed based on experimental and ASPEN

simulation results obtained with a lab-scale unit. The stand-alone unit assembled includes an air pre-treatment stage running an innovative cycle to continuously supply treated feed air to the AgLiLSX beds.

Chapter V describes the study and optimization of two-stage VPSA alternatives for producing 99.5 % oxygen from air. In this chapter, different energy-efficient two-stage VPSA configurations are presented combining equilibrium based PSA or kinetic based PSA with VPSA using AgLiLSX.

Finally, Chapter VI summarizes the main conclusions of this work and provides suggestions for future work.

1.4 References

1. Bird, R., Stewart, W., Ligthfoot, E. *Transport Phenomena*; John Wiley and Sons: New York, 2002.
2. Yang, R.T. *Gas Separation by Adsorption Processes*; Imperial College Press: London, 1997.
3. Sircar, S. Pressure swing adsorption. *Industrial and Engineering Chemistry Research.* **2002**, 41, 1389-1392.
4. Ruthven, D., Farooq, S., Knaebel, K. *Pressure Swing Adsorption*; VCH Publishers: New York, 1994.
5. Kumar, R. Removal of Water and Carbon Dioxide From Atmospheric Air. U.S. Patent 4,711,645, 1987.
6. Sircar, S., Kratz, W.C. Removal of Water and Carbon Dioxide from Air. U.S. Patent 4,249,915, 1981.
7. Jain, R. Pre-Purification of Air for Separation. U.S. Patent 5,232,474, 1993.
8. Rege, S.U., Yang, R.T., Qian, K., Buzanowski, M.A. Air-Prepurification by Pressure Swing Adsorption Using Single/Layered Beds. *Chemical Engineering Science.* **2001**, 56, 2745-2759.
9. Simo, M. Pressure Swing Adsorption Process for Ethanol Dehydration. PhD Thesis, Faculty of the Graduate School of State University of New York, Buffalo, U.S.A, 2008.
10. Kupiec, K., Rakoczy, J., Komorowicz, T., Larwa, B. Heat and Mass Transfer in Adsorption–Desorption Cyclic Process for Ethanol Dehydration. *Chemical Engineering Journal.* **2014**, 241, 485-494.
11. Jeong, J.-s., Jeon, H., Ko, K.-m., Chung, B., Choi, G.-W. Production of Anhydrous Ethanol Using Various PSA (Pressure Swing Adsorption) Processes in Pilot Plant. *Renewable Energy.* **2012**, 42, 41-45.
12. Guan, J., Hu, X. Simulation and Analysis of Pressure Swing Adsorption: Ethanol Drying Process by the Electrical Analogue. *Separation and Purification Technology.* **2003**, 31, 31-35.
13. Ginder, W.F. Method of Removing Water From Ethanol. U.S. Patent 4,407,662, 1983.
14. Winter, P.M. Pressure and Vacuum Swing Adsorption Separation Processes. U.S. Patent 8,734,570, 2014.

15. Skarstrom, C.W. Method and Apparatus for Fractionating Gaseous Mixtures by Adsorption. U.S. Patent 2,944,627, 1960.

16. Skarstrom, C.W. Oxygen Concentration Process. U.S. Patent 3,237,377, 1966.

17. Mendes, A.M.M., Costa, C.A.V.d.C., Rodrigues, A.E. Oxygen Separation from Air by PSA: Modelling and Experimental Results. Part I: Isothermal Operation. *Separation and Purification Technology.* **2001**, 24, 173-188.

18. Gauthier, W.D., Hendricks, M.J., Babcock, R.L. Oxygen Enrichment System for Medical Use. U.S. Patent 4,222,750, 1980.

19. Jee, J.-G., Jung, J.-H., Lee, J.-W., Suh, S.-H., Lee, C.-H. Comparison of Vacuum Swing Adsorption Process for Air Separation Using Zeolite 10X and 13X. *Revue Roumaine de Chimie.* **2006**, 51, 1095-1108.

20. McRobbie, H.W. Separation of an Oxygen-Nitrogen Mixture. U.S. Patent 3,140,931, 1964.

21. Sircar, S. Preparation of High Purity Oxygen. U.S. Patent 4,756,723, 1988.

22. Baksh, M., Rosinski, A. Vacuum Pressure Swing Adsorption Process and Enhanced Oxygen Recovery. U.S. Patent 7,763,100, 2010.

23. Rarig, D.L., Whitley, R.D., LaBuda, M.J. Pressure Swing Adsorption System With Indexed Rotatable Multi-Port Valves U.S. Patent 7,854,793, 2010.

24. Knaebel, K.S., Kandybin, A. Pressure Swing Adsorption System to Purify Oxygen. U.S. Patent 5,226,933, 1993.

25. Dee, D.P., Chiang, R.L., Miller, E.J., Whitley, R.D. High Purity Oxygen Production by Pressure Swing Adsorption. U.S. Patent 6,544,318, 2003.

26. Santos, J.C., Cruz, P., Regala, T., Magalhães, F.D., Mendes, A. High-Purity Oxygen Production by Pressure Swing Adsorption. *Industrial & Engineering Chemistry Research.* **2006**, 46, 591-599.

27. Armond, J.W., Webber, D.A., Smith, K.C. Gas Separation. U.S. Patent 4,190,424, 1980.

28. Miller, G.W., Theis, C.F. Molecular Sieve Oxygen Concentrator with Secondary Oxygen Purifier. U.S. Patent 4,880,443, 1989.

29. Haruna, K., Ueda, K., Inoue, M., Someda, H. Process for Producing High Purity Oxygen Gas from Air. U.S. Patent 4,985,052, 1991.

30. Hayashi, S., Kawai, M., Kaneko, T. Dynamics of High Purity Oxygen PSA. *Gas Separation & Purification.* **1996**, 10, 19-23.

31. Jee, J.-G., Lee, S.-J., Kim, M.-B., Lee, C.-H. Three-Bed PVSA Process for High-Purity O2 Generation from Ambient Air. *AIChE Journal.* **2005**, 51, 2988-2999.

32. Munzner, H., Heimbach, H., Korbacher, W., Peters, W., Juntgen, H., Knoblauch, K., Zundorf, D. Process and Arrangement for the Enrichment of Gases. U.S. Patent 4,015,956, 1977.

33. Münzner, H., Heimbach, H., Körbächer, W., Peters, W., Juntgen, H., Knoblauch, K., Zundorf, D. Process for Enrichment of Gases. U.S. Patent 4,011,065, 1977.

34. Juntgen, H., Knoblauch, K., Reichenberger, J., Heimbach, H., Tarnow, F. Process for the Recovery of Nitrogen-rich Gases from Gases Containing at Least Oxygen as Other Component U.S. Patent 4,264,339, 1981.

35. Schulte-Schulze-Berndt, A., Krabiell, K. Nitrogen Generation by Pressure Swing Adsorption Based on Carbon Molecular Sieves. *Gas Separation & Purification.* **1993**, 7, 253-257.

36. Rodrigues, A.E., LeVan, M.D., Tondeur, D. *Adsorption, Science and Technology*; Kluwer Academic Publishers: Boston, USA, 1989.

37. Gemba, T., Tamaru, T., Matsuura, T. Process for Separating Nitrogen Gas by Pressure Swing Adsorption System. U.S. Patent 4,925,461, 1990.

38. Umeki, M. Process for Producing High Purity Nitrogen. 1985.

39. Schmidt, W.P., Kumar, R., Abel, A.D. Adsorptive Nitrogen Generation Utilizing Multiple Adsorption Beds. U.S. Patent 4,813,977, 1989.

40. Tomomura, M., Haga, T., Nogita, S., Ichihara, K., Ishizu, T. Process for Producing High Purity Nitrogen. U.S. Patent 4,746,332, 1988.

41. Sircar, S., White, T.R. Vacuum Swing Adsorption for Air Fractionation. U.S. Patent 4,264,340, 1981.

42. Grande, C., Cavenati, S., Rodrigues, A.E. Separation Column and Pressure Swing Adsorption Process for Gas Purification. W.O. Patent 2008/072215, 2008.

43. Cavenati, S., Grande, C.A., Rodrigues, A.E. Upgrade of Methane from Landfill Gas by Pressure Swing Adsorption. *Energy & Fuels.* **2005**, 19, 2545-2555.

44. Cavenati, S., Grande, C.A., Rodrigues, A.E. Layered Pressure Swing Adsorption for Methane Recovery from CH4/CO2/N2 Streams. *Adsorption.* **2005**, 11, 549-554.

45. Cavenati, S., Grande, C.A., Rodrigues, A.E. Separation of Mixtures by Layered Pressure Swing Adsorption for Upgrade of Natural Gas. *Chemical Engineering Science.* **2006**, 61, 3893-3906.

46. Monteiro, S. Produção de Biometano: Análise de Mercado e Estudo da Separação por PSA. Master Thesis, Faculty of Engineering of the University of Porto, Porto, Portugal, 2011.

47. Grande, C.A., Rodrigues, A.E. Layered Vacuum Pressure-Swing Adsorption for Biogas Upgrading. *Industrial & Engineering Chemistry Research.* **2007**, 46, 7844-7848.

48. Sircar, S., Kumar, R., Koch, W.R., Vansloun, J. Recovery of Methane from Landfill Gas. U.S. Patent 4,770,676, 1988.

49. Collins, J. Bulk Separation of Carbon Dioxide from Natural Gas. U.S. Patent 3,751,878, 1973.

50. Krishnamurthy, R. Hydrogen and Carbon Monoxide Production by Hydrocarbon Steam Reforming and Pressure Swing Adsorption Purification. U.S. Patent 5,096,470, 1992.

51. Chen, Y., Kapoor, A., Ramprasad, N. Pressure Swing Adsorption Process. European Patent 1,101,522, 2001.

52. Doshi, K.J., Patel, K.M. Pressure Swing Adsorption Recovery. U.S. Patent 4,340,398, 1982.

53. Shen, C., Yu, J., Li, P., Grande, C., Rodrigues, A. Capture of CO2 From Flue Gas by Vacuum Pressure Swing Adsorption Using Activated Carbon Beads. *Adsorption.* **2011**, 17, 179-188.

54. Dantas, T.L.P., Luna, F.M.T., Silva Jr, I.J., Torres, A.E.B., de Azevedo, D.C.S., Rodrigues, A.E., Moreira, R.F.P.M. Carbon Dioxide–Nitrogen Separation Through Pressure Swing Adsorption. *Chemical Engineering Journal.* **2011**, 172, 698-704.

55. Liu, Z., Grande, C.A., Li, P., Yu, J., Rodrigues, A.E. Multi-Bed Vacuum Pressure Swing Adsorption for Carbon Dioxide Capture From Flue Gas. *Separation and Purification Technology.* **2011**, 81, 307-317.

56. Fuderer, A., Rudelstorfer, E. Selective Adsorption Process. U.S. Patent 3,986,849, 1976.

57. Golden, T.C., Kumar, R., Kratz, W.C. Hydrogen Purification. U.S. Patent 4,957,514, 1990.

58. Ribeiro, A.M., Grande, C., Lopes, F.V., Loureiro, J.M., Rodrigues, A.E. A Parametric Study of Layered Bed PSA for Hydrogen Purification. *Chemical Engineering Science.* **2008**, 63, 5258-5273.

59. Lopes, F.V.S., Grande, C.A., Ribeiro, A.M., Loureiro, J.M., Evaggelos, O., Nikolakis, V., Rodrigues, A.E. Adsorption of H2, CO2, CH4, CO, N2 and H2O in Activated Carbon and Zeolite for Hydrogen Production. *Separation Science and Technology.* **2009**, 44, 1045-1073.

60. Ribeiro, A.M., Grande, C.A., Lopes, F.V.S., Loureiro, J.M., Rodrigues, A.E. Four Beds Pressure Swing Adsorption for Hydrogen Purification: Case of Humid Feed and Activated Carbon Beds. *AIChE Journal.* **2009**, 55, 2292-2302.

61. Lopes, F.V.S., Grande, C.A., Rodrigues, A.E. Activated Carbon for Hydrogen Purification by Pressure Swing Adsorption: Multicomponent Breakthrough Curves and PSA Performance. *Chemical Engineering Science.* **2011**, 66, 303-317.

62. Sircar, S., Zondlo, J.W. Hydrogen Purification by Selective Adsorption. U.S.Patent 4,077,779, 1978.

63. Cho, S.H., Bhat, S.G.T., Han, S.S., Park, J.H., Kim, J.N., Jung, H. Pressure Swing Adsorption Apparatus and Method for Hydrogen Purification Using the Same U.S. Patent 8,298,319, 2012.

64. Silva, J.A.C., Rodrigues, A.E. Separation of n/iso-Paraffins Mixtures by Pressure Swing Adsorption. *Separation and Purification Technology.* **1998**, 13, 195-208.

65. Bárcia, P.S., Silva, J.A.C., Rodrigues, A.r.E. Octane Upgrading of C5/C6 Light Naphtha by Layered Pressure Swing Adsorption. *Energy & Fuels.* **2010**, 24, 5116-5130.

66. Silva, J.A.C., Da Silva, F.A., Rodrigues, A.r.E. Separation of n/iso Paraffins by PSA. *Separation and Purification Technology.* **2000**, 20, 97-110.

67. Kaul, B.K., Thurtell, J.H., Santiesteban, J.G., Poturovic, J. Separation of Normal Paraffins from Isoparaffins Using Rapid Cycle Pressure Swing Adsorption. U.S. Patent 2011/0275877, 2011.

68. Silva, F.A.D., Rodrigues, A.E. Propylene/Propane Separation by Vacuum Swing Adsorption Using 13X Zeolite. *AIChE Journal.* **2001**, 47, 341-357.

69. Da Silva, F.A., Rodrigues, A.E. Vacuum Swing Adsorption for Propylene/Propane Separation with 4A Zeolite. *Industrial & Engineering Chemistry Research.* **2001**, 40, 5758-5774.

70. Han, S.-S., Park, J.-H., Kim, J.-N., Cho, S.-H. Propylene Recovery from Propylene/Propane/Nitrogen Mixture by PSA Process. *Adsorption.* **2005**, 11, 621-624.

71. Rege, S.U., Yang, R.T. Propylene/Propane Separation by PSA: Sorbent Comparison and Multiplicity of Cyclic Steady States. *Chemical Engineering Science.* **2002**, 57, 1139-1149.

72. Grande, C.A., Rodrigues, A.E. Propane/Propylene Separation by Pressure Swing Adsorption Using Zeolite 4A. *Industrial & Engineering Chemistry Research.* **2005**, 44, 8815-8829.

73. Das, N., Kumar, P., Mallik, C., Bhandari, R.K. Development of a Helium Purification System Using Pressure Swing Adsorption. *Current Science.* **2012**, 103, 631-634.

74. Baksh, M. Methods and Systems for Helium Recovery. U.S. Patent 2010/0251892, 2010.

75. Doherty, K.S. Separation of Mixtures Especially Gas Mixtures. U.S. Patent 3,838,553, 1974.

76. Bodine, W.M., Seitz, C.A. Helium Purifier. U.S. Patent 3,683,589, 1972.

77. Prasad, R. Helium Recovery Process. U.S. Patent 8,152,898, 2012.

78. Ferreira, A.M. Sistema Adsortivo para Purificação de Hélio - Helisys 20. Master Thesis, Faculty of Engineering of the University of Porto, Porto, Portugal, 2012.

79. Taveira, P., Mendes, A. Xenon External Recycling Unit for Recovery, Purification and Reuse of Xenon in Anaesthesia Circuits. U.S. Patent 7,442,236, 2008.

80. Ryan, P.J., Farha, O.K., Broadbelt, L.J., Snurr, R.Q., Bae, Y.-s. Metal-Organic Frameworks for Xe/Kr Separation. U.S. Patent 2012/0073438 2012.

81. Hayashi, S., Tsuchiya, H., Haruna, K. Process for Obtaining High Concentration Argon by Pressure Swing Adsorption. U.S. Patent 4,529,412, 1985.

82. Jin, X., Malek, A., Farooq, S. Production of Argon from an Oxygen–Argon Mixture by Pressure Swing Adsorption. *Industrial & Engineering Chemistry Research.* **2006**, 45, 5775-5787.

83. Kumar, R., Sircar, S., White, T.R., Greskovich, E.J. Argon Purification. U.S. Patent 4,477,265, 1984.

84. Toyoda, M., Murase, H., Inohara, T., Naotsuka, H., Kobayashi, A., Takano, K., Ohkuma, K., *Application of Pressure Swing Adsorption to SF6 Separation and Liquefaction from SF6/N2 Mixtures* in *Power Engineering Society Winter Meeting*. 2000. p. 2156-2161.

85. Guro, D.E., Bushinsky, J.P., Nicholas, D.M. Purification of Ammonia Syngas. U.S. Patent 4,846,851, 1989.

86. Hidaki, M. Process for Refining an Ammonia Synthesis Gas. U.S. Patent 4,624,841, 1986.

87. Skarstrom, C.W., Crowley, R.P., Heilman, W.O. Pressure Cycling Operation for the Manufacture of Ammonia. U.S. Patent 3,282,647, 1966.

88. Montgareuil, P.G.d., Dominé, D. Process for Separating a Binary Gaseous Mixture by Adsorption. U.S. Patent 3,155,468, 1964.

89. Berlin, N.H., Matawan, N.J. Method for Providing an Oxygen-Enriched Environment. U.S. Patent 3,280,536, 1966.

90. Marsh, W.D., Pramuk, F.S., Hoke, R.C., Skarstrom, C.W. Pressure Equalization Depressuring in Heatless Adsorption. U.S. Patent 3,142,547, 1964.

91. Yavary, M., Ale-Ebrahim, H., Falamaki, C. The Effect of Reliable Prediction of Final Pressure During Pressure Equalization Steps on the Performance of PSA Cycles. *Chemical Engineering Science.* **2011**, 66, 2587-2595.

92. Kumar, R., Guro, D.E., Schmidt, W.P. A New Concept to Increase Recovery From H2 PSA: Processing Different Pressure Feed Streams in a Single Unit. *Gas Separation & Purification.* **1995**, 9, 271-276.

93. Santos, J.C., Portugal, A.F., Magalhães, F.D., Mendes, A. Optimization of Medical PSA Units for Oxygen Production. *Industrial and Engineering Chemistry Research.* **2006**, 45, 1085-1096.

94. Shirley, A.I., Lemcoff, N.O. High-Purity Nitrogen by Pressure-Swing Adsorption. *AIChE Journal.* **1997**, 43, 419-424.

95. White, D.H., Barkley, P.G. The Design of Pressure Swing Adsorption Systems. *Chemical Engineering Programs.* **1989**, 85, 25-33.

96. Grande, C.A. Advances in Pressure Swing Adsorption for Gas Separation. *ISRN Chemical Engineering.* **2012**, 2012, 13.

97. Baksh, M.S.A., Serbezov, A., Notaro, F., Wells, F. Pressure Swing Adsorption Method for Production of an Oxygen-Enriched Gas. U.S. Patent 6,475,265 B1, 2002.

98. Lemcoff, N.O. Nitrogen Separation From Air by Pressure Swing Adsorption. In *Studies in Surface Science and Catalysis;* Volume 120, Part A; Elsevier: 1999; 347-370.

99. Batta, L.B. Selective Adsorption Process. U.S. Patent 3,564,816, 1971.

100. Feldbauer, G.F., Cranford, N.J. Regeneration of Individual Molecular Sieve Compartments. U.S. Patent 3,347,783, 1967.

101. Stark, T.M., Morristown, N.J. Gas Separation by Adsorption Process. U.S. Patent 3,252,268, 1966.

102. Wagner, J.L., Lackawanna, N.Y. Selective Adsorption Process. U.S. Patent 3,430,418, 1969.

103. Cassidy, R.T. Polybed Pressure-Swing Adsorption Hydrogen Processing. In *Adsorption and Ion Exchange with Synthetic Zeolites;* ACS Symposium Series 135; American Chemical Society Symposium Series: 1980; 247-259.

104. Lü, Y., Doong, S.-J., Bülow, M. Pressure-Swing Adsorption Using Layered Adsorbent Beds with Different Adsorption Properties: I—Results of Process Simulation. *Adsorption.* **2003**, 9, 337-347.

105. Lü, Y., Doong, S.-J., Bülow, M. Pressure-Swing Adsorption Using Layered Adsorbent Beds with Different Adsorption Properties: II—Experimental Investigation. *Adsorption.* **2005**, 10, 267-275.

106. Watson, C.F., Whitley, R.D., Meyer, M.L. Multiple Zeolite Adsorbent Layers in Oxygen Separation. U.S. Patent 5,529,610, 1996.

107. Gaffney, T.R. Porous Solids for Air Separation. *Current Opinion in Solid State and Materials Science.* **1996**, 1, 69-75.

108. Boniface, H.A., Ruthven, D.M. Selectivity of Some Zeolites for Adsorption of Atmospheric Gases. *Gas Separation & Purification.* **1993**, 7, 183-184.

109. Budner, Z., Dula, J., Podstawa, W., Gawdzik, A. Study and Modelling of the Vacuum Swing Adsorption (VSA) Process Employed in the Production of Oxygen. *Chemical Engineering Research and Design.* **1999**, 77, 405-412.

110. Jee, J.-G., Lee, C.H. PVSA Processes for High Purity O_2 Generation and Purification from Ambient Air. *AIChE Journal.* **2005**, 51, 2988.

111. Lee, S.-J., Jung, J.-H., Moon, J.-H., Jee, J.-G., Lee, C.-H. Parametric Study of the Three-Bed Pressure−Vacuum Swing Adsorption Process for High Purity O2 Generation from Ambient Air. *Industrial & Engineering Chemistry Research.* **2007**, 46, 3720-3728.

112. Olajossy, A., Gawdzik, A., Budner, Z., Dula, J. Methane Separation from Coal Mine Methane Gas by Vacuum Pressure Swing Adsorption. *Chemical Engineering Research and Design.* **2003**, 81, 474-482.

113. Reinhold, H.E., D'Amico, J.S., Knaebel, K.S. Natural Gas Enrichment Process. U.S. Patent 5,536,300, 1996.

114. Reiß, G. Status and Development of Oxygen Generation Processes on Molecular Sieve Zeolites. *Gas Separation & Purification.* **1994**, 8, 95-99.

115. Reiss, G. Oxygen Enrichment of Air With Molecular Sieve Zeolites Using The PSA/VSA Technique. In *Studies in Surface Science and Catalysis;* Volume 46; Elsevier: 1989; 607-614.

116. Gomes, V.G., Hassan, M.M. Coalseam Methane Recovery by Vacuum Swing Adsorption. *Separation and Purification Technology.* **2001**, 24, 189-196.

117. Russell, G.K. Apparatus and Method for Fractionating Air and Other Gaseous Mixtures. U.S. Patent 4,349,357, 1982.

118. Liow, J.-L., Kenney, C.N. The Backfill Cycle of the Pressure Swing Adsorption Process. *AIChE Journal.* **1990**, 36, 53-65.

119. Jones, R.L., Keller, E., Wells, C. Rapid Pressure Swing Adsorption With High Enrichment Factor. U.S. Patent 4,194,892, 1980.

120. Chai, S.W., Kothare, M.V., Sircar, S. Rapid Pressure Swing Adsorption for Reduction of Bed Size Factor of a Medical Oxygen Concentrator. *Industrial & Engineering Chemistry Research.* **2011**, 50, 8703-8710.

121. Connor, D.J., Doman, D.G., Jeziorowski, L., Keefer, B.G., Larisch, B., McLean, C., Shaw, I. Rotary Pressure Swing Adsorption Apparatus. U.S. Patent 6,406,523, 2002.

122. Keefer, B.G. High Frequency Pressure Swing Adsorption. U.S. Patent 6,176,897, 2001.

123. Keefer, B.G., McLean, C. High Frequency Rotary Pressure Swing Adsorption Apparatus. U.S. Patent 6,056,804, 2000.

124. Ferreira, D., Magalhães, R., Bessa, J., Taveira, P., Sousa, J., Whitley, R.D., Mendes, A. Study of AgLiLSX for Single-Stage High-Purity Oxygen Production. *Industrial & Engineering Chemistry Research.* **2014**, 53, 15508-15516.

125. Silva, B., Solomon, I., Ribeiro, A.M., Lee, U.H., Hwang, Y.K., Chang, J.-S., Loureiro, J.M., Rodrigues, A.E. H2 Purification by Pressure Swing Adsorption Using CuBTC. *Separation and Purification Technology.* **2013**, 118, 744-756.

126. Shi, M., Kim, J., Sawada, J.A., Lam, J., Sarabadan, S., Kuznicki, T.M., Kuznicki, S.M. Production of Argon Free Oxygen by Adsorptive Air Separation on Ag-ETS-10. *AIChE Journal.* **2013**, 59, 982-987.

127. Rahimpour, M.R., Ghaemi, M., Jokar, S.M., Dehghani, O., Jafari, M., Amiri, S., Raeissi, S. The Enhancement of Hydrogen Recovery in PSA Unit of Domestic Petrochemical Plant. *Chemical Engineering Journal.* **2013**, 226, 444-459.

128. Lopes, F.V.S., Grande, C.A., Rodrigues, A.E. Fast-Cycling VPSA for Hydrogen Purification. *Fuel.* **2012**, 93, 510-523.

129. Dong, F., Lou, H., Kodama, A., Goto, M., Hirose, T. A New Concept in the Design of Pressure-Swing Adsorption Processes for Multicomponent Gas Mixtures. *Industrial & Engineering Chemistry Research.* **1998**, 38, 233-239.

130. Dong, F., Lou, H., Kodama, A., Goto, M., Hirose, T. The Petlyuk PSA Process for the Separation of Ternary Gas Mixtures: Exemplification by Separating a Mixture of CO2–CH4–N2. *Separation and Purification Technology.* **1999**, 16, 159-166.

131. Sircar, S. Pressure Swing Adsorption. *Industrial & Engineering Chemistry Research.* **2002**, 41, 1389-1392.

132. Yang, R.T. *Adsorbents. Fundamentals and Applications*; John Wiley & Sons: New Jersey, USA, 2003.

133. Barrer, R.M. *Zeolites and Clay Minerals and Sorbents and Molecular Sieves*; Academic Press Inc.: London, 1978.

134. Breck, W.D. *Zeolite Molecular Sieves*; John Wiley & Sons: New York, USA, 1974.

135. Santos, J.C. Study of New Adsorbents and Operation Cycles for Medical PSA Units. Ph.D. Thesis, Faculty of Engineering of the University of Porto, Porto, Portugal, 2005.

136. Chiang, R.L., Whitley, R.D., Ostroski, J.E., Dee, D.P. Argon/Oxygen Selective X-Zeolite. U.S. Patent 6,432,170, 2002.

137. Joaquín, C. Present and Future Synthesis Challenges for Zeolites. *Chemical Engineering Journal.* **2010**, 156, 236-242.

138. Rege, S.U., T. Yang, R., Buzanowski, M.A. Sorbents for Air Prepurification in Air Separation. *Chemical Engineering Science.* **2000**, 55, 4827-4838.

139. Santos, J.C., Magalhães, F.D., Mendes, A. Contamination of Zeolites Used in Oxygen Production by PSA: Effects of Water and Carbon Dioxide. *Industrial & Engineering Chemistry Research.* **2008**, 47, 6197-6203.

140. Ferreira, D., Magalhães, R., Taveira, P., Mendes, A.l. Effective Adsorption Equilibrium Isotherms and Breakthroughs of Water Vapor and Carbon Dioxide on Different Adsorbents. *Industrial & Engineering Chemistry Research.* **2011**, 50, 10201-10210.

141. Do, D.D. *Adsorption Analysis: Equilibria and Kinetics*; Imperial College Press: London, 1997.

142. Reid, C.R., Thomas, K.M. Adsorption of Gases on a Carbon Molecular Sieve Used for Air Separation: Linear Adsorptives as Probes for Kinetic Selectivity. *Langmuir.* **1999**, 15, 3206-3218.

143. Ruthven, D.M. *Principles of Adsorption and Adsorption Processes*; John Wiley & Sons: New York, 1984.

144. Campo, M. Carbon Molecular Sieve Membranes for Gas Separation: Study, Preparation and Characterization. Ph.D. Thesis, Faculty of Engineering of the University of Porto, Porto, Portugal, 2009.

145. Bae, Y.S., Lee, C.H. Sorption Kinetics of Eight Gases on a Carbon Molecular Sieve at Elevated Pressure. *Carbon.* **2005**, 43, 95-107.

146. Bae, Y.S., Ryu, Y., Lee, C.H. Pressure-Dependent Models for Adsorption Kinetics on a CMS. *Third Pacific Basin Conference.* **2003**, 167-171.

147. Bae, Y.-S., Moon, J.-H., Ahn, H., Lee, C.-H. Effects of Adsorbate Properties on Adsorption Mechanism in a Carbon Molecular Sieve. *Korean Journal of Chemical Engineering.* **2004**, 21, 712-720.

148. Li, J.-R., Kuppler, R.J., Zhou, H.-C. Selective Gas Adsorption and Separation in Metal-Organic Frameworks. *Chemical Society Reviews.* **2009**, 38, 1477-1504.

149. Bárcia, P.S., Bastin, L., Hurtado, E.J., Silva, J.A.C., Rodrigues, A.E., Chen, B. Single and Multicomponent Sorption of CO2, CH4 and N2 in a Microporous Metal-Organic Framework. *Separation Science and Technology.* **2008**, 43, 3494-3521.

150. Bárcia, P.S., Guimarães, D., Mendes, P.A.P., Silva, J.A.C., Guillerm, V., Chevreau, H., Serre, C., Rodrigues, A.E. Reverse Shape Selectivity in the Adsorption of Hexane and Xylene Isomers in MOF UiO-66. *Microporous and Mesoporous Materials.* **2011**, 139, 67-73.

151. Bastin, L., Bárcia, P.S., Hurtado, E.J., Silva, J.A.C., Rodrigues, A.E., Chen, B. A Microporous Metal−Organic Framework for Separation of CO2/N2 and CO2/CH4 by Fixed-Bed Adsorption. *The Journal of Physical Chemistry C.* **2008**, 112, 1575-1581.

152. Bárcia, P. Separation of Light Naphtha for the Octane Upgrading of Gasoline. PhD Thesis, Faculty of Engineering of the University of Porto, Porto, Portugal, 2010.

153. Bárcia, P.S., Zapata, F., Silva, J.A.C., Rodrigues, A.E., Chen, B. Kinetic Separation of Hexane Isomers by Fixed-Bed Adsorption with a Microporous Metal−Organic Framework. *The Journal of Physical Chemistry B.* **2007**, 111, 6101-6103.

154. Nicolau, M.P.M., Bárcia, P.S., Gallegos, J.M., Silva, J.A.C., Rodrigues, A.E., Chen, B. Single- and Multicomponent Vapor-Phase Adsorption of Xylene Isomers and Ethylbenzene in a Microporous Metal−Organic Framework. *The Journal of Physical Chemistry C.* **2009**, 113, 13173-13179.

155. Afonso, R., Mendes, A., Gales, L. Peptide-Based Solids: Porosity and Zeolitic Behavior. *Journal of Materials Chemistry.* **2012**, 22, 1709-1723.

156. Afonso, R., Mendes, A., Gales, L. Hydrophobic Dipeptide Crystals: A Promising Ag-free Class of Ultramicroporous Materials Showing Argon/Oxygen Adsorption Selectivity. *Physical Chemistry Chemical Physics.* **2014**, 16, 19386-19393.

157. Afonso, R.V., Durão, J., Mendes, A., Damas, A.M., Gales, L. Dipeptide Crystals as Excellent Permselective Materials: Sequential Exclusion of Argon, Nitrogen, and Oxygen. *Angewandte Chemie International Edition.* **2010**, 49, 3034-3036.

158. Ansón, A., Kuznicki, S.M., Kuznicki, T., Haastrup, T., Wang, Y., Lin, C.C.H., Sawada, J.A., Eyring, E.M., Hunter, D. Adsorption of Argon, Oxygen, and Nitrogen on Silver Exchanged ETS-10 Molecular Sieve. *Microporous and Mesoporous Materials.* **2008**, 109, 577-580.

159. Golden, T.C., Weist Jr., E.L., Novosat, P.A. Adsorbents for Rapid Cycle Pressure Swing Adsorption Processes. U.S. Patent Application 2006/0236862, 2006.

160. Berlin, N.H. Vacuum Cycle Adsorption. U.S. Patent 3,164,454, 1967.

161. Ruder, J.M., Iles, T.L. Oxygen Air Enrichment Method. U.S. Patent 3,922,149, 1975.

162. Coe, C.G. Moleculary Engineered Adsorbents for Air Separation. *Gas Separation Technology.* **1990**, 149-159.

163. Coe, C.G., Kuznicki, S.M., Srinivasan, R., Jenkins, R.J. Molecularly Engineered, High-Performance Adsorbent. In *Perspectives in Molecular Sieve Science;* ACS Symposium Series 368; American Chemical Society: Washington, DC, 1988; 478-491.

164. Nagy, J.B. *Synthesis, Characterization and Use of Zeolitic Microporous Materials*; DecaGen: 1998.

165. Park, Y.-J., Lee, S.-J., Moon, J.-H., Choi, D.-K., Lee, C.-H. Adsorption Equilibria of O_2, N_2, and Ar on Carbon Molecular Sieve and Zeolites 10X, 13X, and LiX. *Journal of Chemical & Engineering Data.* **2006**, 51, 1001-1008.

166. Kayser, J.C., Knaebel, K.S. Pressure Swing Adsorption: Experimental Study of an Equilibrium Theory. *Chemical Engineering Science.* **1986**, 41, 2931-2938.

167. Jee, J.-G., Kim, M.-B., Lee, C.-H. Pressure Swing Adsorption Processes to Purify Oxygen Using a Carbon Molecular Sieve. *Chemical Engineering Science.* **2005**, 60, 869-882.

168. Kim, M.-B., Jee, J.-G., Bae, Y.-S., Lee, C.-H. Parametric Study of Pressure Swing Adsorption Process To Purify Oxygen Using Carbon Molecular Sieve. *Industrial & Engineering Chemistry Research.* **2005**, 44, 7208-7217.

169. Bansal, R.K. Pressure Swing Adsorption Process and System for Gas Separation. U.S. Patent 4,973,339, 1990.

170. Rege, S.U., Yang, R.T. Kinetic Separation of Oxygen and Argon Using Molecular Sieve Carbon. *Adsorption.* **2000**, 6, 15-22.

171. Shirley, A.I., Lemcoff, N.O. Air Separation by Carbon Molecular Sieves. *Adsorption.* **2002**, 8, 147-155.

172. Jee, J.-G., Lee, S.-J., Lee, C.-H. Comparison of the Adsorption Dynamics of Air on Zeolite 5A and Carbon Molecular Sieve Beds. *Korean Journal of Chemical Engineering.* **2004**, 21, 1183-1192.

173. Jee, J.-G., Lee, S.-J., Moon, H.-M., Lee, C.-H. Adsorption Dynamics of Air on Zeolite 13X and CMS Beds for Separation and Purification. *Adsorption.* **2005**, 11, 415-420.

174. Lee, C.-H. Apparatus for Producing Oxygen and Method for Controlling the same. U.S. Patent 2006/0162565 A1, 2006.

175. Bhide, B.D., Stern, S.A. A New Evaluation of Membrane Processes for the Oxygen-Enrichment of Air. I. Identification of Optimum Operating Conditions and Process Configuration. *Journal of Membrane Science.* **1991**, 62, 13-35.

176. Bhide, B.D., Stern, S.A. A New Evaluation of Membrane Processes for the Oxygen-Enrichment of Air. II. Effects of Economic Parameters and Membrane Properties. *Journal of Membrane Science.* **1991**, 62, 37-58.

177. Hwang, S.-T., Thorman, J.M. The Continuous Membrane Column. *AIChE Journal.* **1980**, 26, 558-566.

178. Hwang, S.-T., Ghalchi, S. Methane Separation by a Continuous Membrane Column. *Journal of Membrane Science.* **1982**, 11, 187-198.

179. Kothe, K.D., Chen, S., Kao, Y.K., Hwang, S.T. A Study of the Separation Behavior of Different Membrane Columns with Respect to Ternary Gas Mixtures. *Journal of Membrane Science.* **1989**, 46, 261-281.

180. Matson, S.L., Lopez, J., Quinn, J.A. Separation of Gases with Synthetic Membranes. *Chemical Engineering Science.* **1983**, 38, 503.

181. Tsuru, T., Hwang, S.T. Production of High-Purity Oxygen by Continuous Membrane Column Combined with PSA Oxygen Generator. *Industrial & Engineering Chemistry Research.* **1994**, 33, 311-316.

182. Mercea, P.V., Hwang, S.-T. Oxygen Separation From Air by a Combined Pressure Swing Adsorption and Continuous Membrane Column Process. *Journal of Membrane Science.* **1994**, 88, 131-144.

183. Wilkerson, B.E. The Adsorption of Argon and Oxygen on Silver Mordenite. Master Thesis, Graduate School of the Ohio State University, Ohio, U.S.A., 1990.

184. Sebastian, J., Jasra, R.V. Sorption of Nitrogen, Oxygen, and Argon in Silver-Exchanged Zeolites. *Industrial & Engineering Chemistry Research.* **2005**, 44, 8014-8024.

185. Hutson, N.D., Rege, S.U., Yang, R.T. Mixed Cation Zeolites: LixAgy-X as a Superior Adsorbent for Air Separation. *AIChE Journal.* **1999**, 45, 724-734.

186. Hutson, N.D., Yang, R.T. Structural Effects on Adsorption of Atmospheric Gases in Mixed Li,Ag–X-Zeolite. *AIChE Journal.* **2000**, 46, 2305-2317.

CHAPTER II

Ferreira, D., Magalhães, R., Taveira, P., Mendes, A. Effective Adsorption Equilibrium Isotherms and Breakthroughs of Water Vapor and Carbon Dioxide on Different Adsorbents. *Industrial & Engineering Chemistry Research.* **2011**, 50, 10201-10210**.**

The author contributed to the planning and execution of all the experiments described in this chapter, except the breakthrough measurements which were carried out by Magalhães, R. The author was also involved on the discussion and interpretation of results, as well as on the preparation of the manuscript.

2 Study of pre-adsorbents for water vapor and carbon dioxide removal

Abstract

Pre-treatment stage is usually a requirement for any adsorption based air separation process. Carbon dioxide and water vapor present in atmosphere act as contaminants, deactivating adsorbents, particularly zeolites used in oxygen pressure swing adsorption processes. Such systems usually present one or more pre-layers to ensure full removal of these two contaminants, protecting the oxygen/nitrogen selective layer. In this section, two 13X-type zeolites, one activated alumina and one highly pure silica are compared in terms of capacity for water vapor and carbon dioxide removal from air. Water and carbon dioxide adsorb irreversibly on these adsorbents up to a certain extension and then effective adsorption isotherms and breakthroughs curves were obtained. The effective properties were attained after three cycles under close to vacuum pressure swing adsorption conditions. A combination of two layers for the pre-columns is suggested: the first, composed by either silica or alumina to remove most of the water without significant loss of cyclic adsorption capacity, and a second, composed by zeolite, to reduce the amount of water and carbon dioxide down to ppm levels. These should prevent contamination and consequent loss of efficiency in the nitrogen/oxygen selective layer.

2.1 Introduction

Over the past decade, oxygen production by equilibrium-based vacuum pressure swing adsorption (VPSA) has increased significantly, limited by a maximum oxygen concentration of 95 % (balanced mostly by argon) [1] in a single-stage. Higher oxygen concentration is not possible because commercial adsorbents do not exhibit Ar/O_2 adsorption selectivity above 1 [2]. However, in 2003, Air Products and Chemicals, Inc.® reported a VPSA for the production of high-purity oxygen from air using a new argon/oxygen selective zeolite, a AgLiLSX (lithium low silica-X silver-based zeolite) [3, 4].

It is known that impurities such as carbon dioxide and water vapor are found to adsorb strongly, and to some extent, irreversibly on the adsorbents used in air separation, affecting drastically both capacity and selectivity [5]. Furthermore, these species usually have high heat of adsorption causing large temperature variations along the adsorption and desorption steps of VPSA operation [5]. Oxygen/nitrogen selective adsorbents, such as LiLSX-type zeolites, and particularly AgLiLSX, are very sensitive to water vapor and carbon dioxide contamination, deactivating when exposed to atmospheric air. Accordingly, a VPSA unit including such adsorbents should consider pre-treating the feed air to reduce carbon dioxide and water vapor contents to the lowest possible levels [6], besides removing possible hydrocarbon contaminants.

In pre-treatment adsorption-based processes, it is important to choose proper adsorbents for the removal of such components from the air feed. For coarse water vapor removal, the most common adsorbent is silica gel and activated alumina, because of its large adsorption capacity and easy regeneration. For residual water vapor removal, down to parts per million (ppm) levels, zeolites are preferred [7, 8]. Zeolites are also the normally chosen adsorbents for carbon dioxide removal. A

significant number of patents concerning air pre-purification processes revealed that the most common adsorbents for water vapor and carbon dioxide removal by PSA are activated alumina and zeolites such as 13X-type zeolite (also known as NaX) [9-11].

Most PSA air treatment designs include a layered bed configuration composed of a combination of adsorbents to minimize purges losses and to keep temperature excursions as low as possible during the pressure swing cycle [5]. Usually, beds with a layer of silica or alumina followed by a zeolite are used to remove water and carbon dioxide.

In 2000, Rege et al. [5] studied two conventional adsorbents for air pre-purification by PSA, a 13X zeolite (Linde) and activated alumina PSD 350 (Alcoa Inc.). These authors found that the adsorption kinetics of carbon dioxide and water vapor on the adsorbents considered is fast enough to assume instantaneous equilibrium and 13X zeolite is ideal for carbon dioxide removal. Later on, the same authors [12] concluded that the overall performance of a layered bed of activated alumina/13X zeolite was better than using the same volume of either adsorbent. Many other studies of carbon dioxide and water vapor adsorption on different adsorbents can be found in the literature [7, 8, 13-20].

All these studies report equilibrium and kinetic data obtained from experiments using fresh adsorbents, i.e. regenerated adsorbents or “as received”. However, in cyclic adsorption processes, such as VPSA, adsorbents are submitted to cyclic pressure operation, in which, after saturation, the adsorbent is partially or totally regenerated by reducing total pressure and by purging with a fraction of the product stream [21]. Therefore, adsorbents submitted to contaminants in cyclic operation, such as carbon dioxide and water vapor, experience some irreversible adsorption and, consequently, some loss of capacity after just a few adsorption/desorption cycles. This process is progressive and it usually stabilizes after some cycles.

In 2000, Gales et al. [22] studied and discussed the adsorption behavior of acetone, ethanol and ethyl acetate on activated carbon when adsorption/desorption cycles are applied, and they concluded that, after ~ 5 cycles, the system reaches a "stationary state", where adsorption and desorption branches cannot be distinguished within experimental error. This new adsorption isotherm mirrors the effective adsorption capacity of the adsorbent when inserted in a cycle adsorption process. On the other hand, when designing cyclic adsorption units based only on adsorbents properties obtained using fresh samples results is an overestimation of the efficiency of pre-treatment stage. In the present work we suggest the use of an effective adsorption isotherm obtained after making the adsorbent to contact with similar cyclic boundary conditions to those observed in the adsorption process for several adsorption/desorption cycles, until a "stationary state" was reached.

Since, the adsorption kinetics of carbon dioxide and water vapor on the adsorbents is considered to be fast enough to assume instantaneous equilibrium, frequently kinetic adsorption is not reported in literature [23-28]. In the present work, the same concept proposed for obtained the effective adsorption isotherms was applied to breakthrough experiments. Then, effective breakthrough curves were obtained after reaching a steady behavior which accounts for both adsorption equilibrium and kinetics.

The present work concerns the characterization of several adsorbents in terms of capability for water vapor and carbon dioxide removal as part of a pre-treatment solution of a VPSA unit (operating between 0.2 and 1.4 bar) for oxygen production. Effective adsorption isotherms were obtained to assess the effective adsorption capacity of the adsorbents towards water vapor and carbon dioxide. Also, a set of effective breakthrough runs were carried out to assess the performance of the adsorbents in cyclic operating conditions.

2.2 Experimental

2.2.1 Materials

The following adsorbents were selected for the present work: adsorbents 13X-type zeolites ZEOX OII and Z10-02ND (Zeochem), activated alumina F200 7x14 Tyler mesh (BASF), and highly pure silica KC-Trockenperlen WS 2050 (BASF). Accordingly to the information from the producers, the Z10-02ND adsorbent is a specially enhanced zeolite for better removal of carbon dioxide; medical-grade ZEOX OII zeolite is used in small PSA oxygen units and can withstand air operation with little pre-treatment; F-200 is one of the most used activated aluminas in the market; and KC-Trockenperlen is a special silica developed to resist to large loadings of water.

Helium picnometry was used to determine the real density of the samples. Surface area, pore volume and average pore diameter, excluding microporosity, and apparent density was determined by mercury porosimetry. The physical properties of the adsorbents are listed in Table 2.1. The adsorbents, as received, were regenerated at high temperature (375 °C for zeolites, 150 °C for alumina and silica) for 6 h in a nitrogen atmosphere with a minimum flowrate of 1 L_{STP}·min^{-1} for each kilogram of adsorbent.

Table 2.1 – Physical properties of the adsorbents.

Property	**ZEOX OII**	**Z10-02ND**	**Alumina**	**Silica**
Geometry	spherical	spherical	spherical	spherical
average pellet radius, mm	0.40	1.05	1.15	1.85
pellet crushing strength, N	1.0	9.5	60	220
apparent density, g·cm^{-3}	1.101	1.047	1.412	0.994
total surface area, m^2·g^{-1}	7.1	15.4	157.5	45.7
pore volume, cm^3·g^{-1}	0.309	0.327	0.265	0.147
structural density, g·cm^{-3}	2.320	2.830	2.967	2.193
meso/macro porosity, %	0.53	0.63	0.52	0.55

2.2.2 Methods

The volumetric method was used to determine the carbon dioxide adsorption isotherms. This method is based on pressure variation of the relevant gas after an expansion [29]. Knowing the pressure decrease and assuming ideal gas behavior for the system under study, it is possible to determine the concentration of the solute adsorbed. The apparatus used, illustrated in Figure 2.1, is composed by two stainless steel tanks, three pressure transducers (Drück PMP 4010, range 0 – 7 bar, 0 – 2 bar and 0 – 350 mbar, ± 0.08 % FS), a vacuum pump (Vacuubrand, model RZ 2.5) and a thermostatic bath (Huber, model CC2+K12) to maintain the temperature inside the system constant.

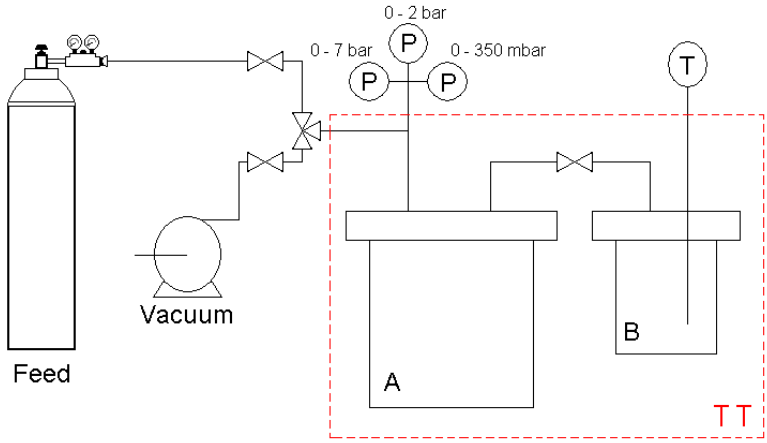

Figure 2.1 – Schematic representation of the volumetric apparatus.

The determination of water vapor equilibrium isotherms was conducted using the gravimetric method, implemented in a magnetic suspension balance from Rubotherm® (metal version and 10^{-5} g of precision). The gravimetric method consists in measuring the adsorbent weight variation when a perturbation is made to the gas pressure in contact with the adsorbent [29]. The variation of mass allows the

determination of the adsorbed amount. The experimental set-up, illustrated in Figure 2.2, consists on the magnetic suspension balance, a 5 L stainless steel buffer tank, two pressure sensors (Drück PMP 4010, range 0 – 7 bar and 0 – 350 mbar, ± 0.08 % FS), a vacuum pump (Edwards, model RV5) and a thermostatic bath (Huber, model CC1+K6) for circulating water in the jacket of the system.

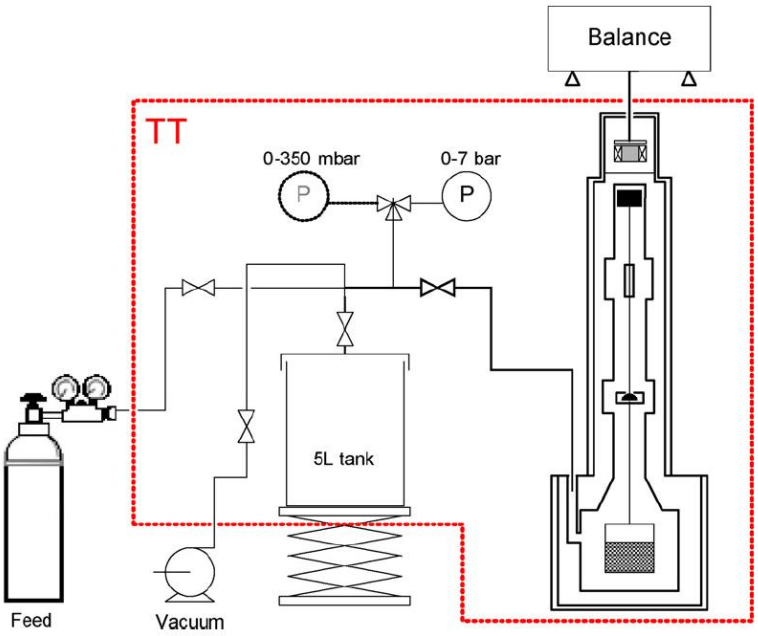

Figure 2.2 – Schematic representation of the gravimetric apparatus [30].

Experiments for obtaining the isotherms were preceded by heating up the sample inside the relevant vessel at 90 °C, using helium followed by vacuum < 0.01 mbar. The procedure was performed repeatedly for 8 times over a period of 4 h to remove any adsorbed contaminant present after the regenerating step.

The breakthrough curves were determined in an in-house built experimental setup, sketched in Figure 2.3. The setup is placed inside of a thermostatic chamber (to ensure isothermal operation). It consists of a column filled with adsorbent, where two

thermocouples were inserted – one at the entrance and the other at the exit – two pressure transducers (Druck PMP 4010, range 0 – 7 bar, ± 0.08 % FS), one feed mass flow controller (Bronkhorst El-flow, 100 mL_{STP}·min^{-1} and range 0 – 2 L_{STP}·min^{-1}, ± 0.5 % Rd plus ± 0.1 % FS), an exit mass flow meter (Bronkhorst El-flow, 0 – 10 L_{STP}·min^{-1} ± 0.5 % Rd plus ± 0.1 % FS), and a vacuum pump (Ilmvac, MPC201T) for the desorption step under low-pressure conditions. The water vapor and carbon dioxide compositions of the outlet flow were determined using a hygrometer (Vaisala DMP74b) and carbon dioxide analyser (Vaisala GMP70), respectively. The bed characteristics and experimental conditions are summarized in Table 2.2.

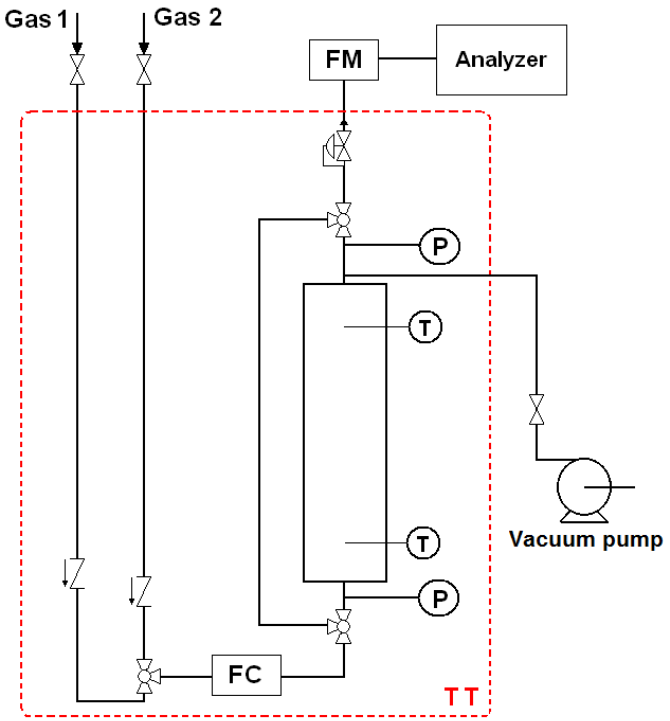

Figure 2.3 – Sketch of the breakthrough apparatus.

Table 2.2 – Conditions for breakthrough experiments.

parameter	value/remark
bed length, cm	31.0
bed diameter, cm	3.15
column volume, cm^3	241.6
inlet dew point, $^{\circ}C$	5
CO_2 composition, ppm	450
temperature, $^{\circ}C$	27
adsorption conditions	
flow rate, $L_{STP} \cdot min^{-1}$	5.2
pressure, bar	1.4
desorption conditions	
flow rate, $L_{STP} \cdot min^{-1}$	0.8 (nitrogen)
pressure, bar	0.2

2.3 Results and discussion

2.3.1 Adsorption equilibrium

In the present study, the carbon dioxide adsorption isotherms were obtained at three temperatures – 15 $^{\circ}C$, 35 $^{\circ}C$ and 55 $^{\circ}C$ – using fresh adsorbents. Concerning the water vapor adsorption isotherms, they were obtained at 35 $^{\circ}C$, also using fresh adsorbents. The adsorption equilibrium isotherms for carbon dioxide on the 13X-type zeolites, activated alumina and silica are plotted in Figure 2.4 and Figure 2.5.

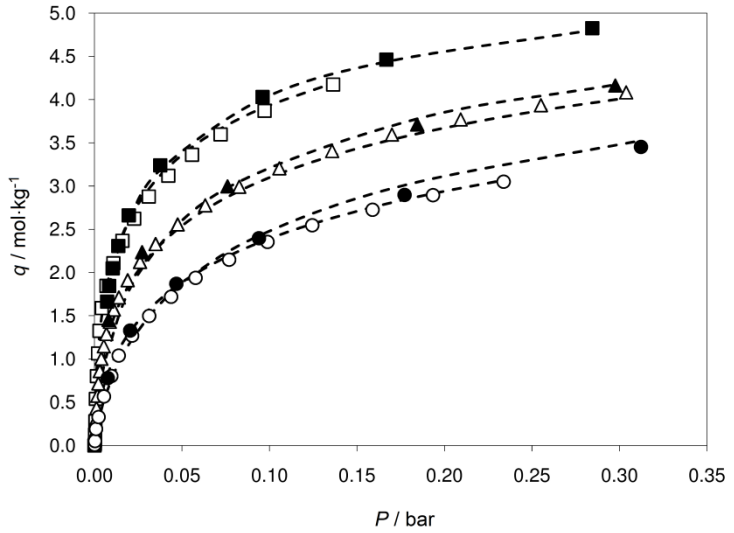

Figure 2.4 – Carbon dioxide isotherms on ZEOX OII (at: □, 15 °C; △, 35 °C; and ○, 55 °C) and Z10-02ND (at: ■, 15 °C; ▲, 35 °C; and ●, 55 °C). The dashed line represents the multi-temperature Toth isotherm fitting.

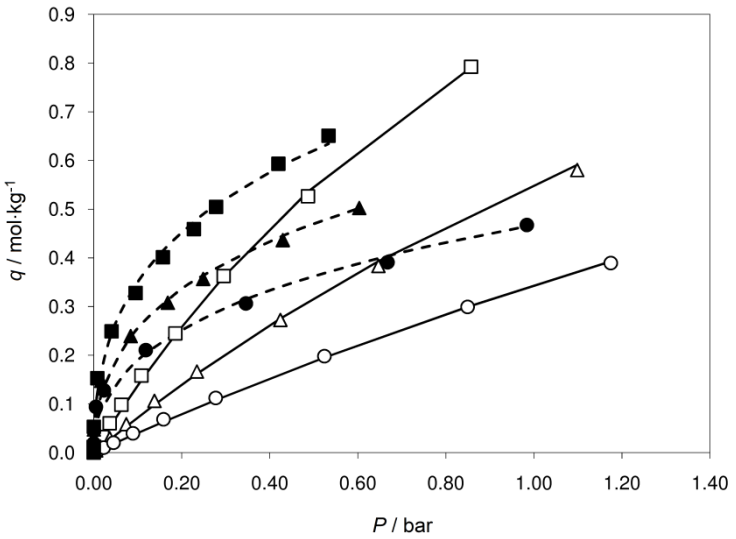

Figure 2.5 – Carbon dioxide isotherms on silica (at: □, 15 °C; △, 35 °C; and ○, 55 °C) and alumina (at: ■, 15 °C; ▲, 35 °C; and ●, 55 °C). The solid line represents multi-temperature Langmuir isotherm fitting; dashed line represents multi-temperature Toth isotherm fitting.

Zeolites show similar carbon dioxide adsorption isotherms while alumina and silica have considerably less adsorption capacity. Silica exhibits the least adsorption capacity for low pressures, and, compared to silica, alumina has the most favorable isotherms. Figure 2.6 shows the carbon dioxide isotherms at 35 °C on the fresh adsorbents on a log-log scale. This figure indicates that zeolites exhibit significantly higher carbon dioxide loadings than alumina or silica. Therefore, based on equilibrium, the selected zeolites are better adsorbents for carbon dioxide removal than silica or alumina.

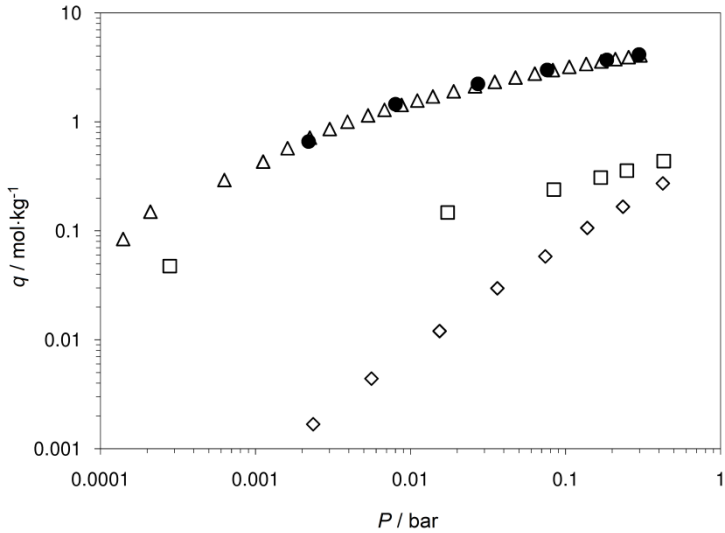

Figure 2.6 – Carbon dioxide isotherms at 35 °C, in log-log scale, on fresh adsorbents: △, ZEOX OII; ●, Z10-02ND; □, alumina; and ◇, silica.

Wang and LeVan [8] and Lee et al. [13] measured the carbon dioxide adsorption on 13X zeolites. The experimental data obtained in these studies were fitted using the Toth multi-temperature model. Adsorption loadings of 3.44 mol·kg^{-1} [8] and 2.46 mol·kg^{-1} [13] at 0.3 bar and 35 °C were reported. In the present work, under similar conditions, the adsorption loading obtained for ZEOX OII was 4.01 mol·kg^{-1} and

for Z10-02ND was 4.18 mol·kg^{-1}. Wang and LeVan reported also isotherms of carbon dioxide on silica gel, referring an adsorption loading of 0.310 mol·kg^{-1} at 0.3 bar and 35 $^{\circ}$C. Under similar conditions, an adsorption loading of 0.203 mol·kg^{-1} was obtained for silica. Rege et al. [5] studied carbon dioxide adsorption on several adsorbents including γ-alumina, and they obtained an adsorption loading of 0.455 mol·kg^{-1} for the previously mentioned conditions, which is similar to the adsorption loading obtained in the present work for alumina, 0.401 mol·kg^{-1}. The broad amplitude of results is to be expected, considering that materials obtained from different suppliers undergo different production processes. One of the key factors in these processes is the binding material; although inert, it is pertinent for the mechanical resistance of the pellets. ZEOX OII is a almost-binderless material, therefore presenting higher adsorption capacities than most of the similar zeolites.

The strongly favorable curvature of carbon dioxide isotherms on zeolites indicates some extent of irreversible adsorption. Effective isotherms, which are the isotherms accounting for partial adsorption deactivation when the material undergoes cyclic pressure operation, were then obtained, up to 0.7 mbar – atmospheric carbon dioxide partial pressure at 1.4 bar. The carbon dioxide effective isotherms were obtained by running various adsorption/desorption cycles until a “stationary state” was attained. Between adsorption cycles, the adsorbents were regenerated during overnight, using vacuum-only conditions (ca. 0.01 mbar). The adsorption cycles were performed up to a maximum total pressure of 0.7 mbar.

The adsorption isotherms, obtained by adsorption/desorption cycles, of carbon dioxide on zeolites ZEOX OII and Z10-02ND at 35 $^{\circ}$C are shown in Figure 2.7 and Figure 2.8, respectively. At low pressure, ZEOX OII exhibited the highest carbon dioxide adsorption capacity and smallest deactivation; therefore, it is the best adsorbent for carbon dioxide removal.

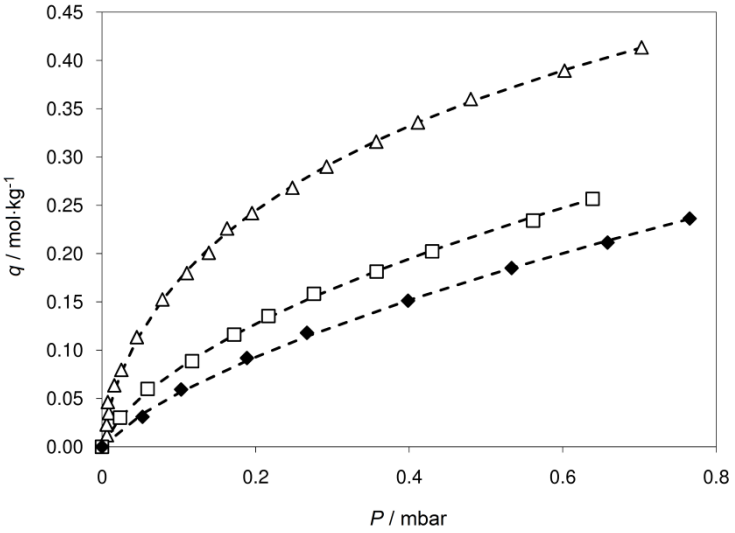

Figure 2.7 – Carbon dioxide isotherms on ZEOX OII at 35 °C (△, isotherm of fresh adsorbent; □, isotherm after first adsorption/desorption cycle; and ◆, effective isotherm). The dashed line represents Toth isotherm fitting.

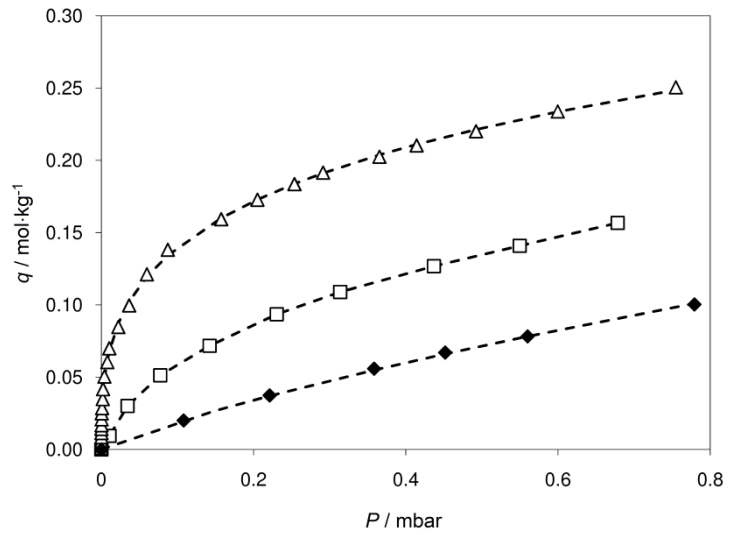

Figure 2.8 – Carbon dioxide isotherms on Z10-02ND at 35 °C (△, isotherm of fresh adsorbent; □, isotherm after first adsorption/desorption cycle; and ◆, effective isotherm). The dashed line represents Toth isotherm fitting.

Adsorption/desorption isotherm cycles of carbon dioxide on alumina and silica have not been determined, because they are not suitable for carbon dioxide removal (small adsorption capacity and slow kinetics).

Concerning water vapor adsorption equilibrium, isotherms were obtained at 35 °C. The results are shown in Figures 2.9 – 2.11. The adsorption equilibrium data was measured to relative pressures up to P/P_0 = 0.4, which corresponds to the maximum relative humidity that can be expected in the air compressor outlet. The adsorption isotherms of water vapor on zeolites, ZEOX OII and Z10-02ND, are shown in Figure 2.9. Both isotherms show Type I behavior. The adsorption isotherms of water vapor on alumina and silica are plotted on Figure 2.10 and Figure 2.11. The shape of these isotherms results from two adsorption mechanisms of water vapor. At low partial pressures, water molecules chemisorb to the surface of the adsorbent, but, as the relative pressure increases, water molecules physisorb on the already chemisorbed molecules.

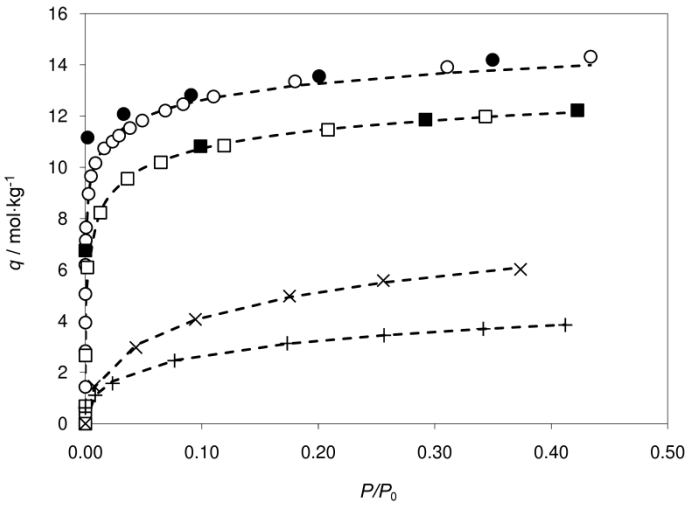

Figure 2.9 – Water vapor isotherms on ZEOX OII at 35 °C (□, adsorption on fresh adsorbent, and ■, desorption, and ×, effective isotherm) and on Z10-02ND at 35 °C (○, adsorption on fresh adsorbent, and ●, desorption, and +, effective isotherm). The dashed line represents Toth isotherm fitting.

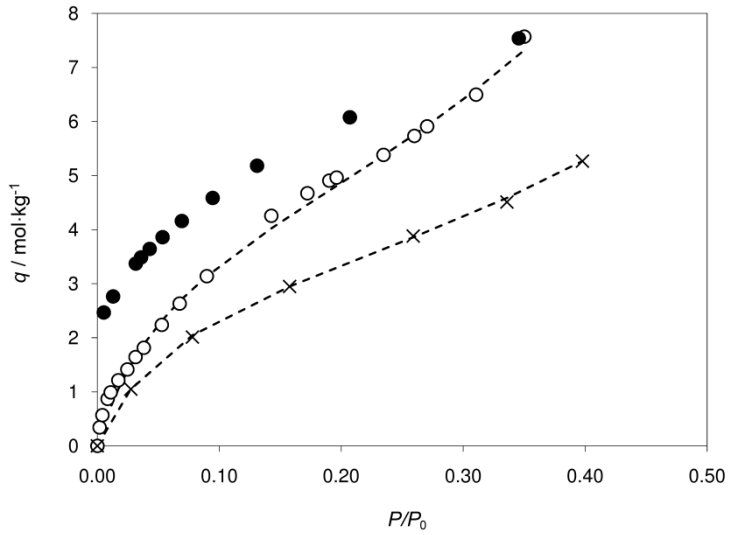

Figure 2.10 – Water vapor isotherms on alumina at 35 °C (○, adsorption on fresh adsorbent, and ●, desorption, and ×, effective isotherm). The dashed line represents the Aranovich-Donohue-Langmuir fitting.

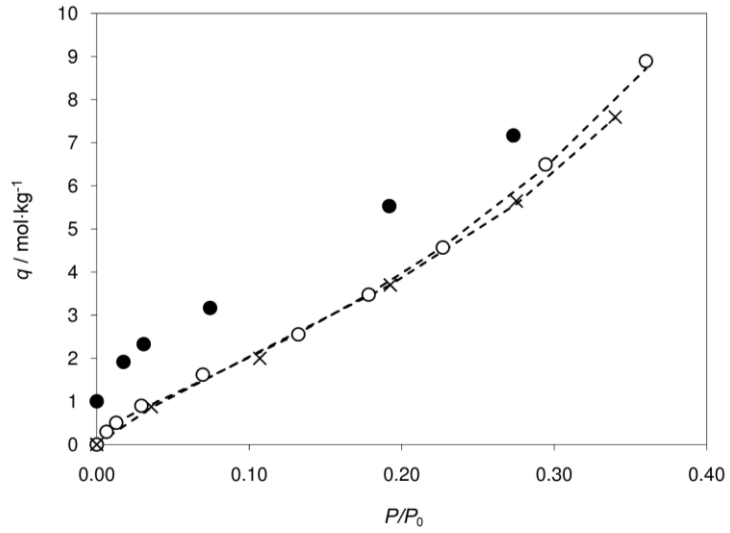

Figure 2.11 – Water vapor isotherms on silica at 35 °C (○, adsorption on fresh adsorbent, and ●, desorption, and ×, effective isotherm). The dashed line represents the Aranovich-Donohue-Langmuir fitting.

Evacuation alone does not remove all of the adsorbed water vapor. The amount of chemisorbed water remains as residual at the end of desorption isotherm, and depends on the adsorbent. Silica, for instance, shows the smallest residual loading, 1.00 mol·kg^{-1}, for alumina, the residual loading is 2.47 mol·kg^{-1}. The zeolites have the highest residual loading: 6.76 mol·kg^{-1} and 11.2 mol·kg^{-1}, respectively ZEOX OII and Z10-02ND.

The strongly favorable curvature for water vapor isotherms on zeolites indicates some extent of irreversibility. Equilibrium isotherms, obtained by adsorption/desorption cycles, for ZEOX OII, Z10-02ND, alumina and silica were obtained up to relative pressures of P/P_0 = 0.4, to assess the extent of deactivation caused by water vapor. Between isotherm determinations, adsorbents were regenerated under vacuum overnight. The decision about the best adsorbent for water vapor removal should be based not only on the fresh adsorbents isotherms, but, essentially, on effective isotherms. Those are represented by cross dots in Figures 2.9 – 2.11. Water vapor affects the capacity of alumina, ZEOX OII, and especially Z10-02ND, while silica shows no deactivation at all.

Figure 2.12 shows the water vapor effective isotherms at 35 $^{\circ}$C. At low relative pressures, both zeolites exhibit better water vapor removal ability than alumina and silica. For higher pressures, alumina and especially silica show an increasing ability to remove water vapor, and, at a relative pressure of P/P_0 = 0.4, silica have the highest adsorption capacity for water vapor, 10.3 mol·kg^{-1}, followed by ZEOX OII, 6.19 mol·kg^{-1}.

Although water vapor adsorption results are not common in literature, Wang and LeVan [8], Kim et al. [14] and Serbezov [15] reported isotherms for water vapor on several adsorbents including several 13X-type zeolites, aluminas and one silica gel. In these studies, aluminas show a Type II isotherm and silica exhibits a Type IV

isotherm. These are consistent with the results obtained in the present work. Furthermore, in the reported studies, zeolites present a Type I behavior with a high adsorption capacity, even at very low relative pressures.

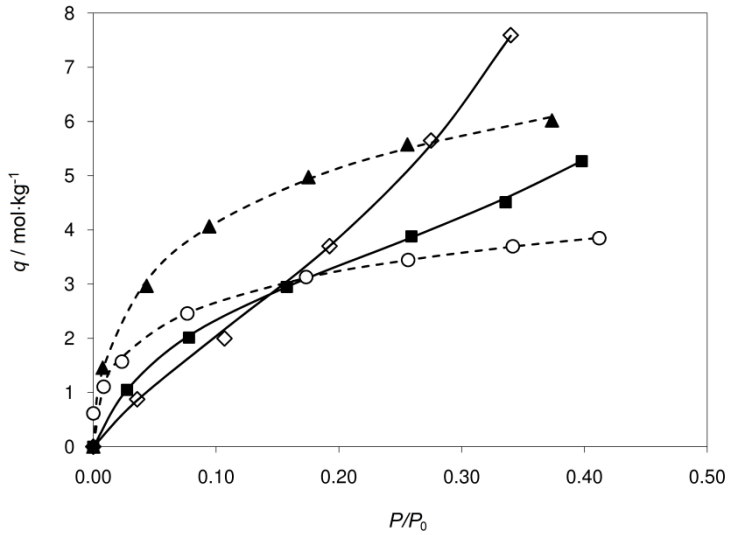

Figure 2.12 – Water vapor effective isotherms at 35 °C on: ▲, ZEOX OII; ○, Z10-02ND; ■, alumina; and ◇, silica. The solid line represents the Aranovich-Donohue-Langmuir fitting; dashed line represents Toth isotherm fitting.

In the present work, the experimental adsorption equilibrium data obtained was fitted to an isotherm model. To fit the carbon dioxide adsorption equilibrium results, they were used two conventional equations: Langmuir and Toth. The Langmuir equation has a relatively simple mathematical formulation, which is thermodynamically consistent [31]:

Langmuir isotherm

$$q = q_m \frac{bP}{1+bP} \tag{2.1}$$

where q is the adsorbed concentration, P is the equilibrium pressure, q_m is the saturation adsorbed concentration and b is the adsorption affinity constant.

The Toth equation is a semi-empirical model that is thermodynamically consistent [31]. This equation has one more parameter than the Langmuir equation and is a good alternative when the Langmuir equation does not fit accurately the data. Toth equation writes as follows:

Toth isotherm

$$q = q_m \frac{bP}{\left[1+\left(bP\right)^t\right]^{1/t}} \tag{2.2}$$

where t is the extra parameter of the Toth equation. When t is equal to the unity, the Toth equation renders Langmuir equation.

The Langmuir and Toth equations can be modified to become temperature dependent, introducing the following relation [31]:

$$b = b^{\infty} \exp\left(\frac{\Delta H}{\Re T}\right) \tag{2.3}$$

where b^{∞} is the adsorption affinity constant at infinite temperature, ΔH is the adsorption heat, $\Re$ is the gas constant and T is the absolute temperature.

The Toth equation was used to fit the water vapor equilibrium data on zeolites. Water isotherms on alumina and silica have a sigmoidal shape, with an inflection point at intermediate relative pressure. Aranovich and Donohue [14] proposed an adsorption equation of the following form:

$$q = \frac{f\left(P\right)}{\left[1-\left(P/P_0\right)\right]^d} \tag{2.4}$$

where P/P_0 is the relative pressure, and d is a model parameter. Substituting $f\left(P\right)$ by the Langmuir equation, eqs. (2.4) can be rewritten as

$$q = q_m \frac{bP}{(1+bP)\left[1-\left(P/P_0\right)\right]^d} \tag{2.5}$$

The Dubinin-Astakhov (DA) equation [31], which is a generalized Dubinin-Radushkevich model, is suited to fit the adsorption equilibrium data of microporous sorbents for low pressures. This equation is written as

$$q = q_m \exp\left\{-\left[\frac{\Re T}{E}\ln\left(\frac{P}{P_0}\right)\right]^m\right\} \tag{2.6}$$

where E is the characteristic energy and m represents the surface heterogeneity. Small m values are found for adsorbents with wide ranges of pore sizes, whereas large m values are related to adsorbents with a narrow pore size distribution of micropores. The DA equation was used to fit the experimental equilibrium values for water vapor on all adsorbents.

Also, in the case of water vapor adsorption on alumina and silica, the BET equation [31], which is frequently employed to fit Type II isotherms, was used. The BET equation is written as

$$q = q_m \frac{C_{\mathrm{BET}}\left(P/P_0\right)}{\left[1-\left(P/P_0\right)\right]\left[1+\left(C_{\mathrm{BET}}-1\right)\left(P/P_0\right)\right]} \tag{2.7}$$

where C_{BET} is the BET fitting parameter that is associated with the convexity of the isotherm at low relative pressures, and q_m is related to the monolayer coverage.

All fitting parameters where obtained by minimizing the relative deviations (Δq) between experimental data and fitting equations:

$$\Delta q(\%) = \frac{100}{k}\sum_{j-1}^{k}\frac{\left|q_j^{\exp} - q_j^{\mathrm{cal}}\right|}{q_j^{\exp}} \tag{2.8}$$

where $q_j^{\exp}$ is the adsorbed concentration experimentally obtained, q_j^{cal} is the adsorbed concentration obtained by fitting the adsorption equilibrium equations, and k is the number of observations.

All experimental equilibrium adsorption data are well described by selected equations and the parameters obtained are listed in Tables 2.3 – 2.5.

Table 2.3 - Toth equation parameters of carbon dioxide adsorption isotherms on the fresh adsorbents studied.

parameter	**ZEOX OII**	**Z10-02ND**	**alumina**	**silica**[a]
q_m , mol·kg^{-1}	8.62	6.45	12.9	2.11
b^{∞} x 10^{-4}, bar^{-1}	1.45	1.09	15.4	0.194
ΔH x 10^{3}, J·mol^{-1}	37.2	34.2	29.8	25.1
t	0.301	0.481	0.133	1
Δq , %	3.4	2.9	4.8	4.8

[a] fitted to Langmuir isotherm.

Table 2.4 – Parameters of water vapor adsorption equilibrium isotherms on the fresh adsorbents studied.

parameter	ZEOX OII	Z10-02ND	alumina	silica
		Toth Isotherm		
q_m, mol·kg^{-1}	16.3	23.1	—	—
b, bar^{-1}	9.04 x 10^5	3.66 x 10^{10}	—	—
t	0.257	0.131	—	—
Δq, %	1.6	1.5	—	—
		Aranovich-Donohue-Langmuir model		
q_m, mol·kg^{-1}	—	—	4.55	2.66
b, bar^{-1}	—	—	3.06 x 10^2	2.57 x 10^2
d	—	—	1.47	3.12
Δq, %	—	—	3.8	4.2
		Dubinin-Astakhov model		
q_m, mol·kg^{-1}	13.0	15.5	15.0	205.5
E x 10^3, J·mol^{-1}	22.8	28.5	3.72	0.186
m	1.20	1.00	0.901	0.440
Δq, %	1.9	0.4	2.2	3.3
		BET isotherm		
q_m, mol·kg^{-1}	—	—	5.11	12.9
C_{BET}	—	—	14.639	1.359
Δq, %	—	—	7.0	16.1

Table 2.5 – Parameters of (a) water vapor and (b) carbon dioxide effective isotherms on the adsorbents studied.

	(a) Water vapor effective isotherms			
parameter	**ZEOX OII**	**Z10-02ND**	**alumina**	**silica**
		Toth isotherm		
q_m, mol·kg^{-1}	17.5	11.3	—	—
b, bar^{-1}	2.15 x 10^3	7.14 x 10^3	—	—
t	0.281	0.241	—	—
Δq, %	1.9	1.0	—	—
		Aranovich-Donohue-Langmuir model		
q_m, mol·kg^{-1}	—	—	3.41	3.47
b, bar^{-1}	—	—	2.82 x 10^2	1.47 x 10^2
d	—	—	1.15	2.63
Δq, %	—	—	0.7	2.3

	(b) Carbon dioxide effective isotherms	
parameter	**ZEOX OII**	**Z10-02ND**
	Toth isotherm	
q_m, mol·kg^{-1}	26.5	15.5
b, bar^{-1}	9.55 x 10^1	2.11 x 10^1
t	0.214	0.288
Δq, %	0.6	1.6

2.3.2 Column dynamics

A set of cyclic adsorption/desorption breakthrough experiments was performed to assess the behavior of the selected adsorbents concerning air contaminants, water vapor and carbon dioxide. The adsorption/desorption breakthroughs cycles were

performed for each adsorbent, starting from a fresh sample in equilibrium with a nitrogen atmosphere until “stationary state” is attained (effective breakthroughs).

The adsorption experiments were performed using air containing 450 ppm of carbon dioxide and a dew point of 5 °C at 5.2 $L_{STP}·min^{-1}$, 1.4 bar and 27 °C. After which, the bed was regenerated between adsorption cycles with nitrogen at 0.8 $L_{STP}·min^{-1}$ and at 200 mbar during the same period of time of the first adsorption breakthrough. The experimental results for cyclic breakthroughs with zeolites, ZEOX OII and Z10-02ND, alumina and silica are shown in Figures 2.13 – 2.18.

Figure 2.13 and Figure 2.14 plot the cyclic breakthroughs of water vapor and carbon dioxide on ZEOX OII, respectively. The adsorption curves exhibit a compressive shape characteristic of favorable isotherms; the adsorption breakthrough of carbon dioxide exits before the corresponding water vapor. The carbon dioxide concentration front travels faster in the column, exiting the column before the corresponding water vapor front. The water adsorption front pushes carbon dioxide out from adsorption sites, originating a concentration peak (focusing effect [32]). The fresh adsorbent, first adsorption cycle, removes carbon dioxide to < 5 ppm and simultaneously originates a stream with a dew point below – 45 °C. The effective breakthrough was obtained after just two cycles. At this stage, the adsorbent retains ca. 19 % of the original capacity for removing water and ca. 6 % for removing carbon dioxide, originating a stream with a dew point of ca. – 39 °C and 5 ppm of carbon dioxide.

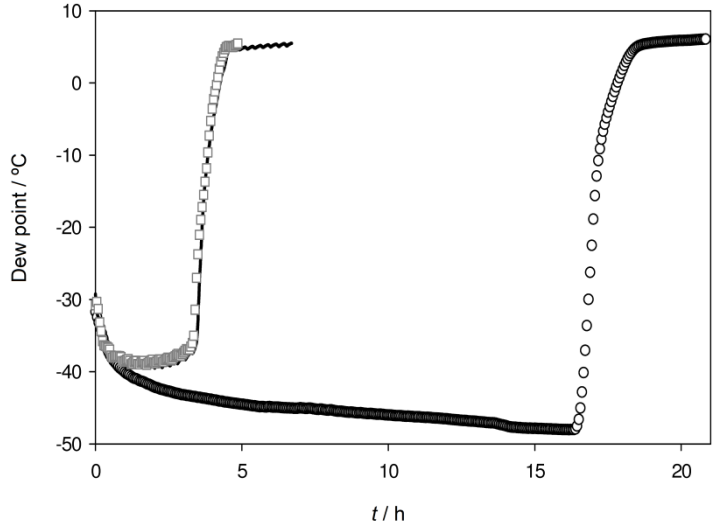

Figure 2.13 – Water vapor cyclic breakthrough curves obtained for air with 450 ppm of carbon dioxide and a dew point of 5 °C at 27 °C on ZEOX OII (○, breakthrough on fresh adsorbent; —, breakthrough after first adsorption/desorption cycle; and □, effective breakthrough).

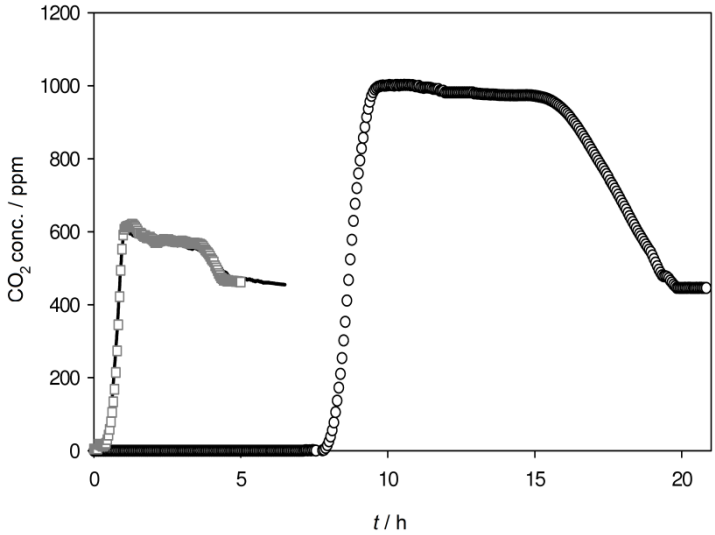

Figure 2.14 – Carbon dioxide cyclic breakthrough curves obtained for air with 450 ppm of carbon dioxide and a dew point of 5 °C at 27 °C on ZEOX OII (○, breakthrough on fresh adsorbent; —, breakthrough after first adsorption/desorption cycle; and □, effective breakthrough).

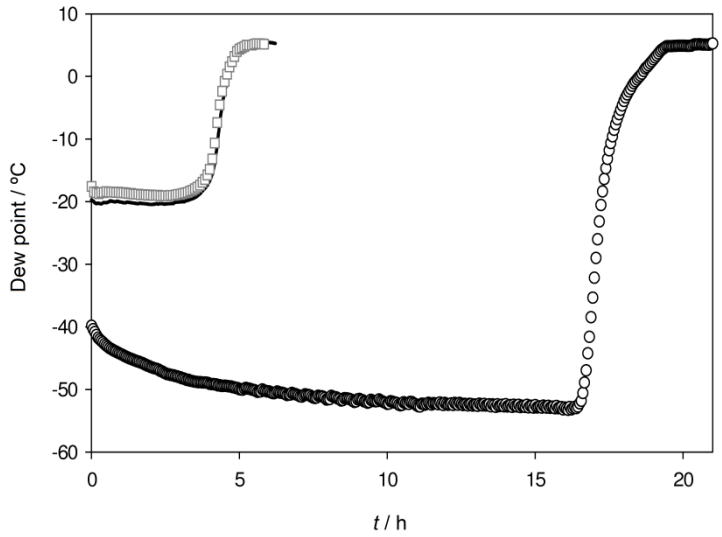

Figure 2.15 – Water vapor cyclic breakthrough curves obtained for air with 450 ppm of carbon dioxide and a dew point of 5 °C at 27 °C on Z10-02ND (○, breakthrough on fresh adsorbent; —, breakthrough after first adsorption/desorption cycle; and □, effective breakthrough).

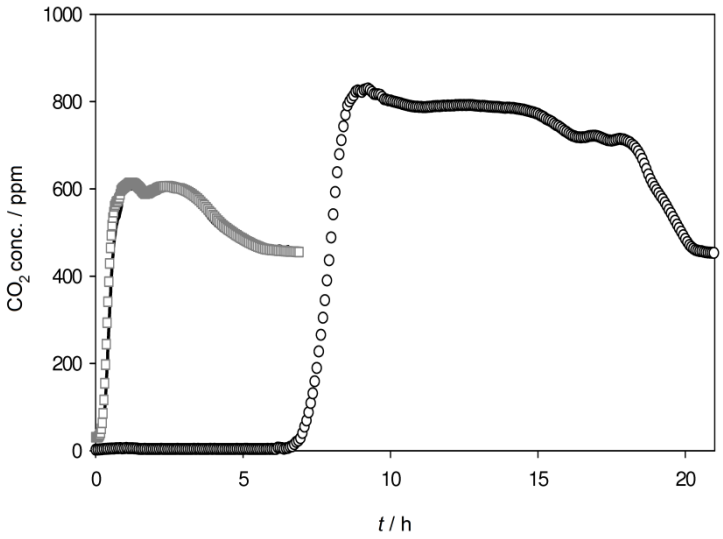

Figure 2.16 – Carbon dioxide cyclic breakthrough curves obtained for air with 450 ppm of carbon dioxide and a dew point of 5 °C at 27 °C on Z10-02ND (○, breakthrough on fresh adsorbent; —, breakthrough after first adsorption/desorption cycle; and □, effective breakthrough).

Figure 2.15 and Figure 2.16 show the cyclic breakthroughs of water vapor and carbon dioxide for Z10-02ND, respectively. The first adsorption cycle originated a stream with a dew point of ca. – 53 °C and < 5 ppm of carbon dioxide. The effective breakthrough was obtained after two cycles, and, at this stage, the adsorption capacity of the adsorbent for removing water was ca. 11 % of the original, and for removing carbon dioxide was ca. 4 % of the original. The stream produced has a dew point of ca. – 20 °C and 30 ppm of carbon dioxide.

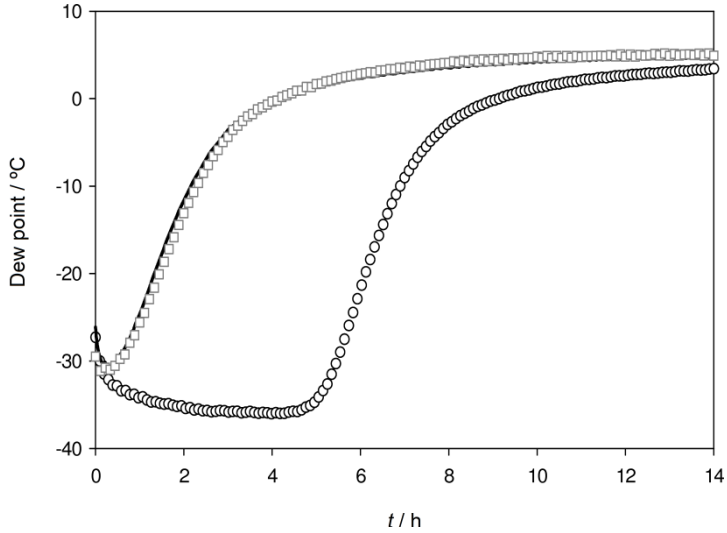

Figure 2.17 – Water vapor cyclic breakthrough curves obtained for air with 450 ppm of carbon dioxide and a dew point of 5 °C at 27 °C on alumina (○, breakthrough on fresh adsorbent; —, breakthrough after first adsorption/desorption cycle; and □, effective breakthrough).

Figure 2.17 shows the cyclic breakthroughs of water vapor for alumina. Carbon dioxide breakthroughs were not recorded, since the adsorption capacity of this specie is negligible – see Figure 2.5. The water front shows a dispersive shape, characteristic of an unfavorable isotherm. Indeed, the adsorption isotherm shows two branches, one of which has an unfavorable shape – see Figure 2.10. Fresh adsorbent produced a stream with a dew point of ca. – 36 °C. The effective breakthrough, obtained after just

two cycles, shows an adsorption capacity for removing water ca. 29 % of the original. The stream produced has a dew point of ca. – 31 °C.

Cyclic breakthroughs of water vapor for silica are represented in Figure 2.18. Carbon dioxide breakthroughs were not considered, since the adsorption capacity of this specie on silica is negligible – see Figure 2.5. The water front shows a dispersive wave, characteristic of an unfavorable isotherm. In fact, the adsorption isotherm shows two branches, one of which has an unfavorable shape – see Figure 2.11. The effective breakthrough is obtained after just two cycles. The adsorbent, at this stage, shows an adsorption capacity of ca. 18 % of the original for removing water originating a stream of dew point of ca. – 18 °C.

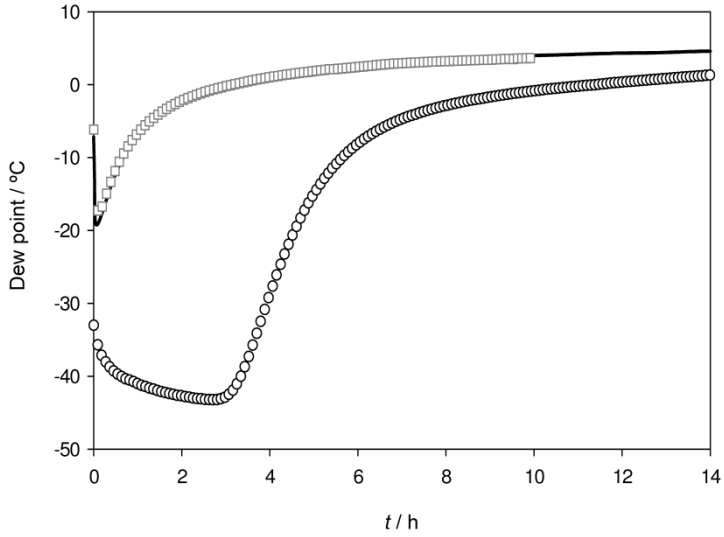

Figure 2.18 – Water vapor cyclic breakthrough curves obtained for air with 450 ppm of carbon dioxide and a dew point of 5 °C at 27 °C on silica (○, breakthrough on fresh adsorbent; —, breakthrough after first adsorption/desorption cycle; and □, effective breakthrough).

Table 2.6 summarizes the effective remaining adsorption capacity of the adsorbents for removing carbon dioxide and water vapor. As can be seen, the

simultaneously presence of carbon dioxide and water vapor causes a higher deactivation than each of these contaminants alone. The adsorbent capacity of silica is not significantly affected by the water vapor or carbon dioxide individually. However, Table 2.6 and Figure 2.17 – 2.18 show that the effective breakthrough time of silica is highly affected by water vapor, unlike alumina. Indeed, the breakthrough depends on both adsorption equilibrium and adsorption kinetics and alumina is faster adsorbing water vapor than silica within the relevant region for cyclic adsorption processes – see Figure 2.19. This figure shows the fractional uptake of water vapor on alumina and silica.

Table 2.6 – Effective adsorption capacity of the adsorbents for removing carbon dioxide and water vapor.

	effective adsorption capacity (%)			
	Isotherms		**breakthroughs**	
adsorbent	**CO_2**	**H_2O**	**CO_2**	**+ H_2O**
ZEOX OII	54	47	6	19
Z10-02ND	38	25	4	11
alumina	—	66	—	29
silica	—	96	—	18

Zeolite ZEOX OII is the best adsorbent for removing water vapor and carbon dioxide in the studied conditions. This conclusion is consistence with results from adsorption equilibrium and breakthroughs. The design of the pre-treatment unit should then consider the use of ZEOX OII. Nevertheless, to protect this zeolite from possible large percents of water in the feed current, it is strongly suggested to use a previous small layer of a highly water-resistant sorbent, such as silica or alumina, to lower the dew point to acceptable values.

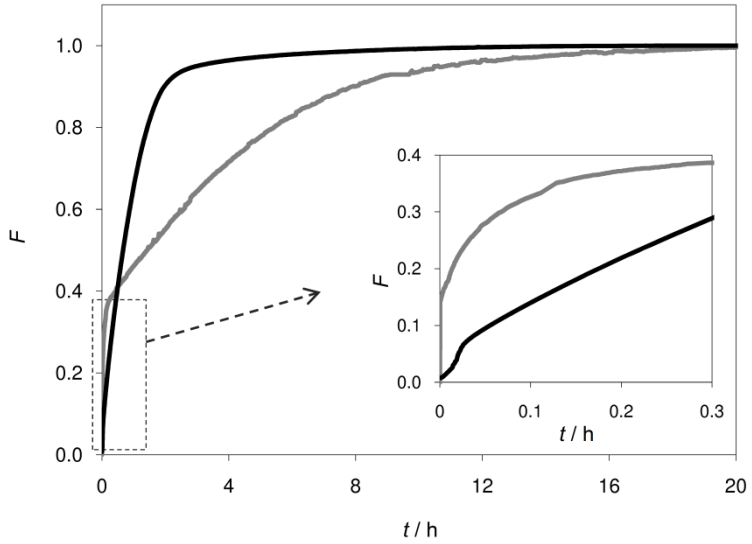

Figure 2.19 – Fractional uptake versus time for water vapor. The gray line indicates the first equilibrium point on alumina. The black line indicates the first equilibrium point on silica.

2.4 Conclusions

Adsorption equilibrium isotherms for carbon dioxide and water vapor were obtained for four commercial adsorbents: two 13X-type zeolites, activated alumina and silica. Carbon dioxide isotherms were determined at 15 °C, 35 °C and 55 °C, using the volumetric method, and water vapor isotherms at 35 °C, using the gravimetric method.

Zeolites exhibit higher carbon dioxide adsorption capacity than alumina or silica. Adsorption isotherms up to 0.7 mbar of carbon dioxide and at 35 °C on zeolites were obtained, after several adsorption/desorption cycles under close to real operating conditions (effective adsorption isotherms). For such conditions, ZEOX OII exhibited both the highest carbon dioxide capacity and smallest deactivation up to the effective isotherm, and therefore is the best adsorbent for carbon dioxide removal.

Water vapor adsorption equilibrium isotherms were also obtained at 35 °C on the same adsorbents. Both zeolites show a Type I isotherm, while alumina and silica, exhibit a sigmoidal shape adsorption isotherm with an inflection point at an intermediate relative pressure. Therefore, zeolites exhibit better water vapor removal ability at low relative pressures; however, for higher pressures, this ability in alumina, and especially silica, increases significantly. Water vapor adsorption/desorption isotherm cycles, up to relative pressure of P/P_0 = 0.4 and at 35 °C, were obtained and it is possible to conclude that water vapor affects the capacity of zeolites, especially Z10-02ND, and alumina, but causes no deactivation on silica.

Cyclic breakthrough experiments were also conducted to assess the behavior of the adsorbents concerning water vapor and carbon dioxide. The adsorption steps were performed with air containing 450 ppm of carbon dioxide and a dew point of 5 °C at 5.2 L_{STP}·min^{-1}, 1.4 bar and 27 °C, and the regeneration was performed with nitrogen at 0.8 L_{STP}·min^{-1} and 200 mbar during the same period of time of the first adsorption breakthrough. The effective breakthrough was reached after only just two cycles for all adsorbents. At the studied conditions, ZEOX OII was the best adsorbent for removing water vapor and carbon dioxide, originating a stream with a dew point of ca. – 39 °C and 5 ppm of carbon dioxide.

It was concluded that a pre-treatment vacuum pressure swing adsorption (VPSA) unit should contain layered beds composed by two adsorbents: an initial layer of silica or alumina, to remove condensable water, acting as a protecting layer of the following one, which should be of ZEOX OII to reduce water and carbon dioxide concentrations to ppm levels. It is important to underline that the choice of material for the first layer should depend on a risk assessment of the VPSA operation. The studied silica was found to have a remarkable resistance to water (even liquid water) without losing capacity. Regarding the second layer, it is important to pinpoint that

ZEOX OII pellets have a considerably smaller size than Z10-02ND, facilitating significantly the mass transfer. However, due to its size, a considerable pressure drop along the columns may be observed.

Acknowledgment

The work of Daniel Ferreira was supported by FCT (through grant ref. SFRH/BDE/51186/2010. The authors would like to acknowledge the funding provided by FCT in the context of the research project ref. PTDC/EQU-EQU/71656/2006. The authors also would like to acknowledge the funding provided by AdI in the context of the research project HPOVPSA (ref. 13488).

2.5 References

1. Park, Y.-J., Lee, S.-J., Moon, J.-H., Choi, D.-K., Lee, C.-H. Adsorption Equilibria of O_2, N_2, and Ar on Carbon Molecular Sieve and Zeolites 10X, 13X, and LiX. *Journal of Chemical & Engineering Data.* **2006**, 51, 1001-1008.
2. Ruthven, D., Farooq, S., Knaebel, K. *Pressure Swing Adsorption*; VCH Publishers: New York, 1994.
3. Chiang, R.L., Whitley, R.D., Ostroski, J.E., Dee, D.P. Argon/Oxygen Selective X-Zeolite. U.S. Patent 6,432,170, 2002.
4. Dee, D.P., Chiang, R.L., Miller, E.J., Whitley, R.D. High Purity Oxygen Production by Pressure Swing Adsorption. U.S. Patent 6,544,318, 2003.
5. Rege, S.U., T. Yang, R., Buzanowski, M.A. Sorbents for Air Prepurification in Air Separation. *Chemical Engineering Science.* **2000**, 55, 4827-4838.
6. Santos, J.C., Portugal, A.F., Magalhães, F.D., Mendes, A. Optimization of Medical PSA Units for Oxygen Production. *Industrial and Engineering Chemistry Research.* **2006**, 45, 1085-1096.
7. Ribeiro, A.M., Sauer, T.P., Grande, C.A., Moreira, R.F.P.M., Loureiro, J.M., Rodrigues, A.r.E. Adsorption Equilibrium and Kinetics of Water Vapor on Different Adsorbents. *Industrial & Engineering Chemistry Research.* **2008**, 47, 7019-7026.
8. Wang, Y., LeVan, M.D. Adsorption Equilibrium of Carbon Dioxide and Water Vapor on Zeolites 5A and 13X and Silica Gel: Pure Components. *Journal of Chemical & Engineering Data.* **2009**, 54, 2839-2844.
9. Sircar, S., Kratz, W.C. Removal of Water and Carbon Dioxide from Air. U.S. Patent 4,249,915, 1981.
10. Jain, R. Pre-Purification of Air for Separation. U.S. Patent 5,232,474, 1993.
11. Kumar, R. Removal of Water and Carbon Dioxide from Atmospheric Air. U.S. Patent 4,711,645, 1987.
12. Rege, S.U., Yang, R.T., Qian, K., Buzanowski, M.A. Air-Prepurification by Pressure Swing Adsorption Using Single/Layered Beds. *Chemical Engineering Science.* **2001**, 56, 2745-2759.
13. Lee, J.-S., Kim, J.-H., Kim, J.-T., Suh, J.-K., Lee, J.-M., Lee, C.-H. Adsorption Equilibria of CO_2 on Zeolite 13X and Zeolite X/Activated Carbon Composite. *Journal of Chemical & Engineering Data.* **2002**, 47, 1237-1242.

14. Kim, J.-H., Lee, C.-H., Kim, W.-S., Lee, J.-S., Kim, J.-T., Suh, J.-K., Lee, J.-M. Adsorption Equilibria of Water Vapor on Alumina, Zeolite 13X, and a Zeolite X/Activated Carbon Composite. *Journal of Chemical & Engineering Data.* **2002**, 48, 137-141.

15. Serbezov, A. Adsorption Equilibrium of Water Vapor on F-200 Activated Alumina. *Journal of Chemical & Engineering Data.* **2003**, 48, 421-425.

16. Desai, R., Hussain, M., Ruthven, D.M. Adsorption of Water Vapour on Activated Alumina. I - Equilibrium Behaviour. *The Canadian Journal of Chemical Engineering.* **1992**, 70, 699-706.

17. Bulck, E. Isotherm Correlation for Water Vapor on Regular-Density Silica Gel. *Chemical Engineering Science.* **1990**, 45, 1425-1429.

18. Hyun, S.H., Danner, R.P. Equilibrium Adsorption of Ethane, Ethylene, Isobutane, Carbon Dioxide, and their Binary Mixtures on 13X Molecular Sieves. *Journal of Chemical & Engineering Data.* **1982**, 27, 196-200.

19. Siriwardane, R.V., Shen, M.-S., Fisher, E.P. Adsorption of CO_2, N_2, and O_2 on Natural Zeolites. *Energy & Fuels.* **2003**, 17, 571-576.

20. Siriwardane, R.V., Shen, M.-S., Fisher, E.P., Poston, J.A. Adsorption of CO_2 on Molecular Sieves and Activated Carbon. *Energy & Fuels.* **2001**, 15, 279-284.

21. De-Xin, Z., Zhi-Jing, X., Zhen, F. Prediction of Breakthrough Curves of Oxygen-Nitrogen Coadsorption System on Molecular Sieves. *Gas Separation & Purification.* **1988**, 2, 184-189.

22. Gales, L., Mendes, A., Costa, C. Hysteresis in the Cyclic Adsorption of Acetone, Ethanol and Ethyl Acetate on Activated Carbon. *Carbon.* **2000**, 38, 1083-1088.

23. Bae, Y.S., Lee, C.H. Sorption Kinetics of Eight Gases on a Carbon Molecular Sieve at Elevated Pressure. *Carbon.* **2005**, 43, 95-107.

24. Campo, M.C., Magalhães, F.D., Mendes, A. Comparative Study Between a CMS Membrane and a CMS Adsorbent: Part I - Morphology, Adsorption Equilibrium and Kinetics. *Journal of Membrane Science.* **2010**, 346, 15-25.

25. Qi, N., Appel, W.S., LeVan, M.D., Finn, J.E. Adsorption Dynamics of Organic Compounds and Water Vapor in Activated Carbon Beds. *Industrial & Engineering Chemistry Research.* **2006**, 45, 2303-2314.

26. Desai, R., Hussain, M., Ruthven, D.M. Adsorption on Activated Alumina. II - Kinetic Behaviour. *The Canadian Journal of Chemical Engineering.* **1992**, 70, 707-715.

27. Gorbach, A., Stegmaier, M., Eigenberger, G. Measurement and Modeling of Water Vapor Adsorption on Zeolite 4A - Equilibria and Kinetics. *Adsorption.* **2004**, 10, 29-46.

28. Ruthven, D.M., Lee, L.K., Yucel, H. Kinetics of Non-Isothermal Sorption in Molecular Sieve Crystals. *AIChE Journal.* **1980**, 26, 16-23.

29. Santos, J.C., Magalhães, F.D., Mendes, A. Contamination of Zeolites Used in Oxygen Production by PSA: Effects of Water and Carbon Dioxide. *Industrial & Engineering Chemistry Research.* **2008**, 47, 6197-6203.

30. Campo, M.C., Lagorsse, S., Magalhães, F.D., Mendes, A. Comparative Study Between a CMS Membrane and a CMS Adsorbent: Part II - Water Vapor Adsorption and Surface Chemistry. *Journal of Membrane Science.* **2010**, 346, 26-36.

31. Do, D.D. *Adsorption Analysis: Equilibria and Kinetics*; Imperial College Press: London, 1997.

32. Wankat, P.C. *Large-Scale Adsorption and Chromatography*; CRC Press: Boca Raton, Fla., 1986.

CHAPTER III

Ferreira, D., Magalhães, R., Bessa, J., Taveira, P., Sousa, J., Whitley, R.D., Mendes, A. Study of AgLiLSX for Single-Stage High-Purity Oxygen Production. *Industrial & Engineering Chemistry Research.* **2014**, 53, 15508-15516.

The author contributed to the planning and execution of all the experiments described in this chapter, except in the development of the breakthrough simulator which was carried out by Bessa, J. The author was also involved on the discussion and interpretation of results, as well as on the preparation of the manuscript.

3 Study and characterization of AgLiLSX zeolite

Abstract

Commercial adsorbents do not exhibit argon/oxygen equilibrium selectivity above 1. However, in the past decade, Air Products and Chemicals developed an argon/oxygen selective silver-based zeolite, AgLiLSX. In this work, the authors studied and characterized the AgLiLSX adsorbent to provide fundamental data to evaluate its potential for high-purity oxygen production in a single-stage PSA unit. Oxygen, nitrogen and argon adsorption isotherms and breakthroughs curves were obtained and moderate equilibrium selectivity (α_{N_2/O_2} = 4.98 and α_{Ar/O_2} = 1.14 at 1 bar and 25 °C), high working capacity (0.45 mol·kg^{-1} for nitrogen, between 1.4 bar and 0.2 bar at 25 °C), and superior performance were observed. It was found that this adsorbent can allow the production of a 95+% oxygen stream in a single-stage PSA operation. It was also found that the adsorbent is very sensitive to carbon dioxide and water vapor, and also shows low mechanical resistance, losing capacity and selectivity when exposed to atmospheric air or if mistreated. An extra care is, therefore, needed when using AgLiLSX adsorbent in a PSA or VPSA operation.

3.1 Introduction

Oxygen generation from air by pressure swing adsorption (PSA) has noticeably increased in the past decade as evidenced by relevant patent activity [1]. These PSA units produce an enriched stream of oxygen limited to 95 %, mostly balanced with argon [2], since commercial adsorbents do not exhibit an Ar/O_2 adsorption selectivity above 1 [3]. There is, however, a significant demand for high-purity oxygen, such as for medical surgeries, where the minimum concentration of oxygen required is 99.5 % in Europe, 99.0 % in USA and 99.6 % in Japan [1]; military and aerospace applications usually require a minimum concentration of 99.5 % as well as the filling of cylinders [4] and welding and cutting processes [5]. To produce purer oxygen streams, several adsorption processes combining two separation stages have been proposed [4-15]. Still, the production of an oxygen stream richer than 95 % using a single-stage PSA remained a goal.

During the 1980s, a new generation of adsorbents was developed with very high capacity and selectivity towards the air separation [16-18]. These new adsorbents are Li-exchanged X-type (LiX) zeolites, low-silica X-type (LSX) zeolites, and Li- or Ca-exchanged LSX-zeolites [17, 19, 20]. However, none of these adsorbents are able to selectively remove argon from the product. In 1990, Wilkerson prepared a silver-mordenite adsorbent with two different silver-exchanged concentrations (reported as highly exchanged silver-mordenite and low percent exchange silver-mordenite) and studied the adsorption equilibrium of argon and oxygen [21]. Only the more thoroughly exchanged silver-mordenite showed selectivity of argon towards oxygen. Following, in 1993, Knaebel and Kandybin disclosed an equilibrium-based PSA, packed with silver-mordenite adsorbent, which reached a product concentration of 99.6 % from a feed of 95 % of oxygen balanced with argon [11]. Silver-exchanged molecular sieves have since then been investigated to make the argon/oxygen

separation [1, 22-24]. In 2000, in two consecutive works [25, 26], Hutson et al. reported the addition of silver to LiX zeolites for improving their adsorption capacity towards air separation. Since these adsorbents exhibit argon/oxygen selectivity slightly smaller than 1, they still show no ability for selectively remove the argon from the product stream. In 2002, Air Products and Chemicals, Inc. patented an argon/oxygen selective zeolite, named AgLiLSX (lithium low silica-X silver based zeolite), with a silver-exchanged content of 20 – 70 mol.% [27]. This patent refers that the new adsorbent is useful for high-purity oxygen production in a single-stage vacuum and pressure swing adsorption (VPSA) or PSA. In 2003, the same company disclosed a VPSA process that, according to patent simulations, could produce a stream of 99 % of oxygen from air, using the newly developed AgLiLSX adsorbent [28]. Following, Sebastian and Jasra [22] prepared and characterized several silver-exchanged zeolites for assessing their argon/oxygen adsorption selectivity. AgA, AgX, AgY, AgMordenite among others were reported to show some degree of adsorption selectivity of argon over oxygen. Authors stated that the unusual adsorption properties, especially towards argon, could be related to the directional properties given by the *d* orbitals of silver ions [22, 23]. They stated that, in their case, the argon/oxygen equilibrium selectivity observed for silver-exchanged zeolites could be explained from the special interactions between bonding molecular orbitals. These authors concluded that AgA zeolite exhibited very high N_2/O_2 and Ar/O_2 adsorption selectivities compatible with use in a single-stage PSA for producing oxygen enriched streams (> 95 %). In 2007, Santos et al. briefly characterized the adsorption equilibrium of oxygen, nitrogen and argon on AgLiLSX adsorbent provided by Air Products and Chemicals and simulated a PSA unit for producing 98.7 % of oxygen, operating between 1 and 3 bar, at 30 $^{\circ}$C and, with a recovery of 5 %. These authors reported that the developed simulator is able to represent accurately a real unit using an air feed free of carbon dioxide and water vapor [1]. In 2008, Ansón et al. studied a

30 mol.% silver-exchanged zeolite ETS-10 and compared it with silver-exchanged mordenite [23]. The authors found Ag-ETS-10 to have an equilibrium argon/oxygen selectivity of 1.28 at 1 bar and 30 °C. However, the adsorbent showed limitations such as low N_2/O_2 selectivity and smaller adsorption capacity when compared with conventional LiLSX-type adsorbents. Later, Shi et al. made a composite adsorbent of Ag-ETS-10 crystals and Ludox HS-40 colloidal silica, weight ratio of 12:5, and obtained an adsorbent that has a high nitrogen/oxygen equilibrium selectivity (α_{N_2/O_2} = 6.23 at 1 bar and 25 °C) and adsorption capacity (q_{N_2} = 0.622 mol·kg^{-1} at 1 bar and 25 °C), maintaining the high argon/oxygen equilibrium selectivity previously reported [24]. However, the nitrogen adsorption capacity was still smaller than reported by Santos et al. for AgLiLSX (q_{N_2} = 0.850 mol·kg^{-1} at 1 bar and 25 °C) [1].

In the present work, the authors studied and characterized the AgLiLSX adsorbent for high-purity oxygen production in a single-stage cyclic adsorption operation. Oxygen, nitrogen and argon adsorption isotherms were obtained up to 7 bar and at 15 °C, 25 °C and 35 °C, to assess the selectivity, working capacity and general performance of the adsorbent. Mono and multicomponent breakthrough experiments, at 25 °C and 1.4 bar, were also carried out to characterize the adsorption kinetics and to assess the adsorbent performance in real operating conditions. The linear driving force model was fitted to the breakthrough experimental results, using an in-house developed simulator, and the corresponding mass transport coefficients were obtained.

A deactivation study was also conducted on the AgLiLSX by measuring the adsorption capacity of nitrogen, oxygen and argon after contamination with atmospheric air containing 600 ppm of carbon dioxide and a dew point of 4 °C at 25 °C; and after crushing a small sample down to ca. 0.15 mm of particle diameter.

3.2 Experimental

3.2.1 Materials

AgLiLSX adsorbent (the starting material is a beaded 93 % Li, 7 % Na+K LSX-type zeolite with 1.0 Si/Al ratio, afterward 40 mol.% silver exchanged [27, 29]) was supplied by Air Products and Chemicals, Inc. Helium picnometry was used to determine the real density, while surface area, pore volume, and average pore diameter, excluding microporosity, and apparent density, were determined by mercury porosimetry. The physical properties of AgLiLSX adsorbent are listed in Table 3.1. The "as received" sample was regenerated at 375 °C (temperature ramp of 1 °C·min^{-1}) for 12 h under a synthetic air stream (79 % N_2, 21 % O_2) with a minimum flow rate of 2 L_{STP}·min^{-1} for each kilogram of adsorbent.

Table 3.1 – Physical properties of AgLiLSX adsorbent.

property	Value
geometry	Spherical
average pellet radius, mm	0.51
pellet crushing strength, N	0.9
apparent density, g·cm^{-3}	1.218
total surface area, m^2·g^{-1}	21.6
pore volume, cm^3·g^{-1}	0.316
structural density, g·cm^{-3}	3.080
meso/macro porosity, %	60.45

3.2.2 Methods

The volumetric method was used to determine the adsorption equilibrium isotherms. This method is based on pressure variation of the relevant gas after an expansion. Knowing the pressure decrease and assuming ideal gas behavior, it is

possible to determine the concentration of the solute adsorbed [30]. The apparatus used is described in the previous section [29]. After introducing the adsorbent sample into the corresponding vessel of the volumetric method apparatus, it was filled with helium at 70 °C followed by evacuation until < 0.01 mbar, and this procedure was repeated six times.

The breakthrough curves were determined using an in-house built experimental setup, also described in the previous chapter [30]. Briefly, it consists of a packed bed column (34.0 cm of length and 3.2 cm of diameter) filled with the adsorbent and placed in a thermostatic chamber, where the feed flow rate was controlled using a mass flow controller (Bronkhorst El-flow, 0 – 2 L_{STP}·min^{-1}, ± 0.5 % Rd plus ± 0.1 % FS), the exiting stream was analysed using a mass spectrometer (Pfeiffer, Omnistar) and the exit pressure was controlled using a back pressure regulator (Equilibar, EB12F2). The temperature was monitored at the entrance and exit of the column using 1/16" thermocouples placed at the axial position of the column. The breakthrough curve represents the composition history of the stream exiting the packed adsorption column when, after saturation, the feed is changed to a different gas or mixture [3]. After loading the adsorption column with the adsorbent sample, this was heated up to 50 °C and evacuated for 2 h at 0.01 mbar. All experiments were performed at 1.4 bar with a feed flow rate of 0.5 and 1 L_{STP}·min^{-1} at 25 °C. The temperature of the thermostatic chamber during the experiments was 25 °C.

3.2.3 Mathematical model

To better understand the dynamic behavior of the adsorbing bed, a mathematical model was developed based on the following main assumptions:

1) ideal gas behavior
2) negligible radial concentration and temperature gradients

3) axially dispersed plug flow
4) thermal equilibrium between the adsorbent, bulk flow and column wall
5) intraparticle mass transport according to linear driving force (LDF) model
6) constant overall heat transfer coefficient of the column
7) uniform cross-sectional void fraction
8) uniform adsorption properties along the column
9) negligible bed pressure drop

According to these assumptions, the model equations can be written as it follows [31]:

Partial and total mass balances to the column

$$\frac{\partial c_i}{\partial t} = \frac{\partial}{\partial x}\left[D_{ax} c_{total} \frac{\partial}{\partial x}\left(\frac{c_i}{c_{total}} \right) \right] - \frac{\partial \left(u c_i \right)}{\partial x} - N_i \tag{3.1}$$

$$\frac{\partial c_{total}}{\partial t} = -\frac{\partial \left(u c_{total} \right)}{\partial x} - \sum_{i=1}^{nc} N_i \tag{3.2}$$

where

$$N_i = \frac{\left(1-\varepsilon_b\right)}{\varepsilon_b} \varepsilon_p \frac{\partial \overline{c}_i}{\partial t} + \frac{\left(1-\varepsilon_b\right)}{\varepsilon_b} \rho_s \frac{\partial \overline{q}_i}{\partial t} \tag{3.3}$$

and c_i is the partial molar concentration, D_{ax} is the axial dispersion coefficient, c_{total} is the total molar concentration, u is the interstitial molar average velocity, N_i is the partial molar flow rate, ε_b is the bed void fraction, ε_p is the particle porosity, ρ_s is the adsorbent apparent density, $\overline{c}_i$ is the partial average molar concentration in the fluid phase, $\overline{q}_i$ is the partial average molar concentration in the adsorbed phase, x is

the spatial coordinate, t is the time variable, and nc is the number of mixture components.

Energy balance to the column

$$\begin{aligned}&\left\{\varepsilon_b\sum_{i=1}^{nc}c_iC_{pg,i}+(1-\varepsilon_b)\varepsilon_p\sum_{i=1}^{nc}\overline{c}_iC_{pg,i}+(1-\varepsilon_b)\rho_s\sum_{i=1}^{nc}\overline{q}_iC_{pg,i}\right.\\&\left.+(1-\varepsilon_b)\rho_pC_{ps}+\varepsilon_w\rho_wC_{pw}\right\}\frac{\partial T}{\partial t}=\\&\varepsilon_b\lambda\frac{\partial^2T}{\partial x^2}-\varepsilon_b\frac{\partial}{\partial x}\left(\sum_{i=1}^{nc}uc_iC_{pg,i}T\right)+\sum_{i=1}^{nc}(-\Delta H_i)(1-\varepsilon_b)\varepsilon_p\frac{\partial\overline{c}_i}{\partial t}\\&+\sum_{i=1}^{nc}(-\Delta H_i)(1-\varepsilon_b)\rho_s\frac{\partial\overline{q}_i}{\partial t}-\frac{2r_w^{ml}}{\left(r_w^i\right)^2}U\left(T-T_\infty\right)\end{aligned}\tag{3.4}$$

where

$$\varepsilon_w=\frac{\left(r_w^e\right)^2-\left(r_w^i\right)^2}{\left(r_w^i\right)^2}\tag{3.5}$$

$$r_w^{ml}=\frac{r_w^e-r_w^i}{\ln\left(\frac{r_w^e}{r_w^i}\right)}\tag{3.6}$$

and $C_{pg,i}$ is the heat capacity of component *i*, C_{ps} is the adsorbent heat capacity, ε_w is the ratio between the cross section wall area and column area, ρ_w is the column wall density, C_{pw} is the wall heat capacity, λ is the axial heat dispersion coefficient, ΔH_i is the heat of adsorption of component *i*, r_w^{ml} is the logarithmic mean radius of the column wall, r_w^e is the external column radius, r_w^i is the internal column radius, U is the overall heat transfer coefficient, T is the temperature, and T_∞ is the external environmental temperature.

The adsorption equilibrium was predicted using the Ideal Adsorbed Solution Theory (IAST), proposed by Myers and Prausnitz [32],

$$\pi = \int_0^{p_i^0} \frac{q_i^0\left(p_i^0\right)}{p_i^0} dp_i^0 \tag{3.7}$$

where π is the spreading pressure, p_i^0 the hypothetical pressure of pure *i*-component, q_i^0 is the adsorbent concentration of pure *i*-component; the multicomponent equilibrium is obtained from the monocomponent isotherms.

The intraparticle mass transport model is given by the Linear Driving Force model (LDF):

$$\frac{\partial \overline{q}_i}{\partial t} = k_i\left(q_i - \overline{q}_i\right) \tag{3.8}$$

where q_i is the adsorbed concentration of component *i* in the particle inner surface, and k_i is the LDF coefficient, $k_i = 15 D_i / r_p^2$, where D_i / r_p^2 is the apparent diffusion time constant [33].

The previous equations can be written in dimensionless form as follows:

Partial mass balance:

$$\frac{\partial c_i^*}{\partial \theta} = \frac{1}{\mathrm{Pe_M}} \frac{\partial}{\partial x^*}\left[c_{total}^* \frac{\partial}{\partial x^*}\left(\frac{c_i^*}{c_{total}^*}\right)\right] - \frac{\partial\left(u^* c_i^*\right)}{\partial x^*} - N_i^* \tag{3.9}$$

Total mass balance:

$$\frac{\partial u^*}{\partial x^*} = -\frac{1}{c_{total}^*}\frac{\partial c_{total}^*}{\partial \theta} - \frac{u^*}{c_{total}^*}\frac{\partial c_{total}^*}{\partial x^*} - \frac{1}{c_{total}^*}\sum N_i^* \tag{3.10}$$

where

$$N_i^* = \varsigma_p \frac{\partial \overline{c_i^*}}{\partial \theta} + \varsigma_a \frac{\partial \overline{q_i^*}}{\partial \theta} \tag{3.11}$$

$$\varsigma_p = \frac{(1-\varepsilon_b)}{\varepsilon_b}\varepsilon_p, \qquad \varsigma_a = \frac{(1-\varepsilon_b)}{\varepsilon_b}\rho_s \frac{q_{ref}}{c_{ref}}$$

and c_i^* is the dimensionless partial molar concentration, θ is the dimensionless time variable, x^* is the dimensionless axial coordinate, c_{total}^* is the dimensionless total molar concentration, u^* is the dimensionless interstitial molar average velocity, q_i^* is the dimensionless partial adsorbed concentration, $\overline{c_i^*}$ is the dimensionless average partial molar concentration, and $\overline{q_i^*}$ is the dimensionless partial average molar concentration in the adsorbed phase. $\mathrm{Pe_M}$ is the mass transfer Peclet number and is defined as $\mathrm{Pe_M} = L_B u_{ref} / D_{ax}$, where L_B is the bed length. ς_p and ς_a are, respectively, the capacity factors of fluid and adsorbed phases.

Energy balance:

$$\begin{aligned}&\left\{\sum_{i=1}^{nc} c_i^* C_{pg,i}^* + \varsigma_p \sum_{i=1}^{nc} \overline{c_i^*} C_{pg,i}^* + \varsigma_a \sum_{i=1}^{nc} \overline{q_i^*} C_{pg,i}^* + R_g^s + R_g^w\right\}\frac{\partial T^*}{\partial \theta} \\ &= \frac{1}{\mathrm{Pe_H}}\frac{\partial^2 T^*}{\partial x^{*2}} - \frac{\partial}{\partial x^*}\left(\sum_{i=1}^{nc} u^* c_i^* T^* C_{pg,i}^*\right) + \frac{1}{C_{p,ref}T_{ref}}\sum_{i=1}^{nc}(-\Delta H_i)N_i^* \\ &-R_g^h\left(T^* - T_\infty^*\right)\end{aligned} \tag{3.12}$$

where

$$R_g^s = \frac{(1-\varepsilon_b)}{\varepsilon_b}\frac{\rho_s C_{ps}}{c_{ref}C_{pg,ref}}, \qquad R_g^w = \frac{\varepsilon_w \rho_w C_{pw}}{\varepsilon_b c_{ref} C_{pg,ref}}, \qquad R_g^h = \frac{2r_w^{ml}\tau_{conv}U}{\varepsilon_b\left(r_w^i\right)^2 c_{ref}C_{pg,ref}}$$

and $C^*_{pg,i}$ is the dimensionless heat capacity of component *i*, T^* the dimensionless temperature, $T_\infty{}^*$ the dimensionless external environmental temperature. The $\mathrm{Pe_H}$ is the thermal Peclet number, defined by $\mathrm{Pe_H} = c_{ref} C_{pg,ref} u_{ref} L_B / \lambda$. The R_g^s, R_g^w and R_g^h are energy balance dimensionless parameters.

Mass transport model:

$$\frac{\partial \overline{q_i^*}}{\partial \theta} = R_p^b \alpha_i^D \left(q_{i,s}^* - \overline{q_i^*} \right) \tag{3.13}$$

where $q_{i,s}^*$ is the dimensionless adsorbed concentration in the particle surface. The R_p^b is the ratio between bed time constant and particle diffusion time constant, given by $R_p^b = k_{ref} \tau_b$, where τ_b is the bed time constant, given by $\tau_b = L_B / u_{ref}$. The α_i^D is the ratio between the LDF coefficient of component *i* and the LDF coefficient of the reference component, $\alpha_i^D = k_i / k_{ref}$.

The dimensionless parameters of the model are:

$$x^* = \frac{x}{L}, \quad \theta = \frac{t}{\tau_{conv}}, \quad u^* = \frac{u}{u_{ref}}, \quad T^* = \frac{T}{T_{ref}}, \quad \overline{q_i^*} = \frac{\overline{q_i}}{q_{ref}}, \quad q_{i,s}^* = \frac{q_{i,s}}{q_{ref}},$$

$$C_{pg,i}^* = \frac{C_{pg,i}}{C_{pg,ref}}, \quad c_i^* = \frac{c_i}{c_{ref}}, \quad c_{total}^* = \frac{c_{total}}{c_{ref}}, \quad T_\infty^* = \frac{T_\infty}{T_{ref}}$$

The boundary and initial conditions of mass and energy balances are given below; the well-known Danckwerts boundary conditions were used.

Initial conditions:

$$c_i^* = c_{i,0}{}^*, \qquad \overline{q_i^*} = q_{i,0}^*, \qquad T^* = T_{in}^*$$

Boundary conditions:

$$x^* = 0: \quad \frac{\partial c_i^*}{\partial x^*} - Pe_M u^* c_i^* \Big|_{x=0^+} = -Pe_M u^* c_{i,\,feed}^*$$

$$T^* = T_{in}^*$$

$$x^* = 1: \quad \frac{\partial c_i^*}{\partial x^*} = 0$$

$$\frac{\partial T^*}{\partial x^*} = 0$$

where T_{in}^* is the dimensionless initial temperature, given by $T_{in}^* = T_{in} / T_{ref}$, and $c_{i,\,feed}^*$ the dimensionless partial molar concentration of feed stream, given by $c_{i,\,feed}^* = c_{i,\,feed} / c_{ref}$.

The space derivatives were solved numerically using the finite difference method with fixed grid implemented in a in-house numerical package DERVX [34]. The system of partial differential equations, coupled with the appropriate boundary and initial conditions for three air components (nitrogen, oxygen and argon), was integrated explicitly in order to obtain the grid point values at the next time step using the package LSODA [35]. This flexible subroutine solves initial boundary problems for stiff or non-stiff systems of first-order ordinary differential equations.

3.3 Results and discussion

3.3.1 Adsorption equilibrium

Characterization of adsorbent

In the present work, monocomponent adsorption equilibrium isotherms of nitrogen, oxygen and argon on AgLiLSX were obtained at three different temperatures – 15 °C, 25 °C and 35 °C – and up to 7 bar. The resulting isotherm plots are shown in Figures 3.1 – 3.3.

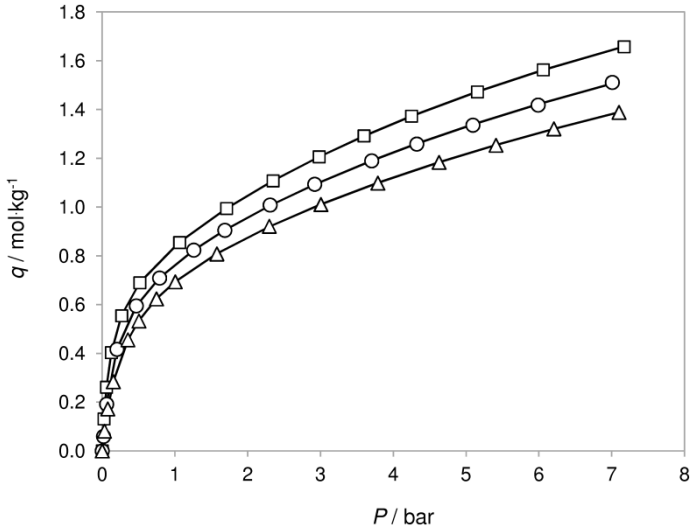

Figure 3.1 – Nitrogen isotherms on AgLiLSX at: □, 15 °C; ○, 25 °C; and △, 35 °C. The solid line represents the dual-site Langmuir isotherm fitting.

Nitrogen exhibits the greatest adsorption capacity and the most favorable isotherms, while oxygen and argon have similar and considerably less adsorption capacity. As expected, argon has slightly more adsorption capacity than oxygen, exhibiting equilibrium Ar/O_2 selectivity above 1 and, therefore, the ability to

selectively remove argon from the feed stream and to produce a product of 95+% of oxygen in a single-stage cyclic adsorption operation.

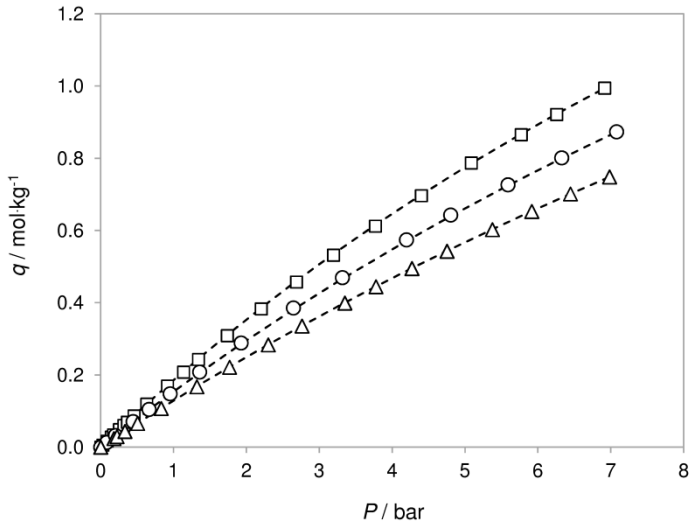

Figure 3.2 – Oxygen isotherms on AgLiLSX at: □, 15 °C; ○, 25 °C; and △, 35 °C. The dashed line represents the Langmuir isotherm fitting.

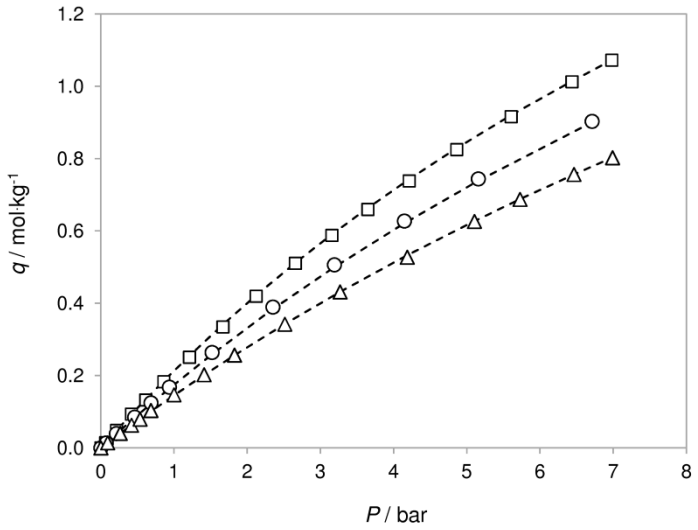

Figure 3.3 – Argon isotherms on AgLiLSX at: □, 15 °C; ○, 25 °C; and △, 35 °C. The dashed line represents the Langmuir isotherm fitting.

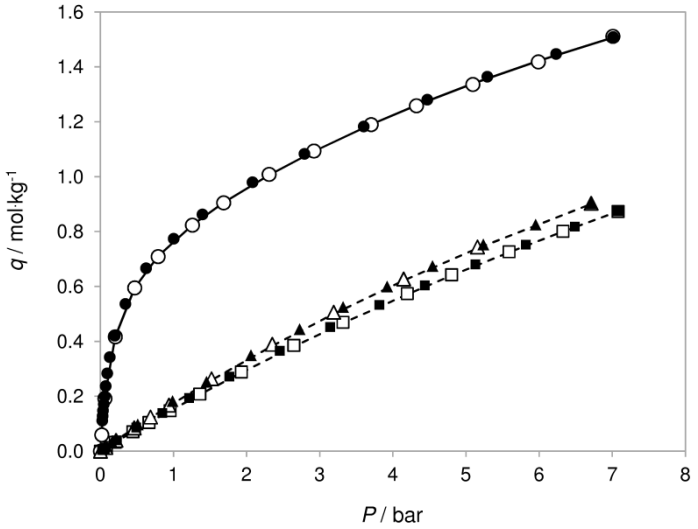

Figure 3.4 – Adsorption (hollow symbols) and desorption (bold symbols) isotherms for: ○, nitrogen; □, oxygen; and △, argon, on AgLiLSX at 25 °C.

Figure 3.4 shows the adsorption and desorption isotherms of nitrogen, oxygen and argon on AgLiLSX at 25 °C. The adsorption and desorption legs overlap – no hysteresis is observed. Also, it was experimentally observed the complete desorption of all gases when the adsorbent was evacuated (< 0.01 mbar for 3 h).

The selectivity values for pairs Ar/O_2 and N_2/O_2 are given in Table 3.2. The N_2/O_2 selectivity shows a hyperbolic behavior characteristic of LiLSX-type zeolites. The equilibrium selectivity Ar/O_2 decreases with pressure and with temperature, from 1.17 to 1.07. Since the adsorbent shows higher Ar/O_2 and N_2/O_2 selectivity at lower pressure, it should be used in a pressure swing process focused around atmospheric pressure (VPSA operation).

The working capacity is the equilibrium loading difference at high (adsorption) and low (regeneration) pressures of a PSA cycle [36]. Considering, for example, a VPSA cycle operating between 1.4 and 0.2 bar, the nitrogen working capacity is

0.45 mol·kg^{-1} at 25 °C, and the Ar/O_2 equilibrium selectivity is 1.13 at 1.4 bar and 25 °C. For a similar adsorbent, Santos et al. [1] obtained a nitrogen working capacity of 0.48 mol·kg^{-1} and Ar/O_2 selectivity of 1.14. The difference between sample lots used may explain the slight difference of these values.

Table 3.2 – Selectivity for pair Ar/O_2 and N_2/O_2 on AgLiLSX at three temperatures.

P (bar)	Ar/O_2			N_2/O_2		
	15 °C	25 °C	35 °C	15 °C	25 °C	35 °C
0.15	1.17	1.15	1.14	15.1	14.8	14.0
0.30	1.16	1.15	1.13	10.1	10.5	10.6
0.50	1.16	1.14	1.13	7.19	7.76	8.12
1.00	1.15	1.14	1.13	4.53	4.98	5.37
1.50	1.14	1.13	1.12	3.51	3.86	4.18
2.00	1.13	1.12	1.12	2.97	3.24	3.52
3.00	1.12	1.11	1.11	2.39	2.59	2.79
4.00	1.10	1.10	1.10	2.08	2.23	2.40
5.00	1.09	1.09	1.09	1.88	2.01	2.15
6.00	1.08	1.08	1.08	1.74	1.86	1.97
7.00	1.07	1.07	1.07	1.64	1.74	1.84

In the present work, Langmuir equation was used to fit the oxygen and argon experimental adsorption equilibrium data. For fitting the nitrogen data, dual-site Langmuir equation was used instead. Both Langmuir and dual-site Langmuir equations have simple mathematical formulations and are thermodynamically consistent [37]. The dual-site Langmuir isotherm renders Langmuir, when $q_{m,2}$ equals to zero.

Langmuir isotherm:

$$q = q_m \frac{bP}{1+bP} \tag{3.14}$$

Dual-site Langmuir model:

$$q = q_{m,1} \frac{b_1 P}{1+b_1 P} + q_{m,2} \frac{b_2 P}{1+b_2 P} \tag{3.15}$$

where q is the adsorbed concentration, P is the equilibrium pressure, q_m is the saturation adsorbed concentration and b is the adsorption affinity constant.

Both equations can be modified to incorporate temperature-dependence by introducing the Van't-Hoff equation [37, 38] :

$$b = b^{\infty} \exp\left(\frac{\Delta H}{\Re T}\right) \tag{3.16}$$

where b^{∞} is the adsorption affinity constant at infinite temperature, ΔH is the adsorption heat, $\Re$ is the ideal gas constant, and T is the absolute temperature.

All fitting parameters were obtained by minimizing the relative deviations, Δq, between experimental and fitting values:

$$\Delta q(\%) = \frac{100}{k} \sum_{j=1}^{k} \frac{\left| q_j^{\exp} - q_j^{cal} \right|}{q_j^{\exp}} \tag{3.17}$$

where q_j is the adsorbed concentration, and k is the number of observations. Superscript "exp" and "cal" stands for experimentally obtained value and obtained by fitting, respectively.

The obtained parameters of Langmuir and dual-site Langmuir equations are given in Table 3.3.

Table 3.3 – Parameters of isotherm fittings on AgLiLSX adsorbent.

Parameters	**Nitrogen**	**Oxygen**	**Argon**
Equation type	DSL[a]	Langmuir	Langmuir
$q_{m,1}$ / mol·kg^{-1}	0.729	3.79	3.29
b_1^{∞} x 10^{-3} / bar^{-1}	0.020	0.151	0.134
ΔH_1 x 10^3 / J·mol^{-1}	31.1	14.0	15.0
$q_{m,2}$ / mol·kg^{-1}	2.66	----	----
b_2^{∞} x 10^{-3} / bar^{-1}	0.051	----	----
ΔH_2 x 10^3 / J·mol^{-1}	17.6	----	----
Δq / %	0.6	0.6	0.9

[a] Dual-site Langmuir.

Deactivation study

As mentioned in the previous section, AgLiLSX adsorbent is very sensitive to water vapor and carbon dioxide contamination, deactivating when exposed to atmospheric air [30]. Adsorption equilibrium isotherms of carbon dioxide and water vapor were obtained at 25 °C, and are plotted in Figure 3.5 and Figure 3.6, respectively. The strongly favorable curvature for both isotherms indicates significant extent of irreversibility. The obtained parameters of dual-site Langmuir isotherm fitting for carbon dioxide and water vapor on AgLiLSX are given in Table 3.4.

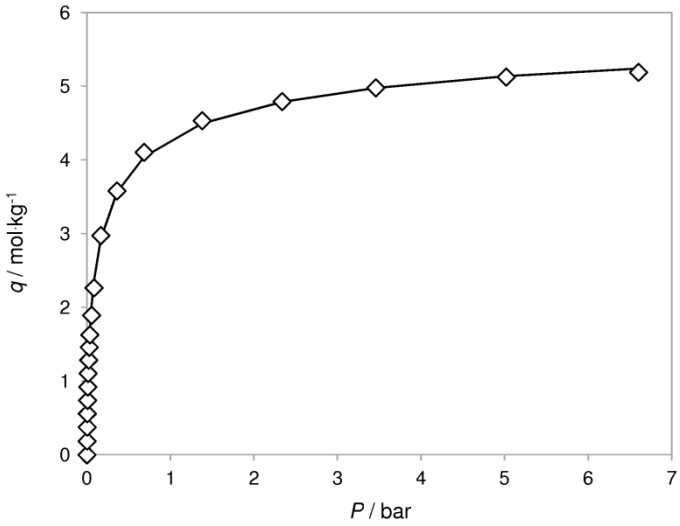

Figure 3.5 – Carbon dioxide isotherm on AgLiLSX at 25 °C. The solid line represents the dual-site Langmuir isotherm fitting.

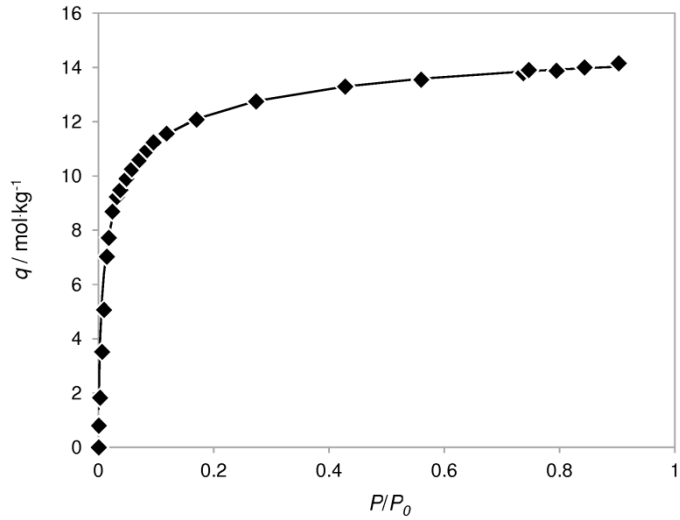

Figure 3.6 – Water vapor isotherm on AgLiLSX at 25 °C. The solid line represents the dual-site Langmuir isotherm fitting.

Table 3.4 – Parameters of dual-site Langmuir isotherm fittings on AgLiLSX adsorbent.

Parameters	Carbon dioxide	Water vapor
$q_{m,1}$ / mol·kg^{-1}	1.671	12.621
b_1 x 10^{-3} / bar^{-1}	89.87	2381
$q_{m,2}$ / mol·kg^{-1}	3.611	6.005
b_2 x 10^{-3} / bar^{-1}	3.29	13.66
Δq / %	1.9	1.7

A study was conducted to quantify the degree of contamination of the AgLiLSX adsorbent when contacted with atmospheric air. This study consisted in let a small sample contact with atmospheric air containing 600 ppm of carbon dioxide and a dew point of 4 °C, at 1 bar and 25 °C, overnight. After that, the sample was placed inside the corresponding vessel of the volumetric method apparatus and regenerated during 12 h, using vacuum-only conditions (ca. 0.01 mbar). Then, the adsorption equilibrium isotherms of nitrogen, oxygen and argon were obtained at 25 °C and compared with the isotherms obtained on the fresh sample. Table 3.5 summarized the remaining adsorption capacity of the contaminated sample for nitrogen, oxygen and argon, as well as the selectivity nitrogen/oxygen and argon/oxygen.

Adsorbents used in PSA operation are often submitted to improper packaging, friction caused by excessive fluid velocities inside the bed, and external mechanical vibrations. The crushing strength of an adsorbent provides information of whether the material is susceptible to abrasion and dusting when submitted to an external force. The crushing strength of AgLiLSX pellets was measured and the results are plotted in Figure 3.7. The low crushing strength of AgLiLSX indicates that this adsorbent has low mechanical resistance and, therefore, if mistreated, can suffer abrasion, dusting and consequent deactivation by destruction of the adsorption sites.

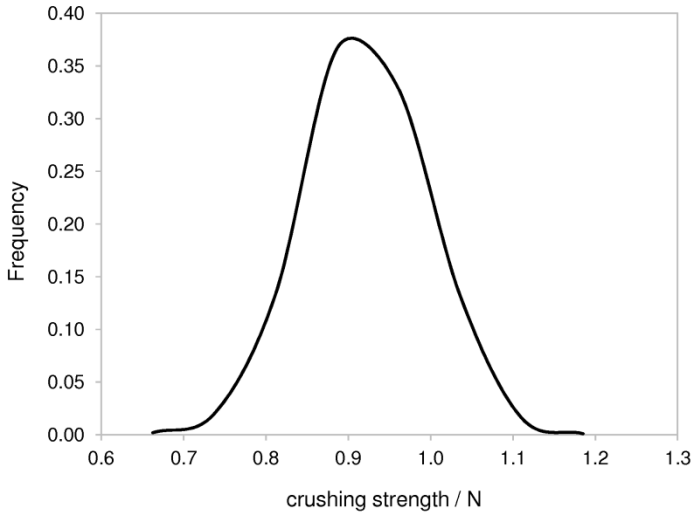

Figure 3.7 – Histogram of crushing strength measured for AgLiLSX pellets.

A study was conducted to measure the extent of deactivation of AgLiLSX when submitted to inappropriate conditions such as improper packaging or friction. A small sample was crushed and make into powder (particle diameter of ca. 0.15 mm). Then, the sample was placed in the corresponding vessel of the volumetric method apparatus and regenerated during 3 h using vacuum-only conditions (ca. 0.01 mbar). Then, the equilibrium isotherms of nitrogen, oxygen and argon were obtained at 25 $^{\circ}$C and compared with the isotherms obtained on the undamaged sample. Table 3.5 summarized the remaining adsorption capacity of the crushed sample for nitrogen, oxygen and argon, as well as the selectivity nitrogen/oxygen and argon/oxygen.

Table 3.5 – Adsorption capacity and selectivity of the AgLiLSX at 1.4 bar and 25 °C after contamination with carbon dioxide and water vapor; and after crushing the pellets down to dust.

	After **contamination**	**Dusting**	**fresh sample**
adsorption capacity (%)			
nitrogen	4.7	15.0	100
oxygen	16.9	39.2	100
argon	15.1	35.6	100
adsorption selectivity			
N_2/O_2	1.12	1.54	4.16
Ar/O_2	1.01	1.03	1.13

3.3.2 Adsorption kinetics

A set of mono and multicomponent breakthrough curves was performed to assess the adsorption kinetics on AgLiLSX adsorbent [39]. The monocomponent breakthroughs of nitrogen, oxygen and argon are plotted in Figure 3.8; the adsorption column was initially filled with helium. The adsorption breakthrough curves for the three components exhibit a compressive shape characteristic of favorable isotherms [39]. Due to the fast adsorption kinetics of the three species on AgLiLSX, the concentration front shows an abrupt behavior. Indeed, in the studied cases, breakthrough time depends almost only on adsorption equilibrium (thermodynamics). Therefore, the less adsorbed gas, oxygen, leaves the column first, residence time of 155 s, followed by argon, 167 s, and the much slower nitrogen, 468 s. Also, the simulation results accurately describe the experimental data. The LDF coefficients that best fitted the experimental curves were: k_{N2} = 0.13 s^{-1}, k_{O2} = 0.25 s^{-1} and k_{Ar} = 0.23 s^{-1}. The temperature profiles at the entrance and exit of the breakthrough column were investigated, recorded and simulated. As expected, the nitrogen shows the higher temperature excursion when compared with oxygen and argon, which shows similar temperature profiles. In Figure 3.9 the temperature

profiles of effluent stream at the exit of the column for oxygen and nitrogen monocomponent breakthroughs are presented.

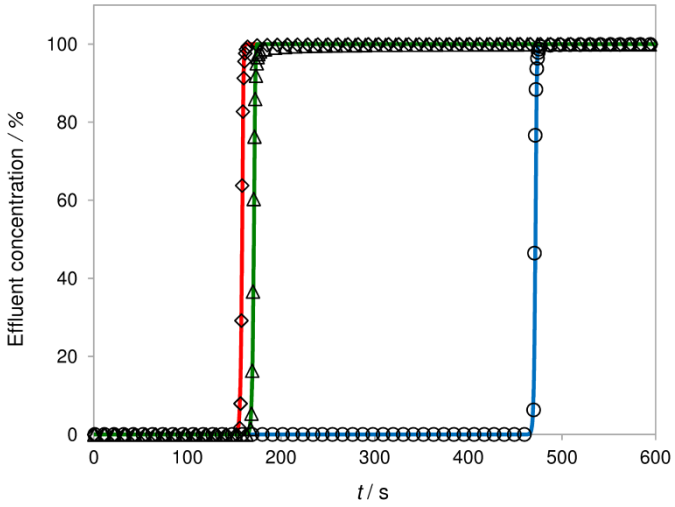

Figure 3.8 – Breakthrough curves of: ○, nitrogen; ◇, oxygen; and △, argon, on AgLiLSX at 1.4 bar (0.5 L_{STP}·min^{-1} flow rate). Bed initially saturated with helium at 25 °C.

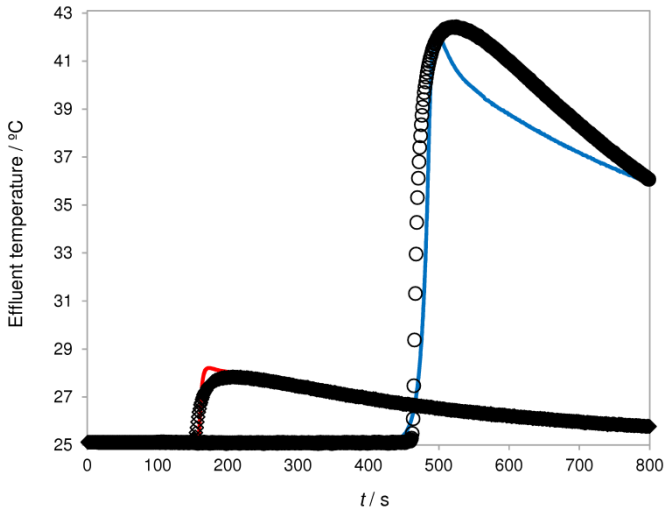

Figure 3.9 – Temperature profiles of the effluent stream, measured at the exit of the column, for ○, nitrogen and ◇, oxygen monocomponent breakthroughs on AgLiLSX at 1.4 bar (0.5 L_{STP}·min^{-1} flow rate). Bed initially saturated with helium at 25 °C.

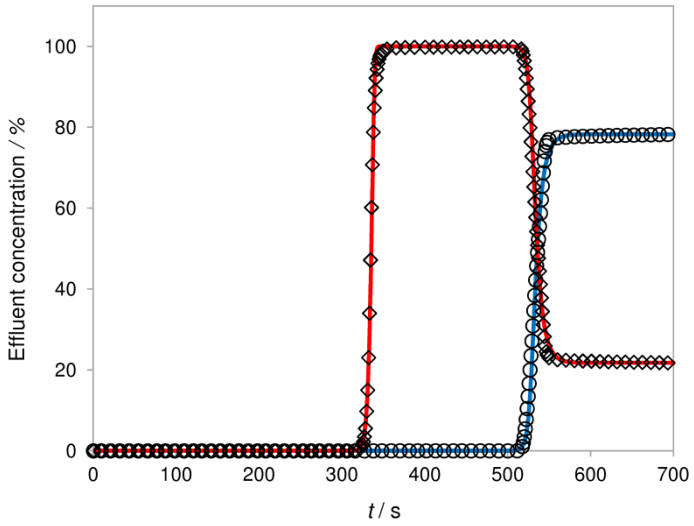

Figure 3.10 – Breakthrough curves of: ○, nitrogen; and ◇, oxygen, obtained for synthetic air (N_2/O_2; 79:21 vol.%) on AgLiLSX at 1.4 bar (0.5 L_{STP}·min^{-1} flow rate). Bed initially saturated with helium at 25 °C.

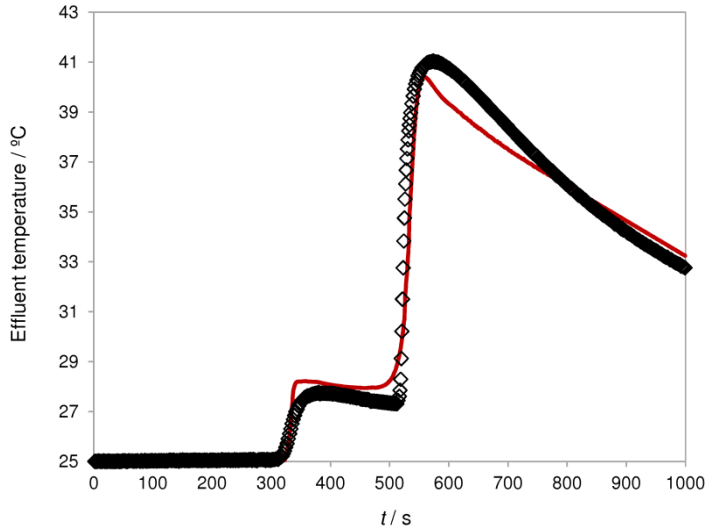

Figure 3.11 – Temperature profile of the effluent stream, measured at the exit of the column, for bicomponent breakthrough (N_2/O_2; 79:21 vol.%) on AgLiLSX at 1.4 bar (0.5 L_{STP}·min^{-1} flow rate). Bed initially saturated with helium at 25 °C.

Figure 3.10 shows the bicomponent breakthrough curves of nitrogen and oxygen – with an inlet concentration of synthetic air (N_2/O_2; 79:21 mol. %) – in the AgLiLSX bed initially filled with helium. The oxygen concentration breaks first at instant 325 s, originating a square wave at the nitrogen breakthrough instant, at 518 s. The LDF coefficients used in simulations are k_{N2} = 0.13 s^{-1} and k_{O2} = 0.23 s^{-1} and, as one can see, the model describes accurately the experimental curves. Figure 3.11 shows the temperature profile of the effluent stream, measured at the exit of the column. Two temperature peaks can be observed: the first one, smaller, when oxygen concentration front exits the column; and a second one, higher, at the nitrogen breakthrough instant.

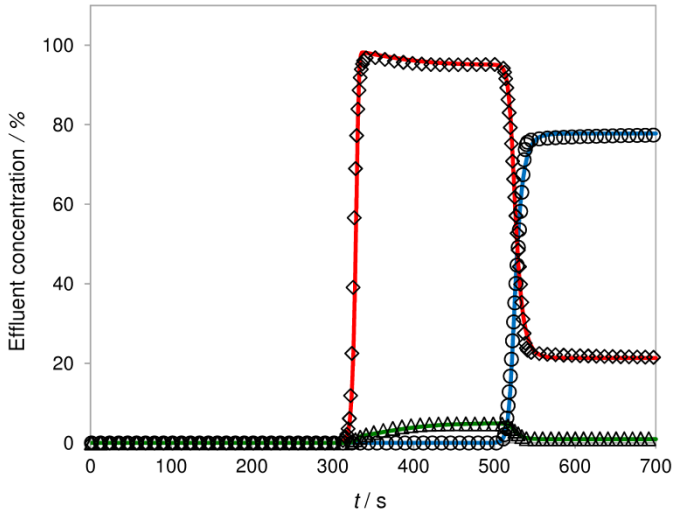

Figure 3.12 – Breakthrough curves of: ○, nitrogen; ◇, oxygen; and △, argon, obtained for synthetic air (N_2/O_2/Ar; 78:21:1 vol.%) on AgLiLSX at 1.4 bar (0.5 L_{STP}·min^{-1} flow rate). Bed initially saturated with helium at 25 °C.

Figure 3.12 shows the multicomponent breakthrough curves of nitrogen, oxygen and argon – inlet of synthetic air (N_2/O_2/Ar; 78:21:1 vol.%) – in the AgLiLSX bed filled initially with helium. The oxygen concentration front travels faster in the column, exiting at instant 315 s, followed by argon, at instant 323 s. These results

clearly indicate that the separation of oxygen from argon is possible despite the time range for the separation being small, which is related to the low Ar/O_2 adsorption selectivity, ca. 1.13 at 1.4 bar and 25 °C. Also, regarding Figure 3.12, it can be seen that the top of the oxygen square wave concentration decreases as a function of the time while the corresponding argon concentration increases; this behavior is related to the breakthrough of argon. The breakthrough of nitrogen occurs at instant 510 s. Similarly, LDF coefficients used in this run are $k_{N2} = 0.13\ s^{-1}$, $k_{O2} = 0.23\ s^{-1}$ and $k_{Ar} = 0.23\ s^{-1}$.

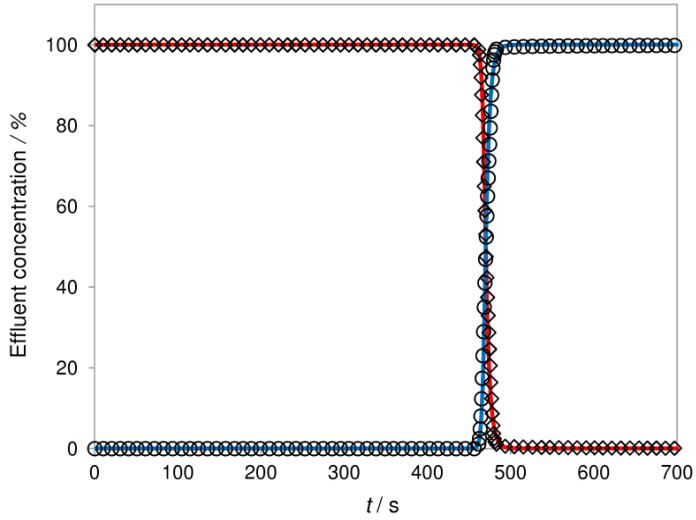

Figure 3.13 – Breakthrough curves of: ○, nitrogen; and ◇, oxygen, obtained for pure nitrogen on AgLiLSX at 1.4 bar (0.5 L_{STP}·min^{-1} flow rate). Bed initially saturated with oxygen at 25 °C.

Pure nitrogen and a ternary mixture ($N_2/O_2/Ar$; 78:21:1 vol.%) were used as feed gases in breakthroughs conducted in the AgLiLSX bed initially saturated with oxygen – see Figure 3.13 and Figure 3.14, respectively. Concerning the nitrogen breakthrough curve – Figure 3.13 – it can be seen that both curves are very steep and show little tailing. This behavior agrees with the higher adsorption of nitrogen that pushes oxygen out of the column originating a compressing wave. The LDF coefficients used in this simulation are $k_{N2} = 0.15\ s^{-1}$ and $k_{O2} = 0.25\ s^{-1}$.

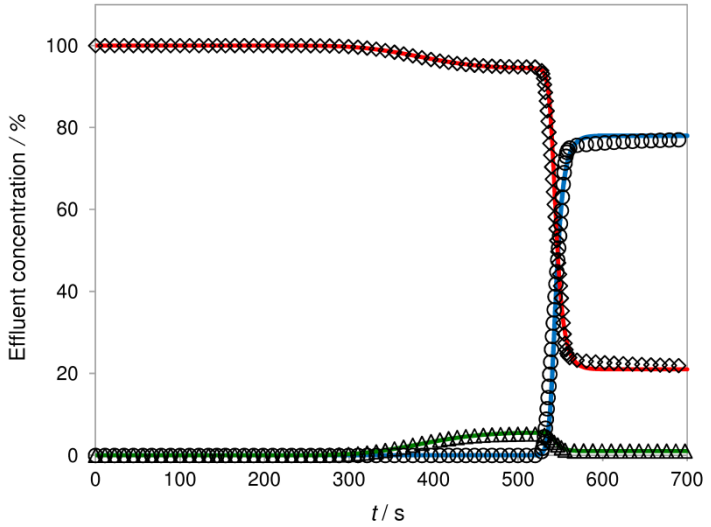

Figure 3.14 – Breakthrough curves of: ○, nitrogen; ◇, oxygen; and △, argon, obtained for synthetic air (N_2/O_2/Ar; 78:21:1 vol.%) on AgLiLSX at 1.4 bar (0.5 L_{STP}·min^{-1} flow rate). Bed initially saturated with oxygen at 25 °C.

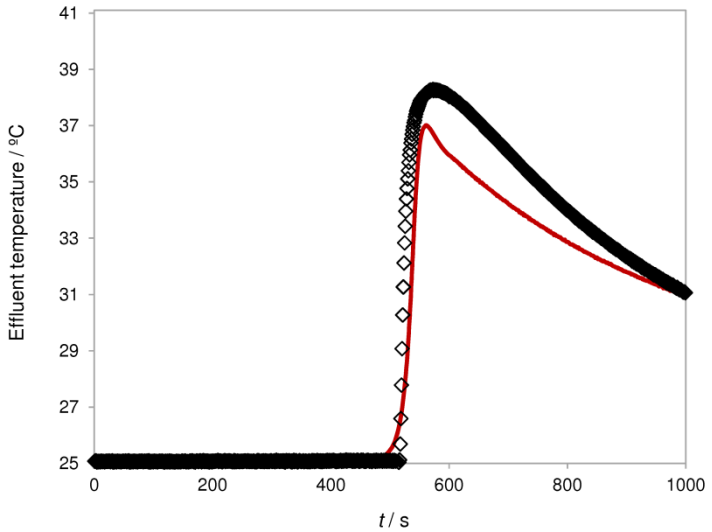

Figure 3.15 – Temperature profile of the effluent stream, measured at the exit of the column, for multicomponent breakthrough (N_2/O_2/Ar; 78:21:1 vol.%) on AgLiLSX at 1.4 bar (0.5 L_{STP}·min^{-1} flow rate). Bed initially saturated with oxygen at 25 °C.

Figure 3.14 shows the multicomponent breakthrough curves of nitrogen, oxygen and argon – inlet of synthetic air (N_2/O_2/Ar; 78:21:1 vol.%) – in the AgLiLSX bed initially saturated with oxygen. These conditions are closer to the ones observed during the adsorption step of a PSA, when a feed stream of atmospheric air enters a column filled with an oxygen-enriched mixture. As it can be seen, argon travels faster, exiting the column at approximately 266 s, before nitrogen. The nitrogen adsorption front displaces argon from the adsorption sites, originating the concentration peak that can be seen between instants 266 s and 526 s. The LDF coefficients used in simulations are k_{N2} = 0.13 s^{-1}, k_{O2} = 0.23 s^{-1} and k_{Ar} = 0.23 s^{-1}. Figure 3.15 shows the temperature profile of the effluent stream, measured at the exit of the column. The single peak observed occurs when nitrogen leaves the column. The breakthrough of argon does not cause a visible temperature peak, due to the small concentration of argon and small adsorption heat on AgLiLSX, similar to that of the oxygen that is displaced from adsorption sites.

The adsorption kinetics of nitrogen, oxygen and argon on AgLiLSX adsorbent were obtained using the chromatographic method [40], based on a simple mass and energy balance model of the breakthrough column and using the LDF model to describe the intraparticle mass transport. A good agreement between the model and the experimental data was obtained – LDF coefficients obtained by the chromatographic method are in the same order of experimental ones obtained by uptake measurements – indicating that the model describes accurately the phenomena involved. Also, in a similar fixed bed study, Jee et al. [41] obtained similar LDF coefficients for nitrogen and oxygen using different zeolite types. Table 3.6 summarizes the LDF coefficients used in the simulations, and on the basis of average mass transport coefficients, the apparent time constant for each gas was also estimated. The proposed model was then used to simulate new mono and multicomponent breakthroughs at a higher feed flow rate, 1 L_{STP}·min^{-1}. LDF

coefficients obtained for previous simulations – Table 3.6 – were used. The simulation and experimental results are shown in Figure 3.16 and Figure 3.17, respectively monocomponent (inlet of pure nitrogen and pure oxygen) and bicomponent breakthrough curves (inlet of synthetic air, N_2/O_2; 79:21 mol. %) of nitrogen and oxygen in the AgLiLSX fixed bed initially saturated with helium. In both cases a good agreement between experimental and simulation curves was obtained.

Table 3.6 – LDF coefficients for nitrogen, oxygen and argon, and corresponding apparent time constants, at 1 bar and 25 °C.

i	k_i **(s^{-1})**	D/r^2 **(s^{-1})**	D **($m^2 \cdot s^{-1}$)**
N_2	0.13	8.9×10^{-3}	1.43×10^{-9}
O_2	0.24	1.6×10^{-2}	2.54×10^{-9}
Ar	0.23	1.5×10^{-2}	2.45×10^{-9}

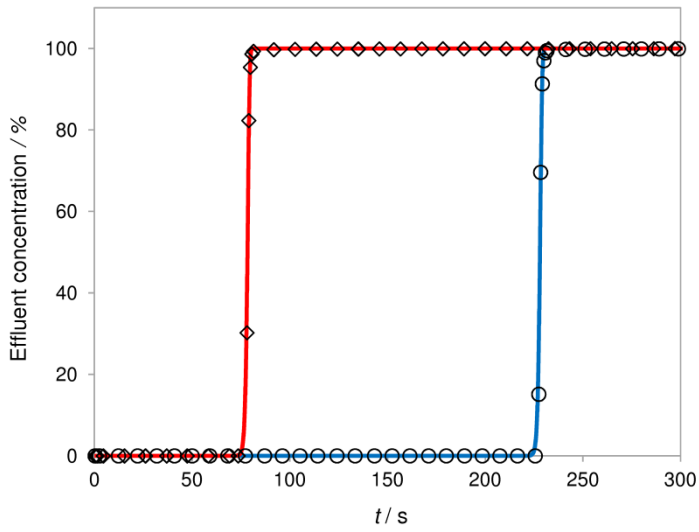

Figure 3.16 – Breakthrough curves of: ○, nitrogen and ◇, oxygen; on AgLiLSX at 1.4 bar (1 $L_{STP} \cdot min^{-1}$ flow rate). Bed initially saturated with helium at 25 °C.

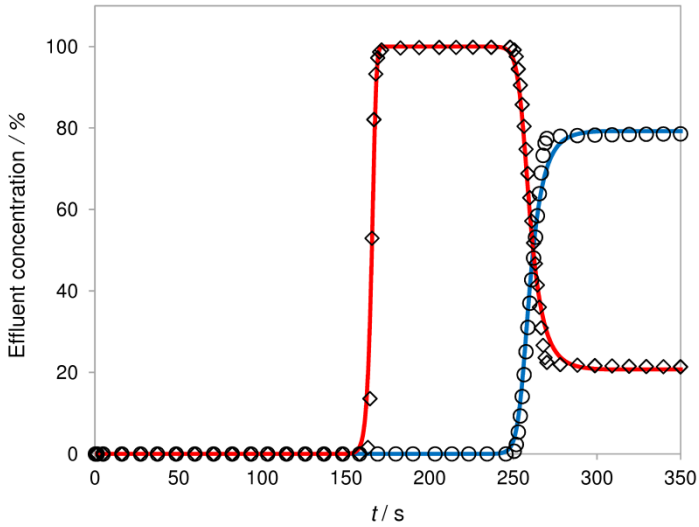

Figure 3.17 – Breakthrough curves of: ○, nitrogen; and ◇, oxygen, obtained for synthetic air (N_2/O_2; 79:21 vol.%) on AgLiLSX at 1.4 bar (1 L_{STP}·min^{-1} flow rate). Bed initially saturated with helium at 25 °C.

3.4 Conclusions

Nitrogen, oxygen and argon adsorption equilibrium isotherms were obtained for zeolite AgLiLSX at 15 °C, 25 °C and 35 °C and up to 7 bar, using the volumetric method. The Langmuir equation was used to fit oxygen and argon isotherm data, while the dual-site Langmuir equation was used for nitrogen. Nitrogen exhibited the strongest adsorption and the most favorable isotherms. However, unlike any commercial adsorbent, zeolite AgLiLSX exhibits equilibrium selectivity Ar/O_2 above 1.13. The high adsorption working capacity and N_2/O_2 equilibrium selectivity for lower pressures combined with the unique selectivity Ar/O_2, indicate that zeolite AgLiLSX can be used for producing high-purity oxygen, 95+ %, in a single-stage PSA/VPSA unit.

Breakthrough experiments were carried out at 1.4 bar (with bed initially saturated with helium or oxygen at 25 °C), with a feed flow rate of 0.5 L_{STP}·min^{-1} and

1 L_{STP}·min^{-1}, to characterize the adsorption kinetics. The results obtained are consistent with adsorption equilibrium data, and the proposed model was able to represent accurately the experimental curves. Nitrogen, oxygen and argon effective diffusivities on AgLiLSX were obtained from the breakthrough experiments based on a simple mass and energy balance model and using the LDF model to describe the intraparticle mass transport. The values of obtained for nitrogen, oxygen and argon are respectively 1.43 x 10^{-9}, 2.54 x 10^{-9} and 2.45 x 10^{-9} m^2·s^{-1}.

Acknowledgment

Daniel Ferreira acknowledges Fundação para a Ciência e Tecnologia (FCT) and Sysadvance, Sistemas de Engenharia S.A. for the Ph.D. Grant (ref. SFRH/BDE/51186/2010). The authors acknowledge the funding provided by Agência de Inovação (AdI) (project HPOVPSA, ref. 13488).

3.5 References

1. Santos, J.C., Cruz, P., Regala, T., Magalhães, F.D., Mendes, A. High-Purity Oxygen Production by Pressure Swing Adsorption. *Industrial & Engineering Chemistry Research.* **2006**, 46, 591-599.
2. Park, Y.-J., Lee, S.-J., Moon, J.-H., Choi, D.-K., Lee, C.-H. Adsorption Equilibria of O_2, N_2, and Ar on Carbon Molecular Sieve and Zeolites 10X, 13X, and LiX. *Journal of Chemical & Engineering Data.* **2006**, 51, 1001-1008.
3. Ruthven, D., Farooq, S., Knaebel, K. *Pressure Swing Adsorption*; VCH Publishers: New York, 1994.
4. Jee, J.-G., Kim, M.-B., Lee, C.-H. Pressure Swing Adsorption Processes to Purify Oxygen Using a Carbon Molecular Sieve. *Chemical Engineering Science.* **2005**, 60, 869-882.
5. Kim, M.-B., Jee, J.-G., Bae, Y.-S., Lee, C.-H. Parametric Study of Pressure Swing Adsorption Process To Purify Oxygen Using Carbon Molecular Sieve. *Industrial & Engineering Chemistry Research.* **2005**, 44, 7208-7217.
6. Mendes, A.M.M., Costa, C.A.V.d.C., Rodrigues, A.E. Oxygen Separation from Air by PSA: Modelling and Experimental Results. Part I: Isothermal Operation. *Separation and Purification Technology.* **2001**, 24, 173-188.
7. Hayashi, S., Kawai, M., Kaneko, T. Dynamics of High-purity Oxygen PSA. *Gas Separation & Purification.* **1996**, 10, 19-23.
8. Bansal, R.K. Pressure Swing Adsorption Process and System for Gas Separation. U.S. Patent 4,973,339, 1990.
9. Haruna, K., Ueda, K., Inoue, M., Someda, H. Process for Producing High-purity Oxygen Gas from Air. U.S. Patent 4,985,052, 1991.
10. Jee, J.-G., Lee, S.-J., Kim, M.-B., Lee, C.-H. Three-Bed PVSA Process for High-Purity O2 Generation from Ambient Air. *AIChE Journal.* **2005**, 51, 2988-2999.
11. Knaebel, K.S., Kandybin, A. Pressure Swing Adsorption System to Purify Oxygen. U.S. Patent 5,226,933, 1993.
12. Lee, S.-J., Jung, J.-H., Moon, J.-H., Jee, J.-G., Lee, C.-H. Parametric Study of the Three-Bed Pressure−Vacuum Swing Adsorption Process for High-purity O2 Generation from Ambient Air. *Industrial & Engineering Chemistry Research.* **2007**, 46, 3720-3728.

13. Mercea, P.V., Hwang, S.-T. Oxygen Separation From Air by a Combined Pressure Swing Adsorption and Continuous Membrane Column Process. *Journal of Membrane Science.* **1994**, 88, 131-144.

14. Rege, S.U., Yang, R.T. Kinetic Separation of Oxygen and Argon Using Molecular Sieve Carbon. *Adsorption.* **2000**, 6, 15-22.

15. Tsuru, T., Hwang, S.T. Production of High-Purity Oxygen by Continuous Membrane Column Combined with PSA Oxygen Generator. *Industrial & Engineering Chemistry Research.* **1994**, 33, 311-316.

16. Yang, R.T. *Adsorbents. Fundamentals and Applications*; John Wiley & Sons: New Jersey, USA, 2003.

17. Gaffney, T.R. Porous Solids for Air Separation. *Current Opinion in Solid State and Materials Science.* **1996**, 1, 69-75.

18. Mendes, A.M.M., Costa, C.A.V., Rodrigues, A.E. Analysis of Nonisobaric Steps in Nonlinear Bicomponent Pressure Swing Adsorption Systems. Application to Air Separation. *Industrial & Engineering Chemistry Research.* **1999**, 39, 138-145.

19. Coe, C.G. Moleculary Engineered Adsorbents for Air Separation. *Gas Separation Technology.* **1990**, 149-159.

20. Coe, C.G., Kuznicki, S.M., Srinivasan, R., Jenkins, R.J. Molecularly Engineered, High-Performance Adsorbent. In *Perspectives in Molecular Sieve Science;* ACS Symposium Series 368; American Chemical Society: Washington, DC, 1988; 478-491.

21. Wilkerson, B.E. The Adsorption of Argon and Oxygen on Silver Mordenite. Master Thesis, Graduate School of Ohio State University, Ohio, USA, 1990.

22. Sebastian, J., Jasra, R.V. Sorption of Nitrogen, Oxygen, and Argon in Silver-Exchanged Zeolites. *Industrial & Engineering Chemistry Research.* **2005**, 44, 8014-8024.

23. Ansón, A., Kuznicki, S.M., Kuznicki, T., Haastrup, T., Wang, Y., Lin, C.C.H., Sawada, J.A., Eyring, E.M., Hunter, D. Adsorption of Argon, Oxygen, and Nitrogen on Silver Exchanged ETS-10 Molecular Sieve. *Microporous and Mesoporous Materials.* **2008**, 109, 577-580.

24. Shi, M., Kim, J., Sawada, J.A., Lam, J., Sarabadan, S., Kuznicki, T.M., Kuznicki, S.M. Production of Argon Free Oxygen by Adsorptive Air Separation on Ag-ETS-10. *AIChE Journal.* **2013**, 59, 982-987.

25. Hutson, N.D., Rege, S.U., Yang, R.T. Mixed Cation Zeolites: LixAgy-X as a Superior Adsorbent for Air Separation. *AIChE Journal.* **1999**, 45, 724-734.

26. Hutson, N.D., Yang, R.T. Structural Effects on Adsorption of Atmospheric Gases in Mixed Li,Ag–X-Zeolite. *AIChE Journal.* **2000**, 46, 2305-2317.

27. Chiang, R.L., Whitley, R.D., Ostroski, J.E., Dee, D.P. Argon/Oxygen Selective X-Zeolite. U.S. Patent 6,432,170, 2002.

28. Dee, D.P., Chiang, R.L., Miller, E.J., Whitley, R.D. High purity Oxygen Production by Pressure Swing Adsorption. U.S. Patent 6,544,318, 2003.

29. Santos, J.C., Magalhães, F.D., Mendes, A. Contamination of Zeolites Used in Oxygen Production by PSA: Effects of Water and Carbon Dioxide. *Industrial & Engineering Chemistry Research.* **2008**, 47, 6197-6203.

30. Ferreira, D., Magalhães, R., Taveira, P., Mendes, A.l. Effective Adsorption Equilibrium Isotherms and Breakthroughs of Water Vapor and Carbon Dioxide on Different Adsorbents. *Industrial & Engineering Chemistry Research.* **2011**, 50, 10201-10210.

31. Cruz, P., Santos, J.C., Magalhães, F.D., Mendes, A. Cyclic Adsorption Separation Processes: Analysis Strategy and Optimization Procedure. *Chemical Engineering Science.* **2003**, 58, 3143-3158.

32. Myers, A.L., Prausnitz, J.M. Thermodynamics of Mixed-Gas Adsorption. *AIChE Journal.* **1965**, 11, 121-127.

33. Mendes, A.M.M., Costa, C.A.V., Rodrigues, A.r.E. PSA Simulation Using Particle Complex Models. *Separation and Purification Technology.* **2001**, 24, 1-11.

34. Cruz, P. Simulação e Optimização de Processos Cíclicos de Adsorção. Ph.D. Thesis, Faculty of Engineering of the University of Porto, Porto, Portugal, 2003.

35. Petzold, L. Automatic Selection of Methods for Solving Stiff and Nonstiff Systems of Ordinary Differential Equations. *SIAM Journal of Scientific and Statistical Computing.* **1983**, 4, 136-148.

36. Ruthven, D.M., Reyes, S.C. Adsorptive Separation of Light Olefins from Paraffins. *Microporous and Mesoporous Materials.* **2007**, 104, 59-66.

37. Do, D.D. *Adsorption Analysis: Equilibria and Kinetics*; Imperial College Press: London, 1997.

38. Ribeiro, R.P.P.L., Grande, C.A., Rodrigues, A.r.E. Adsorption of Water Vapor on Carbon Molecular Sieve: Thermal and Electrothermal Regeneration Study. *Industrial & Engineering Chemistry Research.* **2011**, 50, 2144-2156.

39. Ribeiro, A.M., Sauer, T.P., Grande, C.A., Moreira, R.F.P.M., Loureiro, J.M., Rodrigues, A.r.E. Adsorption Equilibrium and Kinetics of Water Vapor on

Different Adsorbents. *Industrial & Engineering Chemistry Research.* **2008**, 47, 7019-7026.

40. Sheikh, M.A., Hassan, M.M., Loughlin, K.F. Adsorption Equilibria and Rate Parameters for Nitrogen and Methane on Maxsorb Activated Carbon. *Gas Separation and Purification.* **1996**, 10, 161-168.

41. Jee, J.-G., Park, M.-K., Yoo, H.-K., Lee, K., Lee, C.-H. Adsorption and Desorption Characteristics of Air on Zeolite 5A, 10X and 13X Fixed Beds. *Separation Science and Technology.* **2002**, 37, 3465-3490.

CHAPTER IV

Ferreira, D., Bárcia, P., Whitley, R.D., Mendes, A., Single-Stage VPSA for Producing High-Purity Oxygen From Air. *Industrial & Engineering Chemistry Research*. **2015**, 54, 9591-9604.

The author contributed to the design and assembling of stand-alone VPSA unit and to the execution of all the experiments and simulations described in this chapter. The author was also involved on the discussion and interpretation of results, as well as on the preparation of the manuscript.

4 Single-stage VPSA for producing high-purity oxygen from air

Abstract

The maximum oxygen concentration obtained using a conventional single-stage pressure swing adsorption unit is ca. 95 % balanced mostly with argon. However, there are several applications requiring simple and compact units for producing high-purity oxygen (≥ 99 %), such as medical, military or aerospace. This article studies a single-stage vacuum pressure swing adsorption (VPSA) unit, loaded with silver-based zeolite AgLiLSX, for producing ca. 1 L_{STP}·min^{-1} of high-purity oxygen. The unit was designed based on the experimental and simulation results obtained with a lab-scale unit. For a product concentration of 99.0 %, the recovery obtained was ca. 8.0 % with a productivity of 9.0 m^3·hr^{-1}·ton^{-1}.

4.1 Introduction

Since its invention, vacuum pressure swing adsorption (VPSA) technology for oxygen production from air has significantly evolved towards more energy efficient and compact units, using improved adsorption cycles, better adsorbents and new valve technologies [1-3]. However, the oxygen product concentration is limited to ca. 95 % [4, 5], since the equilibrium adsorbents used are not selective towards argon, which is present in the atmospheric air at ca. 0.93 % [6, 7]. To overcome this limitation, dual-stage PSA units were developed when a high-purity product (≥ 99.0 %) is required [8-10]. This process, initially disclosed by Armond et al. in 1980, consists of combining in series two PSA units: the first packed with a carbon molecular sieve for kinetically removing argon (kinetic-stage), and the other packed with zeolite to remove the nitrogen (equilibrium-stage) [11]. However, dual-stage processes are far more complex, energy consuming and often unattractive. In addition, there are several applications that require simple, low energy consuming and compact units, such as military aircrafts, submarines or field hospitals [8, 12]. Thus, the production of high-purity oxygen by single-stage PSA/VPSA remained a goal.

More recently, a few new adsorbents, particularly silver-exchanged molecular sieves [13-16], were developed with the ability to selectively adsorb both argon and nitrogen from the air feed. The first silver-exchanged mordenite showing adsorption equilibrium selectivity to argon over oxygen was reported by Wilkerson [17] in 1990. A decade later, in 2002, Air Products and Chemicals, Inc. patented a AgLiLSX (silver lithium low silica-X-type) zeolite, showing argon/oxygen equilibrium selectivity and a high nitrogen adsorption capacity [18]. In 2005, Sebastian and Jasra prepared several silver-exchanged zeolites to assess their argon/oxygen adsorption capacity. These authors concluded that AgA zeolite exhibited very high N_2/O_2 and Ar/O_2 adsorption selectivities compatible with the use in a single-stage PSA/VPSA for producing high-

purity oxygen [19]. Later, Anson et al. [20] and Shi et al. [21] studied a composite adsorbent of Ag-ETS-10 crystals and Ludox HS-40 colloidal silica, weigh ratio of 12:5, and obtained an adsorbent that has high capacity and adsorption selectivity, including argon/oxygen selectivity of 1.28 at 1 bar and 30 $^{\circ}$C.

Despite the developments in argon/oxygen selective adsorbents, very few studies were conducted using PSA or VPSA units with columns packed with them. In 1993, Knaebel and Kandybin disclosed an equilibrium based single-column PSA, using a Ag-mordenite, and obtained a production stream with 99.5+% of oxygen, with a recovery of 6.6 %, from a feed of 95 % of oxygen balanced with argon [22]. In 2003, Air Products and Chemicals, Inc. disclosed a four-step VPSA unit that, according to simulations, could produce a stream of 99.0 % of oxygen from air, using their developed AgLiLSX zeolite adsorbent [23]. The unit operates between 1.4 bar and 0.34 bar at 38 $^{\circ}$C and shows a recovery of 11 %. In 2007, Santos et al. [8] assembled a lab PSA unit with two columns packed with the AgLiLSX zeolite from Air Products. The unit, operating between 1 and 3 bar, produced a stream of 98.7 % of oxygen from air with a recovery of 5.6 %. No reports of single-stage PSA/VPSA units producing 99 % of oxygen from air were found; the very few existing patents and reports refer only to process simulations [8, 21, 23].

In a previous work, the authors conducted a study characterizing the AgLiLSX zeolite adsorbent by Air Products concerning its ability for high-purity oxygen production in a single-stage PSA/VPSA [13]. The study comprises the experimental determination of adsorption isotherms and breakthroughs; performance parameters obtained, such as nitrogen/oxygen selectivity, $\alpha_{N2/O2}$ = 4.98 at 1 bar and 25 $^{\circ}$C, nitrogen working capacity of 0.45 mol·kg^{-1} between 1.4 and 0.2 bar at 25 $^{\circ}$C, and argon/oxygen selectivity, $\alpha_{N2/O2} \geq 1.14$ at low pressure range (below 1.5 bar), show an adsorbent with great potential for producing a high concentration oxygen stream

from air when used in a VPSA unit [13]. The authors also referred the extreme importance of protecting the AgLiLSX zeolite from contaminants such as carbon dioxide or moisture during its use in pressure swing operation [24, 25].

This work studies a high-purity oxygen single-stage VPSA unit, with columns packed with AgLiLSX zeolite by Air Products, to produce 1 L_{STP}·min^{-1} of high-purity oxygen (≥ 99 %) from air.

4.2 Experimental

4.2.1 VPSA units

The main goal of this work was the development of a stand-alone and compact single-stage VPSA unit for the production of 1 L_{STP}·min^{-1} of high-purity oxygen. Such unit should be able to produce ≥ 99 % of oxygen from atmospheric air within a limited volume (0.7 x 0.5 x 0.85 m^3, ≤ 0.3 m^3), be lightweight (≤ 120 kg) and have low energy consumption (≤ 1.1 kW). The AgLiLSX zeolite, used to selectively remove nitrogen and argon, is very sensitive to water vapor and carbon dioxide, deactivating quickly when exposed to atmospheric air. A stand-alone unit should then include a pre-treatment section for removing water vapor and carbon dioxide down to – 40 °C of dew point and to 5 ppm (at 1.4 bar) respectively, thus protecting the AgLiLSX adsorbent [24]. Two VPSA units were assembled and studied.

The design of the above-mentioned stand-alone unit was based on studies conducted in a lab unit fed with air (78 % N_2, 21 % O_2 and 1 % Ar) previously dried (down to – 60 °C of dew point) and carbon dioxide removed (down to ca. 5 ppm). A schematic representation of the lab VPSA unit is presented in Figure 4.1. The adsorption columns were packed with the AgLiLSX zeolite from Air Products and

Chemicals, Inc.; the adsorbent was previously characterized concerning adsorption equilibrium and kinetics, see Figure 4.2 and Table 4.1 [13].

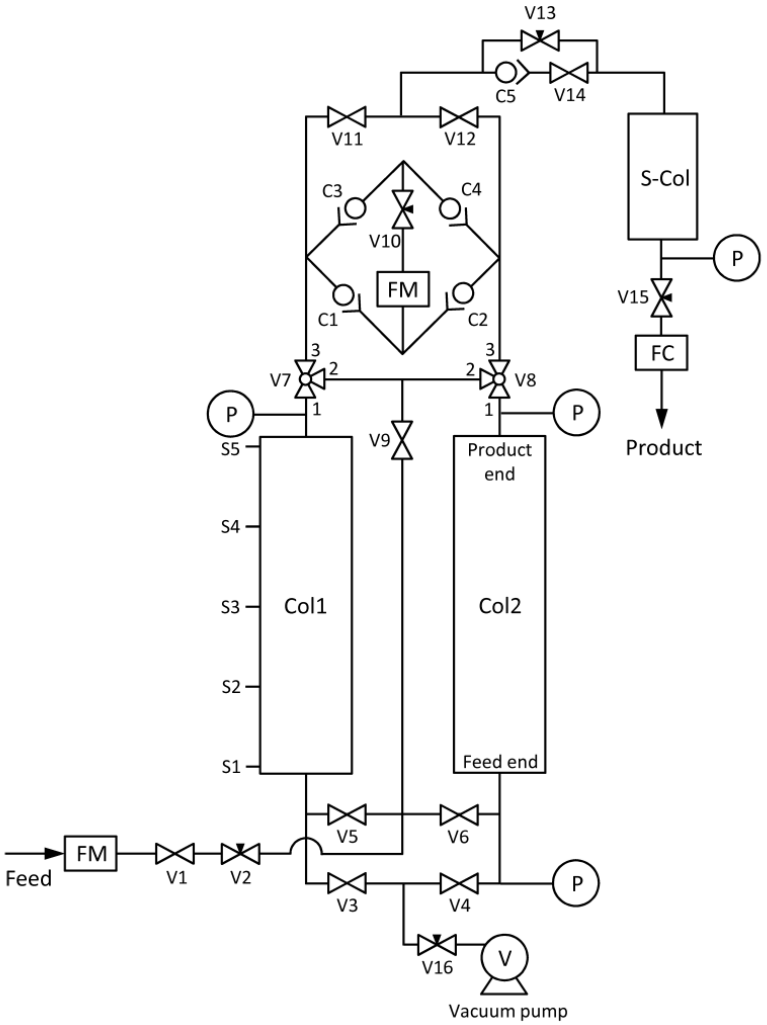

Figure 4.1 – Schematic representation of the lab VPSA unit: Col = column; S-Col = storage column; C1 to C5 = check valves; FM = flow meter; FC = flow controller; P = pressure transducer; S1 to S5 = sampling points; V = vacuum pump; V1 to V16 = electric valves.

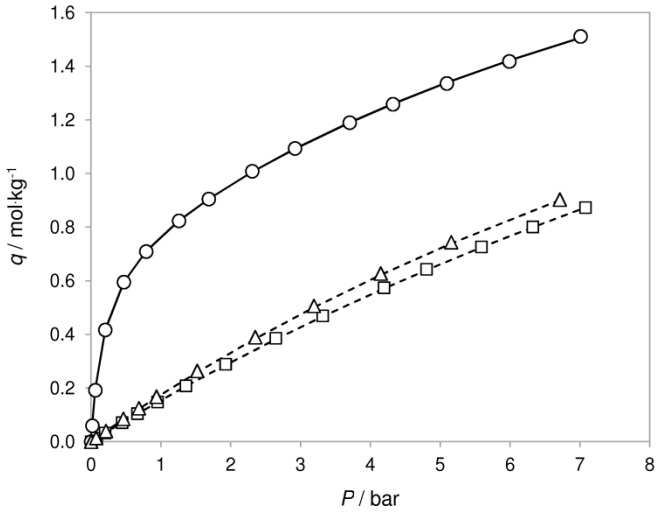

Figure 4.2 – Adsorption isotherms for: ○, nitrogen; □, oxygen; and △, argon, on AgLiLSX at 25 °C.

Table 4.1 – Adsorption equilibrium parameters of nitrogen, oxygen and argon on AgLiLSX [13], NaX zeolite (ZEOX OII), silica (KC-Trockenperlen WS2050) and LiLSX zeolite (Z12-07).

	AgLiLSX	NaX zeolite	silica	LiLSX zeolite
			Nitrogen	
$q_{m,1}$ / mol·kg^{-1}	0.729	3.94	3.29	1.55
$b_1^{\infty} \times 10^{-3}$ / bar^{-1}	0.020	0.042	0.069	0.022
$\Delta H_1 \times 10^3$ / J·mol^{-1}	31.1	19.3	13.1	26.4
$q_{m,2}$ / mol·kg^{-1}	2.66	----	----	2.35
b_2^{∞} / bar^{-1}	0.051	----	----	0.012
ΔH_2 / kJ·mol^{-1}	17.6	----	----	21.5
			Oxygen	
q_m / mol·kg^{-1}	3.79	9.10	7.94	4.80
$b^{\infty} \times 10^{-3}$ / bar^{-1}	0.151	0.098	0.034	0.099
$\Delta H \times 10^3$ / J·mol^{-1}	14.0	12.1	12.4	14.2
			Argon	
q_m / mol·kg^{-1}	3.29	9.56	3.78	6.54
$b^{\infty} \times 10^{-3}$ / bar^{-1}	0.134	0.106	0.081	0.104
$\Delta H \times 10^3$ / J·mol^{-1}	15.0	11.7	12.2	12.7

Table 4.2 – Characteristics of adsorbents and adsorption beds of lab and stand-alone VPSA units.

adsorption beds	Lab VPSA	stand-alone VPSA
bed length, cm	40.4	35.0
bed internal diameter, cm	4.2	12.5
wall thickness, cm	0.2	0.3
L_B/D_B	9.6	2.8
pre-column length, cm	n/a	18.5
pre-column diameter, cm	n/a	12.5
pre-columns silica/NaX zeolite ratio	n/a	1:4
storage column length, cm	17.5	36.0
storage column diameter, cm	8.5	12.5

adsorbent	AgLiLSX	NaX zeolite	Silica	LiLSX zeolite
geometry	spherical	spherical	spherical	spherical
pellet diameter (d_p), mm	1.02	0.80	3.70	1.00
intraparticle voidage (ε_p)	0.605	0.630	0.547	0.580
interparticle voidage (ε_b)	0.36	0.36	0.36	0.36
bulk density (ρ_b), g·cm^{-3}	0.780	0.705	0.636	0.888
macropore radius (r_{pore}), m	3.6 x 10^{-9}	1.7 x 10^{-7}	3.0 x 10^{-9}	4.9 x 10^{-7}
heat capacity (C_{ps}), J·kg^{-1}·K^{-1}	1172	1330	703	1172
thermal conductivity (k_{sx}),W·m^{-1}·K^{-1}	0.3	0.3	0.3	0.3

The characteristics of the designed adsorption beds are listed in Table 4.2. Sampling points (S1 to S5) placed along the beds were used to obtain the concentration profile and history of the column; a mass spectrometer (Pfeiffer, Omnistar) analyzer was used for this purpose. The feed flow rate was measured by a mass flow meter (Bronkhorst High-tech, El Flow F-113C, 0 – 100 L_{STP}·min^{-1}). The purge flow rate was measured using a mass flow meter (Bronkhorst High-tech, El Flow F-111C, 0 – 2 L_{STP}·min^{-1}) and the product flow rate was controlled using a mass flow controller (Bronkhorst High-tech, El-Flow F-201C, 0 – 2 L_{STP}·min^{-1}). The feed, purge and

product flow rates were regulated using needle valves. Several pressure transducers (Druck, PMP 4010, 0 – 7 bar), located along the unit, were used to measure the pressure history inside adsorption beds and at product stream. A set of solenoid and check valves were used to direct the flow according to the adsorption cycle. A vacuum pump (Vacuubrand, model ME 8 NT, 70 mbar) was used during regeneration steps to accomplish required vacuum. The unit includes a storage column that allows to store part of the product and to use it in the backfill step. The product stream concentration was measured using an oxygen analyzer (Servomex, model 5200, from 0 to 100 %, with an accuracy of 0.05 % FS) and a mass spectrometer.

The schematic representation of developed stand-alone VPSA prototype is presented in Figure 4.3. This unit comprises two pre-columns, for pretreating the feed air, packed with a highly-moisture tolerant silica, KC-Trockenperlen WS 2050 from BASF, followed by a special NaX type zeolite, ZEOX OII from Zeochem, in a ratio of 1:4 [24]. The main columns, used to selectively remove nitrogen and argon, were packed with AgLiLSX zeolite. The characteristics of adsorbents and adsorption beds are listed in Table 4.2; the adsorption isotherm parameters are presented in Table 4.1. Sampling points (S1 to S7) were used to obtain the concentration profile and history of the column; a mass spectrometer analyzer was used for this purpose. The prototype unit was fed with atmospheric air (composition of ca. 78 % N_2, 21 % O_2 and 1 % Ar). An air compressor (GAST, model 75R645-P101-H302CX, 7.2 $m^3 \cdot hr^{-1}$ at 1.4 bar, 0.25 kW) was used to feed the unit and the feed flow rate was measured using a volumetric flow meter (SMC, PF2A521-F03-1, 1.2 – 12 $m^3 \cdot hr^{-1}$). The purge and product flow rates, both regulated using needle valves, were measured using also volumetric flow meters (SMC, PFM725-F01-E, 0.03 – 1.5 $m^3 \cdot hr^{-1}$). Several pressure transducers (SMC, ISE10-01-E, 0 – 11 bar) were used to measure the pressure history inside the system during operation. A set of co-axial valves and one check valve were used to direct the flow according to the adsorption cycle. A vacuum pump (Elmo Rietschle, model VTL-10,

11,7 $m^3 \cdot hr^{-1}$ at 150 mbar, 0.37 kW) was used during regeneration steps to attain the required vacuum pressures. The unit includes two pre-columns, two main columns and two storage columns. The first storage column, B-Col, was packed with a LiLSX-type zeolite, Z12-07 from Zeochem, to increase the storage capacity of it. The product stream concentration was measured using an oxygen analyzer and a mass spectrometer.

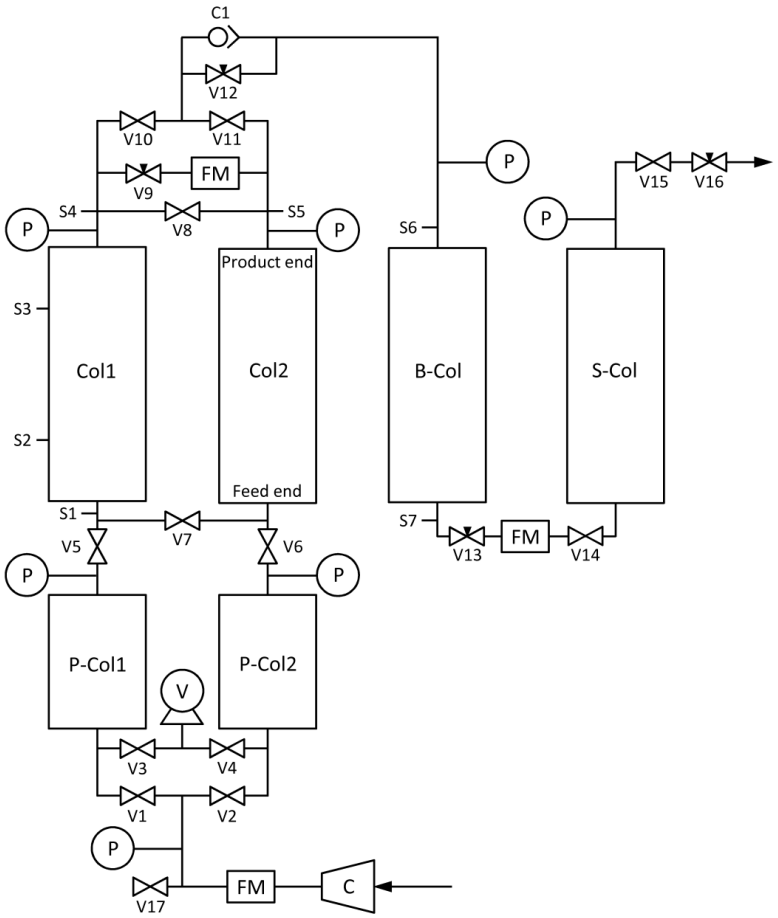

Figure 4.3 – Schematic representation of the stand-alone VPSA prototype: Col = main column; P-Col = pre-column; B-Col = backfill column; S-Col = storage column; C = air compressor, C1 = check valve; FM = flow meter; P = pressure transducer; S1 to S7 = sampling points; V = vacuum pump; V1 to V17 = co-axial and needle valves.

4.2.2 VPSA process description

The VPSA runs a seven-step cycle as shown in Table 4.3. During pressurization (PR), the bed is pressurized cocurrently with feed up to the high operating pressure. Following, during adsorption (AD) high-pressure feed flows through the main bed and nitrogen and argon are selectively retained; an oxygen-enriched stream then leaves the columns as product. During this step, a fraction of the product is used to purge in counter-current the other main bed at the low operating pressure. After the adsorption step is completed the two main beds are connected to equalize the pressure (E). Following, during the evacuation step (VA), the top end of this column is kept closed while vacuum is applied to the feed end. After this step, vacuum is maintained for counter-current purge (VP) with a fraction of the product stream. An equalization step then takes place, and afterward is the backfill (B), in which part of the product stored in the backfill column is used to counter-currently pressurize the adsorption bed. The backfill step, although not new is an unusual step, and it was considered here as part of an innovative solution to increase the oxygen concentration in the product stream up to high-purity levels.

Table 4.3 – Sequence of the seven-step VPSA cycle.

	1	**2**	**3**	**4**	**5**	**6**	**7**	**8**
P-Col 1[¥]	VA	VP			PR		AD	
Col 1	E	VA		VP	E	B	PR	AD
P-Col 2[¥]	PR		AD		VA	VP		
Col 2	E	B	PR	AD	E	VA		VP

[¥] integrated pre-treatment four-step cycle occurs in stand-alone VPSA only.

The cycle described was applied for both lab and prototype units. As previously mentioned, the stand-alone unit also comprises a pre-treatment section for carbon dioxide and moisture removal. The pre-treatment cycle was designed to run

combined with the main cycle, running a four-step cycle: pressurization, adsorption, evacuation and purge under vacuum – Table 4.3. The pre-cycle continuously supplies treated feed air (≤ – 40 °C dewpoint; ≤ 5 ppm CO_2) to the AgLiLSX columns during pressurization and adsorption steps; the pre-beds are vacuum regenerated, with and without a purging stream using dried waste gas from the main columns.

4.2.3 VPSA mathematical model

The main assumptions of the mathematical model used for simulating both VPSA units are:

1) ideal gas behavior
2) negligible radial concentration and temperature gradients
3) non-isothermal and non-adiabatic conditions with gas and solid heat conduction
4) intraparticle mass transport according to linear driving force (LDF) model
5) uniform cross-sectional void fraction
6) adsorption equilibrium described by dual-site multicomponent Langmuir isotherm
7) pressure drop described by Ergun's equation

According to these assumptions, the model can be written as it follows [26]:

Mass balance

$$-\varepsilon_b D_{ax}\frac{\partial^2 c_i}{\partial x^2}+\frac{\partial\left(uc_i\right)}{\partial x}+\varepsilon_t\frac{\partial c_i}{\partial t}+\left(1-\varepsilon_b\right)\rho_s\frac{\partial \overline{q}_i}{\partial t}=0 \qquad (4.1)$$

where c_i is the partial molar concentration, D_{ax} is the axial dispersion coefficient, u is the interstitial molar average velocity, ε_b is the interparticle voidage, ε_t is the total

bed voidage, ρ_s is the adsorbent apparent density, $\overline{q}_i$ is the partial average molar concentration in the adsorbed phase, x is the spatial coordinate, and t is time. The dispersion coefficient, D_{ax}, varies along the length of the bed following the correlation [27]:

$$D_{ax} = 0.73D_m + \frac{u \cdot r_p}{\varepsilon_b \left(1 + 9.49\varepsilon_b D_m / 2u \cdot r_p\right)} \tag{4.2}$$

where r_p is the particle radius. The molecular diffusion coefficient, D_m, is estimated from the Chapman-Enskog equation [28].

The momentum balance is given by the Ergun's equation as follows [29]:

Momentum balance

$$-\frac{\partial P}{\partial x} = \frac{1.5\times10^{-3}\left(1-\varepsilon_b\right)^2}{\left(2r_p\right)^2 \varepsilon_b{}^3}\mu \cdot u + 1.75\times10^{-5} M \rho_g \frac{\left(1-\varepsilon_b\right)}{2r_p \varepsilon_b{}^3} u \cdot |u| \tag{4.3}$$

where P is the total pressure, ρ_g is the gas-phase molar density, μ is the dynamic viscosity, and M is the molecular weight.

The intraparticle mass transfer model is expressed by the linear driving force model [26]:

$$\frac{\partial \overline{q}_i}{\partial t} = k_i \left(q_i - \overline{q}_i\right) \tag{4.4}$$

where q_i is the adsorbed concentration of the component i in the particle inner surface, and k_i is LDF coefficient, here given by the macropore diffusion term as follows [30, 31]:

$$\frac{1}{k_i} = \frac{r_p{}^2}{15\varepsilon_p D_{pi}} \tag{4.5}$$

where ε_p is the intraparticle voidage, and the macropore diffusion coefficient, D_{pi}, obtained from the Bosanquet equation [6]:

$$\frac{1}{D_{pi}} = \tau_p \left(\frac{1}{D_{Ki}} + \frac{1}{D_{mi}} \right) \tag{4.6}$$

where τ_p is the tortuosity factor, and D_{Ki} is the Knudsen diffusion coefficient given by $D_{Ki} = 97 r_{pore} \left(T/M_i \right)^{0.5}$, where r_{pore} is the mean macropore radius and T is the absolute temperature.

The adsorbed amount of each species in the solid-phase is given by the dual-site Langmuir equation, which renders Langmuir when $q_{m,2}$ equals to zero, as follows [32]:

Adsorption equilibrium model

$$q_i = q_{m,1} \frac{b_1 P}{1 + b_1 P} + q_{m,2} \frac{b_2 P}{1 + b_2 P} \tag{4.7}$$

where q_i is the adsorbed concentration of the component i, P is the equilibrium pressure, q_m is the saturation adsorbed concentration and b is the adsorption affinity constant, assumed to vary with temperature, according to the Van't-Hoff equation [32]:

$$b = b^{\infty} \exp\left(\frac{\Delta H}{\Re T} \right) \tag{4.8}$$

where b^{∞} is the adsorption affinity constant at infinite temperature, ΔH is the adsorption heat, and $\Re$ is the ideal gas constant.

Gas-phase energy balance

$$-k_{gx}\varepsilon_b \frac{\partial^2 T_g}{\partial x^2} + C_{vg}\rho_g u \frac{\partial T_g}{\partial x} + \varepsilon_b C_{vg}\rho_g \frac{\partial T_g}{\partial t} + P\frac{\partial u}{\partial x} + h_p \cdot a_p \left(T_g - T_s\right) + \\ + \frac{4h_w}{D_B}\left(T_g - T_w\right) = 0 \tag{4.9}$$

where C_{vg} is the gas-phase heat capacity at constant volume, $a_p = 3\left(1-\varepsilon_b\right)/r_p$ is the specific particle surface per unit volume of the bed, D_B is the internal bed diameter, and T_g, T_s, T_w are, respectively, the gas, solid and internal wall temperatures. The axial gas-phase thermal conductivity coefficient, k_{gx}, is given by

$$k_{gx} = \rho_g C_{pg} \sum_{i}^{nc} D_{ax} y_i \tag{4.10}$$

where C_{pg} is the gas-phase heat capacity at constant pressure, y_i is the mole fraction of component i in the gas phase, and nc is the number of components in the mixture.

The gas-solid heat-transfer coefficient, h_p, is estimated using the Colburn j factor for the heat transfer as follows:

$$h_p = j\rho_g C_{pg} u \cdot Pr^{-2/3} \tag{4.11}$$

where $j = 1.66Re^{-0.51}$ if Re < 190, otherwise $j = 0.983Re^{-0.41}$, and $Pr = \mu C_{pg}/k_{gx}M$ is the Prandl number. Re is the particle Reynolds number, $Re = 2r_p M\rho_g u/\mu$.

The gas-wall heat-transfer coefficient, h_w, is obtained from Nusselt number by the following correlation,

$$h_w = \mathrm{Nu_w}\frac{k_{gx}}{2r_p} \tag{4.12a}$$

$$\mathrm{Nu_w} = \frac{-2\times10^{-6}\cdot \mathrm{Pe_H}^2 + 0.0477\cdot \mathrm{Pe_H} + 22.11}{1+12L_B/D_B\cdot \mathrm{Pe_H}} \tag{4.12b}$$

where $\mathrm{Pe_H} = 2r_pM\rho_gC_{pg}u/k_{gx}$ is the gas-wall heat-transfer Peclet number, and L_B is the bed length.

Solid-phase energy balance

$$-k_{sx}\frac{\partial^2 T_s}{\partial x^2} + \rho_b C_{ps}\frac{\partial T_s}{\partial t} + \rho_b\sum_{i=1}^{nc}\left(\Delta H_i\frac{\partial \overline{q}_i}{\partial t}\right) - h_p\cdot a_p\left(T_g - T_s\right) = 0 \tag{4.13}$$

where k_{sx} is the axial solid-phase thermal conductivity coefficient, C_{ps} is the adsorbent heat capacity, and ρ_b is the adsorbent bulk density.

Wall energy balance

$$-h_w\alpha_w\left(T_g - T_w\right) + h_\infty\alpha_w^{ml}\left(T_w - T_\infty\right) = 0 \tag{4.14}$$

where α_w is the ratio of the internal surface area to the volume of the column wall, α_w^{ml} is the ratio of the logarithmic mean surface area to the volume of the column wall, h_∞ is the wall-ambient heat-transfer coefficient, and T_∞ is the external environmental temperature.

The boundary conditions are formulated separately for each VPSA step and are given bellow [26]:

Boundary conditions for pressurization (PR) step

$$x = 0: \qquad \varepsilon_b D_{ax} \frac{\partial c_i}{\partial x} = u\left(c_i - c_{i,in}\right) \qquad T = T_{in}$$

$$z = L: \qquad \frac{\partial c_i}{\partial x} = 0 \qquad u = 0 \qquad \frac{\partial T}{\partial x} = 0$$

Boundary conditions for adsorption (AD) step

$$x = 0: \qquad \varepsilon_b D_{ax} \frac{\partial c_i}{\partial x} = u\left(c_i - c_{i,in}\right) \qquad T = T_{in}$$

$$x = L: \qquad \frac{\partial c_i}{\partial x} = 0 \qquad u = u_{PROD} \qquad \frac{\partial T}{\partial x} = 0$$

Boundary conditions for top-to-top equalization (E) step

column providing equalization

$$x = 0: \qquad \frac{\partial c_i}{\partial x} = 0 \qquad u = 0 \qquad \frac{\partial T}{\partial x} = 0$$

$$x = L: \qquad \frac{\partial c_i}{\partial x} = 0 \qquad u = u_E \qquad \frac{\partial T}{\partial x} = 0$$

column receiving equalization

$$x = 0: \qquad \frac{\partial c_i}{\partial x} = 0 \qquad u = 0 \qquad \frac{\partial T}{\partial x} = 0$$

$$x = L: \qquad \varepsilon_b D_{ax} \frac{\partial c_i}{\partial x} = u\left(c_i - c_i\big|_{x=L,\ column\ providing\ E}\right) \qquad u = u_E \qquad \frac{\partial T}{\partial x} = 0$$

Boundary conditions for backfill (B) step

$$x=0: \qquad \frac{\partial c_i}{\partial x}=0 \qquad u=0 \qquad \frac{\partial T}{\partial x}=0$$

$$x=L: \qquad \varepsilon_b D_{ax}\frac{\partial c_i}{\partial x}=u\left(c_i-c_i\big|_{x=L,\ column\ runing\ AD}\right) \qquad u=u_B \qquad \frac{\partial T}{\partial x}=0$$

Boundary conditions for evacuation (VA) step

$$x=0: \qquad \frac{\partial c_i}{\partial x}=0 \qquad \frac{\partial T}{\partial x}=0 \qquad u=u_{VA}$$

$$x=L: \qquad \frac{\partial c_i}{\partial x}=0 \qquad u=0 \qquad \frac{\partial T}{\partial x}=0$$

Boundary conditions for purge under vacuum (VP) step

$$x=0: \qquad \frac{\partial c_i}{\partial x}=0 \qquad \frac{\partial T}{\partial x}=0 \qquad u=u_{VP}$$

$$x=L: \qquad \varepsilon_b D_{ax}\frac{\partial c_i}{\partial x}=u\left(c_i-c_i\big|_{x=L,\ column\ runing\ AD}\right) \qquad u=u_{PG} \qquad \frac{\partial T}{\partial x}=0$$

The molar velocities across the valve orifices, during equalization (E) and backfill (B) steps, are described by [8]:

$$u\cdot p=\begin{cases} 2.035\times10^{-2}\,\dfrac{C_v\cdot p^{STP}}{\varepsilon_b A\cdot T^{STP}}\sqrt{\dfrac{p_u^2-p_d^2}{p_d M}}T, & p_d>0.53p_u \\ 2.035\times10^{-2}\,\dfrac{C_v\cdot p^{STP}}{\varepsilon_b A\cdot T^{STP}}\,p_u\sqrt{\dfrac{1}{p_d M}}T, & p_d\le 0.53p_u \end{cases} \tag{4.15}$$

where p_u and p_d are the upstream and downstream pressures, respectively, C_v is the valve parameter, and A is the area of the orifice. The superscript "STP" stands for standard temperature and pressure conditions.

The set of model equations here described was numerically solved using Aspen Adsorption 7.3. The Aspen Adsorption simulator uses the method of lines [33] to solve the time-dependent partial differential equations. The spatial derivatives were discretized over a uniform grid of 40 points using the quadratic upwind differencing scheme; the resulting equations were integrated as a function of the time using subroutine Gear. Physical properties of the components in the process are locally estimated through integration with the Aspen Properties database. The input parameters of the model are listed in Table 4.2.

4.3 Results and discussion

The performance – purity and recovery – of the VPSA units depends on several process variables such as high and low operating pressures (P_H , P_L), temperature of operation (T), equalization (t_E), backfill (t_B), pressurization (t_{PR}) and adsorption (t_{AD}) times, pressurization/depressurization (F_{PR}), equalization (F_E), purge (F_{PG}), backfill (F_B) and product (F_{PROD}) flow rates. Different equalization configurations (top-to-top, bottom-to-bottom, cross and total equalization) also have strong effects on process performance. Simultaneous optimization of all these operating variables is an unreasonable task. Prior to operating cycle optimization, several tests were conducted in a lab unit to select the best equalization configuration. All the above-mentioned configurations were tested, and top-to-top equalization proved to be the

best one, resulting in better performance. Backfill flow rate (F_B) was also evaluated and it was observed that it is not an operating variable with strong influence in the performance of the unit and, because of that, the backfill flow rate should be high enough to allow the equalization between the adsorption column and the backfill column to occur in the shortest time possible. Therefore no restrictions in the backfill flow rate were considered. As to pressurization/depressurization flow rate (F_{PR}), it was not fixed, depending on the high pressure and flow rate delivered by the compressor and the vacuum pump. Product flow rate was set to 0.1 L_{STP}·min^{-1} for the lab unit and 1 L_{STP}·min^{-1} for the stand-alone prototype unit, according to the main goal of this work. The operating temperature was the lab room temperature, ca. 25 °C for the lab unit and slighty higher for the stand-alone unit, between 25–28 °C, due to higher ambient temperature in the prototype surroundings.

4.3.1 Lab VPSA

The lab VPSA unit was studied and optimized using response surface methodology (RSM), which is a combination of mathematical and statistic tools that are effective for studying and modeling processes in which responses are dependent on several operating variables [34]. RSM analysis was conducted using JMP7.0 (Statistical Analysis Software). A central composite design (CCD), which is the most used method for fitting second order models, was selected [34]. The process responses are purity (*Pur*) and recovery (*Rec*) and the factors considered were pressurization (t_{PR}), adsorption (t_{AD}) and backfill (t_B) times, purge flow rate (F_{PG}) and high pressure (P_H). These are key operating variables controlling a VPSA unit. Some of these variables were preset, like equalization time (t_E), set to 4 s, since it was found to be the minimum time necessary to allow beds to equalize completely;

the complete equalization was found to give the best purity and recovery results. The low pressure (P_L) although not fixed, depends on the high pressure, cycle duration and capacity of the vacuum pump, and varies between 0.2 and 0.3 bar. Table 4.4 shows the design operating variables and their levels, and also the values of the preset operating variables.

Table 4.4 – Operating conditions for lab VPSA runs.

feed composition, %	78.0 N_2: 21.0 O_2: 1.0 Ar		
feed flow rate, L_{STP}·min^{-1}	5.0 – 8.6		
pressure low, bar	≤ 0.3		
temperature, $^{\circ}C$	ca. 25		
equalization time, s	4		
product flow rate, L_{STP}·min^{-1}	0.10		
DoE factors	**Min**		**Max**
pressurization time, s	4	-	6
adsorption time, s	6	-	12
backfill time, s	0.5		1.5
purge flow rate, L_{STP}·min^{-1}	0.1	-	0.4
pressure high, bar	1.4	-	1.6

Table 4.5 – Design of experiments and experimental and simulation results of the lab VPSA.

run	t_{PR}	t_{AD}	t_B	F_{PG}	P_H	experimental (%)		RSM predicted (%)		simulation (%)	
	(s)	(s)	(s)	(L·min^{-1})	(bar)	Pur	Rec	Pur	Rec	Pur	Rec
1	4	6	0.5	0.4	1.6	99.10	5.87	99.09	5.89	99.03	6.01
2	7	9	1	0.1	1.5	99.01	7.72	99.02	7.75	99.01	7.67
3	4	12	0.5	0.1	1.6	98.98	7.33	98.98	7.33	98.88	7.31
4	10	12	0.5	0.4	1.6	98.88	8.58	98.89	8.61	98.90	8.59
5	7	9	1	0.25	1.5	99.03	7.76	99.02	7.70	99.04	7.71
6	10	12	1.5	0.4	1.4	98.90	9.49	98.90	9.52	98.92	9.69
7	4	12	1.5	0.4	1.6	98.98	7.36	98.98	7.35	98.96	7.31
8	10	12	1.5	0.1	1.6	98.90	9.06	98.90	9.05	98.89	9.15
9	10	9	1	0.25	1.5	98.95	8.46	98.96	8.50	99.02	8.43
10	10	6	0.5	0.1	1.6	99.02	7.42	99.02	7.42	99.04	7.32
11	7	9	0.5	0.25	1.5	98.99	7.57	99.00	7.58	99.01	7.55
12	7	9	1	0.25	1.4	99.00	8.04	99.01	8.07	99.05	8.00
13	4	12	0.5	0.4	1.4	98.95	7.79	98.96	7.75	98.95	7.84
14	10	6	1.5	0.4	1.6	99.02	7.63	99.02	7.60	99.05	7.66
15	10	6	0.5	0.4	1.4	99.01	7.95	99.00	7.94	99.07	8.12
16	7	9	1	0.25	1.5	99.03	7.68	99.02	7.70	99.04	7.71
17	4	9	1	0.25	1.5	99.04	7.01	99.04	6.98	99.07	6.97
18	7	9	1	0.25	1.5	99.02	7.70	99.02	7.70	99.04	7.71
19	7	9	1.5	0.25	1.5	99.02	7.80	99.02	7.81	99.06	7.72
20	7	9	1	0.4	1.5	99.02	7.59	99.03	7.57	99.03	7.62
21	7	12	1	0.25	1.5	98.98	8.39	98.96	8.38	98.95	8.40
22	4	12	1.5	0.1	1.4	98.98	8.26	98.98	8.29	99.00	8.20
23	4	6	1.5	0.1	1.6	99.11	6.15	99.11	6.16	99.10	6.15
24	7	9	1	0.25	1.5	99.03	7.69	99.02	7.70	99.04	7.71
25	10	12	0.5	0.1	1.4	98.83	9.63	98.82	9.61	98.86	9.51
26	7	9	1	0.25	1.6	99.03	7.44	99.03	7.42	99.03	7.37
27	4	6	0.5	0.1	1.4	99.02	6.53	99.03	6.54	99.01	6.56
28	7	6	1	0.25	1.5	99.07	6.98	99.08	7.01	99.07	6.95
29	10	6	1.5	0.1	1.4	99.02	8.35	99.02	8.31	99.04	8.40
30	4	6	1.5	0.4	1.4	99.10	6.61	99.10	6.62	99.14	6.64

Table 4.5 summarizes the CCD runs and the experimental results obtained for each run. Runs 5, 16, 18 and 24 are center point replicates for assessing the experimental reproducibility. Second order polynomial models were fitted for purity and recovery from the CCD results, which describe the effect of the selected factors on the process responses. Model parameters with *p*-values higher than 0.15 were eliminated [35].

$$Pur = a_0 + a_1 \cdot t_{PR} + a_2 \cdot t_{AD} + a_3 \cdot t_B + a_4 \cdot F_{PG} + a_5 \cdot P_H + a_6 \cdot t_{PR} \cdot t_{AD} + \\ + a_7 \cdot t_B \cdot F_{PG} + a_8 \cdot t_B \cdot P_H + a_9 \cdot F_{PG} \cdot P_H + a_{10} \cdot {t_{PR}}^2 + a_{11} \cdot {t_B}^2 \quad (4.16)$$

$$Rec = a_0 + a_1 \cdot t_{PR} + a_2 \cdot t_{AD} + a_3 \cdot t_B + a_4 \cdot F_{PG} + a_5 \cdot P_H + a_6 \cdot t_{PR} \cdot P_H + \\ + a_7 \cdot t_{AD} \cdot P_H + a_8 \cdot t_{AD} \cdot F_{PG} + a_9 \cdot F_{PG} \cdot P_H + a_{10} \cdot {t_{PR}}^2 + a_{11} \cdot {P_H}^2 \quad (4.17)$$

where a_0 to a_{11} parameters of eq. (4.16) and eq. (4.17) are given in Table 4.6.

Table 4.6 – Parameters of second order polynomial equations (4.16) and (4.17).

	Pur *eq (16)*	*Rec* *eq (17)*
a_0	98.3261	14.8070
a_1	0.0284	0.2872
a_2	- 0.0144	0.3998
a_3	0.4454	0.2267
a_4	0.9917	- 2.3102
a_5	0.4625	-12.3768
a_6	$- 8.33 \times 10^{-4}$	- 0.0521
a_7	- 0.0833	- 0.0979
a_8	- 0.2000	- 0.0931
a_9	- 0.5833	1.7083
a_{10}	- 0.0025	0.0031
a_{11}	- 0.0484	3.3226

Table 4.7 – Optimum conditions and results predicted by RSM, simulation and experimentally tested on lab VPSA.

run	t_{PR} (s)	t_{AD} (s)	t_E (s)	t_B (s)	F_{PG} (L_{STP}·min^{-1})	P_H (bar)	experimental (%)		RSM predicted (%)		simulation (%)		Productivity (m^3·hr^{-1}·ton^{-1})
							Pur	Rec	Pur	Rec	Pur	Rec	
31	5	6	4	1.2	0.1	1.6	99.12	6.35	99.11	6.33	99.07	6.25	7.31
32	5.5	6	4	1.5	0.4	1.4	99.12	6.49	99.10	7.00	99.12	7.03	6.70
33	9	8.5	4	1.5	0.4	1.4	99.00	8.34	99.01	8.47	99.05	8.57	7.03
34	4	6	4	1.5	0.3	1.4	99.09	6.58	99.10	6.67	99.15	6.69	7.01

An analysis of variance of the model was performed and *p*-values lower than 0.0001 were obtained indicating that the polynomial model has a very high significance. The fitting models were used to interpolate the response values for purity and recovery, and compared with the experimental ones – parity plots (Table 4.5). The determination coefficients, R^2, are very close to unity for both purity, $R^2 = 0.992$, and recovery, $R^2 > 0.999$, indicating that the empiric models accurately describe the experimental results.

Table 4.5 shows product oxygen concentrations of 99.1+% at reasonable recoveries for various operating conditions. Second order empirical models given by the JMP software were used to find the optimum conditions for purity and recovery (Table 4.7). The maximum purity obtained was 99.12 % with 6.4 % of recovery, when $t_{PR} = 5$ s, $t_{AD} = 6$ s, $t_E = 4$ s, $t_B = 1.2$ s, $P_H = 1.6$ bar, $P_L = 0.25$ bar and $F_{PG} = 0.1\ \mathrm{L_{STP}} \cdot \mathrm{min}^{-1}$ (run 31). For the conditions of run 33 ($t_{PR} = 9$ s, $t_{AD} = 8.5$ s, $t_E = 4$ s, $t_B = 1.5$ s, $P_H = 1.4$ bar, $P_L = 0.2$ bar and $F_{PG} = 0.4\ \mathrm{L_{STP}} \cdot \mathrm{min}^{-1}$), high-purity oxygen, 99.0 %, and higher recovery, 8.3 % are obtained. The productivity of the unit was computed from the ratio between the product flow rate and the amount of adsorbent used. Reasonable productivity of ca. 7.0 $m^3 \cdot hr^{-1} \cdot ton^{-1}$ was obtained.

ASPEN was used to simulate the experimental results. The results obtained by ASPEN simulations are summarized in Table 4.5 and Table 4.7 and can be compared with RSM predicted ones and with experimental results. Figure 4.4 presents the simulated and experimental pressure history for run 31; vertical dashed lines mark the cycle steps. The simulated profile on this figure was obtained with ASPEN simulations. By analyzing Table 4.5, Table 4.7 and Figure 4.4 it can be concluded that the ASPEN phenomenological simulator is able to accurately represent the experimental results.

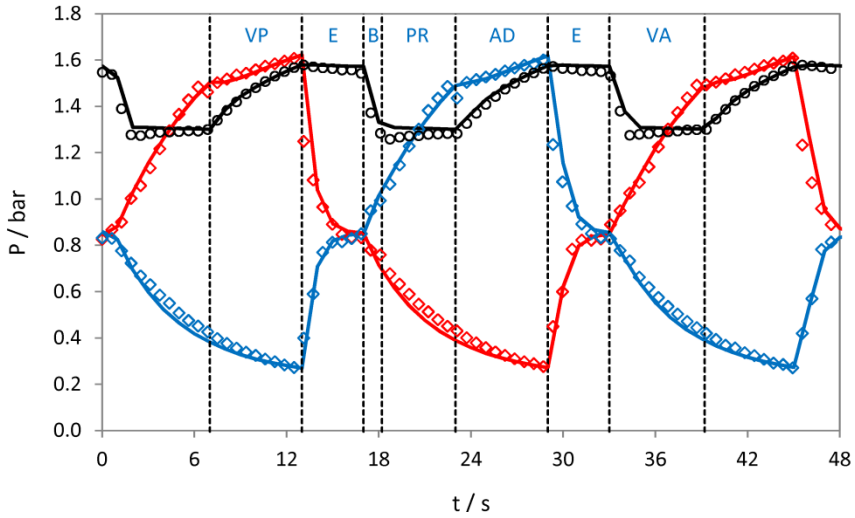

Figure 4.4 – Simulated (solid line) and experimental (dots) pressure history inside the columns for run 31. Red dots (◇) refer to Col1; blue dots (◇) refer to Col2; black dots (○) refer to S-Col. Vertical dashed lines mark the cycle steps; the upper legend refers to Col2 steps.

Oxygen concentration history inside the adsorption bed was recorded using a mass spectrometer connected to the five sampling points placed along one of the main beds (S1 to S5, see Figure 4.3). Figure 4.5 plots the concentration profiles obtained during one cycle of run 31. The axial position goes from 0 (feed end) to 1 (product end). The adsorption cycle steps are marked with different colors for readability. Figure 4.5 shows that the oxygen concentration inside adsorption beds increases along the bed, with the maximum obtained during the AD step at the column product end. This figure also shows the importance of VP, E, and B steps on removing the impurities and increasing oxygen concentration along the bed. The complete purge of the impurities adsorbed during PR and AD steps are essential to obtain a high-purity product.

The ASPEN simulator was used to simulate the temperature profile inside the column during one cycle of run 31 – see Figure 4.6. Again, the axial position goes from 0 (feed end) to 1 (product end). The temperature variation inside the column is ca. 4.5 $^{\circ}$C so that the process could be assumed isothermal.

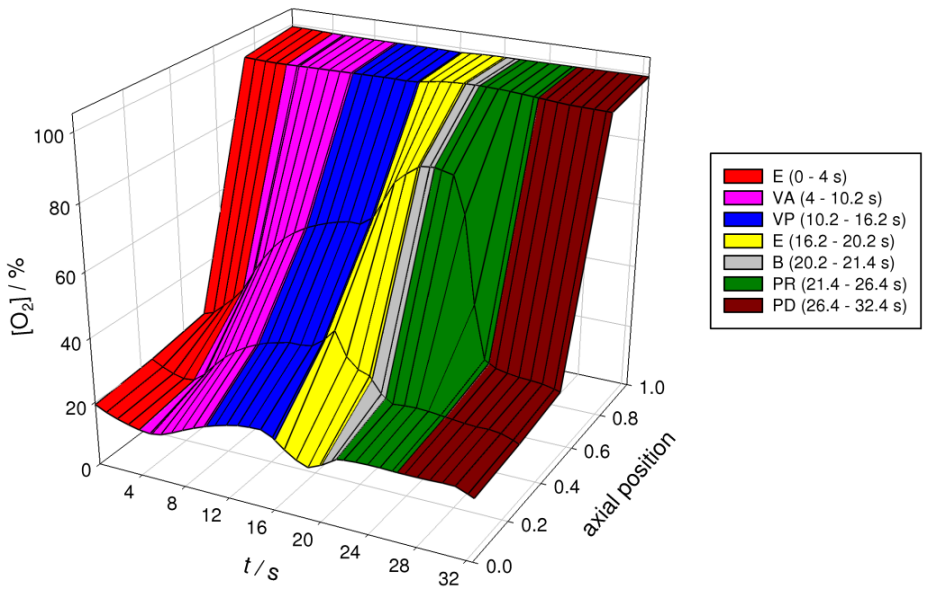

Figure 4.5 – Experimental oxygen concentration 3D profile inside the column during one cycle of run 31. Axial position goes from 0 (feed end) to 1 (product end). Different steps are marked with different colors according to the figure label.

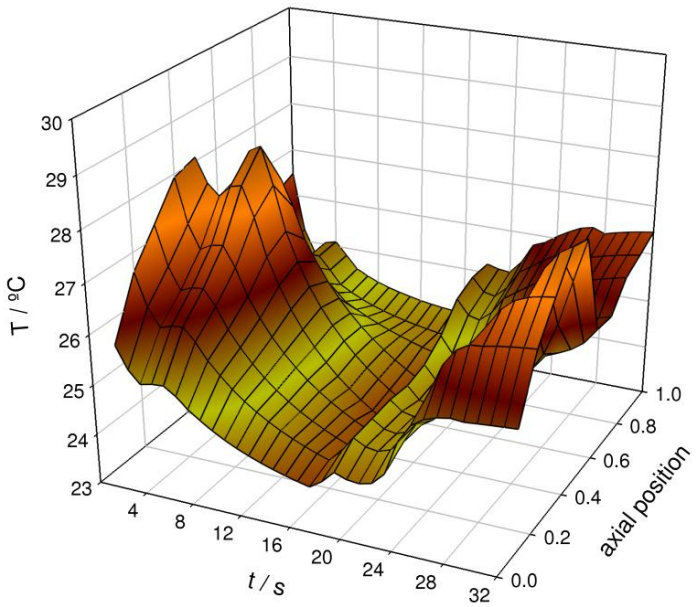

Figure 4.6 – Simulated temperature 3D profile inside the column during one cycle of run 31. Axial position goes from 0 (feed end) to 1 (product end).

4.3.2 Stand-alone VPSA prototype

As previously referred, the stand-alone VPSA prototype was designed and assembled based on the results obtained in the lab unit. This stand-alone unit was designed to produce a steam of 1 L_{STP}·min^{-1} with 99+% oxygen from air. The scale-up was made to obtain equal or better productivity than the lab unit, for the same conditions of purity and recovery. Also, the stand-alone unit was designed to minimize overall size, weight and power consumption. The length to diameter ratio (L_B/D_B) of the lab size adsorbent beds is 9.6, unfeasible in a prototype scale, since the unit should be compact and obey tight dimensions. The main columns of the stand-alone VPSA unit have length to diameter ratio of 2.8. The small L_B/D_B value is ideal for minimizing pressure drop especially during the evacuation steps – an aspect of critical relevance. The L_B/D_B ratio does not affect the separation if axial dispersion and temperature radial gradients can be neglected and for high bulk-particle mass transfer rates. Cruz et al. showed that isothermal operation is a reasonable assumption for oxygen separations from air [26], so this was considered here. This assumption is supported by the simulation results on the lab-scale unit (Figure 4.6).

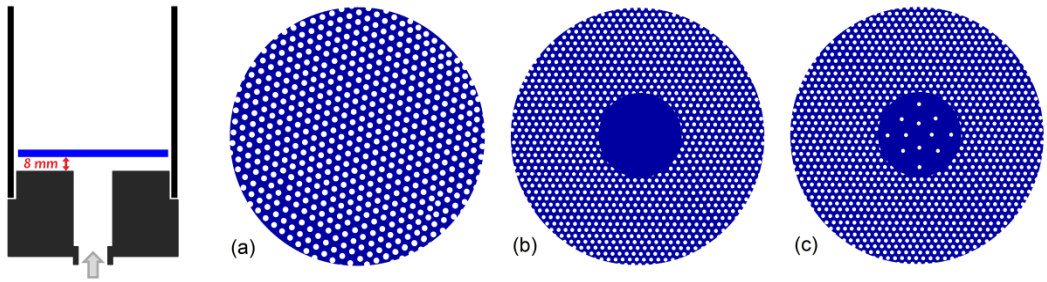

Figure 4.7 – Schematic representation of the column feed end, with the distributor indicated with blue color and the distributors tested showing: (a) central preferential air flowing; (b) peripheral preferential air flowing; and (c) even gas distribution.

Since even gas distribution over the cross section of the adsorption column is critical for achieving the high separation, several distributors configurations were

tested for high and low flow rates in both ends of the adsorption columns. Figure 4.7 illustrates the feed end of an adsorption bed; when feeding the column, air contacts first with the central part of the adsorbent cross section spreading afterward to cover the entire cross section, resulting in stagnant volumes. The same figure shows several distributors tested. From left to right in Figure 4.7: (a) the first configuration tested showed central preferential air flowing; (b) the second configuration tested showed central preferential air flowing only for high velocities; after several tests, (c) the optimum configuration resulted in an even gas distribution for both low and high velocities, provided that a space of 8 mm is given between the flange and the distributor. Figure 4.8 shows that the oxygen concentration profiles measured near to the feed end of the column, at the center and periphery of the cross section, overlap. The same was observed through the column.

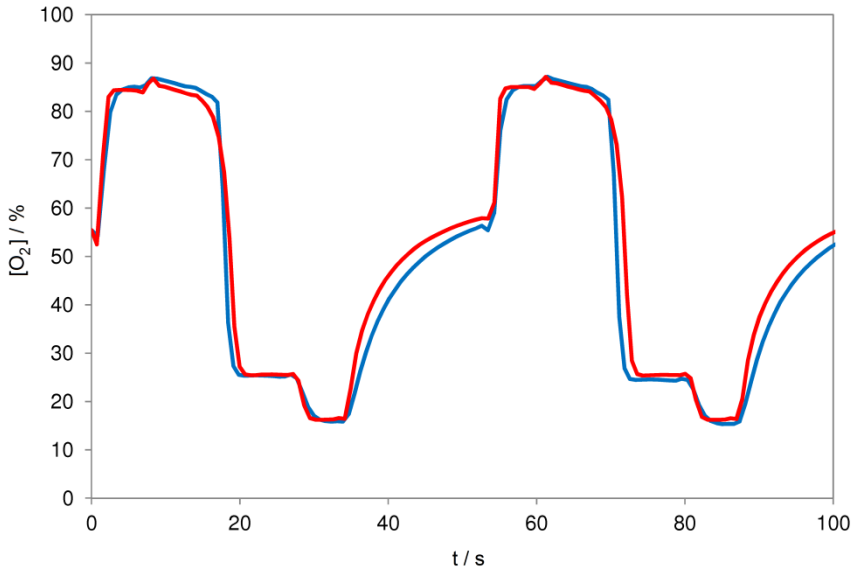

Figure 4.8 – Experimental oxygen concentration profiles measured, near the column feed end (sampling point S2): blue line, at the center of the column; and red line, at the periphery of the column.

The stand-alone VPSA performance – purity (*Pur*) and recovery (*Rec*) – was optimized using the phenomenological model. The critical operating variables controlling the process are pressurization (t_{PR}) and adsorption (t_{AD}) times and purge flow rate (F_{PG}). Based on lab unit experiments some operating variables were preset, such as backfill time (t_B), since it was observed that the maximum product purity occurs at maximum backfill time (Table 4.7); thus, t_B was set to 2 s since it is the time required to allow the adsorption bed and the backfill column to completely equalize the pressure. The high pressure (P_H) was set to 1.4 bar based on lab unit experiments and because the low pressure (P_L), set to 0.3 bar, is limited by the P_H since the vacuum pump power was preset. Concerning the prototype unit, equalization flow rate was found to be an extremely import operating variable, since it significantly affects the performance of the unit. The equalization valve coefficient, C_V, was found to be crucial and it was optimized. After several tests, the valve was modified to allow a complete equalization between adsorption beds in 2.5 s, and the equalization time (t_E) was therefore fixed. The preset operating conditions for the stand-alone VPSA runs are summarized in Table 4.8.

Table 4.8 – Preset operating conditions for stand-alone VPSA runs.

feed composition, %	78.0 N_2: 21.0 O_2: 1.0 Ar
feed flow rate, L_{STP}·min^{-1}	58 – 72
pressure high, bar	1.4
pressure low, bar	≤ 0.3
Temperature, ºC	25 – 28
Equalization step time, s	2.5
Backfill step time, s	2.0
Product flow rate, L_{STP}·min^{-1}	1.0

Table 4.9 presents the experimental and ASPEN simulation results for several runs. Purity oxygen concentrations of 99+% at reasonable recoveries can be observed for almost all operation conditions tested. Table 4.9 shows that the ASPEN simulator was able to represent accurately the experimental results (determination coefficients, R^2, of the parity plots are 0.898 and 0.963 for purity and recovery, respectively).

Table 4.9 – Experimental and simulation results of the stand-alone VPSA unit.

run	t_{PR}	t_{AD}	F_{PG}	experimental (%)		simulation (%)	
	(s)	(s)	(L_{STP}·min^{-1})	Pur	Rec	Pur	Rec
1	4	10	0.8	99.07	6.01	99.07	6.03
2	4	12	0.5	99.01	6.68	99.03	6.45
3	4	12	1.1	99.05	6.37	99.02	6.38
4	4	14	0.8	98.98	6.93	99.01	7.09
5	5.5	8	0.5	99.12	5.81	99.12	5.49
6	5.5	8	0.8	99.10	5.43	99.09	5.59
7	5.5	10	0.5	99.13	6.19	99.12	6.22
8	5.5	10	1.1	99.06	6.09	99.03	6.09
9	5.5	12	0.8	99.08	7.46	99.09	7.04
10	5.5	14	0.5	99.01	7.37	99.00	7.41
11	5.5	14	1.1	99.01	7.24	99.04	7.43
12	7	10	0.8	99.07	6.79	99.06	6.62
13	7	12	0.5	99.06	7.18	99.04	7.17
14	7	12	1.1	98.99	7.13	99.01	7.14
15	7	14	0.8	98.99	7.97	99.02	7.98

ASPEN simulations were conducted to study the effect of operating variables pressurization time (t_{PR}), adsorption time (t_{AD}) and purge flow rate (F_{PG}), in the product purity (*Pur*) and recovery (*Rec*) (see Figure 4.9 – 4.14). The three variables

studied have strong influence on product purity. Figure 4.9 shows a pronounced parabolic curvature describing the combined influence of t_{PR} and t_{AD} in the purity. As it can be seen, purity slowly increases with t_{AD}, reaching a maximum purity value when t_{AD} is equal to 10 s; and over that point, higher t_{AD} causes an abrupt decrease in the purity. An optimum t_{AD} value allows sufficient time for the oxygen concentration front to leave the column and it is short enough for preventing Ar front to breakthrough. Similar behavior is observed for t_{PR}, with a (local) maximum purity, 99.10 %, obtained for t_{PR} = 5.5 s and t_{AD} = 10 s (with F_{PG} = 0.8 L_{STP}·min^{-1}). Similarly, Figure 4.13 shows that the optimum purity, ca. 99.12 %, can be obtained when F_{PG} is between 0.5 – 0.6 L_{STP}·min^{-1}, and t_{AD} is 10 s (with t_{PR} = 5.5 s). This figure shows that, for higher t_{AD} values, F_{PG} has no significant influence on the purity; however, for smaller t_{AD} values, the purity depends considerably on F_{PG}, increasing as it decreases. Thus, a small part of the product should be used to purge the beds; this is crucial to remove contaminants during evacuation steps allowing better performance. Small F_{PG} values are enough to guarantee high-purity product if vacuum conditions are sufficient to purge the beds, and the loss of F_{PG} during this step causes significant decrease in purity (Figure 4.13). Concerning recovery, Figure 4.12 and Figure 4.14 show that variations in the F_{PG}, within the range studied, do not affect significantly the product recovery; product recovery increases with t_{PR} and mainly with t_{AD} (see Figure 4.10). This occurs because the increase of t_{PR} and t_{AD} allow a more thorough retention of oxygen, avoiding being vented.

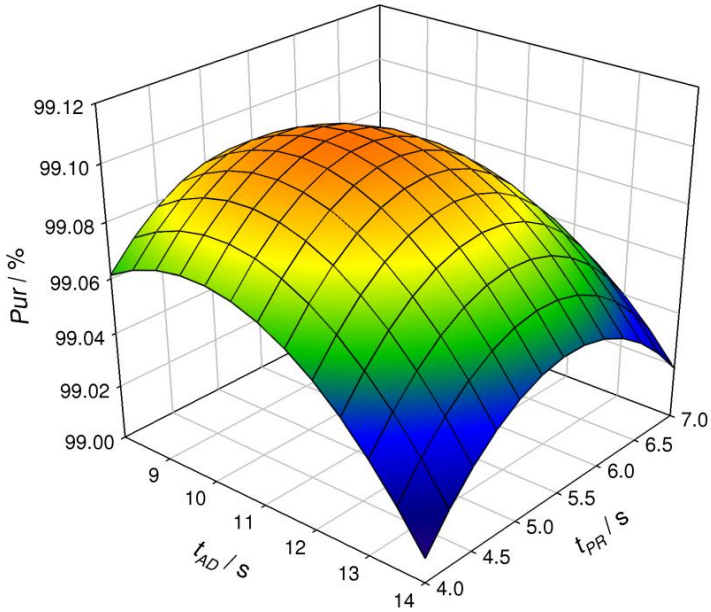

Figure 4.9 – Purity as a function of pressurization and adsorption times, with purge flow rate kept constant at 0.8 L_{STP}·min^{-1}.

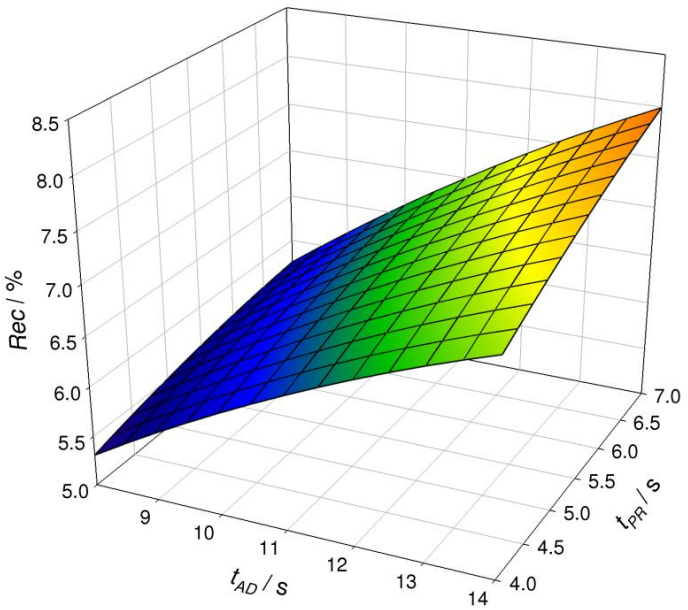

Figure 4.10 – Recovery as a function of pressurization and adsorption times, with purge flow rate kept constant at 0.8 L_{STP}·min^{-1}.

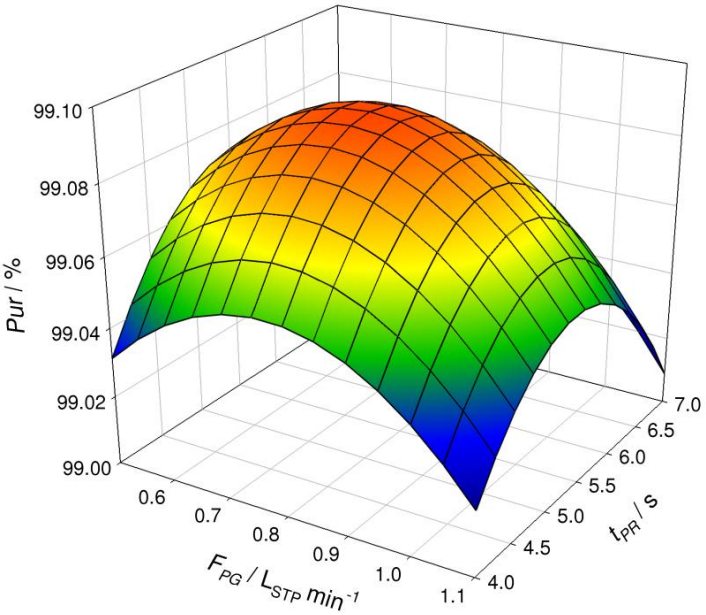

Figure 4.11 – Purity as a function of pressurization time and purge flow rate; adsorption time was kept constant at 12 s.

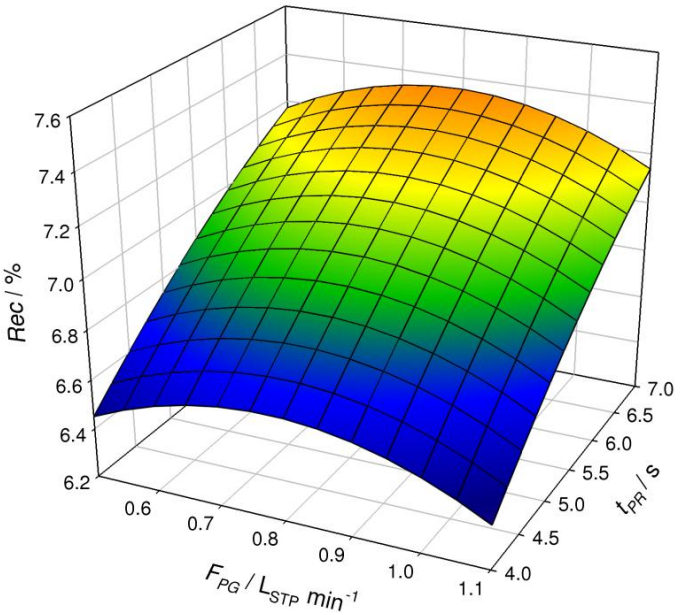

Figure 4.12 – Recovery as a function of pressurization time and purge flow rate; adsorption time was kept constant at 12 s.

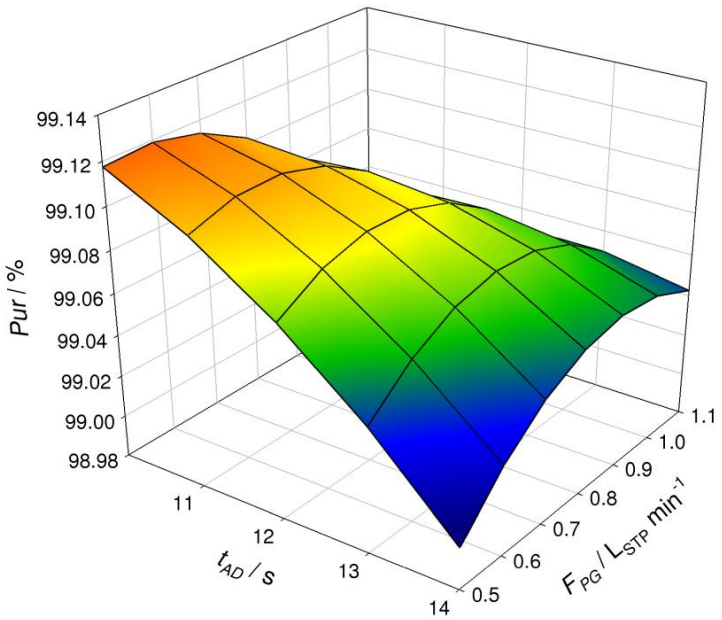

Figure 4.13 – Purity as a function of adsorption time and purge flow rate; pressurization time was kept constant at 5.5 s.

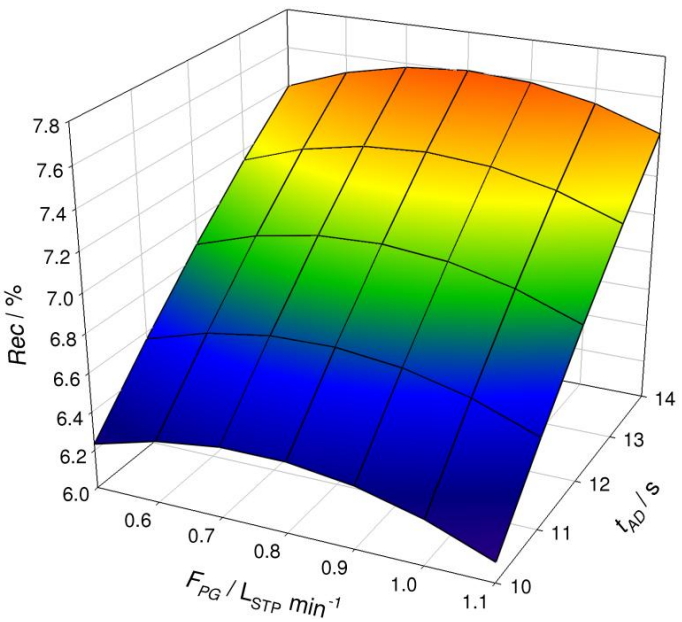

Figure 4.14 – Recovery as a function of adsorption time and purge flow rate; pressurization time was kept constant at 5.5 s.

According to ASPEN simulator, the maximum oxygen purity that can be expected is 99.12 % (with 6.2 % of recovery) when t_{PR} is 5.5 s, t_{AD} is 10 s and F_{PG} is 0.5 L_{STP}·min^{-1} (run 7). These conditions were experimentally tested (run 7) and a slightly better purity was obtained, 99.13 % (with 6.2 % of recovery). Also, run 15 shows that high-purity oxygen, ≥ 99.0 %, can still be obtained with a higher recovery, 8.0 %, when t_{PR} is 7 s, t_{AD} is 14 s and F_{PG} is 0.8 L_{STP}·min^{-1}; experimental and simulated values are equal. The productivity of the unit was computed from the ratio between the product flow rate and the amount of AgLiLSX used and a productivity of ca. 8.97 m^3·hr^{-1}·ton^{-1} was obtained. This is similar to the productivity reported by Santos et al. [8] in a simulation study of a single-stage lab PSA unit using AgLiLSX for the production of 99 % of oxygen, which is 14 m^3·hr^{-1}·ton^{-1}. When compared to the productivity of a two-stage VPSA for the production of 97 % of oxygen, 0.21 m^3·hr^{-1}·ton^{-1}, one can find the productivity here obtained considerably higher [3].

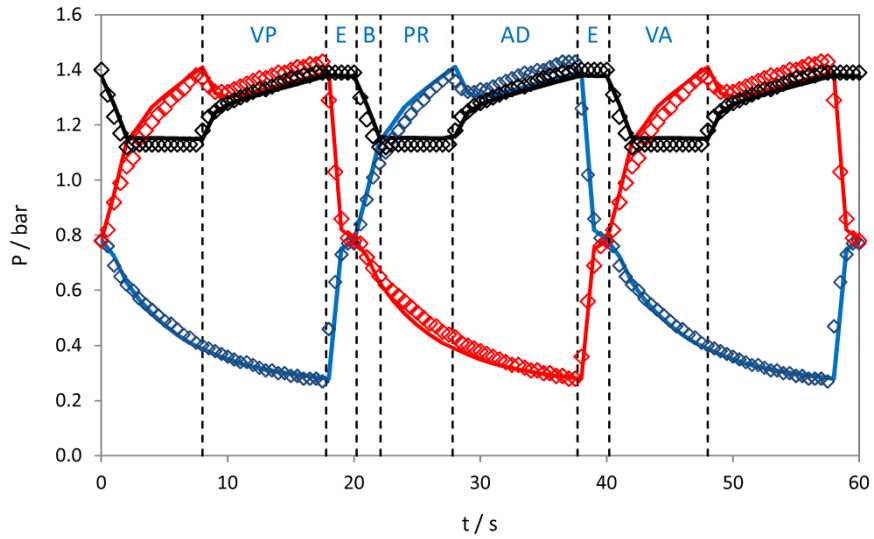

Figure 4.15 – Simulated (solid line) and experimental (dots) pressure history inside the main-columns for run 7. Red dots (◇) refer to Col1; blue dots (◇) refer to Col2; black dots (◆) refer to B-Col. Vertical dashed lines mark the cycle steps; the upper legend refers to Col2 steps.

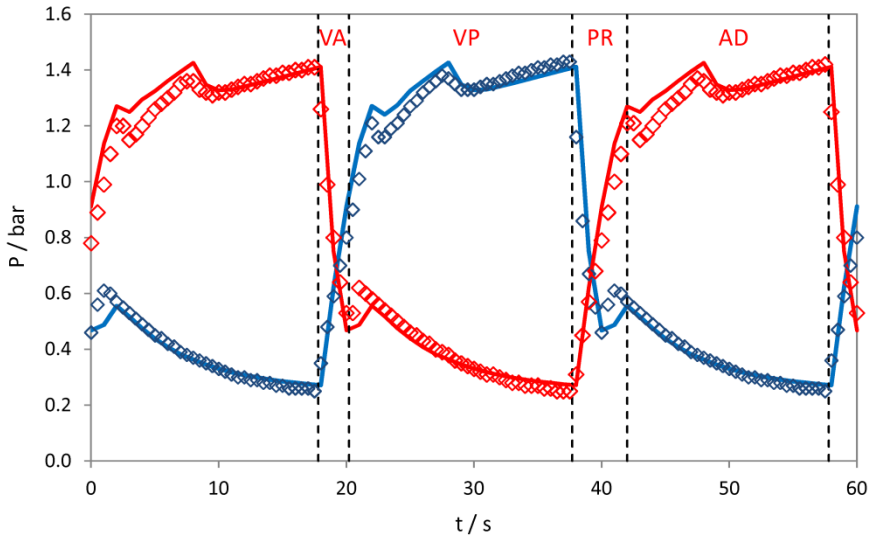

Figure 4.16 – Simulated (solid line) and experimental (dots) pressure history inside the pre-columns for run 7. Red dots (◇) refer to P-Col1; blue dots (◇) refer to P-Col2. Vertical dashed lines mark the pre-cycle steps; the upper legend refers to P-Col2 steps.

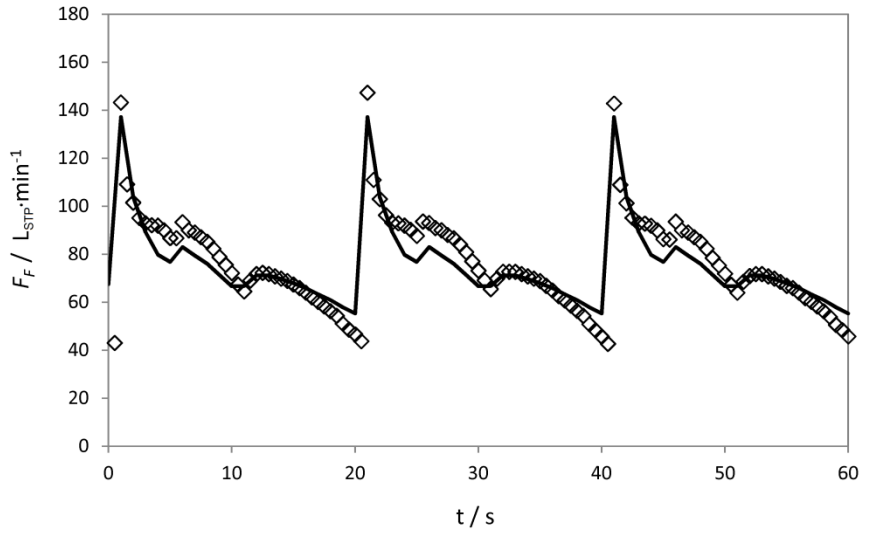

Figure 4.17 – Simulated (solid line) and experimental (dots) feed flow rate measured for run 7.

Figure 4.15 and Figure 4.16 show experimental and ASPEN simulated pressure histories for run 7 in both main-columns and pre-columns, respectively; vertical dashed lines mark the cycle steps. The stand-alone VPSA prototype operates between 1.4 and 0.25 bar. Figure 4.17 shows the experimental and simulated feed flow rate for the same run; an average feed flow rate of 76 $L_{STP} \cdot min^{-1}$ was computed. Oxygen concentration profile inside the adsorption bed for run 7 was simulated, using ASPEN, and it is plotted in Figure 4.18. Oxygen concentration increases through the column and the maximum oxygen concentration is observed near to the top of the column. Equalization step plays a key role on this cycle, increasing oxygen concentration, thus preparing the bed to produce high-purity product. The oxygen concentration of the feed stream during the pressurization step is slightly above 21 % because of the oxygen enrichment by pre-columns. Figure 4.19 plots the oxygen concentration profile inside the pre-column for run 7. This figure shows that the pre-cycle, besides removing both carbon dioxide and moisture from the feed stream, slightly enriches the feeding stream in oxygen. The experimental average oxygen concentration of the feed stream to the main columns (packed with AgLiLSX zeolite) is 24.7 % and the simulated one is 25.1 %.

Figure 4.20 shows the temperature profile inside the adsorption bed for run 7, according to ASPEN simulations. The operating temperature inside the bed varies between 24.2 $^{\circ}C$ - 30.8 $^{\circ}C$, corresponding to an amplitude of ca. 6.6 $^{\circ}C$, slightly greater than the temperature amplitude observed in the lab VPSA, where the amplitude was ca. 4.5 $^{\circ}C$ (Figure 4.6). This can be explained due to the large difference in the diameter of the adsorption columns of the two units, since smaller diameter columns dissipate heat more easily.

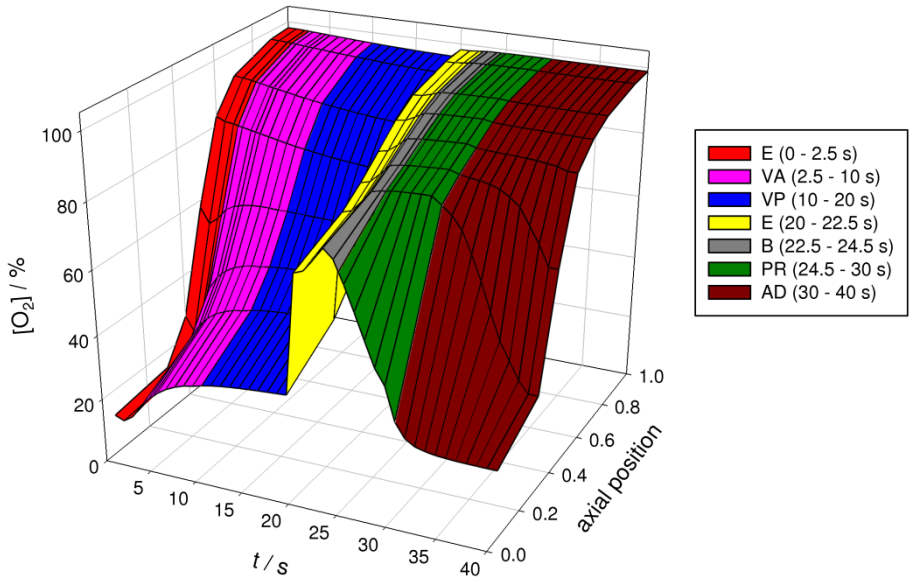

Figure 4.18 – Simulated oxygen concentration 3D profile inside the main column during one cycle of run 7. Axial position goes from 0 (feed end) to 1 (product end). Different steps are marked with different colors according to the figure label.

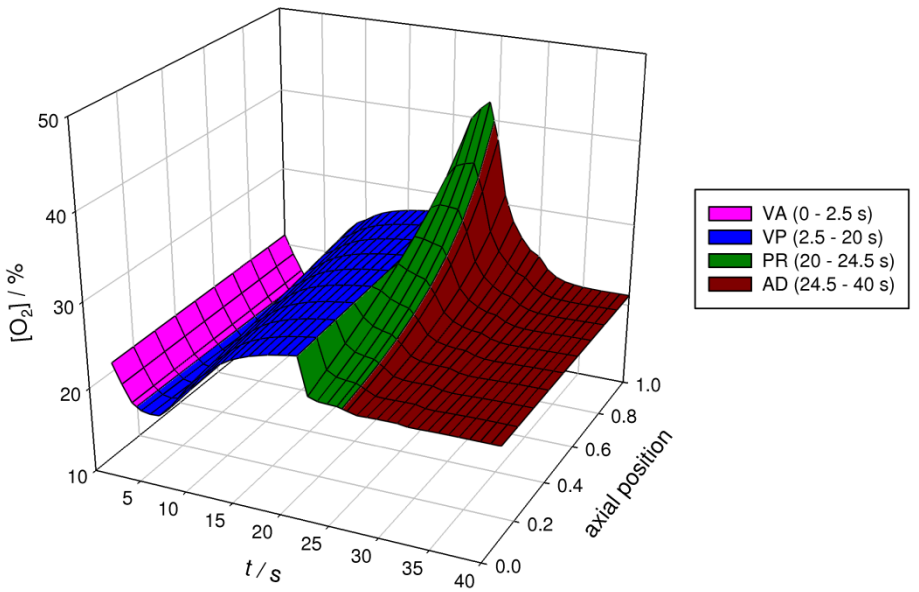

Figure 4.19 – Simulated oxygen concentration 3D profile inside the pre-column during one cycle of run 7. Axial position goes from 0 (feed end) to 1 (product end). Different steps are marked with different colors according to the figure label.

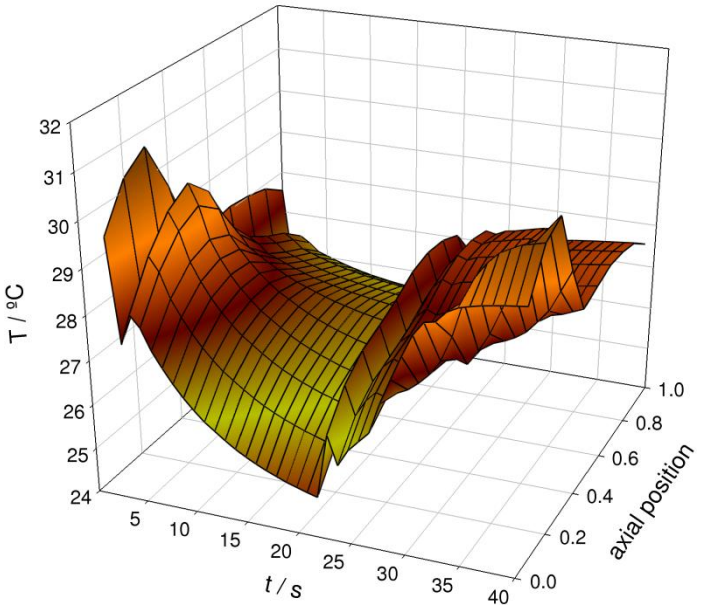

Figure 4.20 – Simulated temperature 3D profile inside the main column during one cycle of run 7. Axial position goes from 0 (feed end) to 1 (product end).

The results obtained in the stand-alone unit (99.13 % oxygen, with 6.2 % of recovery and a productivity of 9.0 $m^3 \cdot hr^{-1} \cdot ton^{-1}$) are consistent with the ones obtained in the lab unit (99.12 % oxygen, with 6.4 % of recovery and a productivity of 7.3 $m^3 \cdot hr^{-1} \cdot ton^{-1}$). The differences in the productivity of the two units are related to the oxygen enrichment by the pre-columns of the stand-alone unit. These pre-beds, crucial in a stand-alone unit to prevent the contamination of AgLiLSX with carbon dioxide and moisture, somewhat enrich the oxygen concentration in the feed stream, slightly improving the separation.

4.4 Conclusions

A single-stage VPSA for the production of high-purity oxygen from air was designed, built and studied using AgLiLSX zeolite by Air Products. A lab VPSA unit was designed for producing 0.1 L_{STP}·min^{-1} of 99+% of oxygen stream from air (previously dried and carbon dioxide removed). The unit, comprises two adsorption beds packed with AgLiLSX zeolite, operating between 0.2 and 1.6 bar at room temperature running a seven-step cycle. The cycle comprises the following steps: pressurization, adsorption, top-to-top equalization, evacuation, purge under vacuum, and backfill. The unit was optimized using RSM methodology and an optimum purity of 99.12 % oxygen from air, with 6.4 % of recovery and productivity of 7.3 m^3·hr^{-1}·ton^{-1} was obtained when the following operation conditions were observed: $t_{PR} = 5\ \text{s}$, $t_{AD} = 6\ \text{s}$, $t_E = 4\ \text{s}$, $t_B = 1.2\ \text{s}$, $P_H = 1.6\ \text{bar}$, $P_L = 0.25\ \text{bar}$ and $F_{PG} = 0.1\ \text{L}_{\text{STP}} \cdot \text{min}^{-1}$. The unit was also simulated using ASPEN simulator, which represented accurately the experimental results.

Based on studies conducted in the lab unit, a compact (dimensions of 0.7 x 0.5 x 0.85 m^3, 0.3 m^3 vol.), lightweight (120 kg) and low energy consuming (average power consumption of 1.0 kW) stand-alone VPSA was designed and assembled for the production of 1 L_{STP}·min^{-1} of 99+% oxygen stream from air. The unit, operating between 1.4 and 0.2 bar at 25 °C, includes two pre-beds running an innovative pre-treatment four-step cycle synchronized with the seven-step main cycle to continuously supply treated feed air (– 40 °C dew point and 5 ppm of CO_2) to the AgLiLSX beds. This pre-treatment section is crucial in such a stand-alone unit to protect and prevent AgLiLSX from deactivation. The developed ASPEN-based simulator was used to study the influence of several operating variables on the product purity and recovery and to optimize the performance of the unit. The

optimized stand-alone unit produced an experimental stream of 99.13 % oxygen from air, with a recovery of 6.2 % when $t_{PR} = 5.5\ \text{s}$, $t_{AD} = 10\ \text{s}$, $t_E = 2.5\ \text{s}$, $t_B = 2\ \text{s}$, $P_H = 1.4\ \text{bar}$, $P_L = 0.25\ \text{bar}$ and $F_{PG} = 1\ \text{L}_{\text{STP}} \cdot \text{min}^{-1}$. The unit was also able to produce a 99 % oxygen stream with higher recovery, 8 %, when the following conditions are observed: $t_{PR} = 7\ \text{s}$, $t_{AD} = 14\ \text{s}$, $t_E = 2.5\ \text{s}$, $t_B = 2\ \text{s}$, $P_H = 1.4\ \text{bar}$, $P_L = 0.25\ \text{bar}$ and $F_{PG} = 0.8\ \text{L}_{\text{STP}} \cdot \text{min}^{-1}$. The productivity of the unit is 9.0 $m^3 \cdot hr^{-1} \cdot ton^{-1}$. It was concluded that the stand-alone unit was able to produce high-purity oxygen from air, with good recovery and productivity, using a single-stage VPSA packed with AgLiLSX.

Acknowledgment

Daniel Ferreira acknowledges Fundação para a Ciência e Tecnologia (FCT) and Sysadvance, Sistemas de Engenharia S.A. for the PhD grant (SFRH/BDE/51186/2010). The authors acknowledge the funding provided by Agência de Inovação (AdI) (project HPOVPSA, ref 13488). We kindly thank Pedro Taveira for the relevant assistance on designing the cycle of the stand-alone unit.

4.5 References

1. Grande, C.A. Advances in Pressure Swing Adsorption for Gas Separation. *ISRN Chemical Engineering.* **2012**, 2012, 13.
2. Jee, J.-G., Lee, S.-J., Moon, H.-M., Lee, C.-H. Adsorption Dynamics of Air on Zeolite 13X and CMS Beds for Separation and Purification. *Adsorption.* **2005**, 11, 415-420.
3. Lee, S.-J., Jung, J.-H., Moon, J.-H., Jee, J.-G., Lee, C.-H. Parametric Study of the Three-Bed Pressure−Vacuum Swing Adsorption Process for High Purity O2 Generation from Ambient Air. *Industrial & Engineering Chemistry Research.* **2007**, 46, 3720-3728.
4. Jee, J.-G., Lee, S.-J., Lee, C.-H. Comparison of the Adsorption Dynamics of Air on Zeolite 5A and Carbon Molecular Sieve Beds. *Korean Journal of Chemical Engineering.* **2004**, 21, 1183-1192.
5. Park, Y.-J., Lee, S.-J., Moon, J.-H., Choi, D.-K., Lee, C.-H. Adsorption Equilibria of O_2, N_2, and Ar on Carbon Molecular Sieve and Zeolites 10X, 13X, and LiX. *Journal of Chemical & Engineering Data.* **2006**, 51, 1001-1008.
6. Ruthven, D., Farooq, S., Knaebel, K. *Pressure Swing Adsorption*; VCH Publishers: New York, 1994.
7. Yang, R.T. *Gas Separation by Adsorption Processes*; Imperial College Press: London, 1997.
8. Santos, J.C., Cruz, P., Regala, T., Magalhães, F.D., Mendes, A. High-Purity Oxygen Production by Pressure Swing Adsorption. *Industrial & Engineering Chemistry Research.* **2006**, 46, 591-599.
9. Hayashi, S., Kawai, M., Kaneko, T. Dynamics of High Purity Oxygen PSA. *Gas Separation & Purification.* **1996**, 10, 19-23.
10. Haruna, K., Ueda, K., Inoue, M., Someda, H. Process for Producing High Purity Oxygen Gas from Air. U.S. Patent 4,985,052, 1991.
11. Armond, J.W., Webber, D.A., Smith, K.C. Gas Separation. U.S. Patent 4,190,424, 1980.
12. Santos, J.C., Portugal, A.F., Magalhães, F.D., Mendes, A. Optimization of Medical PSA Units for Oxygen Production. *Industrial and Engineering Chemistry Research.* **2006**, 45, 1085-1096.

13. Ferreira, D., Magalhães, R., Bessa, J., Taveira, P., Sousa, J., Whitley, R.D., Mendes, A. Study of AgLiLSX for Single-Stage High-Purity Oxygen Production. *Industrial & Engineering Chemistry Research.* **2014**, 53, 15508-15516.

14. Bae, Y.-S., Moon, J.-H., Ahn, H., Lee, C.-H. Effects of Adsorbate Properties on Adsorption Mechanism in a Carbon Molecular Sieve. *Korean Journal of Chemical Engineering.* **2004**, 21, 712-720.

15. Kim, M.-B., Jee, J.-G., Bae, Y.-S., Lee, C.-H. Parametric Study of Pressure Swing Adsorption Process To Purify Oxygen Using Carbon Molecular Sieve. *Industrial & Engineering Chemistry Research.* **2005**, 44, 7208-7217.

16. Jee, J.-G., Jung, J.-H., Lee, J.-W., Suh, S.-H., Lee, C.-H. Comparison of Vacuum Swing Adsorption Process for Air Separation Using Zeolite 10X and 13X. *Revue Roumaine de Chimie.* **2006**, 51, 1095-1108.

17. Wilkerson, B.E. The Adsorption of Argon and Oxygen on Silver Mordenite. Master Thesis, Graduate School of Ohio State University, Ohio, USA, 1990.

18. Chiang, R.L., Whitley, R.D., Ostroski, J.E., Dee, D.P. Argon/Oxygen Selective X-Zeolite. U.S. Patent 6,432,170, 2002.

19. Sebastian, J., Jasra, R.V. Sorption of Nitrogen, Oxygen, and Argon in Silver-Exchanged Zeolites. *Industrial & Engineering Chemistry Research.* **2005**, 44, 8014-8024.

20. Ansón, A., Kuznicki, S.M., Kuznicki, T., Haastrup, T., Wang, Y., Lin, C.C.H., Sawada, J.A., Eyring, E.M., Hunter, D. Adsorption of Argon, Oxygen, and Nitrogen on Silver Exchanged ETS-10 Molecular Sieve. *Microporous and Mesoporous Materials.* **2008**, 109, 577-580.

21. Shi, M., Kim, J., Sawada, J.A., Lam, J., Sarabadan, S., Kuznicki, T.M., Kuznicki, S.M. Production of Argon Free Oxygen by Adsorptive Air Separation on Ag-ETS-10. *AIChE Journal.* **2013**, 59, 982-987.

22. Knaebel, K.S., Kandybin, A. Pressure Swing Adsorption System to Purify Oxygen. U.S. Patent 5,226,933, 1993.

23. Dee, D.P., Chiang, R.L., Miller, E.J., Whitley, R.D. High Purity Oxygen Production by Pressure Swing Adsorption. U.S. Patent 6,544,318, 2003.

24. Ferreira, D., Magalhães, R., Taveira, P., Mendes, A.l. Effective Adsorption Equilibrium Isotherms and Breakthroughs of Water Vapor and Carbon Dioxide on Different Adsorbents. *Industrial & Engineering Chemistry Research.* **2011**, 50, 10201-10210.

25. Santos, J.C., Magalhães, F.D., Mendes, A. Contamination of Zeolites Used in Oxygen Production by PSA: Effects of Water and Carbon Dioxide. *Industrial & Engineering Chemistry Research.* **2008**, 47, 6197-6203.

26. Cruz, P., Santos, J.C., Magalhães, F.D., Mendes, A. Cyclic Adsorption Separation Processes: Analysis Strategy and Optimization Procedure. *Chemical Engineering Science.* **2003**, 58, 3143-3158.

27. Ruthven, D.M. *Principles of Adsorption and Adsorption Processes*; John Wiley & Sons: New York, 1984.

28. Bird, R., Stewart, W., Ligthfoot, E. *Transport Phenomena*; John Wiley and Sons: New York, 2002.

29. Ergun, S. Fluid Flow Through Packed Columns. *Chemical Engineering Progress.* **1952**, 48, 89-94.

30. Bárcia, P.S., Silva, J.A.C., Rodrigues, A.r.E. Adsorption Dynamics of C5−C6 Isomerate Fractions in Zeolite Beta for the Octane Improvement of Gasoline. *Energy & Fuels.* **2010**, 24, 1931-1940.

31. Bárcia, P.S., Silva, J.A.C., Rodrigues, A.r.E. Octane Upgrading of C5/C6 Light Naphtha by Layered Pressure Swing Adsorption. *Energy & Fuels.* **2010**, 24, 5116-5130.

32. Do, D.D. *Adsorption Analysis: Equilibria and Kinetics*; Imperial College Press: London, 1997.

33. Schiesser, W. *The Numerical Method of Lines*; Academic Press: San Diego, CA, 1991.

34. Catarino, M., Ferreira, A., Mendes, A. Study and Optimization of Aroma Recovery From Beer by Pervaporation. *Journal of Membrane Science.* **2009**, 341, 51-59.

35. Montgomery, D.C. *Design and Analysis of Experiments*; John Wiley & Sons: New York, 2001.

CHAPTER V

Ferreira, D., Boaventura, M., Bárcia, P., Whitley, R.D., Mendes, A., Two-stage VPSA Using AgLiLSX Zeolite for Producing 99.5+% Oxygen from Air. *Industrial & Engineering Chemistry Research*. **2016**, 55, 722-736.

The author conducted all the experimental work and simulations described in this chapter, and was involved on the discussion and interpretation of results, as well as on the preparation of the manuscript.

5 Two-stage VPSA using AgLiLSX zeolite for producing 99.5+% oxygen from air

Abstract

Oxygen concentrations above 99.5 % are required for several applications, mainly in the medical and aerospace fields. Two-stage PSA processes, combining kinetic separation with equilibrium separation, have been developed for producing 99+% oxygen from air. Argon and nitrogen are kinetically removed from the air feed using a carbon molecular sieve adsorbent and the remaining nitrogen is removed using a N_2/O_2 selective zeolite. Despite that, two-stage processes are often unattractive, complex and energy consuming, requiring two or more compressors/vacuum pumps. Moreover, most of the two-stage units described in literature are unable to reach the required oxygen purity of 99.5 %.

This work studies three energy-efficient two-stage VPSA processes, combining an equilibrium based PSA (EPSA) or a kinetic based PSA (KPSA) for the first stage, with a VPSA unit packed with the Ar/O_2 selective zeolite AgLiLSX for the second stage, aiming at to produce 99.5+% of oxygen; the use of zeolite AgLiLSX allows removing argon besides nitrogen. The best two-stage VPSA configuration allowed obtaining a 99.8 % of oxygen stream at 6 % of recovery and a 99.5+% of oxygen stream at 14+% of recovery.

5.1 Introduction

The sales of pressure swing adsorption (PSA) units for producing 95 % of oxygen from air has increased noticeably in the past decades [1]. There is, however, a great demand for oxygen 99+% for various industrial applications, namely: a) medical applications, such as surgeries where the minimum oxygen concentration required is 99 % in United States and 99.6 % in Japan [2]; b) military and aerospace applications where minimum concentration of 99.5 % is required; c) semiconductor industry where concentrations higher than 99.8 % is required [3]; and d) for metal welding and cutting processes [4]. Despite this increasing demand, only cryogenic separation has been recognized effective for producing high-purity oxygen (99+%) [5]. For small and medium scale production and for oxygen concentrations up to 95 %, PSA is the state-of-the-art technology [6]. Additionally, the low installation costs, simplicity and easy start/stop operation of a PSA unit are major advantages that cannot be realized with the cryogenic processes [7].

Since the 1980s several PSA designs have been proposed for producing high-purity oxygen. The first process was disclosed by Armond et al. [6] in 1980 and consists of a PSA unit packed with a carbon molecular sieve (CMS) adsorbent followed by another PSA unit packed with a nitrogen selective zeolite. The CMS stage served to kinetically remove essentially argon from the air and the second stage for removing the remaining nitrogen. The process was complex and had low energy efficiency since it used three air compressors/vacuum pumps. Following, in 1989 Miller and Theis [8] proposed a similar two-stage PSA process, where the equilibrium stage (beds packed with zeolite) comes first, followed by the kinetic stage (beds packed with CMS). The process, operating between 3.1 bar and 1.0 bar, delivers a 99.1 % oxygen product stream at atmospheric pressure. Similar processes were disclosed in the following years with small improvements compared with the original two-stage PSA process [9, 10], such as introducing a buffer tank for storing enriched oxygen from the desorption

step of the CMS-stage; this stored gas is then used to pressurize and feed the zeolite-stage and to purge the CMS-stage, thus improving the process purity and productivity [9]. More recently, Lee et al. [11-13] reported a two-stage three-bed PSA unit for producing a stream of 99.2 % oxygen with a recovery of ca. 47 %. This unit comprised a PSA loaded with 10X-type zeolite followed by a CMS column, running a ten-step cycle with two consecutive blowdown/backfill steps. The high recovery results were possible because the use of a very high selective CMS adsorbent ($D_{O_2} = 2.4 \times 10^{-2}\ s^{-1}$; $D_{Ar} = 4.7 \times 10^{-5}\ s^{-1}$ and $D_{N_2} = 9.0 \times 10^{-5}\ s^{-1}$). However, despite the higher recovery and purity, this was not enough to fulfill the demand of 99.5+% oxygen [11, 12].

During the 1990s, new generations of highly selective adsorbents, such as LiX-, LSX-, LiLSX-type zeolites and, particularly, silver-exchanged zeolites, contributed to a significant increase in the productivity and economic efficiency of oxygen air separation by PSA-based processes [14-21]. In 1993, Knaebel and Kandybin disclosed a single-column PSA process using a silver-exchanged mordenite. This mordenite has selectivity to argon and the process is reported to produce a stream with 99.5 % of oxygen and 12 % of recovery from a feed containing 95 % of oxygen balanced with argon. In 2002, Air Products and Chemicals, Inc. also patented an argon/oxygen selective zeolite, named AgLiLSX (lithium low silica X-type silver-based zeolite), with a silver-exchanged content of 20–70 mol.% [22, 23]. The AgLiLSX zeolite is able to produce a stream of 99.1 % oxygen from air in a single-stage VPSA operation [2, 4, 24], unlike present commercial zeolites that are limited to 95 % oxygen (balanced mostly with argon) since they do not exhibit argon/oxygen adsorption selectivity above 1 [25].

This work studies three energy-efficient two-stage VPSA processes, combining an equilibrium based PSA (EPSA) or a kinetic based PSA (KPSA) for the first stage, with a VPSA packed with AgLiLSX zeolite for the second stage, aiming at to produce a

99.5+% oxygen stream from air. It covers the simulation and optimization of the three two-stage VPSA configurations and corresponding experimental validation. The proposed model was solved using ASPEN.

5.2 Experimental

5.2.1 Two-stage VPSA configurations

Three configurations of a two-stage VPSA unit are proposed and studied for producing a stream of 99.5+% oxygen from air:

a) conventional equilibrium based PSA unit for producing a gas stream of ca. 95 % oxygen balanced with argon and nitrogen, followed by a VPSA unit packed with the new AgLiLSX adsorbent for removing the argon and nitrogen – named EPSA/VPSA;
b) kinetic conventional PSA, packed with a CMS adsorbent, followed by a VPSA unit packed with the new AgLiLSX adsorbent; the VPSA unit receives the low pressure product stream from the kinetic PSA, depleted of nitrogen and argon – named KPSA/VPSA;
c) kinetic conventional PSA, packed with a CMS adsorbent, followed by a VPSA unit packed with the new AgLiLSX adsorbent; an intermediate blower is introduced to repressurize the product stream from the kinetic PSA to feed the VPSA unit, allowing a higher product purity and recovery – named KPSA/RP/VPSA;

EPSA/VPSA unit

This configuration comprises a conventional equilibrium based PSA (EPSA) unit for producing 95 % oxygen stream from air, followed by a second equilibrium based VPSA unit loaded with zeolite AgLiLSX for argon removal and oxygen purification up to 99.5+%.

The first stage, not reported, is an equilibrium based PSA loaded with a commercial zeolite such as NaX-, CaX-, LiX- or LiLSX-types, and producing a stream of ca. 95 % of oxygen balanced with argon and nitrogen [18, 26, 27]. The authors studied only the VPSA stage of this configuration (second stage), loaded with AgLiLSX. The first stage was assumed to provide a feed stream of 95 % oxygen (balanced with argon), at 1.4 bar, to the second stage.

The VPSA stage run a seven-step cycle previously studied by the team and illustrated in Table 5.1 [24]. During pressurization step (PR), the bed is co-currently pressurized with feed up to high operating pressure. Following, during the adsorption step (AD), high-pressure feed flows through the bed while argon is selectively retained thus producing an oxygen-enriched stream. A fraction of the product is used to counter-currently purge the other bed at low operating pressure, during the purge under vacuum (VP) step. After the adsorption step, equalization (E) takes place where the two beds are top-to-top connected until pressure equalization. During the evacuation step (VA), vacuum is applied to the bed feed end while product end is kept closed. After the VA step, vacuum is maintained while bed is counter-currently purged with a fraction of the product stream. Following, the second equalization takes place and afterwards the backfill (B) step, where part of the product stored in the product storage tank is used to counter-currently re-pressurize the adsorption bed.

Table 5.1 – Sequence of the seven-step VPSA cycle.

	1	**2**	**3**	**4**	**5**	**6**	**7**	**8**
Col 1	E	VA		VP	E	B	PR	AD
Col 2	E	B	PR	AD	E	VA		VP

KPSA/VPSA unit

The KPSA/VPSA configuration comprises a conventional kinetic PSA unit (KPSA), loaded with a CMS adsorbent for argon and nitrogen kinetic removal, producing an

oxygen-enriched stream as blowdown product (extract stream). This extract stream is fed to the second stage, a VPSA unit loaded with AgLiLSX zeolite, which removes the remaining nitrogen and argon to produce a high-purity oxygen product. This configuration does not require a compressor/blower to repressurize the first stage blowdown stream and redirect gas flow to the second stage; first stage low pressure product (blowdown) provides feed and sets the high operating pressure of the second stage; this configuration just uses a feed compressor to the first stage and a vacuum pump for the evacuating steps in the second stage.

The KPSA run a conventional Skarstrom cycle with equalization as illustrated in Table 5.2. The six-step Skarstrom cycle comprises a pressurization step (PR) where the bed is pressurized with feed air to the high operating pressure; an adsorption step (AD), where high-pressure feed flows through the bed; an equalization step (E) where the two adsorption beds are top-to-top connected for pressure equalization; a blowdown step (BD) where the feed entrance is opened and the oxygen adsorbed in the bed is counter-currently depressurized and fed to the second stage; a purge step (PG) where a fraction of the raffinate stream from the other bed is used to counter-currently purge the bed at atmospheric pressure. Here, raffinate means the gas which is not adsorbed during the AD step, exiting the column through the top [25]. The species desorbed at low pressure (also known as “extracted” [25]) are called intermediate product or blowdown product.

Table 5.2 – Sequence of the six-step KPSA cycle.

	1	**2**	**3**	**4**	**5**	**6**
Col 1	PR	AD	E	BD	PG	E
Col 2	BD	PG	E	PR	AD	E

The VPSA stage run the seven-step cycle described above (Table 5.1). Both cycles, KPSA and VPSA stage, run independently, using an intermediate buffer tank.

KPSA/RP/VPSA unit

This configuration differs from the previous one only for the introduction of an intermediate blower between the first and second stages. The use of a blower allows KPSA blowdown at atmospheric pressure and repressurizes the first stage blowdown product stream up to the feed pressure of the second stage. The KPSA and VPSA cycles described above and are shown in Table 5.2 and Table 5.1, respectively. Both cycles run independently, using an intermediate buffer tank.

5.2.2 Two-stage VPSA apparatus

A general-purpose two-stage VPSA experimental set-up was used to run the three configurations aforementioned – Figure 5.1. The adsorption beds and storage columns are made of stainless steel; the characteristics of the beds are listed in Table 5.3. Sampling points (S1 to S10) placed along the beds were used to obtain the concentration history under operation; a mass spectrometer (Pfeiffer, Omnistar) was used to analyze the concentration of these sampling points. The feed and purge flowrates of the first PSA unit (first stage) were measured using mass flow meters (Bronkhorst High-tech, El Flow F-113C, 0 – 100 $L_{STP}{\cdot}min^{-1}$ and Bronkhorst High-tech, El Flow F-111C, 0 – 2 $L_{STP}{\cdot}min^{-1}$, respectively); the feed and purge flowrates of the second PSA unit (second stage) were measured using mass flow meters (Bronkhorst High-tech, El Flow F-112C, 0 – 10 $L_{STP}{\cdot}min^{-1}$ and Bronkhorst High-tech, El Flow F-201C, 0 – 2 $L_{STP}{\cdot}min^{-1}$, respectively); the raffinate and product flowrates of respectively the first and second PSA units were controlled using mass flow controllers (Bronkhorst High-tech, El-Flow F-201C, 0 – 2 $L_{STP}{\cdot}min^{-1}$ and Bronkhorst High-tech, El-Flow F-201C, 0 – 2 $L_{STP}{\cdot}min^{-1}$, respectively). The purge and raffinate flow rates of both PSA units were regulated using needle valves. Several pressure sensors (Druck, PMP 4010, 0 – 7 bar), located at the bottom and top of the adsorption columns and on the product exit,

were used to measure the pressure history inside adsorption beds and at the product streams. A set of solenoid and check valves are used to direct the flow according to the adsorption cycles. A vacuum pump (Vacuubrand, model ME 8 NT, 70 mbar) was used to evacuate the adsorption columns at the VPSA unit. Each PSA unit includes a storage column that allows to store part of the product and to use it in the backfill step if applicable. Between each stage a storage tank was placed to serve as buffer to the second stage feed. The product stream concentration was measured using an oxygen analyzer (Servomex, model 5200, from 0 to 100 %, with an accuracy of 0.05 % FS) and a mass spectrometer.

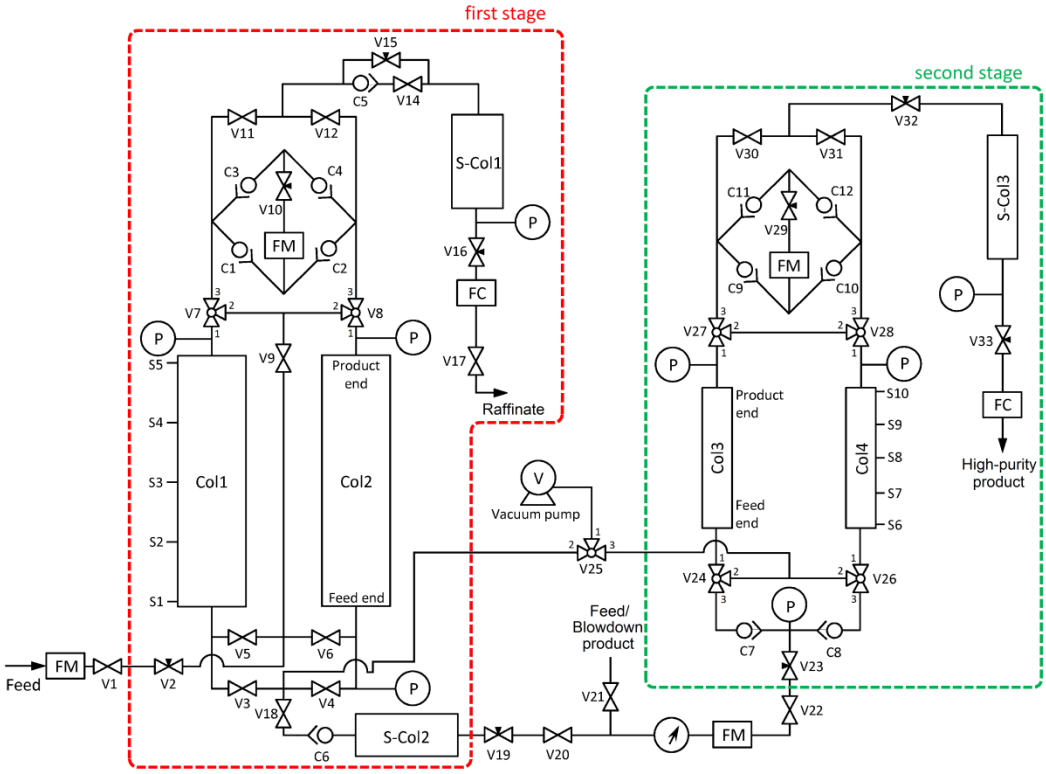

Figure 5.1 – Schematic representation of the two-stage VPSA unit: Col = column; S-Col = storage column; C1 to C12 = check valves; FM = flow meter; FC = flow controller; P = pressure transducer; S1 to S10 = sampling points; V = vacuum pump; V1 to V33 = electric valves.

Table 5.3 – Characteristics of adsorbents and adsorption beds.

adsorption beds	**1st stage PSA unit**	**2nd stage PSA unit**
bed length, cm	40.4	26.2
internal diameter, cm	4.2	2.6
wall thickness, cm	0.2	0.2
storage column volume, cm^3	1017	109
storage column (S-Col2) volume, cm^3	1038	

Adsorbent	**AgLiLSX**	**CMS**
geometry	spherical	pellet
pellet diameter (d_p), mm	1.02	2.10
intraparticle voidage (ε_p)	0.605	0.487
interparticle voidage (ε_b)	0.36	0.38
bulk density (ρ_b), $g \cdot cm^{-3}$	0.780	0.609
macropore radius (r_{pore}), m	3.6×10^{-9}	3.5×10^{-7}
micropore radius ($r_{micropore}$), m	---	0.6×10^{-10}
heat capacity (C_{ps}), $J \cdot kg^{-1} \cdot K^{-1}$	1172	963
thermal conductivity (k_{sx}), $W \cdot m^{-1} \cdot K^{-1}$	0.3	0.3

AgLiLSX adsorbent (Air Products and Chemicals, Inc.) and a CMS (Kuraray) were used as adsorbents. The physical properties of the adsorbents are listed in Table 5.3. AgLiLSX adsorbent was previously characterized by the team [2]; the adsorption parameters of O_2, N_2 and Ar are given in Table 5.4. The adsorption equilibrium isotherms and adsorption kinetics on CMS adsorbent of O_2, N_2 and Ar were obtained at three temperatures, 10 °C, 25 °C and 40 °C using the volumetric method [28]. The isotherms obtained for O_2, N_2 and Ar at 25 °C are shown in Figure 5.2 and the pressure-dependence of the apparent time constant, $D_\mu = D/r^2$ (where D is the diffusivity and r is the crystals radius), of O_2, N_2 and Ar at 25 °C are shown in Figure 5.3.

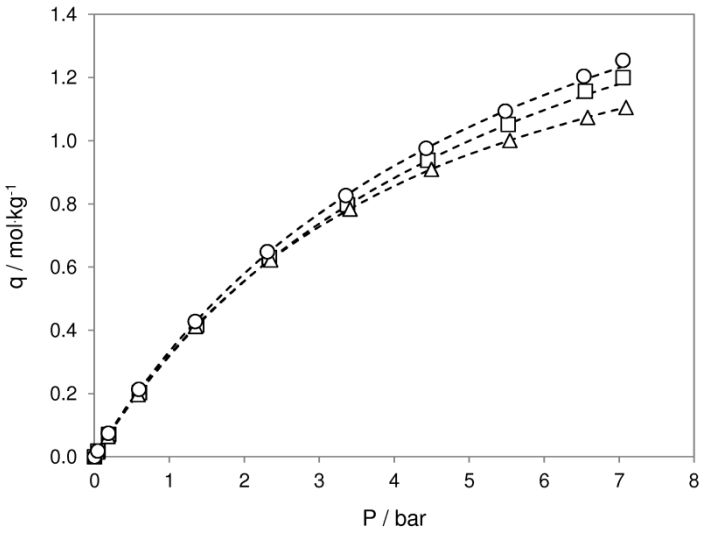

Figure 5.2 – Adsorption isotherms for: △, nitrogen, ○, oxygen; and □, argon, on CMS at 25 °C.

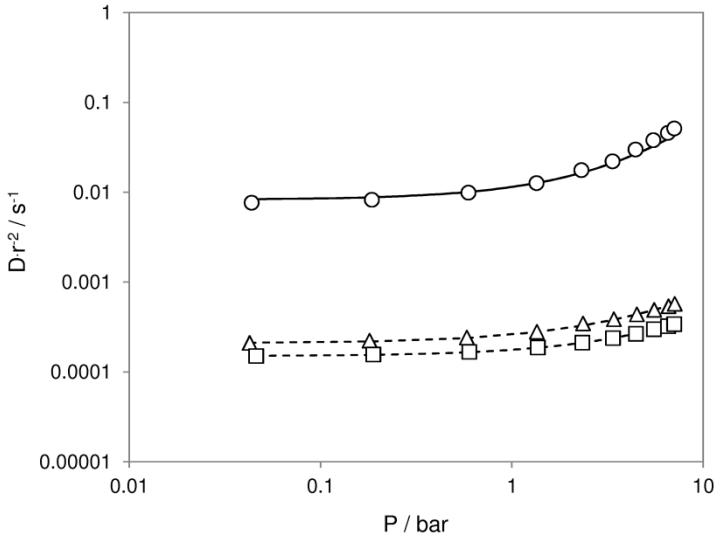

Figure 5.3 – Pressure-dependence of the apparent time constant for: △, nitrogen, ○, oxygen; and □, argon, on CMS at 25 °C.

Table 5.4 – Parameters of the adsorption isotherms on AgLiLSX and on CMS adsorbents and adsorption kinetic parameters on CMS adsorbent.

	nitrogen	**oxygen**	**argon**
		AgLiLSX	
$q_{m,1}$ / mol·kg^{-1}	0.729	3.79	3.29
$b_1^{\infty}\times10^{-3}$ / bar^{-1}	0.020	0.151	0.134
$\Delta H_1\times10^{3}$ / J·mol^{-1}	31.1	14.0	15.0
$q_{m,2}$ / mol·kg^{-1}	2.66	---	---
$b_2^{\infty}\times10^{-3}$ / bar^{-1}	0.051	---	---
$\Delta H_2\times10^{3}$ / J·mol^{-1}	17.6	---	---
		CMS	
q_m / mol·kg^{-1}	1.74	2.23	2.14
$b^{\infty}\times10^{-3}$ / bar^{-1}	0.118	0.092	0.120
$\Delta H\times10^{3}$ / J·mol^{-1}	18.9	18.7	18.1
$D_{\mu 0}^{\infty}$ / s^{-1}	4.22 x 10^{1}	5.38 x 10^{2}	5.86 x 10^{1}
$E_a\times10^{3}$ / J·mol^{-1}	30.3	27.8	31.9
m	1	0.0222·*T*(K) - 4.2022	1

Langmuir and dual-site Langmuir equations were used to fit the experimental adsorption equilibrium data. Both equations have simple mathematical formulations and are thermodynamically consistent. The dual-site Langmuir equation, which renders Langmuir equation when $q_{m,2}$ equals to zero, is given by:

$$q = q_{m,1}\frac{b_1 P}{1+b_1 P} + q_{m,2}\frac{b_2 P}{1+b_2 P} \tag{5.1}$$

where q is the adsorbed concentration, P is the equilibrium pressure, q_m is the saturation adsorbed concentration and b is the adsorption affinity constant, assumed to vary with temperature according to the van't-Hoff equation:

$$b = b^{\infty} \exp\left(\frac{\Delta H}{\Re T}\right) \tag{5.2}$$

where b^{∞} is the adsorption constant at infinite temperature, ΔH is the heat of adsorption, $\Re$ is the ideal gas constant, and T is the absolute temperature.

The Darken and Bae-Lee models combined with Langmuir isotherm were used to fit the pressure dependence of apparent time constants on CMS. The model proposed by Bae and Lee, which renders Darken model when m is equal to the unity, is given by:

$$D_{\mu} = D_{\mu 0} \cdot \exp\left(1 + bP\right)^{m} \tag{5.3}$$

where $D_{\mu 0}$ is the apparent time constant at zero pressure, P is the equilibrium pressure, b is the adsorption affinity constant, assumed to vary with temperature according to eq.(5.2), and m is the Bae-Lee equation parameter. The diffusivity temperature dependence follows the Arrhenius relation:

$$D_{\mu 0} = D_{\mu 0}^{\infty} \cdot \exp\left(-\frac{E_a}{\Re T}\right) \tag{5.4}$$

where $D_{\mu 0}^{\infty}$ is the apparent time constant at zero pressure and infinite temperature and E_a is the activation energy.

5.2.3 Mathematical model

The main assumptions of the mathematical model used for simulating the two-stages PSA units are:

1) ideal gas behaviour
2) negligible radial concentration and temperature gradients
3) axially dispersed plug flow
4) thermal equilibrium between adsorbent particles and bulk flow

5) uniform cross-sectional void fraction
6) adsorption equilibrium described by dual-site multicomponent Langmuir isotherm
7) pressure drop described by Ergun's equation

According to these assumptions, the model can be written as it follows [29]:

Mass balance

$$-\varepsilon_b D_{ax}\frac{\partial^2 c_i}{\partial x^2}+\frac{\partial\left(uc_i\right)}{\partial x}+\varepsilon_t\frac{\partial c_i}{\partial t}+\left(1-\varepsilon_b\right)\rho_s\frac{\partial\overline{q}_i}{\partial t}=0 \tag{5.5}$$

where c_i is the partial molar concentration, D_{ax} is the axial dispersion coefficient, u is the interstitial molar average velocity, ε_b is the interparticle voidage, ε_t is the total bed voidage, ρ_s is the adsorbent apparent density, $\overline{q}_i$ is the partial average molar concentration in the adsorbed phase, x is the spatial coordinate, and t is the time variable. The dispersion coefficient, D_{ax}, varies along the length of the bed following the correlation [30]:

$$D_{ax}=0.73D_m+\frac{u\cdot r_p}{\varepsilon_b\left(1+9.49\varepsilon_b D_m/2u\cdot r_p\right)} \tag{5.6}$$

where r_p is the particle radius. The molecular diffusion coefficient, D_m, is estimated from the Chapman-Enskog equation [31].

The momentum balance is given by the Ergun's equation as follows [32]:

Momentum balance

$$-\frac{\partial P}{\partial x}=\frac{1.5\times10^{-3}\left(1-\varepsilon_b\right)^2}{\left(2r_p\right)^2\varepsilon_b{}^3}\mu\cdot u+1.75\times10^{-5}M\rho_g\frac{\left(1-\varepsilon_b\right)}{2r_p\varepsilon_b{}^3}u\cdot|u| \tag{5.7}$$

where P is the total pressure, ρ_g is the gas-phase molar density, μ is the dynamic viscosity, and M is the molecular weight.

The general linear driving force (LDF) model, assuming constant diffusivity, was applied for the sorption rate of AgLiLSX zeolite and the modified LDF model with Bae-Lee or Darken pressure- and temperature-dependent diffusivity, eq.(5.3) and eq.(5.4) was applied for CMS [12]:

$$\frac{\partial \overline{q}_i}{\partial t} = k_i \left(q_i - \overline{q}_i \right) \tag{5.8}$$

where q_i is the adsorbed concentration of the component i in the particle inner surface, and k_i is LDF coefficient, given by [33]:

$$\frac{1}{k_i} = \frac{r_p{}^2}{15 \varepsilon_p D_{eff}} \tag{5.9}$$

where ε_p is the intraparticle voidage, and D_{eff} is the effective diffusivity, obtained from eq.(3) and eq.(4) in the case of CMS, and from the Bosanquet equation, as follows, in the case of AgLiLSX [25]. It was assumed that the binder network of macro/mesopores controls the mass transport inside the adsorbent [4]:

$$\frac{1}{D_{pi}} = \tau_p \left(\frac{1}{D_{Ki}} + \frac{1}{D_{mi}} \right) \tag{5.10}$$

where τ_p is the tortuosity factor, and D_{Ki} is the Knudsen diffusion coefficient given by $D_{Ki} = 97 r_{pore} \left(T / M_i \right)^{0.5}$, where r_{pore} is the mean macropore radius and T is the absolute temperature.

The adsorbed amount of each species in the solid-phase is given by the dual-site Langmuir equation above described, eq.(1) [34].

Gas-phase energy balance

$$-k_{gx}\varepsilon_b \frac{\partial^2 T_g}{\partial x^2} + C_{vg}\rho_g u \frac{\partial T_g}{\partial x} + \varepsilon_b C_{vg}\rho_g \frac{\partial T_g}{\partial t} + P\frac{\partial u}{\partial x} + h_p \cdot a_p \left(T_g - T_s\right) + \\ + \frac{4h_w}{D_B}\left(T_g - T_w\right) = 0 \tag{5.11}$$

where C_{vg} is the gas-phase heat capacity at constant volume, $a_p = 3\left(1-\varepsilon_b\right)/r_p$ is the specific particle surface per unit volume of the bed, D_B is the internal bed diameter, and T_g, T_s, T_w are, respectively, the gas, solid and internal wall temperatures. The axial gas-phase thermal conductivity coefficient, k_{gx}, is given by

$$k_{gx} = \rho_g C_{pg} \sum_i^{nc} D_{ax} y_i \tag{5.12}$$

where C_{pg} is the gas-phase heat capacity at constant pressure, y_i is the mole fraction of component i in the gas phase, and nc is the number of mixture components.

The gas-solid heat-transfer coefficient, h_p, is estimated using the Colburn j factor for the heat transfer as follows [33]:

$$h_p = j\rho_g C_{pg} u \cdot Pr^{-2/3} \tag{5.13}$$

where $j = 1.66Re^{-0.51}$ if Re < 190, otherwise $j = 0.983Re^{-0.41}$, and $Pr = \mu C_{pg}/k_{gx}M$ is the Prandl number.

The gas-wall heat-transfer coefficient, h_w, is obtained from Nusselt number by the following correlation,

$$h_w = Nu_w \frac{k_{gx}}{2r_p} \tag{5.14a}$$

$$Nu_w = \frac{-2\times10^{-6}\cdot Pe_H{}^2 + 0.0477\cdot Pe_H + 22.11}{1+12L_B/D_B\cdot Pe_H} \tag{5.14b}$$

where $Pe_H = 2r_p M\rho_g C_{pg} u / k_{gx}$ is the gas-wall heat-transfer Peclet number, and L_B is the bed length.

Solid-phase energy balance

$$-k_{sx}\frac{\partial^2 T_s}{\partial x^2} + \rho_b C_{ps}\frac{\partial T_s}{\partial t} + \rho_b\sum_{i=1}^{nc}\left(\Delta H_i\frac{\partial \overline{q}_i}{\partial t}\right) - h_p\cdot a_p\left(T_g - T_s\right) = 0 \tag{5.15}$$

where k_{sx} is the axial solid-phase thermal conductivity coefficient, C_{ps} is the adsorbent heat capacity, and ρ_b is the adsorbent bulk density.

Wall energy balance

$$-h_w\alpha_w\left(T_g - T_w\right) + h_\infty\alpha_w^{ml}\left(T_w - T_\infty\right) = 0 \tag{5.16}$$

where α_w is the ratio of the internal surface area to the volume of the column wall, α_w^{ml} is the ratio of the logarithmic mean surface area to the volume of the column wall, h_∞ is the wall-ambient heat-transfer coefficient, and T_∞ is the external environmental temperature.

The two-stage VPSA unit combines in series two individual PSA units. The two sets of boundary conditions were applied to the CMS-bed and AgLiLSX-bed separately.

The boundary conditions for the KPSA are as follows [11, 29]:

Boundary conditions for pressurization (PR) step

$$x = 0: \qquad \varepsilon_b D_{ax}\frac{\partial c_i}{\partial x} = u\left(c_i - c_{i,in}\right) \qquad T = T_{in}$$

$$z = L: \qquad \frac{\partial c_i}{\partial x} = 0 \qquad u = 0 \qquad \frac{\partial T}{\partial x} = 0$$

Boundary conditions for adsorption (AD) step

$$x = 0: \qquad \varepsilon_b D_{ax} \frac{\partial c_i}{\partial x} = u\left(c_i - c_{i,in}\right) \qquad T = T_{in}$$

$$x = L: \qquad \frac{\partial c_i}{\partial x} = 0 \qquad u = u_{PROD} \qquad \frac{\partial T}{\partial x} = 0$$

Boundary conditions for top-to-top equalization (E) step

column providing equalization

$$x = 0: \qquad \frac{\partial c_i}{\partial x} = 0 \qquad u = 0 \qquad \frac{\partial T}{\partial x} = 0$$

$$x = L: \qquad \frac{\partial c_i}{\partial x} = 0 \qquad u = u_E \qquad \frac{\partial T}{\partial x} = 0$$

column receiving equalization

$$x = 0: \qquad \frac{\partial c_i}{\partial x} = 0 \qquad u = 0 \qquad \frac{\partial T}{\partial x} = 0$$

$$x = L: \qquad \varepsilon_b D_{ax} \frac{\partial c_i}{\partial x} = u\left(c_i - c_i\big|_{x=L,\ column\ providing\ E}\right) \qquad u = u_E$$

Boundary conditions for blowdown (BD) step

$$x = 0: \qquad \frac{\partial c_i}{\partial x} = 0 \qquad \frac{\partial T}{\partial x} = 0$$

$$x = L: \qquad \frac{\partial c_i}{\partial x} = 0 \qquad u = 0 \qquad \frac{\partial T}{\partial x} = 0$$

Boundary conditions for purge (PG) step

$$x = 0: \qquad \frac{\partial c_i}{\partial x} = 0 \qquad \frac{\partial T}{\partial x} = 0$$

$$x = L: \qquad \varepsilon_b D_{ax} \frac{\partial c_i}{\partial x} = u\left(c_i - c_i\big|_{x=L,\ column\ runing\ AD}\right) \qquad u = u_{PG} \qquad \frac{\partial T}{\partial x} = 0$$

The boundary conditions for the equilibrium-based VPSA (AgLiLSX beds) are as follows [29]:

Boundary conditions for pressurization (PR) step

$$x = 0: \qquad \varepsilon_b D_{ax} \frac{\partial c_i}{\partial x} = u\left(c_i - c_{i,in}\right) \qquad T = T_{in}$$

$$z = L: \qquad \frac{\partial c_i}{\partial x} = 0 \qquad u = 0 \qquad \frac{\partial T}{\partial x} = 0$$

Boundary conditions for adsorption (AD) step

$$x = 0: \qquad \varepsilon_b D_{ax} \frac{\partial c_i}{\partial x} = u\left(c_i - c_{i,in}\right) \qquad T = T_{in}$$

$$x = L: \qquad \frac{\partial c_i}{\partial x} = 0 \qquad u = u_{PROD} \qquad \frac{\partial T}{\partial x} = 0$$

Boundary conditions for top-to-top equalization (E) step

column providing equalization

$$x = 0: \qquad \frac{\partial c_i}{\partial x} = 0 \qquad u = 0 \qquad \frac{\partial T}{\partial x} = 0$$

$$x = L: \qquad \frac{\partial c_i}{\partial x} = 0 \qquad u = u_E \qquad \frac{\partial T}{\partial x} = 0$$

column receiving equalization

$$x = 0: \qquad \frac{\partial c_i}{\partial x} = 0 \qquad u = 0 \qquad \frac{\partial T}{\partial x} = 0$$

$$x = L: \qquad \varepsilon_b D_{ax} \frac{\partial c_i}{\partial x} = u\left(c_i - c_i\big|_{x=L,\ column\ providing\ E}\right) \qquad u = u_E$$

Boundary conditions for backfill (B) step

$$x = 0: \qquad \frac{\partial c_i}{\partial x} = 0 \qquad u = 0 \qquad \frac{\partial T}{\partial x} = 0$$

$$x = L: \qquad \varepsilon_b D_{ax} \frac{\partial c_i}{\partial x} = u\left(c_i - \overline{c}_i\big|_{x=L,\ column\ runing\ AD}\right) \qquad u = u_B \qquad \frac{\partial T}{\partial x} = 0$$

Boundary conditions for vacuum (VA) step

$$x = 0: \qquad \frac{\partial c_i}{\partial x} = 0 \qquad \frac{\partial T}{\partial x} = 0 \qquad u = u_{VA}$$

$$x = L: \qquad \frac{\partial c_i}{\partial x} = 0 \qquad u = 0 \qquad \frac{\partial T}{\partial x} = 0$$

Boundary conditions for vacuum with purge (VP) step

$$x = 0: \qquad \frac{\partial c_i}{\partial x} = 0 \qquad \frac{\partial T}{\partial x} = 0 \qquad u = u_{VP}$$

$$x = L: \qquad \varepsilon_b D_{ax} \frac{\partial c_i}{\partial x} = u\left(c_i - c_i\big|_{x=L,\ column\ runing\ AD}\right) \qquad u = u_{PG} \qquad \frac{\partial T}{\partial x} = 0$$

The molar velocities across the valve orifices, during equalization (E) and backfill (B) steps, are described by [4]:

$$u \cdot p = \begin{cases} 2.035 \times 10^{-2} \dfrac{C_v \cdot p^{STP}}{\varepsilon_b A \cdot T^{STP}} \sqrt{\dfrac{p_u^2 - p_d^2}{p_d M}} T, & p_d > 0.53 p_u \\ 2.035 \times 10^{-2} \dfrac{C_v \cdot p^{STP}}{\varepsilon_b A \cdot T^{STP}} p_u \sqrt{\dfrac{1}{p_d M}} T, & p_d \le 0.53 p_u \end{cases} \tag{5.17}$$

where p_u and p_d are the upstream and downstream pressures, respectively, C_v is the valve parameter, and A is the area of the orifice. The superscript "STP" stands for standard temperature and pressure conditions.

The set of model equations was solved numerically using Aspen Adsorption 7.3. The Aspen Adsorption simulator uses the method of lines [35] to solve the time-dependent partial differential equations. The spatial derivatives were discretized over a uniform grid of 40 points using the quadratic upwind differencing scheme; the resulting equations were integrated as a function of the time using subroutine Gear. Physical gas properties were locally estimated based on the Aspen Properties database. The input parameters of the model are listed in Table 5.3 and Table 5.4.

5.3 Results and discussion

Three configurations of the two-stage VPSA unit were studied for producing a stream of 99.5+% of oxygen from air at the highest recovery, as described before. The two-stage VPSA unit has several operating variables (see Table 5.5) that should be simultaneously optimised, originating an extremely complex to solve optimization problem. Moreover, when combining two PSA units, new boundary conditions arise, namely the product flow rate and pressure of the first PSA unit must match with the feed flow rate of the second PSA unit, which must be taken into account. Based on the preliminary experiments and on previous knowledge only high operating pressure (P_H) and raffinate flow rate (F_{RAFF}) of first stage, adsorption time (t_{AD}) of both stages and pressurization step (t_{PR}) of second stage were studied and selected for optimization. Also, the role of these operating variables in the process performance was evaluated, where purity is the oxygen molar fraction of the product stream and recovery is the molar ratio between the amount of oxygen produced and fed to the PSA unit per adsorption cycle when the PSA unit is operating at cycle steady-state.

The three simulators were checked for their ability to reproduce accurately the experimental results and the optimum operating conditions obtained. The discussion of the results is detailed for each configuration as follows.

5.3.1 EPSA/VPSA unit

The second stage, AgLiLSX loaded VPSA unit, was fed with a synthetic gas mixture of 95 % oxygen and 5 % argon and optimized to produce 99.5 % of oxygen. The feed composition was assumed constant and fully available throughout the entire VPSA cycle. From previous experience [24] several operating variables were set constant – Table 5.5. The role of pressurization (t_{PR}) and adsorption (t_{AD}) times on

Table 5.5 – Operating variables of configuration KPSA/VPSA.

KPSA		
variable	*name*	*comment*
P_H	high operating pressure	studied and optimized
P_L	low operating pressure	set by boundary condition; depends on $P_{H \mid KPSA}$ and also on $F_{FEED \mid VPSA}$ and $P_{H \mid VPSA}$
t_{PR}	pressurization time	set to 4 s; minimum time necessary to allow beds to reach $P_{H \mid KPSA}$
t_{AD}	adsorption time	studied and optimized
t_E	equalization time	set to 2 s; minimum time necessary to allow complete equalization
P/F *ratio*	purge to feed ratio	set to 0.01; process does not require purge
F_{FEED}	feed flow rate	set by boundary condition; depends on $P_{H \mid KPSA}$, cycle duration and flow rate delivered by the compressor
F_{PR}	pressurization flow rate	set by boundary condition; depends on $P_{H \mid KPSA}$ and flow rate delivered by the compressor
F_{RAFF}	raffinate flow rate	studied and optimized
F_{bPROD}	blowdown product flow rate	set by boundary condition; depends on $F_{RAFF \mid KPSA}$ and $F_{FEED \mid KPSA}$
F_E	equalization flow rate	set by boundary condition; depends on $P_{H \mid KPSA}$, $P_{L \mid KPSA}$ and equalization valve coefficient
T	temperature	set to room temperature (ca. 25 °C)

Table 5.5 (cont.) – Operating variables of configuration KPSA/VPSA.

VPSA		
variable	*name*	*comment*
P_H	high operating pressure	set (1.4 bar or 1.5 bar); based on previous knowledge and optimization
P_L	low operating pressure	set by boundary condition (ca. 0.2 bar); depends on $P_{H\mid VPSA}$, cycle duration and vacuum pump capacity
t_{PR}	pressurization time	studied and optimized
t_{AD}	adsorption time	studied and optimized
t_E	equalization time	set to 4s; minimum time necessary to allow complete equalization
t_B	backfill time	set to 0.5 s; previously optimized, should be the shortest time possible
$P/F\ ratio$	purge to feed ratio	set to 0.01 (< 0.05 for EPSA/VPSA configuration); previously optimized
F_{FEED}	feed flow rate	set by boundary condition; depends on product flow rate from the first stage
F_{PR}	pressurization flow rate	set by boundary condition; depends on $P_{H\mid VPSA}$ and product flow rate from the first stage
F_{PROD}	product flow rate	set to 0.04 $L_{STP}\cdot min^{-1}$ or 0.1 $L_{STP}\cdot min^{-1}$ to match the required productivity
F_E	equalization flow rate	set by boundary condition; depends on $P_{H\mid VPSA}$, $P_{L\mid VPSA}$ and equalization valve coefficient
F_B	backfill flow rate	set by boundary condition; should be high enough for backfill to occur in the shortest time possible
T	temperature	set to room temperature (ca. 25 °C)

product purity and recovery were experimentally investigated; the searching range of the selected optimization variables was based on previous studies. t_{PR} was varied between 4 s and 6 s; this is the step time range required for the bed to reach high operating pressure and small variations within this range has significant effect on purity and recovery. t_{AD} was varied between 4 s and 8 s; it was calculated that the oxygen concentration front exits the bed within this step time range.

The details of operating conditions are shown in Table 5.6. The experimental and simulation results are plotted in Figure 5.4 and Figure 5.5. It is noticeable the good fitting of the simulation to the experimental results (average relative difference of 0.005 % for purity and 0.820 % for recovery).

Table 5.6 – Operating conditions for VPSA unit loaded with AgLiLSX.

Run	Feed (%)	P_H (bar)	P_L (bar)	P/F ratio	F_{PROD} (L_{STP}·min^{-1})	cycle steps (s) PR - AD - E - VA - VP - E - B
1	95:5 (O_2:Ar)	1.40	0.17	0.03	0.10	**4** - **4** - 4 - **5.2** - **4** - 4 - 1.2
2						**5** - **4** - 4 - **6.2** - **4** - 4 - 1.2
3						**6** - **4** - 4 - **7.2** - **4** - 4 - 1.2
4				0.04		**4** - **6** - 4 - **5.2** - **6** - 4 - 1.2
5						**5** - **6** - 4 - **6.2** - **6** - 4 - 1.2
6						**6** - **6** - 4 - **7.2** - **6** - 4 - 1.2
7				0.05		**4** - **8** - 4 - **5.2** - **8** - 4 - 1.2
8						**5** - **8** - 4 - **6.2** - **8** - 4 - 1.2
9						**6** - **8** - 4 - **7.2** - **8** - 4 - 1.2

The product purity decreases as t_{AD} increases and similar behavior is observed when t_{PR} increases, particularly for higher values of t_{AD} (Figure 5.4). The maximum product purity obtained, 99.28 %, was for $t_{PR} = 4s$ and $t_{AD} = 4s$ (run 1), recovery of 8.6 %. Concerning recovery, it increases as t_{PR} and t_{AD} increase; the maximum oxygen recovery was ca. 12 % (run 9), purity of 99.15 %, when $t_{PR} = 6s$ and $t_{AD} = 8s$ (Figure 5.5). Since operating variables, t_{PR} and t_{AD}, have opposite responses on purity and recovery, a compromise between purity and recovery should be considered.

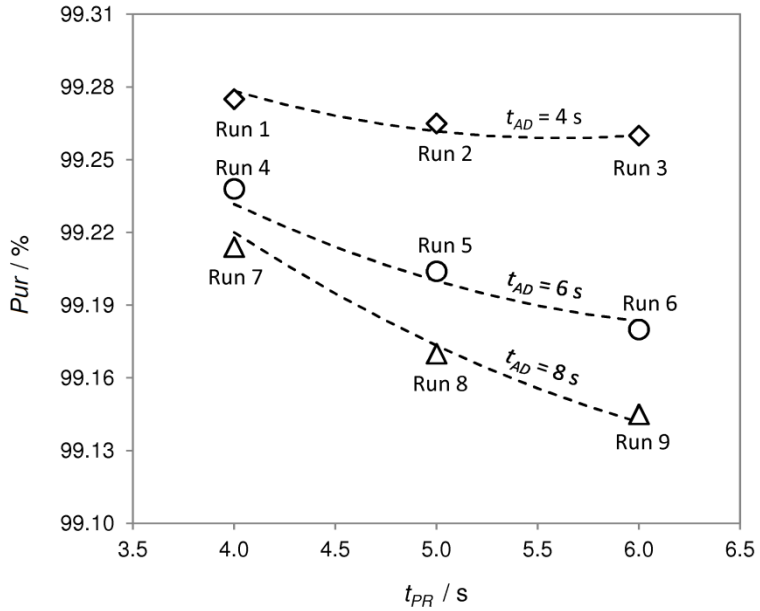

Figure 5.4 – Effects of VSPA cycle pressurization and adsorption times on product purity; dots are experimental and lines are simulation results – configuration EPSA/VPSA.

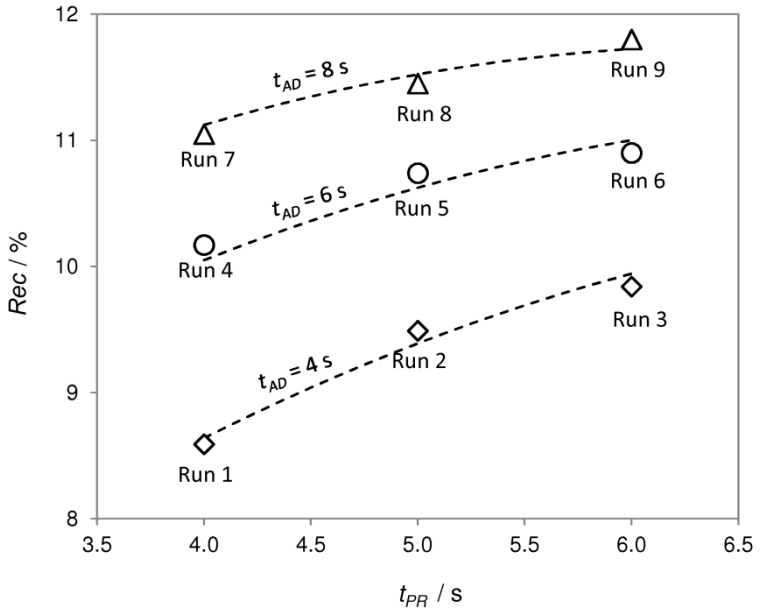

Figure 5.5 – Effects of VSPA cycle pressurization and adsorption times on oxygen recovery; dots are experimental and lines are simulation results – configuration EPSA/VPSA.

Oxygen concentration history inside an adsorption bed was recorded using a mass spectrometer connected to five sampling points (S1 to S5, see Figure 5.1) placed along the adsorption bed. Figure 5.6 plots the concentration profiles obtained during one cycle of run 3 ($t_{PR} = 6s$ and $t_{AD} = 4s$; oxygen purity of 99.26 % with 9.8 % recovery), after reaching the cyclic steady-state; the normalized axial position goes from 0 (feed end) to 1 (product end). The adsorption cycle steps are marked with different colors for readability. Oxygen concentration inside adsorption beds varies between ca. 90 % and 99.26 %; the minimum concentration occurs during VP step, near to the entrance of the column, where the gas phase is richer in desorbed argon; the oxygen concentration increases along the bed and it is always higher than 98.5 % near to the product end, with the maximum concentration (ca. 99.26 %) observed during the AD step.

The EPSA/VPSA combined unit did not allow reaching the target oxygen concentration of 99.5+%. In fact, despite the high oxygen concentration (95 %) at the VPSA feed stream, the separation between oxygen and argon is hard to achieve. The VPSA unit using AgLiLSX was able to produce 0.1 $L_{STP}{\cdot}min^{-1}$ at ca. 99.3 % of oxygen, with a reasonable recovery of 9+%. The productivity of the VPSA stage, computed from the ratio between the product flow rate and the amount of adsorbent used, is 7.3 $m^3{\cdot}hr^{-1}{\cdot}ton^{-1}$. This result is considerably better than that reported by Dee et al. [23], who indicates a maximum product concentration of 99 %, with 4.3 % recovery, from a feed stream of 95 % oxygen balanced with argon, obtained from simulation. The reason for this difference seems to be related mostly to the use by Dee at al. of columns packed with a LiLSX zeolite with only a layer of AgLiLSX.

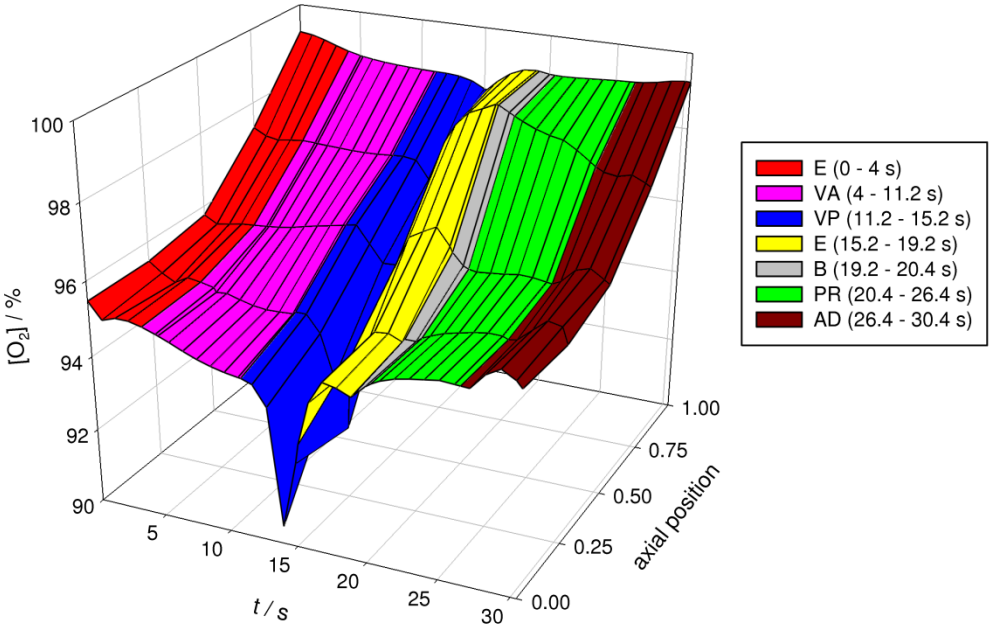

Figure 5.6 – Steady state experimental oxygen concentration profile inside the column during one cycle of run 3. Axial position goes from 0 (feed end) to 1 (product end). Different steps are marked with different colors according to figure label – configuration EPSA/VPSA.

5.3.2 KPSA/VPSA unit

The role of the following operating variables on the product purity and recovery were studied: KPSA high operation pressure ($P_{H\,|\,KPSA}$), KPSA adsorption time ($t_{AD\,|\,KPSA}$) and KPSA raffinate flow rate ($F_{RAFF\,|\,KPSA}$), VPSA pressurization time ($t_{PR\,|\,VPSA}$) and VPSA adsorption time ($t_{AD\,|\,VPSA}$); the searching range of the selected optimization operating variables was based on preliminary studies. $P_{H\,|\,KPSA}$ was varied between 3.8 bar and 4.4 bar; this pressure range was selected based on CMS adsorption capacity and uptake rates and also because $P_{H\,|\,VPSA}$ should not be higher than 1.5 bar [24]; since this configuration does not use a blower to pressurize the first stage

blowdown stream to the second stage, the first stage low-pressure product sets the high operating pressure for the second stage ($P_{L\,|\,KPSA} \approx P_{H\,|\,VPSA}$). $t_{AD\,|\,KPSA}$ was varied between 20 and 26 s; this was found to be the time range that originates the highest product concentrations. $F_{RAFF\,|\,KPSA}$ was varied from 1 L_{STP}·min^{-1} and 5 L_{STP}·min^{-1} to cover the entire recovery range. $t_{PR\,|\,VPSA}$ was varied from 4 s and 6 s, and $t_{AD\,|\,VPSA}$ was varied from 6 s and 8 s, as previously mentioned [24]. The complete list of pre-set variables and their values and the optimization variables and their searching ranges are shown in Table 5.7.

Table 5.7 – Operating conditions of configuration KPSA/VPSA.

k-PSA	
pressure low (P_L), bar	1.60
pressurization time (t_{PR}), s	4.0
equalization time (t_E), s	2.0
purge to feed ratio (P/F ratio)	0.01
temperature (T), °C	25
pressure high (P_H), bar	3.8 - 4.4
raffinate flow rate (F_{RAFF}), L_{STP}·min^{-1}	1 - 5
adsorption time (t_{AD}), s	20 - 26
E-VPSA	
pressure high (P_H), bar	1.50
pressure low (P_L), bar	0.20
equalization time (t_E), s	4.0
backfill time (t_B), s	0.5
purge to feed ratio (P/F ratio)	0.01
temperature (T), °C	25
pressurization time (t_{PR}), s	4 - 6
adsorption time (t_{AD}), s	6 - 8

Table 5.8 – Experimental and simulation results of configuration KPSA/VPSA.

	KPSA			VPSA		Experimental		Simulated	
Run	P_H (bar)	$F_{RAFF\ top}$ (L_{STP}·min^{-1})	t_{AD} (s)	t_{PR} (s)	t_{AD} (s)	Pur. (%)	Rec. (%)	Pur. (%)	Rec. (%)
1	4.40	1	20	4	8	99.43	5.59	99.42	5.60
2	4.40	5	26	4	8	99.55	2.48	99.55	2.50
3	4.10	3	26	5	7	99.57	3.54	99.56	3.57
4	3.80	5	20	6	6	99.51	2.56	99.53	2.56
5	4.10	3	23	4	7	99.55	3.51	99.54	3.47
6	4.10	3	23	5	7	99.56	3.57	99.57	3.56
7	4.40	1	26	4	6	99.46	5.42	99.46	5.43
8	4.10	3	20	5	7	99.54	3.48	99.54	3.47
9	3.80	1	20	6	8	99.45	6.24	99.43	6.22
10	4.10	3	23	5	7	99.56	3.59	99.57	3.56
11	4.40	1	26	6	8	99.44	6.13	99.44	6.12
12	4.40	5	20	6	8	99.44	2.54	99.44	2.55
13	3.80	1	26	4	8	99.41	6.14	99.41	6.10
14	4.40	1	20	6	6	99.43	5.66	99.43	5.69
15	4.10	3	23	5	7	99.56	3.56	99.57	3.56
16	4.40	5	26	6	6	99.59	2.55	99.59	2.56
17	4.10	5	23	5	7	99.58	2.54	99.58	2.49
18	3.80	1	26	6	6	99.45	6.32	99.46	6.29
19	4.40	3	23	5	7	99.56	3.58	99.57	3.50
20	4.10	3	23	5	8	99.56	3.63	99.56	3.65
21	3.80	1	20	4	6	99.45	5.75	99.42	5.78
22	4.10	3	23	5	6	99.58	3.54	99.57	3.53
23	4.40	5	20	4	6	99.57	2.46	99.57	2.49
24	3.80	5	20	4	8	99.56	2.59	99.54	2.58
25	4.10	1	23	5	7	99.49	5.77	99.48	5.83
26	3.80	5	26	4	6	99.55	2.56	99.53	2.50
27	3.80	3	23	5	7	99.58	3.64	99.57	3.73
28	3.80	5	26	6	8	99.56	2.62	99.58	2.61
29	4.10	3	23	6	7	99.53	3.62	99.54	3.67

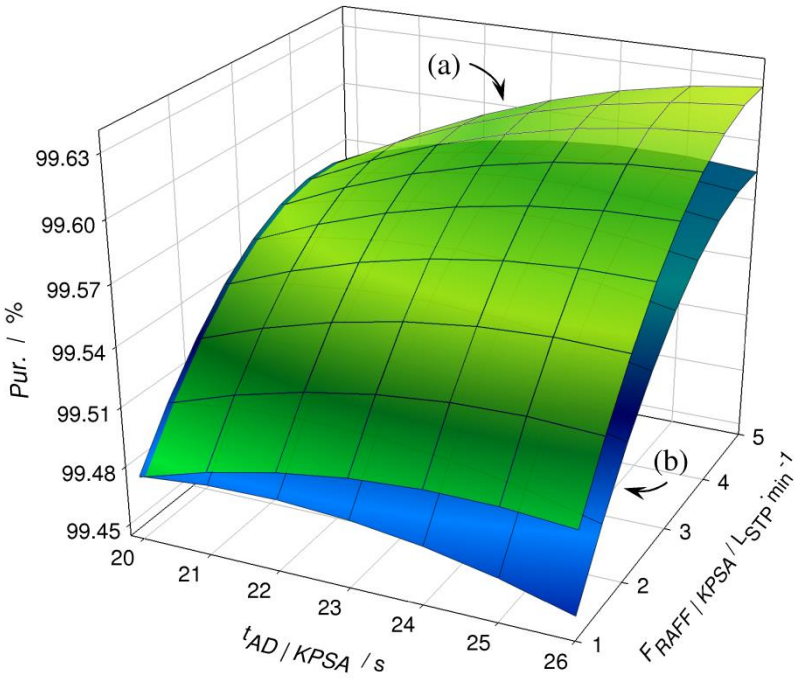

Figure 5.7 – Oxygen concentration as a function of KPSA adsorption time ($t_{AD\,|\,KPSA}$) and KPSA raffinate flow rate ($F_{RAFF\,|\,KPSA}$) when: (a) $P_{H\,|\,KPSA} = 4.4\,\text{bar}$, $t_{PR\,|\,VPSA} = 5\,\text{s}$ and $t_{AD\,|\,VPSA} = 6\,\text{s}$; and (b) $P_{H\,|\,KPSA} = 3.8\,\text{bar}$, $t_{PR\,|\,VPSA} = 5\,\text{s}$ and $t_{AD\,|\,VPSA} = 6\,\text{s}$ – configuration KPSA/VPSA.

Table 5.8 summarizes the runs conducted and the experimental and simulated results obtained; again, the simulator fits quite well the experimental results (average relative difference of 0.009 % for purity and 0.769 % for recovery). The role of $t_{AD\,|\,KPSA}$ on product purity is illustrated in Figure 5.7 and Figure 5.9. The product purity increases as $t_{AD\,|\,KPSA}$ increases, particularly for higher values of $F_{RAFF\,|\,KPSA}$. Concerning recovery, the influence of the $t_{AD\,|\,KPSA}$ on recovery is negligible – see Figure 5.8 and Figure 5.10; therefore, variable $t_{AD\,|\,KPSA}$ was set to 26 s.

Figure 5.7 and Figure 5.8 show, respectively, the effect of $F_{RAFF\,|\,KPSA}$ on product purity and recovery. This operating variable has a strong influence on the process performance; as it can be seen oxygen product concentration increases with $F_{RAFF\,|\,KPSA}$ from 99.48 % to ca. 99.63 %, and the opposite happens for recovery, decreasing from ca. 6 % to ca. 2.5 %. Increasing $F_{RAFF\,|\,KPSA}$ allows slow nitrogen and argon molecules to purge more efficiently from the adsorption bed, preventing them from contaminating the extract (blowdown) stream obtained during BD and PG steps; however, higher $F_{RAFF\,|\,KPSA}$ values originate a reduction in the intermediate product flowrate as well as the loss of non-adsorbed oxygen in the raffinate stream and then a reduction in the recovery.

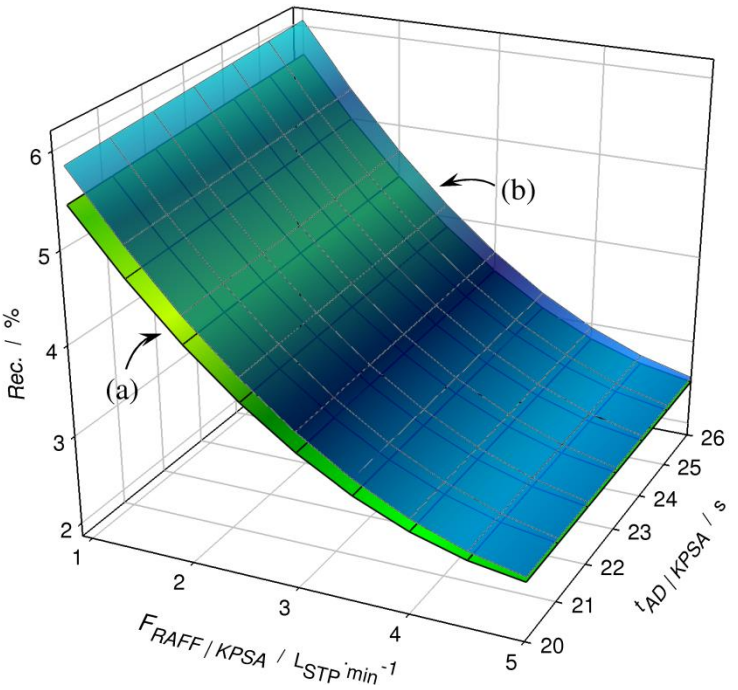

Figure 5.8 – Oxygen recovery as a function of KPSA adsorption time ($t_{AD\,|\,KPSA}$) and KPSA raffinate flow rate ($F_{RAFF\,|\,KPSA}$) when: (a) $P_{H\,|\,KPSA} = 4.4\,\text{bar}$, $t_{PR\,|\,VPSA} = 5\,\text{s}$ and $t_{AD\,|\,VPSA} = 6\,\text{s}$; and (b) $P_{H\,|\,KPSA} = 3.8\,\text{bar}$, $t_{PR\,|\,VPSA} = 5\,\text{s}$ and $t_{AD\,|\,VPSA} = 6\,\text{s}$ – configuration KPSA/VPSA.

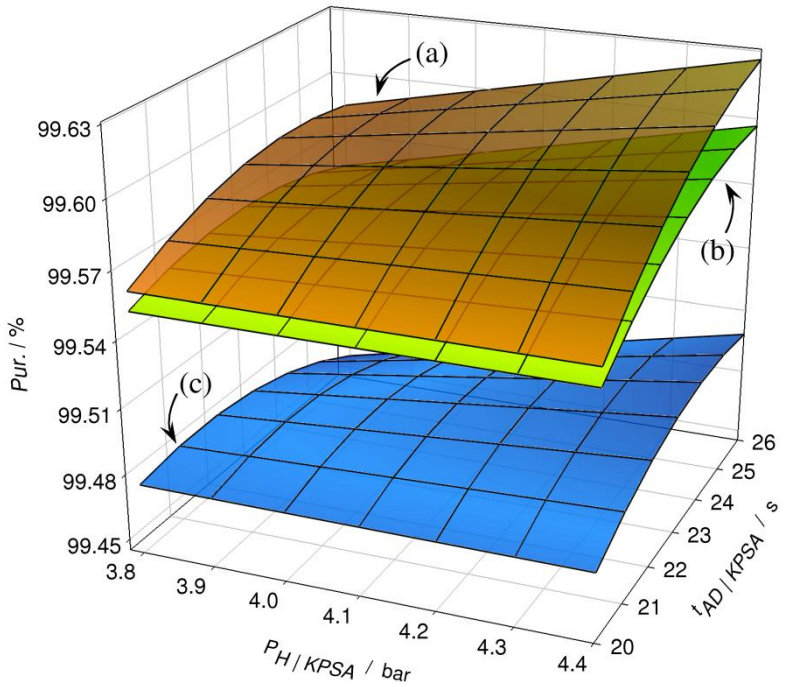

Figure 5.9 – Oxygen concentration as a function of KPSA high operating pressure ($P_{H\,|\,KPSA}$) and KPSA adsorption time ($t_{AD\,|\,KPSA}$) when: (a) $F_{RAFF\,|\,KPSA} = 5\,\mathrm{L_{STP}}\cdot\mathrm{min^{-1}}$, $t_{PR\,|\,VPSA} = 5\,\mathrm{s}$ and $t_{AD\,|\,VPSA} = 6\,\mathrm{s}$; (b) $F_{RAFF\,|\,KPSA} = 3\,\mathrm{L_{STP}}\cdot\mathrm{min^{-1}}$, $t_{PR\,|\,VPSA} = 5\,\mathrm{s}$ and $t_{AD\,|\,VPSA} = 6\,\mathrm{s}$; and (c) $F_{RAFF\,|\,KPSA} = 1\,\mathrm{L_{STP}}\cdot\mathrm{min^{-1}}$, $t_{PR\,|\,VPSA} = 5\,\mathrm{s}$ and $t_{AD\,|\,VPSA} = 6\,\mathrm{s}$ – configuration KPSA/VPSA.

The influence of $P_{H\,|\,KPSA}$ on product purity is illustrated in Figure 5.9. The effect of this operating variable in the product purity deeply depends on operating variables $t_{AD\,|\,KPSA}$ and $F_{RAFF\,|\,KPSA}$; for instance, when $t_{AD\,|\,KPSA}$ = 20 s, product purity hardly depends on $P_{H\,|\,KPSA}$ and when $t_{AD\,|\,KPSA}$ = 26 s, product purity increases with the increase of $P_{H\,|\,KPSA}$ (particularly for higher $F_{RAFF\,|\,KPSA}$). The maximum product purity is obtained when $t_{AD\,|\,KPSA}$ is 26 s and $F_{RAFF\,|\,KPSA}$ is 5 L_{STP}·min^{-1}. It is noteworthy that for these conditions the oxygen concentration only slightly increases when

$P_{H\,|\,KPSA}$ moves from 3.8 bar to 4.4 bar (see Figure 5.9), while the recovery slightly decreases (see Figure 5.10). Taking into account the pressurization energy, working at the lowest pressure limit is advantageous.

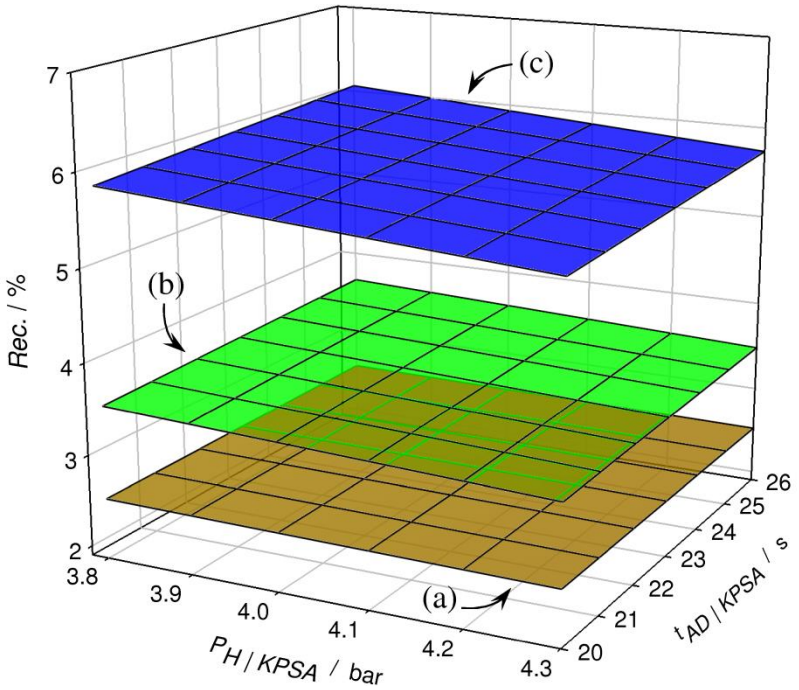

Figure 5.10 – Oxygen recovery as a function of KPSA high operating pressure ($P_{H\,|\,KPSA}$) and KPSA adsorption time ($t_{AD\,|\,KPSA}$) when: (a) $F_{RAFF\,|\,KPSA} = 5\mathrm{L_{STP}} \cdot \mathrm{min^{-1}}$, $t_{PR\,|\,VPSA} = 5\mathrm{s}$ and $t_{AD\,|\,VPSA} = 6\mathrm{s}$; (b) $F_{RAFF\,|\,KPSA} = 3\mathrm{L_{STP}} \cdot \mathrm{min^{-1}}$, $t_{PR\,|\,VPSA} = 5\mathrm{s}$ and $t_{AD\,|\,VPSA} = 6\mathrm{s}$; and (c) $F_{RAFF\,|\,KPSA} = 1\mathrm{L_{STP}} \cdot \mathrm{min^{-1}}$, $t_{PR\,|\,VPSA} = 5\mathrm{s}$ and $t_{AD\,|\,VPSA} = 6\mathrm{s}$ – configuration KPSA/VPSA.

The effect of $t_{PR|VPSA}$ and $t_{AD\,|\,VPSA}$ of second PSA stage (AgLiLSX stage) on product purity is illustrated in Figure 5.11. As it can be seen, decreasing $t_{AD\,|\,VPSA}$ leads to a significant increase of the product purity (particularly for higher $P_{H\,|\,KPSA}$ values; when $P_{H\,|\,KPSA}$ = 3.8 bar, product purity hardly depends on $t_{AD\,|\,VPSA}$). For higher $t_{AD\,|\,VPSA}$ values argon starts breakthrough the column and contaminating the product

stream. However, $t_{AD\,|\,VPSA}$ plays also an important role on the productivity since for $t_{AD\,|\,VPSA}$ < 6 s the unit is no longer able to produce the required product flowrate of 0.1 L_{SPT}·min^{-1}; this operating variable should then be set to balance the purity and recovery. Figure 5.11 shows the effect of $t_{PR\,|\,VPSA}$ on the product purity; purity reaches a local maximum for $t_{PR\,|\,VPSA}$ = 5 s. Figure 5.12 shows that recovery has a minimal dependence on $t_{AD\,|\,VPSA}$ but depends significantly on $t_{PR\,|\,VPSA}$; recovery increases as $t_{PR\,|\,VPSA}$ increases. Therefore, this operating variable should also be set to balance the purity and recovery.

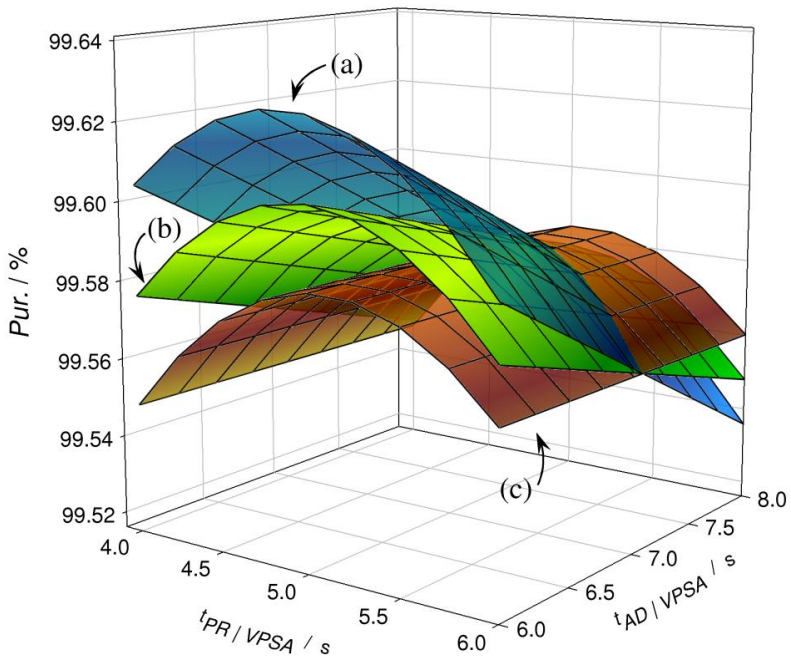

Figure 5.11 – Oxygen concentration as a function of VPSA pressurization ($t_{PR\,|\,VPSA}$) and adsorption time ($t_{AD\,|\,VPSA}$) when: (a) $P_{H\,|\,KPSA} = 4.4\,\text{bar}$, $t_{AD\,|\,KPSA} = 26\,\text{s}$ and $F_{RAFF\,|\,KPSA} = 5\,\text{L}_{\text{STP}} \cdot \text{min}^{-1}$; (b) $P_{H\,|\,KPSA} = 4.1\,\text{bar}$, $t_{AD\,|\,KPSA} = 26\,\text{s}$ and $F_{RAFF\,|\,KPSA} = 5\,\text{L}_{\text{STP}} \cdot \text{min}^{-1}$; and (c) $P_{H\,|\,KPSA} = 3.8\,\text{bar}$, $t_{AD\,|\,KPSA} = 26\,\text{s}$ and $F_{RAFF\,|\,KPSA} = 5\,\text{L}_{\text{STP}} \cdot \text{min}^{-1}$ – configuration KPSA/VPSA.

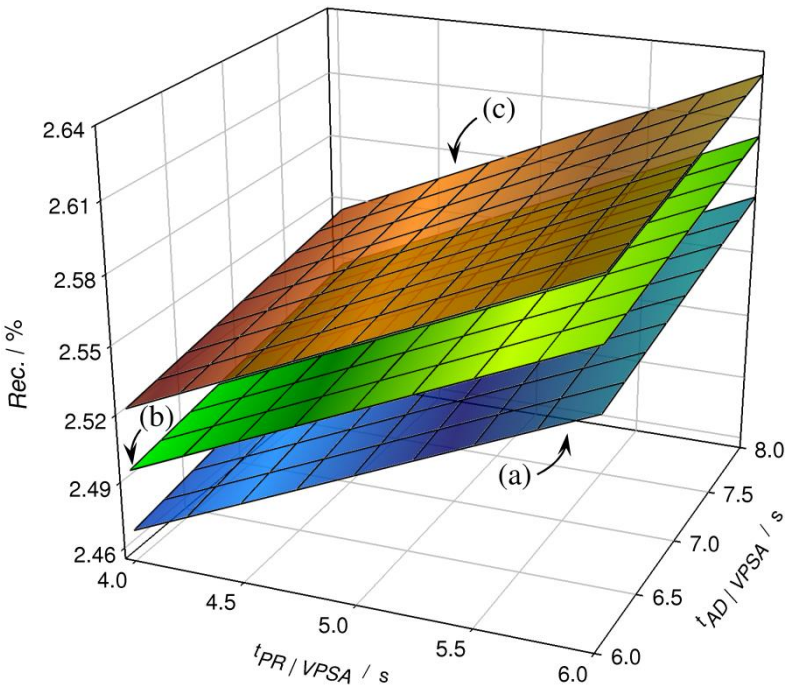

Figure 5.12 – Oxygen recovery as a function of VPSA pressurization ($t_{PR\,|\,VPSA}$) and adsorption time ($t_{AD\,|\,VPSA}$) when: (a) $P_{H\,|\,KPSA} = 4.4\,\text{bar}$, $t_{AD\,|\,KPSA} = 26\,\text{s}$ and $F_{RAFF\,|\,KPSA} = 5\,\text{L}_{\text{STP}} \cdot \text{min}^{-1}$; (b) $P_{H\,|\,KPSA} = 4.1\,\text{bar}$, $t_{AD\,|\,KPSA} = 26\,\text{s}$ and $F_{RAFF\,|\,KPSA} = 5\,\text{L}_{\text{STP}} \cdot \text{min}^{-1}$; and (c) $P_{H\,|\,KPSA} = 3.8\,\text{bar}$, $t_{AD\,|\,KPSA} = 26\,\text{s}$ and $F_{RAFF\,|\,KPSA} = 5\,\text{L}_{\text{STP}} \cdot \text{min}^{-1}$ – configuration KPSA/VPSA.

Simulations were performed to find the optimum operating conditions for obtaining the maximum oxygen purity. The conditions obtained (run 30) were experimentally tested and results are presented in Table 5.9. It was experimentally observed a maximum purity of 99.6 % with an oxygen recovery of 2.8 % (oxygen recovery of KPSA is 44.5 % and of VPSA is 6.2 %). If the oxygen target concentration is set to 99.5 %, higher recoveries can be obtained; it was experimentally observed a purity of 99.52 % with a reasonable recovery, 5.9 % (oxygen recovery of KPSA is 82.8 % and of VPSA is 7.1 %) - run 31.

Table 5.9 – Optimum conditions and experimental results for configuration KPSA/VPSA.

	KPSA					VPSA						
Run	P_H (bar)	P_L (bar)	P/F ratio	F_{RAFF} (L_{STP}·min^{-1})	cycle steps (s) PR-**AD**-E-BD-**PG**-E	P_H (bar)	P_L (bar)	P/F ratio	F_{PROD} (L_{STP}·min^{-1})	cycle steps (s) **PR**-**AD**-E-**VA**-**VP**-E-B	Pur (%)	Rec (%)
30	**4.40**	1.60	0.01	**4.5**	4 - **26** - 2 - 4 - **26** - 2	1.50	0.20	0.01	0.04	**5** - **6** - 4 - **5.5** - **6** - 4 - 0.5	99.60	2.75
31	**3.80**	1.60	0.01	**1.2**	4 - **23** - 2 - 4 - **23** - 2	1.50	0.20	0.01	0.04	**5.5** - **8** - 4 - **6** - **8** - 4 - 0.5	99.52	5.92
32	**4.80**	1.60	0.01	**5.0**	4 - **26** - 2 - 4 - **26** - 2	1.50	0.20	0.01	0.04	**5** - **4** - 4 – **5.5** - **4** - 4 - 0.5	99.65	2.45
33	**3.50**	1.60	0.01	**1.2**	4 - **22** - 2 - 4 - **22** - 2	1.50	0.20	0.01	0.04	**5.5** - **8** - 4 – **6** - **8** - 4 - 0.5	99.51	6.25

Table 5.10 – Optimum operating conditions and experimental results for configuration KPSA/RP/VPSA.

	k-PSA						
Run	P_H (bar)	P_L (bar)	P/F ratio	F_{RAFF} (L_{STP}·min^{-1})	cycle steps (s) PR - AD - E - BD - PG - E	intermediate product composition – extract (%)	Rec (%)
34	6.00	1.00	0.01	3	4 – 30 – 2 – 4 – 30 – 2	59.24 % N_2; 40.13 % O_2; 0.63 % Ar	93.70

	VPSA								
Run	P_H (bar)	P_L (bar)	P/F ratio	F_{PROD} (L_{STP}·min^{-1})	cycle steps (s) PR - AD - E - VA - VP - E - B	Pur (%)	Rec (%)	Productivity (m^3·hr^{-1}·ton^{-1})	Overall Rec (%)
34a	1.50	0.20	0.01	0.04	5.5 – 8 – 4 – 6 – 8 - 4 – 0.5	99.75	5.95	10.2	5.6
34b	1.50	0.20	0.01	0.10	5.5 – 9 – 4 – 6 – 9 - 4 – 0.5	99.51	15.1	25.4	14.2

Since the ASPEN simulator was found to fit quite well the experimental results, several other runs were conducted to find other local optima, outside the initial searching domain, maximizing oxygen purity with the highest recovery possible. Maximum oxygen purity of 99.65 % with small recovery, 2.5 % (oxygen recovery of KPSA is 45.8 % and of VPSA is 5.3 %), were experimentally obtained (run 32) for $P_{H\,|\,KPSA}$ = 4.8 bar and $t_{AD\,|\,VPSA}$ = 4 s. Also, for an oxygen product concentration of 99.5 %, the maximum experimental oxygen recovery obtained was 6.3 % (oxygen recovery of KPSA is 86.8 % and of VPSA is 7.2 %) – run 33, for $P_{H\,|\,KPSA}$ = 3.5 bar. The productivity of the VPSA stage is 10.7 $m^3 \cdot hr^{-1} \cdot ton^{-1}$.

5.3.3 KPSA/RP/VPSA unit

KPSA oxygen-enriched (blowdown) stream is obtained at low pressure, during the blowdown step. The configuration previously reported, where the low pressure of the first stage is equal to the high operating pressure of the second stage ($P_{L\,|\,KPSA} \approx P_{H\,|\,VPSA}$), saves an intermediate blower and allows to produce a product stream of 99.5+% oxygen with reasonable oxygen recovery (6+%). However, higher recoveries can be obtained if this intermediate blower exists. Since the proposed model was found to fit quite well the experimental results, this two-stage configuration was simulated and optimized using ASPEN simulator and the accuracy of the results assessed experimentally for the optimized operating conditions.

According to the simulator, the maximum oxygen purity of 99.73 % was obtained for run 34/34a (Table 5.10), with an oxygen recovery of 5.7 %. The operating conditions were experimentally tested and it was observed a product purity of 99.75 % with a recovery of 5.6 % (run 34/34a). The productivity of the VPSA stage was 10.7 $m^3 \cdot hr^{-1} \cdot ton^{-1}$. On the other hand, for an oxygen product concentration of

99.53 %, the highest recovery was 14.5 % – run 34/34b in Table 5.10. For this run, the experimental oxygen concentration was 99.51 % with a recovery of 14.2 %. The productivity of the VPSA stage was 25.4 $m^3 \cdot hr^{-1} \cdot ton^{-1}$. Again, it was observed a good fit with the experimental values.

Figure 5.13 shows the simulated cyclic steady-state oxygen mole fraction profiles and axial temperature along the bed at initial and final instants of the adsorption (AD) step (run #34a). The oxygen mass-transfer zone travels the column during this step; the oxygen concentration reaches its maximum near to the product end of the column. The thermal wave follows the mass-transfer zone and shows small temperature excursion (ca. 2.5 °C); the thermal excursion is related mostly to the nitrogen adsorption and it is observed only in the first half of the bed.

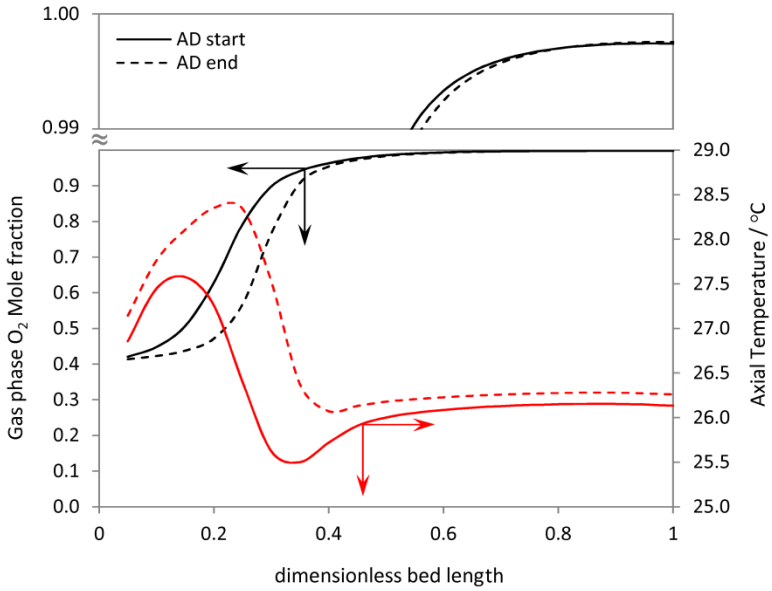

Figure 5.13 – Oxygen mole fraction and axial temperature profiles inside the adsorption column at the initial and final instants of adsorption (AD) step of run 34a.

The cyclic steady-state oxygen mole fraction profiles and axial temperature along the bed at initial and final instants of the evacuation (VA) and evacuation with purge (VP) steps (run 34a) are plotted in Figure 5.14. Again, the oxygen mass-transfer zone is traveling through the bed, followed by the thermal wave. Figure 5.14 illustrates the relevance of VA and VP steps to raise the oxygen concentration inside the bed. During these steps the adsorbed nitrogen and argon are displaced from the adsorption sites (causing the abrupt temperature decrease), slightly increasing the oxygen concentration in the bed.

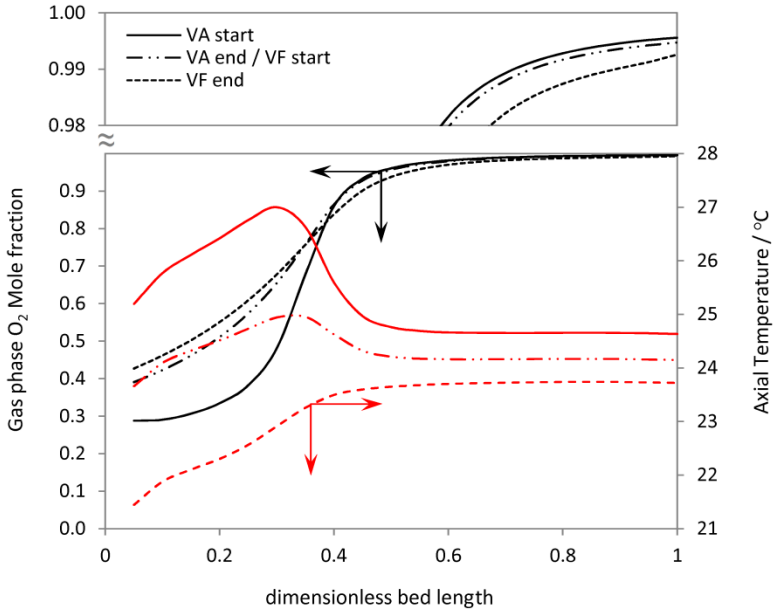

Figure 5.14 – Oxygen mole fraction and axial temperature profiles inside the adsorption column at the initial and final instants of evacuation (VA) and purge under vacuum (VP) step of run 34a.

Figure 5.15 shows the cyclic steady-state oxygen mole fraction profiles and axial temperature in the bed at the initial and final instants of equalization (E) and backfill (B) steps (run 34a). After the evacuation steps (VA and VP), the complete equalization takes place allowing the pressurizing bed to reach the maximum oxygen gas-phase concentration. Both equalization and backfill steps play an important role for the

oxygen concentration increase, thus preparing the bed for the adsorption step that should deliver a high oxygen product concentration.

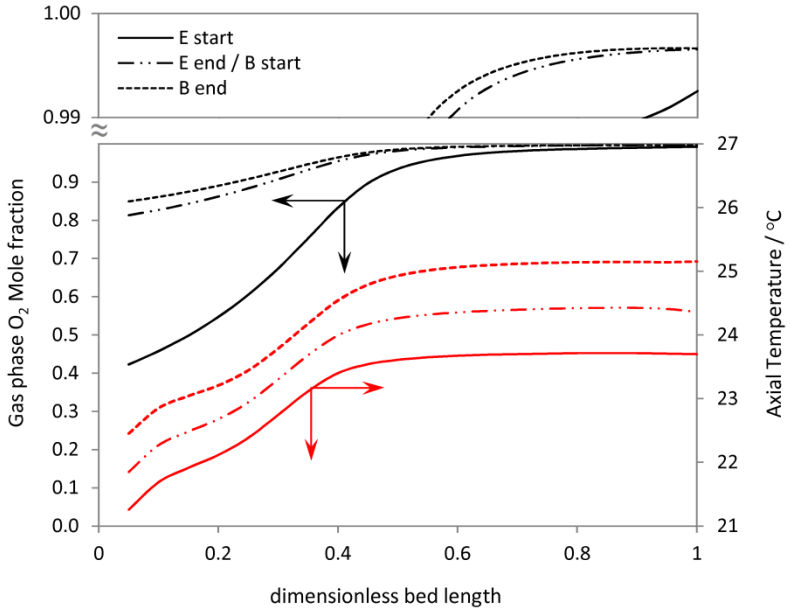

Figure 5.15 – Oxygen mole fraction and axial temperature profiles inside the adsorption column at the initial and final instants of equalization (E) and backfill (B) step of run 34a.

The two-stage VPSA configurations were compared with single-stage VPSA units for high-purity oxygen production using AgLiLSX, of this work and reported in the literature – see Figure 5.16. This figure clearly shows an almost linear dependy between purity and recovery. It also shows that the two-stage processes studied (KPSA/VPSA, EPSA/VPSA and KPSA/RP/VPSA) produce higher purities and recoveries than the reported single-stage processes. The single-stage units, although simpler and low energy consuming (theoretical work [29] of ca. 2.0 J·m^3), cannot attain purities higher than 99.2 %. The two-stage KPSA/RP/VPSA unit though more complex and requiring more energy (theoretical work of ca. 5.3 J·m^3) is the one that produces the highest purities and recoveries, well above the other technologies. Moreover, taking

into account the specific energy consumption, the KPSA/VPSA (theoretical work of ca. 3.9 J·m^3) could be a reasonable option for oxygen concentrations of 99.5 %.

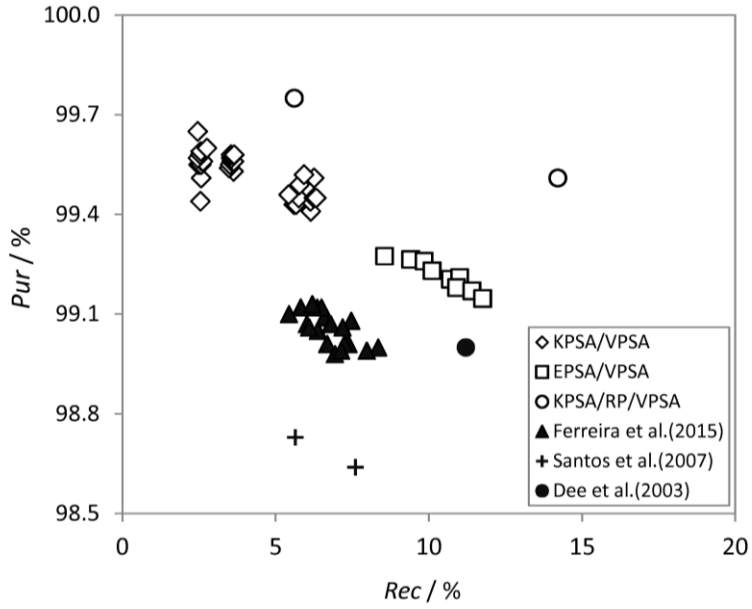

Figure 5.16 – Pareto plot of the purity as function of recovery for the two-stage VPSA configurations and single-stage VPSA units for high-purity oxygen production using AgLiLSX.

5.4 Conclusions

Three configurations of two-stage VPSA unit were studied, where the second stage uses the argon/oxygen selective zeolite AgLiLSX, for producing a stream of 99.5+% oxygen from air.

The EPSA/VPSA configuration comprises a conventional equilibrium based PSA stage producing a 95 % oxygen stream (balanced with argon), followed by a VPSA unit, packed with AgLiLSX for argon removal. The VPSA unit, operating between 1.4 bar and 0.2 bar, run a seven-step cycle, comprising pressurization, adsorption,

equalization, evacuation, purge under vacuum and backfill. The unit was optimized using a model implemented in ASPEN simulator; the simulator proved to represent accurately the experimental data. An experimental oxygen maximum concentration of 99.28 %, with 8.6 % of recovery and productivity of 7.3 $m^3 \cdot hr^{-1} \cdot ton^{-1}$ were obtained. It was concluded that the EPSA/VPSA configuration did not allow reaching the target oxygen concentration of 99.5+%.

Configuration KPSA/VPSA comprises a conventional kinetic based PSA, packed with CMS adsorbent, in series with a VPSA unit, packed with AgLiLSX. The KPSA, run a conventional Skarstrom cycle with equalization; the low operating pressure of the first KPSA stage was equal to the high operating pressure of the second VPSA stage – no intermediate blower was considered. The role of several operating variables – $P_{H \mid KPSA}$, $t_{AD \mid KPSA}$, $F_{RAFF \mid KPSA}$, $t_{PR \mid VPSA}$ and $t_{AD \mid VPSA}$ – on product purity and recovery was assessed using the ASPEN simulator, and a maximum oxygen product concentration of 99.6 % and a recovery of 2.8 % were obtained. On the other hand, for a product oxygen concentration of 99.5 %, the maximum recovery obtained by simulation and experimentally was 6.3 %; the productivity was 10.7 $m^3 \cdot hr^{-1} \cdot ton^{-1}$.

The KPSA/RP/VPSA configuration, differing from the previous configuration because it considers an intermediate blower (RP) between the first and second stages, was also studied. This configuration allowed obtaining higher product purities and recoveries. The maximum oxygen product concentration obtained using the simulation was 99.73 % with 5.7 % of recovery while the corresponding experimental values are an oxygen concentration of 99.75 % and a recovery of 5.6 %. On the other hand, for a product oxygen concentration of 99.5 %, the maximum recovery obtained by simulation and experimentally was 14.2 %; the productivity was 10.7 $m^3 \cdot hr^{-1} \cdot ton^{-1}$.

Acknowledgment

Daniel Ferreira acknowledges Fundação para a Ciência e Tecnologia (FCT) and Sysadvance, Sistemas de Engenharia S.A. the PhD grant (ref SFRH/BDE/51186/2010). The authors acknowledge the funding provided by Agência de Inovação (AdI) (project HPOVPSA, ref 13488).

5.5 References

1. Jee, J.-G., Lee, S.-J., Moon, H.-M., Lee, C.-H. Adsorption Dynamics of Air on Zeolite 13X and CMS Beds for Separation and Purification. *Adsorption.* **2005**, 11, 415-420.
2. Ferreira, D., Magalhães, R., Bessa, J., Taveira, P., Sousa, J., Whitley, R.D., Mendes, A. Study of AgLiLSX for Single-Stage High-Purity Oxygen Production. *Industrial & Engineering Chemistry Research.* **2014**, 53, 15508-15516.
3. Kim, M.-B., Jee, J.-G., Bae, Y.-S., Lee, C.-H. Parametric Study of Pressure Swing Adsorption Process To Purify Oxygen Using Carbon Molecular Sieve. *Industrial & Engineering Chemistry Research.* **2005**, 44, 7208-7217.
4. Santos, J.C., Cruz, P., Regala, T., Magalhães, F.D., Mendes, A. High-Purity Oxygen Production by Pressure Swing Adsorption. *Industrial & Engineering Chemistry Research.* **2006**, 46, 591-599.
5. Jee, J.-G., Kim, M.-B., Lee, C.-H. Pressure Swing Adsorption Processes to Purify Oxygen Using a Carbon Molecular Sieve. *Chemical Engineering Science.* **2005**, 60, 869-882.
6. Armond, J.W., Webber, D.A., Smith, K.C. Gas Separation. U.S. Patent 4,190,424, 1980.
7. Hayashi, S., Kawai, M., Kaneko, T. Dynamics of High Purity Oxygen PSA. *Gas Separation & Purification.* **1996**, 10, 19-23.
8. Miller, G.W., Theis, C.F. Molecular Sieve Oxygen Concentrator with Secondary Oxygen Purifier. U.S. Patent 4,880,443, 1989.
9. Haruna, K., Ueda, K., Inoue, M., Someda, H. Process for Producing High Purity Oxygen Gas from Air. U.S. Patent 4,985,052, 1991.
10. Stanford, R.A., Jenkins, C.E. Two Stage Super-Enriched Oxygen Concentrator. U.S. Patent 5,137,549, 1992.
11. Jee, J.-G., Lee, S.-J., Kim, M.-B., Lee, C.-H. Three-Bed PVSA Process for High-Purity O2 Generation from Ambient Air. *AIChE Journal.* **2005**, 51, 2988-2999.
12. Lee, S.-J., Jung, J.-H., Moon, J.-H., Jee, J.-G., Lee, C.-H. Parametric Study of the Three-Bed Pressure−Vacuum Swing Adsorption Process for High Purity O2 Generation from Ambient Air. *Industrial & Engineering Chemistry Research.* **2007**, 46, 3720-3728.

13. Lee, C.-H. Apparatus for Producing Oxygen and Method for Controlling the same. U.S. Patent 2006/0162565 A1, 2006.

14. Yang, R.T. *Adsorbents. Fundamentals and Applications*; John Wiley & Sons: New Jersey, USA, 2003.

15. Gaffney, T.R. Porous Solids for Air Separation*. Current Opinion in Solid State and Materials Science.* **1996**, 1, 69-75.

16. Coe, C.G. Moleculary Engineered Adsorbents for Air Separation*. Gas Separation Technology.* **1990**, 149-159.

17. Coe, C.G., Kuznicki, S.M., Srinivasan, R., Jenkins, R.J. Molecularly Engineered, High-Performance Adsorbent. In *Perspectives in Molecular Sieve Science;* ACS Symposium Series 368; American Chemical Society: Washington, DC, 1988; 478-491.

18. Rege, S.U., Yang, R.T. Limits for Air Separation by Adsorption with LiX Zeolite*. Industrial & Engineering Chemistry Research.* **1997**, 36, 5358-5365.

19. Hutson, N.D., Rege, S.U., Yang, R.T. Mixed Cation Zeolites: LixAgy-X as a Superior Adsorbent for Air Separation*. AIChE Journal.* **1999**, 45, 724-734.

20. Wilkerson, B.E. The Adsorption of Argon and Oxygen on Silver Mordenite. Master Thesis, Graduate School of the Ohio State University, Ohio, U.S.A., 1990.

21. Knaebel, K.S., Kandybin, A. Pressure Swing Adsorption System to Purify Oxygen. U.S. Patent 5,226,933, 1993.

22. Chiang, R.L., Whitley, R.D., Ostroski, J.E., Dee, D.P. Argon/Oxygen Selective X-Zeolite. U.S. Patent 6,432,170, 2002.

23. Dee, D.P., Chiang, R.L., Miller, E.J., Whitley, R.D. High Purity Oxygen Production by Pressure Swing Adsorption. U.S. Patent 6,544,318, 2003.

24. Ferreira, D., Bárcia, P., Whitley, R.D., Mendes, A., *Single-Stage VPSA for Producing High-Purity Oxygen From Air.* Industrial & Engineering Chemistry Research, **2015**, 54, 9591-9604.

25. Ruthven, D., Farooq, S., Knaebel, K. *Pressure Swing Adsorption*; VCH Publishers: New York, 1994.

26. Mofarahi, M., Towfighi, J., Fathi, L. Oxygen Separation from Air by Four-Bed Pressure Swing Adsorption*. Industrial & Engineering Chemistry Research.* **2009**, 48, 5439-5444.

27. Jee, J.-G., Lee, J.-S., Lee, C.-H. Air Separation by a Small-Scale Two-Bed Medical O2 Pressure Swing Adsorption. *Industrial & Engineering Chemistry Research.* **2001**, 40, 3647-3658.

28. Ferreira, D., Magalhães, R., Taveira, P., Mendes, A.l. Effective Adsorption Equilibrium Isotherms and Breakthroughs of Water Vapor and Carbon Dioxide on Different Adsorbents. *Industrial & Engineering Chemistry Research.* **2011**, 50, 10201-10210.

29. Cruz, P., Santos, J.C., Magalhães, F.D., Mendes, A. Cyclic Adsorption Separation Processes: Analysis Strategy and Optimization Procedure. *Chemical Engineering Science.* **2003**, 58, 3143-3158.

30. Ruthven, D.M. *Principles of Adsorption and Adsorption Processes*; John Wiley & Sons: New York, 1984.

31. Bird, R., Stewart, W., Ligthfoot, E. *Transport Phenomena*; John Wiley and Sons: New York, 2002.

32. Ergun, S. Fluid Flow Through Packed Columns. *Chemical Engineering Progress.* **1952**, 48, 89-94.

33. Bárcia, P.S., Silva, J.A.C., Rodrigues, A.r.E. Adsorption Dynamics of C5−C6 Isomerate Fractions in Zeolite Beta for the Octane Improvement of Gasoline. *Energy & Fuels.* **2010**, 24, 1931-1940.

34. Do, D.D. *Adsorption Analysis: Equilibria and Kinetics*; Imperial College Press: London, 1997.

35. Schiesser, W. *The Numerical Method of Lines*; Academic Press: San Diego, CA, 1991.

CHAPTER VI

6 General conclusions and future work

Several industrial applications require oxygen with concentrations above 99 % - 99.5 %. The main objective of this work is the development of a single-stage pressure swing adsorption (PSA) process for the production of high-purity oxygen (≥ 99 %) from air. Also, two-stage PSA processes were studied to produce higher oxygen purities (≥ 99.5 %). Such processes should use argon/oxygen selective zeolite to obtain the desired separation. The newly-developed silver-exchange zeolite, AgLiLSX, was characterized in terms of nitrogen, oxygen and argon adsorption equilibrium. The adsorbent was found to have argon/oxygen selectivity above 1.13 in the low-pressure range (below 1.4 bar and at 25 °C) and high working capacity for nitrogen, 0.45 mol·kg^{-1}, in the same pressure range. The unique selectivity argon/oxygen, particularly at the low-pressure range, indicates that AgLiLSX potentially allows the production of 95+% purity oxygen in a single-stage vacuum pressure swing adsorption (VPSA) operation. Mono and multi-component breakthrough experiments were obtained to assess the adsorption kinetics; AgLiLSX zeolite was found to have fast adsorption kinetics. A phenomenological model, considering mass and energy balances and employing the LDF model to describe the intraparticle mass transport, was developed to describe the intraparticle mass transport and to obtain nitrogen, oxygen and argon diffusitivites on AgLiLSX adsorbent; these diffusivities are respectively 1.43 x 10^{-9} m^2·s^{-1}, 2.54 x 10^{-9} m^2·s^{-1} and 2.45 x 10^{-9} m^2·s^{-1}.

AgLiLSX zeolite was found to be very sensitive to carbon dioxide and water vapor contamination, easily deactivating when exposed to atmospheric air. The designed PSA unit considers then a section to remove these contaminants below the required threshold before the depleted air stream reach the AgLiLSX adsorbent; the

threshold limits are – 40 °C of dew point and 10 ppm of carbon dioxide. Four commercial adsorbents – two 13X-type zeolites (ZEOX OII and Z10-02ND), activated alumina (F200 7x14 Tyler mesh) and silica (KC-Trockenperlen WS 2050) – were characterized and their ability for carbon dioxide and water vapor removal assessed. Effective adsorption equilibrium isotherms were determined; zeolites, and particularly ZEOX OII, were found to have higher capacity for carbon dioxide removal and also exhibited better water vapor removal ability at low partial pressures. Also, silica KC-Trockenperlen WS 2050 was found to have a remarkable resistance to water (even liquid water) without losing capacity. Cyclic breakthrough experiments were conducted, which allowed assessing the performance of these adsorbents in near-real VPSA operating conditions. ZEOX OII was found to be the best adsorbent for removing water vapour and carbon dioxide, originating a stream with a dew point of ca. – 39 °C and 5 ppm of carbon dioxide from an ambient air stream containing ca. 450 ppm of carbon dioxide and 40 % relative humidity at 25 °C (dew point of 11 °C). Thus, a layered-bed pre-treatment section was designed comprising an initial layer of silica to remove most of the water, including condensed water, and acting as a protecting layer of the following layer of ZEOX OII. This zeolite layer aims to reduce water and carbon dioxide concentrations to the required levels; the length ratio of these two layers is 1:4 of silica:zeolite.

The layered pre-beds were designed to be included in a stand-alone single-stage VPSA unit for producing 1 L_{STP}·min^{-1} of high-purity oxygen (≥ 99 %) from air. Based on lab VPSA preliminary experiments and ASPEN simulations, a compact (dimensions of 0.7 x 0.5 x 0.85 m^3, 0.3 m^3), lightweight (120 kg) and low energy consuming (average power consumption of 1.0 kW) stand-alone VPSA was designed, assembled and optimized. Such unit, operating between 1.4 and 0.2 bar at 25 °C, comprises two beds packed with AgLiLSX (main beds) and two pre-columns packed with KC-Trockenperlen WS 2050 and ZEOX OII. The unit also includes a backfill column

to allow a backfill step, which highly improves the oxygen product concentration. An innovative and very efficient cycle was developed, synchronizing the pre-columns and four-step cycle (pressurization, adsorption, evacuation and purge under vacuum) with the main columns and seven-step cycle (pressurization, adsorption, top-to-top equalization, evacuation, purge under vacuum, backfill and again equalization). RSM methodology applied to the experimental set-up and ASPEN-based simulator were used to study the role of several operating variables on the product purity and recovery and to optimize the performance of the unit; the unit can produce a stream of 99.13 % oxygen from air, with a recovery of 6.2 % and a productivity of 9.0 $m^3 \cdot hr^{-1} \cdot ton^{-1}$.

Targeting higher oxygen purities (≥ 99.5 %) and better recoveries (≥ 10 %), two-stage VPSA processes were considered. Several configurations were tested: EPSA/VPSA (conventional equilibrium based PSA stage for producing a 95 % oxygen stream, balanced with argon, followed by a VPSA unit, packed with AgLiLSX for argon removal); KPSA/VPSA (comprising a conventional kinetic based PSA, packed with CMS adsorbent, in series with a VPSA unit, packed with AgLiLSX); and KPSA/RP/VPSA (differing from the previous for the introduction of an intermediate blower between the first and second stages).

The EPSA/VPSA configuration was studied and optimized. However, it was concluded that it was not able to reach neither the target oxygen concentration of 99.5 % nor the target recovery (≥ 10 %). The KPSA/VPSA configuration was optimized using ASPEN simulator and the role of several operating variables on product purity and recovery studied. The two-stage KPSA/VPSA unit where the KPSA stage runs a conventional Skarstrom cycle with equalization, between 1.6 bar (production pressure) and 3.5 bar (purging pressure), and the VPSA stage runs an seven-step cycle (pressurization, adsorption, top-to-top equalization, evacuation, purge under vacuum,

backfill and again equalization), between 1.5 bar (feed pressure) and 0.2 bar (evacuating pressure), was able to produce an product stream of 99.5+% purity oxygen with a recovery of 6.3 % and a VPSA stage productivity of 10.7 $m^3 \cdot hr^{-1} \cdot ton^{-1}$. Despite unable to match the required product recovery, this two-stage unit can be considered very attractive for several applications, mainly because of its low energy consumption (it does not use an intermediate compressor).

The KPSA/RP/VPSA configuration, which is similar to the previous KPSA/VPSA configuration but including an intermediate compressor, was studied. Upon optimization, RP/VPSA configuration was able to delivery a product stream with 99.5+% of oxygen with a recovery of 14+% and a VPSA stage productivity of 25.4 $m^3 \cdot hr^{-1} \cdot ton^{-1}$. The unit was also optimized to produce a very high-purity product, 99.75 % with a smaller recovery, 5.6 %, and VPSA stage productivity, 10.2 $m^3 \cdot hr^{-1} \cdot ton^{-1}$.

Future work

This thesis focuses on the production of high-purity oxygen by VPSA, achieving very interesting and innovative results, such as 99+% oxygen production in a single-stage, or 99.5+% oxygen production in a two-stage. In fact, VPSA technology for oxygen production from air has significantly evolved in the past decades towards more energy efficient, compact and low-cost units, now capable of higher purity products. Still, VPSA performance depends heavily on the adsorbent characteristics and namely in its ability to remove simultaneously nitrogen and argon from the air feed. The very few adsorbents available with argon/oxygen selectivity, such as AgLiLSX, AgMordenite or Ag-ETS-10, are still expensive, fragile and very low moisture and carbon dioxide resistant. Several companies are trying to develop new silver-free

adsorbents with high resistance to contaminants and easier to regenerate, high mechanical strength and well controlled microporosity. Present developments indicate that highly performing and low-cost materials (such as VA-class hydrophobic dipeptides) may soon be disclosed displaying argon/oxygen selectivity. Such materials, combined with ultimate valve technology and optimized PSA and VPSA cycles – such as the one developed – would soon allow the development and commercialization of high-performance, energy-efficient and low-cost PSA and VPSA units for the production of high-purity oxygen, replying to a great market demand.

APPENDIX A

Appendix A – Experimental Set-ups

A.1 Crushing strength setup

A setup for measuring crushing strength properties of adsorbent pellets was assembled by the author. This setup was used to measure pellet crushing strength of pre-adsorbents studied (Chapter II) and AgLiLSX zeolite (Chapter III).

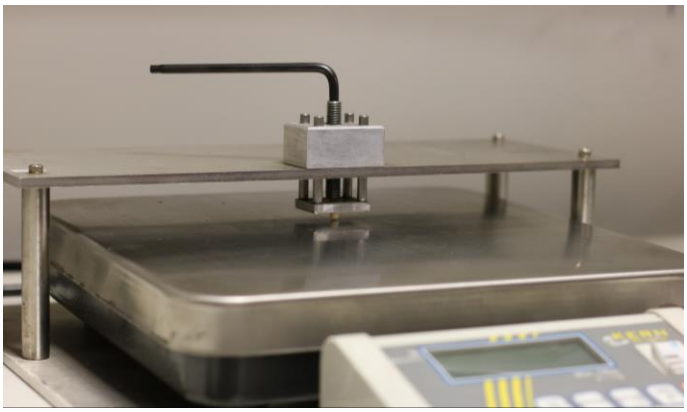

Figure A.1 – Picture of the crushing strength setup.

A.2 Adsorption setup – volumetric method

A setup for measuring adsorption isotherms and uptake curves of nitrogen, oxygen, argon and carbon monoxide was assembled by the author. This setup was used to determine carbon dioxide isotherms presented in Chapter II and to characterize AgLiLSX zeolite (Chapter III) and CMS adsorbent (Chapter V).

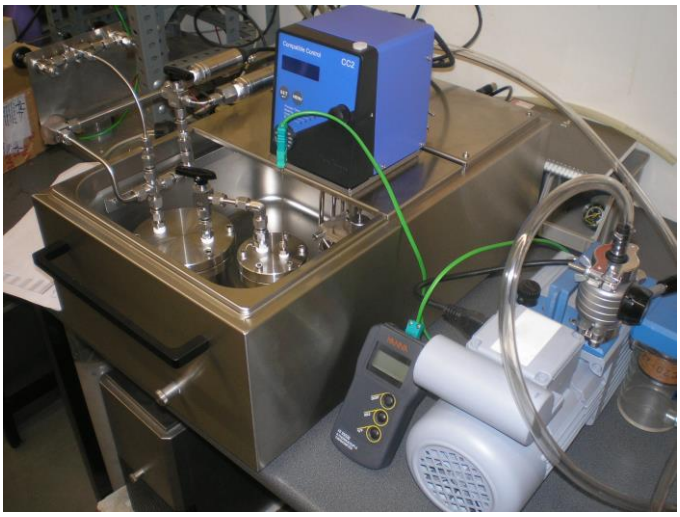

Figure A.2 – Picture of the volumetric method setup.

A.3 Adsorption setup – gravimetric method

The water vapor adsorption isotherms of pre-adsorbents (Chapter II) and AgLiLSX zeolite (Chapter III) were determined in a gravimetric method setup already assembled.

Figure A.3 – Picture of the gravimetric method setup.

A.4 Breakthrough setup

The breakthrough experiments, presented in Chapter II and Chapter III, were determined in an experimental setup assembled by the author.

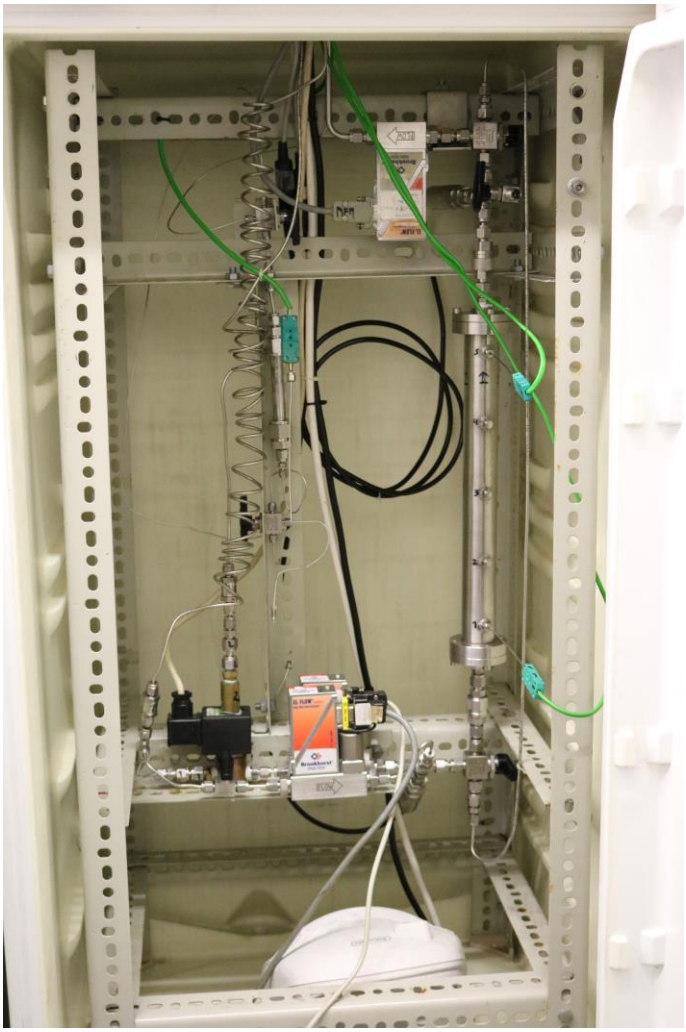

Figure A.4 – Picture of the breakthrough experimental setup.

A.5 lab VPSA

A lab PSA unit already assembled was adapted and upgraded by the author to allow VPSA operation and new cycle steps. Also, the adsorption columns were modified and sampling points were introduced along the beds to obtain the concentration profile and history of the columns. This lab VPSA unit was used to run the seven-step cycle experiments for producing high-purity oxygen in a single stage VPSA operation (Chapter IV) and it was then modified to allow different two-stage VPSA configurations, as described in Chapter V.

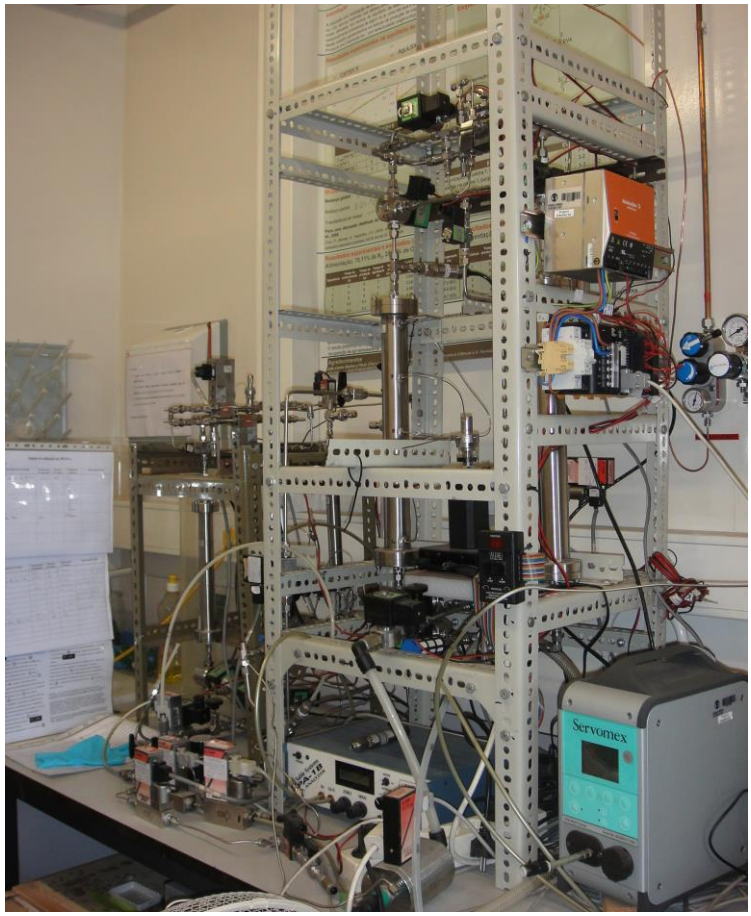

Figure A.5 – Picture of the VPSA lab unit.

A.6 Stand-alone VPSA prototype

A stand-alone VPSA unit was designed, partially assembled and tested by the author for the production of 1 L_{STP}·min^{-1} of high-purity oxygen in a single-stage operation. The technical specifications of the VPSA prototype are 120 kg of weight, 70 x 50 x 85 cm^3 of volume and average power consumption of 1 kW. The unit, including two pre-beds to continuously supply treated feed air to the main beds loaded with AgLiLSX, is fully described in Chapter IV. As presented in the same chapter, the unit was optimized for the production of 1 L_{STP}·min^{-1} of 99.1+% oxygen from air.

Figure A.6 – Picture of the VPSA prototype.

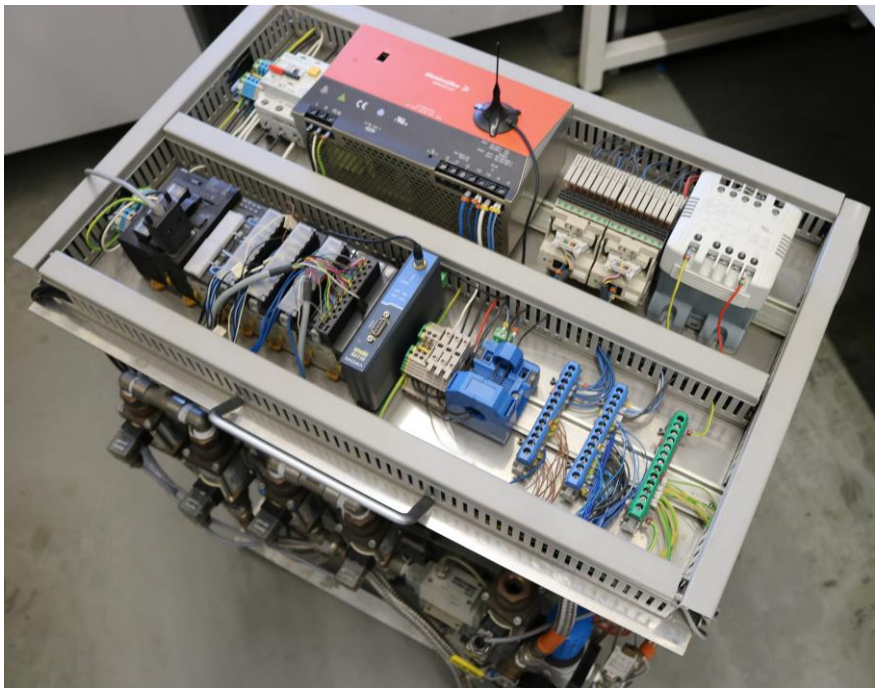

Figure A.7 – Picture of the VPSA prototype (top view).

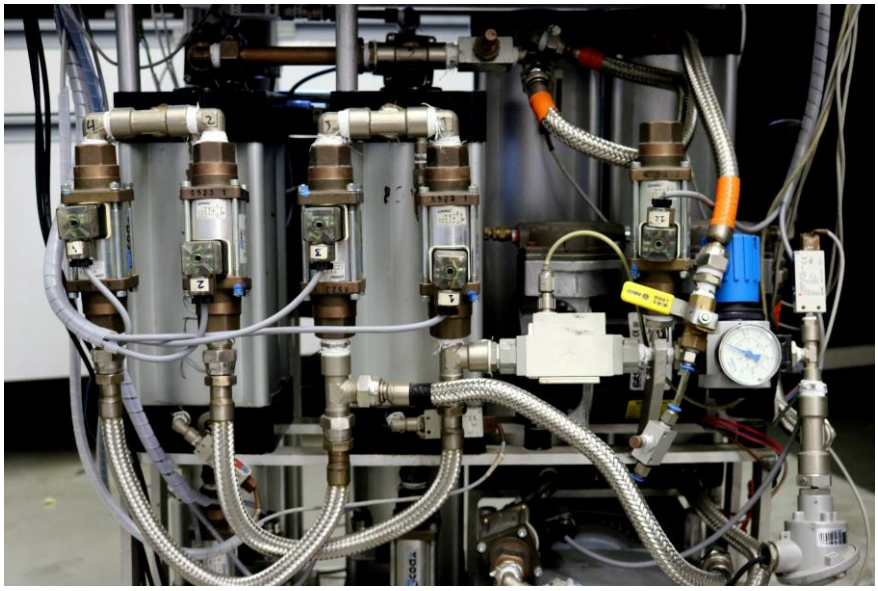

Figure A.8 – Picture of the VPSA prototype (front view).

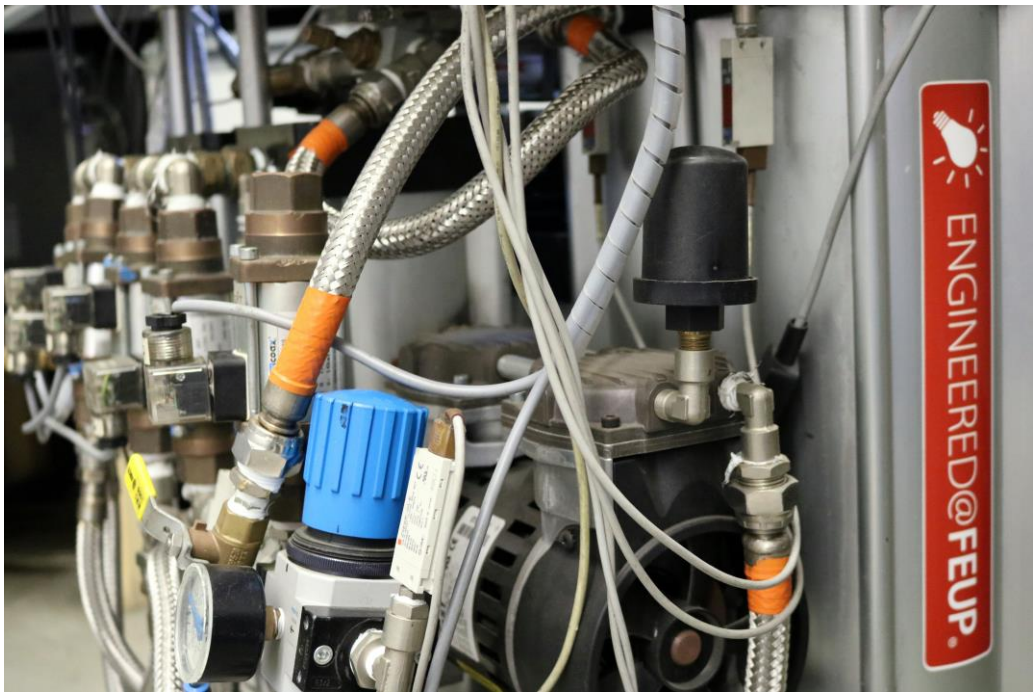

Figure A.9 – Picture of the VPSA prototype (side view).